Spring 4-7-2017

VALIDATION OF THE PRE-B CELL RECEPTOR AS A THERAPEUTIC TARGET IN B CELL PRECURSOR ACUTE LYMPHOBLASTIC LEUKEMIA

Michael F. Erasmus
University of New Mexico Medical School

M. FRANK ERASMUS
Candidate

BIOMEDICAL SCIENCES - PATHOLOGY
Department

This dissertation is approved, and it is acceptable in quality and form for publication:

Approved by the Dissertation Committee:

BRIDGET S. WILSON, Ph.D. , Chairperson

DIANE S. LIDKE, Ph.D.

GNANA S. GNANAKARAN, Ph.D.

STUART S. WINTER, M.D.

VALIDATION OF THE PRE-B CELL RECEPTOR AS A THERAPEUTIC TARGET IN B CELL PRECURSOR ACUTE LYMPHOBLASTIC LEUKEMIA

by

M. FRANK ERASMUS

B.S. Biological Sciences, California Polytechnic, USA, 2008
M.S. Molecular & Cell Biology, San Diego State Univ., USA, 2012

DISSERTATION

Submitted in Partial Fulfillment of the
Requirements for the Degree of

Doctor of Philosophy
Biomedical Sciences

The University of New Mexico
Albuquerque, New Mexico

May 2017

DEDICATION

To my amazing wife and love of my life, Evan Feldman, for her relentless support and patience through the ups-and-downs of this process. I could not have been able to get through this without her commitment and belief in my ability to achieve this degree. To my loving mother-in-law and father-in-law, Lori Brody and Fabrizio Giovannini, for their unconditional love and support. And I dedicate this dissertation to my grandfather-in-law Edmond Brody for the reminding me of the importance of hard work and positive thinking as the means to a happy life.

ACKNOWLEDGEMENTS

To my incredible mentor, Dr. Bridget Wilson. Her dedication and drive throughout this process was truly inspirational. Thank you for continually pushing me through every step of the way. I truly appreciate all of your constructive criticism that fostered my skills as a scientist. There were many memorable moments over the years and I could not have asked for a better mentor. It is an honor to have been your graduate student. I knew from the get-go this was a very intriguing idea. Thank you for taking me on for the ride.

To my dissertation committee. Dr. Diane Lidke, for her guidance on a large portion of this project. I have always been intrigued by your incredible work, so it was a true inspiration to learn from you over the years. All of your advice has been essential to the progress of these projects. Thank you for being a great mentor and critical leader. Dr. Gnanakaran, it was a tremendous privilege to work with you up at Los Alamos and to be exposed to all of the exciting research that you are doing. I am very appreciative for always keeping me in the loop to fascinating discussions and cutting-edge science. The ability to engage with you and your postdocs was very enlightening. I took a lot away from this experience, especially over the past year. I look forward to continuing to incorporate theory into my work due to this exhilarating experience. Dr. Winter, I cannot thank you enough for all of our talks and your support through the years. The ‘B Cells Gone Bad’ group was essential in keeping the clinical component a central feature of this project. I am very grateful to have had the opportunity to work with you over the past four years. From this experience I will always be reminded to keep a translational component in mind.

VALIDATION OF THE PRE-B CELL RECEPTOR AS A THERAPEUTIC TARGET IN B CELL PRECURSOR ACUTE LYMPHOBLASTIC LEUKEMIA

by

M. FRANK ERASMUS

B.S., Biological Sciences, California Polytechnic St. University, USA, 2008
M.S., Molecular & Cell Biology, San Diego St. University, USA, 2012
Ph.D., Biomedical Sciences, University of New Mexico, USA, 2017

ABSTRACT

This dissertation is built upon the fundamental idea that the pre-B cell receptor (pre-BCR) is important to leukemia cell survival and a logical therapeutic target in B cell precursor acute lymphoblastic leukemia (BCP-ALL). The pre-BCR is expressed early at a specific stage during B cell development where it plays a central role in survival of healthy B lymphocytes. This receptor is composed of the membrane heavy chain (mIgμ) associated with surrogate light chain components, λ5 and VpreB. Through the use of advanced imaging modalities, in particular two-color single particle tracking (SPT), we showed that pre-BCRs formed transient, homotypic interactions. These receptors displayed correlated motion at short separation distances that is consistent with the formation of dimers. These encounters were sufficient to generate an autonomous signal that helped to maintain leukemia blast survival. Incubation of the BCP-ALL cells with galectin-1, which can bind both λ5 and glycans, led to aggregate formation that drastically slowed down the diffusion of pre-BCRs. This correlated to a downregulation of pre-BCR signaling through proximal Syk activation. Blocking galectin-1's lectin-binding capability with saturating concentrations of β-lactose partially restored diffusion to "tonic" levels. The introduction of this sugar also impacted the downstream signaling profile. Due to these differential

diffusion and signaling profiles observed in experimental procedures we turned computational biology to gain additional structural insight. Molecular dynamics (MD) simulations supported the idea that the pre-BCR can allosterically control galectin-1's binding capacity at its distal carbohydrate-binding site (CBS). We generated a monovalent Fab against the dimer interface of the pre-BCR using phage display technologies and showed that it not only could disrupt dimerization but also disrupted downstream signaling. Due to recent clinical advances in chimeric antigen receptor (CAR) T cell therapy, we reformatted our Fab into a scFv, the binding region of the CAR, using genetic cloning techniques. Through the use of computer-aided design we successfully generated a scFv with high affinity to the VpreB target. This antibody binding fragment was cloned into a lentiviral vector containing the CD28 co-stimulatory domain and immunoreceptor tyrosine-based activation motif (ITAM)-containing TCR-CD3ζ. After efficient transduction of primary CD8+ T cells, we have shown efficient *in vitro* efficacy against BCP-ALL cells.

Table of Contents

LIST OF FIGURES

LIST OF TABLES

CHAPTER 1: INTRODUCTION

Model system: B cell precursor acute lymphoblastic leukemia

Acute lymphoblastic leukemia is the most common cancer in children (*1*) and an aggressive neoplasm in adolescents and adults (*2*). While conventional chemotherapy has improved the overall long-term survival rate, there are still concerns with existing treatment options (*3*). In children, early administration of harsh chemotherapeutic agents has been shown to severely hinder long-term development (*4*). In addition, relapse-free survival rates of patients with high-risk leukemia have plateaued with conventional therapy options (*5*). Over 20% of patients treated in the relapse setting and 5% of newly diagnosed patients treated with chemotherapy died due to complications associated with immune suppression (*6, 7*). These factors alone motivate a push for better diagnostic procedures and targeted therapy that can lead to more individualized care. Appropriate patient stratification based upon cytogenetics (*8*) and protein expression profiles (*9*) can be used to administer a more personalized approach to treatment. Further, the number of targeted drug options continues to increase, which includes tyrosine kinase inhibitors (TKIs) (*10, 11*) and antibody-based therapies (*12, 13*). Together, better diagnostics and therapy options will allow oncologists to optimize the therapeutic window by maximizing drug efficacy and minimizing off-target effects. This continued push to characterize the diverse signaling capacity of leukemia and the incorporation of novel therapies will be essential if we hope to improve upon the long-term success that extends beyond relapse-free survival.

Acute lymphocytic leukemia arises from both early B and T lymphocyte lineages, with precursor B ALL (BCP-ALL) accounting for approximately 70% of cases. This dissertation reports significant strides in the characterization of a novel target in BCP-ALL. Through the use of advanced imaging modalities and computational biology, we have identified mechanistic evidence to support targeting the pre-B cell receptor (pre-BCR) in this B cell malignancy. We show that the pre-BCR is not only essential to the survival of leukemic B cells but also has unique features that make it a highly desirable target. This

evidence led us to the development of a novel chimeric antigen receptor (CAR) T cell therapy against the pre-BCR that is currently being tested for preclinical efficacy. We propose that pre-BCR targeting offers potential advantages over current anti-CD19 targeted CAR T therapies (*14*, *15*), by avoiding the loss of mature B cells and maintaining existing adaptive immunity against common pathogens. The high risk of opportunistic infections has hindered the treatment success in BCP-ALL (*6*, *7*).

The dissertation contains three principal aims, each based around the central premise that the pre-BCR is a contributor to leukemia cell survival and a legitimate therapeutic target in BCP-ALL. The first aim set out to experimentally identify the key initiating mechanism of the pre-BCR in context of leukemia and its role in supporting leukemia blast survival. The second aim applied current computational approaches to examine the dynamic behavior of pre-BCR interactions with galectin, a lectin and pre-BCR ligand abundant in the bone marrow microenvironment that has been implicated in BCP-ALL resistance to therapy. The third aim focused on the preclinical development of a targeted therapy against the pre-BCR, as a proof-of-principal for use in human trials.

The pre-BCR checkpoint in B cell development

Early in B cell development, there is an important transition from pro-B cells to pre-B cells (*16*). This requires a shift in the dependence from the IL-7/IL-7R pathway to pre-B cell receptor (pre-BCR) signaling pathway (*17*) and bypassing a series of important checkpoint controls (**Figure 1** – adapted from review by (*18*)). To initiate this switch, a functionally rearranged Ig heavy chain (μHC)

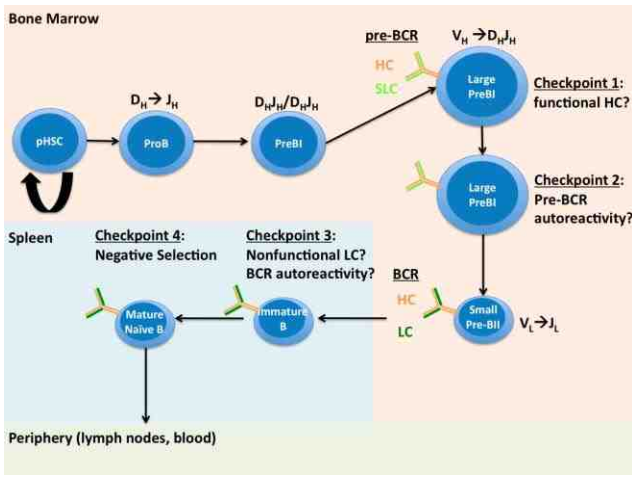

Figure 1. Early B cell development checkpoints

must associate with surrogate light chain components (VpreB/CD179a and λ5/CD179b)(*19*) (**Figure 2**). This complex must be expressed on the membrane surface of the B cell, where it triggers a weak signal through the pre-BCR's signaling subunits (Igα/CD79a and Igβ/CD79b)(*20-22*). The pre-BCR signaling pathway is initiated by Lyn-mediated phosphorylation of immunoreceptor tyrosine-based activation motifs (ITAMs) on the cytoplasmic tails of both Igα and Igβ (*22*). Phosphorylated ITAMs generate a binding site for dual SH2-domains of spleen tyrosine kinase (Syk) leading to activation of its direct binding partners including phospholipase Cγ (PLCγ), phosphoinositide 3-kinase (PI3K), and SH2 domain-containing SLP65 (BLNK) (*23*). Activation through this pathway leads to several different cell-fate decisions including cell cycle exit (*24, 25*), chromatin remodeling (*26*), gene transcription (*27, 28*), and production of factors associated with the control of central B cell tolerance (*29-31*). In Chapter 2, we show that these autonomous (aka "tonic") signals are mediated through homotypic interactions through the pre-BCR and are essential for the survival of leukemic B cells (*20*).

Tens of millions of pre-B cells are produced in a healthy individual daily and eradicated via this essential pre-BCR checkpoint (*32, 33*). In its role as a contributor to early B cell malignancies, autonomous signaling by the pre-BCR is finely-tuned and is disrupted by either cell-permeable inhibitors of the positive signaling axis or negative regulators that tip the balance towards hyper-activation (*34*). Constitutive activation of the pre-BCR signaling pathway has recently been used to stratify pre-BCR+ versus pre-BCR- BCP-ALL populations (*9*). Patients with defining genetic lesions such as t(1;19)(q23;p13) exhibited enhanced pre-BCR signaling profiles that correlated with decreased relapse-free survival (*9*). This pre-BCR+ subset, not only exhibited constitutive activation of pre-BCR signaling but also showed a consistent upregulation of the transcriptional activator, BCL6. BCL6 has been described as a classical proto-oncogene (*35*) and serves as an activator of key signaling components of the pre-BCR pathway (*IGLL1, VPREB1, BLK, BANK1, SYK*) (*9*). The expression of the pre-BCR and BCL6 were undetectable in a predominant number of cases (85%) including MLLr, BCR-ABL1, ETV6-RUNX1 and hyperdiploid ALL (*9*). Interestingly, treatment of this pre-BCR- subset (i.e. Ph+ leukemia) with small molecule TKI therapy induced strong upregulation of BCL6 (*36*). In contrast, targeted TKI therapy

against the pre-BCR signaling components, such as Syk and BTK, in the pre-BCR+ subset led to a significant reduction in BCL6 expression (*9*). It was shown that a "retro-inverso" BCL6 peptide inhibitor induced cell cycle arrest, impaired colony formation and sensitized the pre-BCR+ ALL blasts to chemotherapy (*9*).

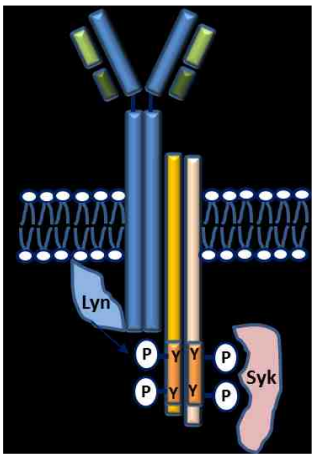

Figure 2. The preBCR

Hyperactivation of the pre-BCR signaling pathway also lead to the induction of apoptosis (*20, 37*). Further, it was shown that malignant transformation of leukemic B cells tolerate this increased signaling by the concurrent upregulation of negative regulatory molecules including SPRY2, DUSP6, ETV5 (*38*). These data suggest that, similar to healthy B cells which tolerate only delicately tuned balance of negative and positive signals, leukemic B cells are also regulated by a similar process. Thus, in addition to the more common therapeutic strategy of inhibiting oncogenic addiction (*37, 39, 40*), placing the pre-BCR in overdrive may also trigger cell death and represent new opportunities for leukemia therapy. In Chapter 2, we set out to understand the biophysical mechanisms that tune the autonomous signaling threshold in live leukemic B cells. We also explore the possibility for combination therapy, where pre-BCR targeting may lower the required dose of chemotherapy.

Several different initiating mechanisms have been proposed to drive pre-BCR signaling. These include self-association between μHC or surrogate light chain (SLC) components (*21, 41, 42*) and crosslinking by stromal-bound galectin-1 (*43*). We were particularly interested in addressing questions such as: how do serial engagement and duration of pre-BCR homo-interactions tune the strength of the pre-BCR signaling in leukemic B cells? Is there a difference in the receptor dynamics when galectin-1 is introduced to the system to aggregate pre-BCR? How do these distinct mechanisms of engaging the pre-BCR impact the downstream signaling profile in leukemic B cells?

Technical Approach I: Single Particle Tracking

Many techniques have been employed to measure the lateral diffusion of particles on the membrane surface. Common approaches that have been used include fluorescence recovery after photobleaching (FRAP) and fluorescence correlation spectroscopy (FCS)(*44-47*). Though effective in determining ensemble averages of fluorescently-tagged molecules, these methods are limited in their ability to detect small-scale heterogeneities or short-lived molecular interaction (*48*). To gain a better spatiotemporal resolution, single particle tracking (SPT) approaches have been employed. SPT can capture trajectories of individual particles at relatively fast (millisecond) time-scales (*48, 49*). This is achieved by particle localization of individual proteins labeled with advanced fluorescent markers that can bring the localization accuracies down to single-digit nanometer scale, as described in this section.

SPT has seen a major revolution since early studies back in the 1980s, which used gold nanoparticles to visualize surface properties and later moving receptors on live cells (*50, 51*). A major advantage in the use of gold, latex, or silica particles, which ranged in size from 200-1000nm, was inherent in their physical and optical properties such as a large scattering cross-section that enabled optimal spatial localization down to 1nm and enhanced photostability, which substantially reduced photobleaching. These factors allowed for longer sequence acquisitions (up to minutes) at relatively fast frame rates (*48, 52*). However, though the large cross-sections were beneficial to optical properties of these particles, these bulky probes posed a problem in that they could putatively interfere with the protein's local environment (*53*). It had been shown that these particles could induce cross-linking, alter the diffusion profile, and sterically hinder the protein's interaction network (*53, 54*). These experimental artifacts led many groups to develop probes with more optimal phyico-chemical (smaller size) and optical properties (limited photobleaching).

Small molecule fluorescent dyes with diameters several orders of magnitude smaller than gold nanoparticles (1-2nm) would ensure little/no impact on the proteins environment.

Major advances in the use of fluorescent molecules occurred in the early 1990s when researchers showed that single molecules dyes coupled to molecular targets could be detected at room temperature (*55*). Soon after, these small organic dyes were being applied to study lipid motion (*56*) and later receptors (*57*). Unfortunately, due to their reduced photostability and decreased absorption cross-section, photobleaching and poor localization accuracies plagued the experimental design, respectively. These artifacts restricted molecular tracking to just seconds and increased the localization indeterminations (*48*). To reduce photobleaching, scientists added free oxygen scavengers, which were toxic to cells and (*58*) severely limited the capacity to do live cell imaging. Thus, it became evident that an improvement to SPT experimental design would come as a balance between the physico-chemical and optical properties of these probes.

Quantum dots (QDs) offer a medium between the size and optical limitation of small organic dyes and larger gold nanoparticles materials, respectively. Two seminal papers published in *Science* back in 1998 (*59, 60*) showed that Quantum dots (QDs) could be conjugated to biomolecules to selectively target specific biomolecules on the cell surface. This opened the door to QD-SPT experiments with a large increase in their use into the present day (*61*). QDs are ten times as bright as organic dyes with an increased photostability that removes artifacts associated with photobleaching and allows for longer acquisition times (up to tens of minutes) (*48*). Additionally, QDs exhibit a broad absorption spectra and narrow emission, which allows for multiplex imaging via simultaneous excitation of spectrally distinct QDs (*61*). Multi-color SPT experiments with different spectral properties have been applied to several studies (*62, 63*). Under this setting distinct emissions can be sent to separate channels linked to the same charge-coupled device (CCD) camera. While smaller than gold particles detailed above, QDs are still relatively large (10-30nm diameter). Again it has been postulated and shown that certain features of the QD such as polyvalency (multiple binding sites) might severely impact the local interaction network. To overcome these hurdles, improved bioconjugation have been implemented to minimize the number of probes per QD and/or obtain more predictable ratios. Further, manufacturing efforts are being incorporated to reduce the size of the QDs (*64, 65*). Another major shortcoming of QDs is due to blinking, also called power-law on-off

intermittent emitting behavior (*66*, *67*). Different nanochemistry designs (*68*, *69*) or post-processing algorithms to reconnect trajectories (*62*, *69*, *70*) have been implemented to overcome this QD limitation.

Incorporation of QDs into SPT experiments allows for the quantitative measurements including diffusion rates, co-localization and organization within live cells (*61*). The technique has been applied to the biomedical research to answer several important questions involving membrane receptor dynamics (*64*, *71*, *72*) and to a variety of other molecules in a range of systems (*73*). SPT data consists of trajectories of diffraction-limited images of particles captured by microscope. One of the first steps required in SPT is to quantitatively determine the location of the particle with subdiffraction resolution. The theoretical framework is based on the fact that a single point is displayed in the detector as a concentric ring with decaying intensity as the distance from the center gets larger. The centermost ring, called the Airy disk, exhibits the greatest intensity and thus its location can be estimated using the 2D spatial fit to microscopes point spread function (PSF). This allows for a positional precision and accuracy to within a few nanometers. Another important criterion to achieve this level of resolution is through low density labeling whereby individual spots must be well resolved in space. This represents a limitation to SPT experiment as only a small sample of molecules from the entire population can be investigated during a given acquisition sequence. After acquiring thousands of images at select rates (we used 20 frames/sec), these centroid positions are linked to reconstruct trajectories of individual particles (*71*, *74*, *75*). An essential problem to overcome during the reconnection phase is to account for lost blinking particles or exhibited aberrant localization. Several groups have developed algorithms to account for these problems (*62*, *69*, *76*) and we have incorporated them into our tracking algorithms to study pre-BCR dynamics (*20*). Additional algorithms are subsequently employed in order to characterize the dynamics of proteins, which is often achieved through mean-square displacement (MSD) calculations from which the diffusion coefficient can be extrapolated based on type of underlying motion that is being modeled (i.e. Brownian, confined, immobile, directed, and anomalous)(*49*). Further, multi-color QD tracking have been utilized to provide insight into interactions that occur at the membrane surface and provide additional quantitative

information such as correlated motion, state-specific diffusion, and dimer lifetimes (*20, 62, 77, 78*).

Many receptor interactions, such as pre-BCR/pre-BCR dimers, at the membrane are fundamental to cell response regulation. Torreno-Pina et al (*73*), have characterized molecular interactions into two broad categories from homo-interactions to hetero-interactions based on the nature of the species (identical versus different) involved in the interactions. Early studies suggested that the fluid mosaic model could readily explain lateral diffusion of receptors through the lipid bilayer, whereby hetero- and homo-interactions between proteins would occur from collisions between particles that displayed purely Brownian diffusion (*79*). However, efforts over the years have revealed several different flavors of motion occurring at the membrane, which includes Brownian, directed, confined and anomalous diffusion [see (*49*) for early extensive review]. SPT has provided insight into the role oligomerization plays in initiating signaling in variety of immune response (*80*). Roles that have been implicated for receptor oligomers include an enhanced capacity to bind multimeric ligands, or forming signaling scaffolds at the cell membrane (*81-83*). Characterization of hetero-interactions with SPT technologies, especially through the interactions to the extracellular glycocalyx matrix, is also gaining an increased level of attention (*84*). We provide a more detailed description of the use of two-color SPT experiments in our paper (*20*), or can be found elsewhere (*62*).

Insights into pre-BCR Homotypic Interactions through Quantitative Imaging

Our goal in this study was not only to estimate global diffusion patterns of individual receptors but also to reliably distinguish and capture two different particles engaging on the surface of live cells. Capturing two interacting dimers on the extracellular surface of live cells is non-trivial. The first goal was to generate bright, stable fluorescent probes that could track individual pre-BCRs for relatively long periods of time. We opted to use Quantum dots (QD) coupled to monovalent probes. As detailed above, the enhanced photo-stability and narrow emission spectra properties that allow for long acquisition periods and concurrent collection of spectrally distinct particles (*62, 77, 85, 86*). Next, we needed to

overcome the limitations of the diffraction limit of conventional fluorescence microscopy (~250nm), by adopting modern practices for single particle tracking of different receptors with two spectrally distinct probes (*62*, *63*). This approach uses a beam splitter to project spectrally distinct emissions of quantum dots onto a CCD camera, as detailed above. We used a custom-designed image registration algorithm that allowed us to map the relative positions of each spectrally distinct trajectory (*62*). Third, we needed to avoid potentially disrupting the pre-BCR dimer itself via crosslinking and/or inhibiting the dimer interface. We achieved this by targeting the pre-BCR's Igβ signaling subunit with a monovalent Fab. This prevented crosslinking artifacts and avoided regions implicated in dimerization (*21*, *41*). The relative positions of these two-color trajectories were then processed by a set of post-processing algorithms that could calculate dimer lifetimes, correlated motion, and state-specific diffusion (i.e. dimer-state versus free-state)(*62*). These important measures provided quantitative information that could be used to compare the impact of selective modulators that target the pre-BCR pathway.

Using this advanced imaging modality, we were able show that dimer events occur on surface of live BCP-ALL cell lines and patient samples. These were characterized by transient homotypic interactions mediated through the SLC. We designed a monovalent Fab fragment specific for the SLC using phage display technologies. Incorporation of this Fab as a dimer-blocking agent in our SPT experiments disrupted homotypic interactions as exemplified by increased pre-BCR diffusion, decreased correlated motion and faster dimer off-rates. Fab treatment impacted both short- and long-term signaling, leading to decreased phosphorylation of activation markers (pITAM,pSyk) and downregulation of BCL6 expression, respectively. These downstream signaling readouts were very similar to profiles observed when directly inhibiting downstream signaling partners such as Lyn and Syk. Further, this data correlated with decreased survival pre-BCR+ leukemic B cells. In conjunction with recent evidence that suggested advantages to using potent tyrosine kinase inhibitors against downstream effector molecules of the pre-BCR pathway, we showed that we could also target the initiating mechanism at its source to directly impact leukemia cell survival. After validating that weak signals mediated through the pre-BCR were sufficient

to maintain leukemogenesis, we also evaluated how larger and more stable pre-BCR aggregates might impact the signaling profile in BCP-ALL.

Galectin, a pre-BCR crosslinking agent

Galectin-1 belongs to a family of β-galactoside binding proteins known for their carbohydrate binding properties (*87*). These lectins can form a homodimer of 14kDa subunits with each monomeric unit containing a single carbohydrate-binding site (CBS)(*88*). After secretion into the extracellular space, galectin-1 exists in a monomer/dimer equilibrium with a binding constant of ~7μM (*89*), which is mediated through the extreme N- and C-terminal regions of each monomeric unit (*87*). It has been shown that upon carbohydrate binding the dimer/monomer equilibrium shifts in favor of dimerization (*90*). Many have suggested that the multivalent nature of galectins entail crosslinking capabilities that are important to an array of biological responses (*91-94*). This includes aggregation of specific cell surface glycoreceptors that have been shown to promote signal transduction (*89, 95, 96*). Galectin-1 is of special interest in the context of BCP-ALL, since it can binds directly to the pre-BCR. As discussed further below, this binding site is distinct from the carbohydrate binding site (*96*).

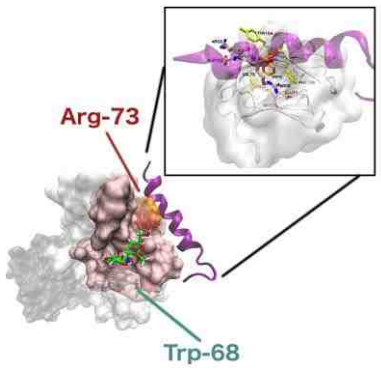

Figure 3 – Galectin-1 Structure. Galectin-1 with chain A (white) bound to λ5 (purple) and carbohydrate (green). CBS (pink) and λ5-binding region (orange) are displayed. Key Trp-68 & Arg-73 residues shown as bonds. Critical λ5 binding sites magnified.

Bone marrow stromal cells can present galectin-1 by virtue of binding to glycoreceptors, including integrins, on their extracellular surfaces (*97*). Interactions between galectin-1 and the pre-BCR trigger the formation of a "developmental synapse" at the contact zone between stromal and B cells, which has important roles during precursor B cell development (*98*). These stromal/pre-B cell interactions have also been shown to have an important role in B cell malignancies (*99-101*), with some suggesting galectin-1 as a valid therapeutic target (*102, 103*). Considerable evidence has shown that galectin-1 serves as an unusual pre-BCR ligand (*43, 104, 105*). Dimeric galectin-1 can aggregate the pre-BCR at the membrane surface (*43, 96, 106*). Structural evidence for this hypothesis has been supported through NMR experiments, where it was shown that galectin-1 could directly bind to the pre-BCR's λ5 region via protein/protein interactions (*96*). To understand these multivalent galectin-1 interactions in the context of pre-BCR+ leukemia, we employed SPT to measure how exogenous galectin-1 impacts pre-BCR dynamics. Our results not only revealed drastic changes in the pre-BCR's biophysical profile but also notable changes in downstream signaling profiles in leukemic B cells.

Introduction of galectin-1 *in vitro* resulted in large clusters of the pre-BCR that could be readily captured by confocal microscopy. This also corresponded to a drastic slowdown of the pre-BCR in SPT experiments. In contrast to what might be expected, galectin-1 introduction correlated to a decreased pre-BCR activation profile. Blocking galectin-1's lectin-binding properties increased receptor diffusion. This also, increased phospho-activation of the pre-BCR pathway above that seen under tonic signaling conditions. These findings suggest that galectin-1/pre-BCR and galectin-1/glycoreceptor interactions may be important in driving different signaling profiles in both healthy and malignant settings.

Interestingly, introducing galectin-1 in both of these conditions (+/- carbohydrate) led to the downregulation of BCL6 expression. Modulation of the finely balanced pre-BCR signal upward or downward impacts the expression of a positive feedforward loop implicated in BCP-ALL. This information adds additional complexity to the pre-BCR signal initiating mechanism and reveals the differential signaling capacity that can be propagated through this transmembrane receptor.

Recent studies have suggested that pre-BCR/galectin-1 interactions lead to a changing affinity of galectin-1 for specific sugars. A recent model proposed that pre-BCR binding weakens galectin-1 affinity to β-linked N-Acetylactosamine (LacNAc) sugars in favor of α3-SiaLacNAc groups found more preferentially on pre-B cells. This finding points to galectin-1 as the link between the pre-BCRs and eventual escape to new signaling niches within the bone marrow microenvironment (*97*). To understand the influence of pre-BCR and carbohydrate binding on galectin-1 at a more detailed structural level, we turned to theoretical biology.

Technical Approach II: Molecular Dynamics

Advantages of Coupling Molecular Simulations to Experiments

We are in an age that can understand macromolecular function at a more sophisticated level (*107*). Just as SPT continues to be used to overcome spatial and temporal limitations inherent to low-resolution microscopy (diffraction limit or ensemble average limitation of FRAP experiments), structural biology and molecular simulations offer a more refined resolution at shorter spatial and temporal scales (*108*). Intrinsic to this are advances in electron microscopy, nuclear magnetic resonance (NMR), and X-ray crystallography that have significantly expanded our understanding of protein interactions. The protein data bank (PDB) contains over 100,000 entries with over 20,000 small molecules bound to macromolecules (*109*). It is evident that the conformational space, thermodynamic properties and intermolecular attractions cannot be understood at the desired level of atomic detail from these experiments alone. Pioneering research back in the 1970s started to merge experimental (*110, 111*) and theoretical work (*112*) to derive function from

molecular motion. In the advent of enhanced computational power, improved sampling procedures, and more accurate potential energy functions, we can now construct models that show a stronger correlation to experimental data. The predominant approaches currently employed for molecular simulations include molecular dynamics (MD) simulations and normal mode analysis (NMA). MD simulations are widely used to sample local (0.1-0.5nm, 10fs-0.1s), rigid body (0.1-1.0nm, 10ns to 1s), and large-scale motions (>0.5nm, 10μs to minutes) representative of different distributions (*113*). Implementation of advanced sampling algorithms coupled with computation parallelization, such as hybridization that couple CPU/GPU capabilities, have significantly increased the scale of biomolecular system (*114*). Through the use of spatial decomposition, the entire system may be distributed to different processors whereby only a small portion of the system needs to be simulated by each processor. Due to these improved computing technologies, simulations that involve > 50,000 atoms are now routine and simulations over $1x10^6$ atoms are even practical, so long as computing resources are available (*109*).

Theoretical Framework of MD

A comprehensive description of MD theory can be found elsewhere (*115, 116*). The basic premise of MD simulations requires the integration of Newton's equations of motions at specified time steps, typically in the femtosecond ranges to account for fastest motions of the system (i.e. hydrogen bond vibrations). After a defined period of time (typically tens to several thousands of nanoseconds, depending on computational power), one obtains molecular trajectories containing information of the positions, velocities and accelerations of the atoms within a system through the course of the simulation. To develop molecular trajectories of motion that are more representative of experimental systems, appropriate assumptions and functions defining the potential energy surface are required. A precise molecular description of any given system would depend upon solving the time-dependent Shrödinger equation of N-particle wave function that depends upon both nuclear and electronic degrees of freedom. Because macromolecular systems involve thousands to hundreds of thousands of interacting particles, this approach would readily become computationally exhaustive. The Born-Oppenheimer approximation allows us to assume that electrons can take on the motion of the nuclei. Thus, only nuclear motion needs to be

considered while the degrees of freedom of electrons impact the dynamics of the nuclei through the potential energy surface. With nuclear motion described in this way, to solve for the potential energy, a large number of semi-empirical energy functions can characterize both bonded and non-bonded interactions. These force fields are complex equations but they are relatively easy to calculate. The bonded terms include harmonic potentials for bond length and angles, periodic functions for bond rotations or improper dihedrals. Non-bonded terms include Coulombic interactions and Lennard-Jones for electrostatic and van der Waals interactions, respectively. The defined parameters within these semi-empirical force fields equations (AMBER (*117*), CHARMM (*118*), GROMOS (*119*), OPLS(*120*) are of specific flavors that take on slightly different forms and have been incorporated into the framework of different molecular dynamic simulations programs (i.e. AMBER, CHARMM, GROMACS, NAMD).

Practical Application of MD Simulations to Study Protein Allostery

The ability of MD simulations to explore space and timescales concurrently makes it a particularly useful tool to study protein allostery (*121*), as we did in this study. Allostery is defined as a stimulus at one site altering the properties at a different site, often through a change in conformation and/or dynamics of the protein (*122, 123*). MD simulations have shown to be increasingly useful for determination of allosteric effects because they give an all-atom level of detail at both spatial and temporal scales and allow for defined perturbations to be introduced into the biomolecular system (*121*). Allostery is not only important in understanding basic biological function of proteins, but has also been shown to be important for immunological escapes (*124*), drug-design (*125*), and protein engineering (*126*). The allostery problem must consider several different factors. First, appropriate docking of the protein into the binding site is an essential criterion to understand the impact of distal binding effects. When there is no information about the binding site ("blind docking"), several approaches can be employed (*127, 128*). When experimental data can provide information on the binding epitope then the determination of the binding mode can be much more readily predicted. In this manner, one can position the ligand at the allosteric site at the start of the simulation and allow the protein to undergo conformational changes so as to adapt during the simulation (*129, 130*). Second, it is

important to understand the nature of allosteric coupling. This aims at addressing questions related to how a stimulus at one end may alter interactions of the protein at a different site or how sites not initially implicated might be under allosteric control. One of the most straightforward approaches to studying allostery is to look for interdependent motions at particular sites of interest (i.e. binding site of interest). This can be done through basic measurements such as distance distributions or dihedral angles between four consecutive atoms of interest over the course of the simulation. The determination of allosteric effects is often challenging because changes that influence one site may be very subtle. This is made more difficult by the continuous fluctuations inherent in protein dynamics. To overcome this hurdle a variety of methods have been described to identify residues coupled allosterically (*131*). These include protein topological analyses (graph theory, statistical coupling analysis and perturbation algorithms)(*132-134*), interaction energy (*135*) or correlated matrices (*136-138*).

Importance of Statistical Mechanics & Advanced Sampling Procedures

Another macroscopic property that can be derived from MD simulations and is important to understanding the protein interaction network is the free energy of binding. The most straightforward approach to extrapolate binding energy of a ligand to given protein pocket would be to run lengthy simulations that could capture different ligand conformations in both bound and unbound states. However, though improved computing power may allow for this "brute force" approach, ligand binding still may occur at timescales that are too slow to be sampled by MD simulations. To overcome this hurdle, a large number of short simulations may be coupled to statistical modeling to bias the system toward a particular phenomenon (i.e. ligand in bound versus unbound state). Apart from just understanding the motion of particles, much more information can be extrapolated about a system through probabilistic configurations. For a more detailed review of statistical mechanics as it applies to determining thermodynamic properties through molecular dynamics see here (*139*). Through the use of statistical mechanics and its treatment of systems at equilibrium with a set of probability functions, we can then extrapolate macroscopic properties of a system (temperature, chemical potential, free energy) through these microscopic simulations. In order to calculate free energy change of a biomolecular phenomenon, such

as carbohydrate affinity within galectin'1 binding pocket, one can bias the simulation with an additional potential along a reaction coordinate (i.e. center-of-mass distance from the binding pocket). Several different methods have been employed to estimate binding free energies from MD simulations using these advanced sampling procedures including free energy perturbation (FEP) (*140*), Molecular Mechanic/Poisson-Boltzmann surface area (MM/PBSA) (*141*), linear interaction energy (LIE) (*142*), metadynamics (*143*), replica exchange umbrella sampling (REUS) (*144*), or umbrella sampling (US)(*145*). In this study, we employed many of these techniques, including linear interaction energy and umbrella sampling, to show that the conformational changes induced by pre-BCR binding significantly altered the binding affinity for select carbohydrates. These approaches were also applied to aid in the discovery of probable binding sites of the scFv within the pre-BCR's VpreB. An introduction to these findings are detailed here.

MD Simulations Reveal Allosteric Control of Galectin-1 by the pre-BCR

A model proposed by (*97*) shows the flexible nature of galectin-1/glycan interactions upon pre-BCR engagement and may have important implications in pre-BCR signaling profiles. Further with experimental data also suggesting that galectin-1's dimer/monomer equilibrium may be disrupted upon carbohydrate binding (*90*) led us to reason that pre-BCR binding might also impact galectin-1's dimer stability. Chapter 3 shows our approach to study the dynamic behavior of this pre-BCR/galectin-1 protein/protein interaction, based upon use of all-atom MD simulations and statistical mechanics to corroborate experimental findings in the literature. Using structural coordinates and critical intermolecular information derived from X-Ray and NMR structures, we built molecular models of the galectin-1 protein bound to the λ5 region of the pre-BCR (*96*). Next, we constructed an explicit solvent system and conducted large-scale (>100,000 atoms) MD simulations using GPU/CPU hybrid acceleration to show that the pre-BCR allosterically modified the structural integrity of galectin-1's carbohydrate-binding site (CBS). Through the use correlated matrices detailing molecular motion, particularly principal component analysis (PCA)(*137*), we not only showed that the pre-BCR stimulus exhibited a distal disruptions that would influence galectin-1's carbohydrate binding interactions but also might impact

dimer/monomer equilibrium. Further, we employed linear interaction energy (*146*) and umbrella sampling (*145*) to show that the conformational changes induced by pre-BCR binding significantly altered the free energy of binding for select carbohydrates. This work shows another application of MD simulations to study allostery in proteins as well as incorporation of advanced MD algorithms to extrapolate biophysical measurements that can be directly compared to experimentally derived calculations.

Small molecule and antibody-based therapeutics for leukemia

There is currently a major call for effective targeted therapies in BCP-ALL, including small molecule inhibitors of signaling pathways that drive leukemogenesis or promote cell survival (*10, 14*). Potential targets in the acute leukemias include Jak-Stat, Abl, PI3K, Map Kinases, Syk and Btk. Because these proteins are widely expressed in both innate and adaptive immune cells (*9, 37, 147*), there is high risk for off-target effects including dampening of the immune response to secondary infections. Further, treatment with TKIs in BCP-ALL has shown many reported cases of relapse (*36, 148*). The potential escape mechanisms are inherent in the complexities of the B cell signaling network, which can be easily influenced by microenvironmental factors (*99*), receptor crosstalk (*149*), upregulation of negative feedback regulators(*38*), genetic lesions (*150*), protein expression levels(*9*), and oncogenic mutations (*151*).

The other predominant choice for targeted therapy in leukemia involves the use of antibody-based technologies that target B cell markers expressed on the membrane of precursor B cells (*152, 153*). For example, therapy based upon delivery of intact IgG1 induces direct killing of the leukemic B cells via antibody-dependent cytotoxicity (ADCC) and phagocytosis (ADCP), antibody-dependent toxin delivery(*154, 155*). As discussed below, there have been considerable clinical advances with methods that employ the adoptive transfer of genetically modified immune effector cells (*156, 157*).

The design and promise of CAR T cell therapy.

Dating to more than half a century ago, it has been known that T cells that have been adoptively transferred may have the potential to find and destroy cancer cells (*158*). In many of early studies involving adoptive transfer, T cells did not have sufficient capacity to kill the cancer (*159-161*). To improve the ability to hone in on the cancer to improve efficacy, groups started to engineer T cells with receptors that would improve their targeting potential. Clinical trials that incorporated engineered T cells first used T cell receptors (TCRs) with specificity for proteins expressed on tumor cells. While this approach would allow for the targeting of both intracellular and extracellular targets, cancer cells resisted this targeted approach by downregulation of MHC class I expression (*162*). To overcome this MHC-restriction, required for recognition via the TCR, chimeric antigen receptors (CARs) have been developed. CAR T cell therapy is based upon genetic modification of the patient's T cells made to express a chimeric antigen receptor that can target membrane receptors on the surface of the malignant B cells (*156, 157*). "First generational" CAR constructs were composed of an extracellular domain that recognizes the target of interest, usually in the form of a single-chain fragment variable (scFv), coupled with the transmembrane domain and intracellular ITAM-bearing tail of CD3-ζ (*163, 164*). (Figure 4). Early clinical trials involving first generational CAR+ T cells exhibited low *in vivo* expansion and rapid clearance after infusion (*165, 166*). This led to the development of "second generational" and "third generational" CARs that incorporated additional costimulatory regions (i.e. 4-1BB, CD28) within the cytoplasmic domain (*167, 168*)[see **Figure 4**]. This addition enhanced *in vivo* expansion and persistence of anti-target effector function for months to years post-injection (*169*). The adoptive transfer of CAR T cells has resulted in complete remission in refractory and relapsed B cell cancers (*15, 170, 171*). The reason for the extensive use of CAR T's in B cell malignances is inherent to the relatively large number of patients, target accessibility, conservation of surface markers, tolerance of B cell aplasia, and high rates of success (*172*). This success has extended beyond B cell malignancies with reported success in synovial cell sarcoma and multiple myeloma (*173, 174*).

The current CAR T target in BCP-ALL is CD19, a cell surface receptor that are widely expressed throughout the different stages of B cell development. We note that CD19

therapy ablates both healthy and malignant B cells, with complications already being reported due to the onset of opportunistic infections (86) as well as cytokine storm (*175*).

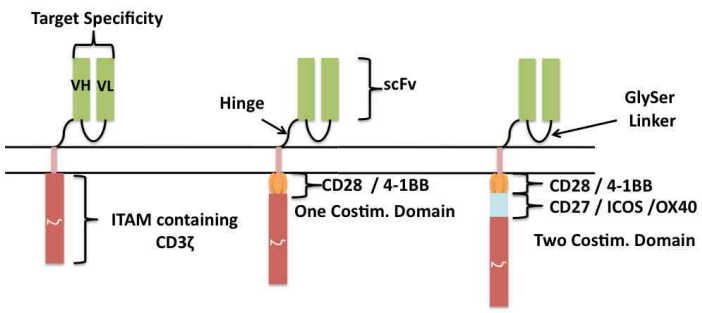

Figure 4. First, Second & Third generation Chimeric Antigen Receptors (CAR).

Cases of relapse have also been reported due to loss of CD19 expression on the target cells (87) due to downregulation (*176*), mutation (*177*), or alternative splicing (*177*) in the tumor cell. Still, other cases have reported reduced CAR T efficacy even though CD19+ leukemic cells are detectable in the blood (88). Reduced CAR T expression or T cell exhaustion (89) may be important factors for loss of therapeutic potency. To overcome this, groups are targeting different markers such as CD20 and CD22 for use in B cell malignancies (*178-180*). An anti-CD20 CAR T recently revealed little/no efficacy due to complete loss of detection of the cells from 1 to 9 weeks after transfer (*181*). Multivalent targeting CAR T cells have been utilized with a combo of CD123 and CD19 and prevented the escape of CD19- mutants in the preclinical setting (*182*).

Considering all these factors, we set out to test the hypothesis that the pre-BCR could represent a much more specific target for T-cell mediated therapy in pre-BCR+ leukemias. We reasoned that the unique structural and development properties of the pre-BCR make it an optimal target in BCP-ALL. The pre-BCR's SLC, composed of λ5 and VpreB, are non-polymorphic and contain non-Ig portions, which show no sequence homology to any other genes (*33, 183*). In contrast to targeting downstream effectors and/or other surface receptors like CD19, targeting SLC would protect the mature population of B cells that are fundamental to a patient's adaptive immune response. Further, different from the CD19, we showed that pre-BCR+ leukemias require the pre-BCR for survival. Thus, downregulation of the pre-BCR, as seen in CD19, may be detrimental to the leukemia cells that require expression for survival. Targeting receptors on tumors that are central to

survival confer a proliferative disadvantage and an unlikely source of resistance. This idea has been suggested previously (*172*) and has been shown to be advantageous for B cell maturation antigen (BCMA or TNFRSF17), in plasma cells malignancies (*184, 185*) and ROR1 in both ALL and CLL (*149, 186*).

Several different gene modification strategies have been proposed to engineer T cells. Retroviral and lentiviral vectors are among the most popular due to their efficiency and well-developed protocols (*187*). Of these two, lentiviral vectors are favored because they can integrate in non-dividing primary human cells and limited risk of insertional mutagenesis to-date (*188, 189*). However, these successes with lentiviral vectors have not ruled out transposon-based systems (*190*), zinc-finger nucleases (ZFNs), transcription activator-like effector nucleases (TALENs) and RNA-based (CRISPR-Cas9) that may be used to engineer T cells or modify T cells that are resistant to tumor-mediated suppression (*191-196*). These latter concept of additional T cell modification to improve CAR T function is a hot topic. Different groups have proposed the incorporation of molecular switches. For instance, cells can be produced to engineer deactivating (*197, 198*) or activating activity (*199, 200*). T cells may also be engineered to express certain types of chemokine receptors such as CCR2b, which has been used to enhance tumour infiltration (*201*).

Chapter 4 presents the pre-clinical development of a 2nd-generational CAR T that targets the pre-BCR. Starting with the DNA sequence of the full-length anti-VpreB murine antibody that had been shown to block pre-BCR dimerization (*20*), we employed computational design principals to successfully engineer an scFv. This scFv retained the specificity and subnanomolar binding affinity to the VpreB. The scFv was then incorporated into a lentiviral expression vector that contained a CD28 juxtamembrane domain and C-terminal region composed of the CD3-ζ cytoplasmic tail. We produced CD8+ human CAR T cells that were effective killers of pre-BCR+ BCP-ALL cell lines. Due to the bivalent nature of the pre-BCR, our CAR T represents the first reported CAR that is directed toward a multivalent antigen. This structural feature may provide select

advantages for signaling and motivate future studies that will look into the impact of target antigen valency on signaling proficiency of CAR T cells.

TKIs or antibody-based therapies (ADCs or ADCC) have shown tremendous potential in long-term survival in variety of cancers (*202, 203*); however, relapse is still common (*36, 149, 153*). Further, recurrent treatment through these therapies entails a high cost burden (*204*). Therefore, adoptive transfer of CAR T cells with single administration requirements confers select advantages to existing treatment options (*169*). Additional strategies for treatment of B cell malignancies have been proposed to combine CART cells with small molecule TKI therapy. In fact, Bruton's tyrosine kinase inhibitor, ibrutinib, has been tested and has shown improved anti-CD19 CAR T expansion and improved CD8+ T-cell function by altering the suppressive effects of PD-1 and CD200 expression (*205*). Additional preclinical tests are incorporating anti-PD1 treatments in combination treatments, which has been shown to prevent immunosuppression and boost CAR T therapy (*206*). Due to variations seen with the existing repertoire of T cells used to manufacture CAR Ts, groups have proposed the development of "universal" T cells that could be readily engineered to express a CAR T toward a given target in addition to provide benefits such as the minimization of graft-versus-host disease (*207*). As we build upon the existing library of available targets, improve CAR T design and understand the differential signaling network as a case-by-case basis, we expect to see a boost in the number of clinical trials utilizing this therapy.

CHAPTER 2

Dynamic pre-BCR homodimers fine-tune autonomous survival signals in B cell precursor acute lymphoblastic leukemia

M. Frank Erasmus,[1,2] Ksenia Matlawska-Wasowska,[2,3] Ichiko Kinjyo,[1,2] Avanika Mahajan,[1,2],Stuart S. Winter,[2,3] Li Xu,4 Michael Horowitz,[4] Diane S. Lidke,[1,2] Bridget S. Wilson[1,2]*

[1]Department of Pathology, University of New Mexico Health Sciences Center, Albuquerque,NM 87131, USA. [2]UNM Comprehensive Cancer Center, University of New Mexico Health Sciences Center, Albuquerque, NM 87131, USA. [3]Department of Pediatrics, University of New Mexico Health Sciences Center, Albuquerque, NM 87131, USA. [4]Sea Lane Biotechnologies, 2450 Bayshore Parkway, Mountain View, CA 94043, USA.

*Corresponding author. Email: bwilson@salud.unm.edu

ABSTRACT

The pre-B cell receptor (pre-BCR) is an immature form of the BCR critical for early B lymphocyte development. It is composed of the membrane-bound immunoglobulin (Ig) heavychain, surrogate light chain components, and the signaling subunits Igα and Igβ. We developed monovalent Quantum Dot (QD)-labeled probes specific for Igβ to study the behavior of pre-BCRs engaged in autonomous, ligand-independent signaling in live B cells. Single-particle tracking revealed that QD-labeled pre-BCRs engaged in transient, but frequent, homotypic interactions. Receptor motion was correlated at short separation distances, consistent with the formation of dimers and higher-order oligomers. Repeated encounters between diffusing pre-BCRs appeared to reflect transient co-confinement in plasma membrane domains. In human B cell precursor acute lymphoblastic leukemia (BCP-ALL) cells, we showed that frequent, short-lived, homotypic pre-BCR interactions

stimulated survival signals, including expression of BCL6, which encodes a transcriptional repressor. These survival signals were blocked byinhibitory monovalent antigen-binding antibody fragments (Fabs) specific for the surrogate light chain components of the pre-BCR or by inhibitors of the tyrosine kinases Lyn and Syk. For comparison, we evaluated pre-BCR aggregation mediated by dimeric galectin-1, which has binding sites for carbohydrate and for the λ5 component of the surrogate light chain. Galectin-1 binding resulted in the formation of large, highly immobile pre-BCR aggregates, which was partially relieved by the addition of lactose to prevent the crosslinking of galectin-BCR complexes to other glycosylated membrane components. Analysis of the pre-BCR and its signaling partners suggested that they could be potential targets for combination therapy in BCP-ALL.

INTRODUCTION

The cell surface expression of the multimeric pre-B cell receptor (pre-BCR) complex is required for the survival and differentiation of B cell progenitors. This complex is composed of the immunoglobulin (Ig) heavy chain (surface μHC), two surrogate light chain components VpreB (also known as CD179a) and λ5 (also known as CD179b), and the signaling subunits Igα (also known as CD79a) and Igβ (also known as CD79b). Pre-BCR signaling stimulates the phosphorylation of Immunoreceptor Tyrosine-based Activation Motifs (ITAMs) in the cytoplasmic tails of both of the Igα and Igβ subunits by the tyrosine kinase Lyn (1). The phosphorylated ITAMs form binding sites for the dual Src homology 2 (SH2) domains of spleen tyrosine kinase (Syk), a critical component of downstream signaling cascades that determine cell fate decisions (2, 3).

The functional pre-BCR serves several crucial roles in B cell differentiation, including (i) initiating cell cycle exit (4, 5) and chromatin remodeling (6), which are critical for rearrangementof the genes encoding the light chains; (ii) regulating major changes in transcription (7, 8); (iii) providing quality control for Ig heavy chains (9); and (iv) balanced negative and positive selection of self-reactivity (10-12). Although it is broadly appreciated that the pre-BCR is positioned at a critical B cell developmental checkpoint, there remain some controversies regarding the primary signal initiating mechanism. Evidence exists for the following scenarios: Igα and Igβ signaling in the absence of external factors that might crosslink the Igα-Igβ heterodimer (13); pre-BCR recognition of self-antigens (14); involvement of μHC glycosylation at Asn46 (15); and pre-BCR aggregation by soluble or stromal-bound galectin-1, a lectin that has distinct binding sites for λ5 and for carbohydrates on glycoproteins and glycolipids (16). However, mutagenesis (17) and structural studies (18) suggest that autonomous signaling is driven by ligand-independent self-association of the λ5 components of the surrogate light chains. The weak signals attributed to these homotypic pre-BCR interactions have led some to refer to it as “tonic signaling” (19). The compelling evidence for homotypic pre-BCR associations motivates these questions: Can these interactions be directly measured and what is their lifetime? Do they engage in serial interactions (20)? How does the relative duration of pre-BCR

homotypic interactions govern the strength and outcome of pre-BCR signaling? These questions can now be addressed through high-resolution imaging modalities, such as single particle tracking (SPT) methods that have captured the diffusion, clustering, and dynamics of the mature BCR (21, 22) and FcεRI (23, 24).

Our model system is B cell precursor acute lymphoblastic leukemia (BCP-ALL) (25), for which a substantial fraction of cases depend on pre-BCR autonomous signals for survival, expression of the gene encoding the transcriptional repressor BCL-6 (B-cell lymphoma 6 protein), and suppression of p53-mediated apoptosis (26). In these cases, there are parallels between the role of the BCR as a driver of or contributor to diffuse large B-cell lymphoma and chronic lymphocytic leukemia (27, 28). The knowledge that the BCR generates survival and proliferative signaling in mature B cell neoplasms provided motivation for successful clinical trials targeting Syk, Bruton's tyrosine kinase (BTK), and other downstream signaling components (29). There is now strong interest in determining whether targeted agents against the pre-BCR and its signaling partners (such as Lyn and Syk) (30-32) will also have therapeutic potential for an important subset of BCP-ALL, particularly in the setting of adjuvant or combination therapy. New insights into the mechanisms governing pre-BCR activation also have profound implications for normal B cell development, as well as autoimmunity (33).

Here, we used state-of-the-art SPT methods to capture dimer events between pre-BCRs in real time. These studies provide evidence that pre-BCRs undergo homotypic interactions through their surrogate light chain components, and that these interactions stimulate autonomous signaling. We demonstrated that VpreB-specific monovalent Fab antibodies blocked self-association and inhibited autonomous signaling. Treatment with anti-VpreB Fabs resulted in an overall faster pre-BCR diffusion rate by eliminating the proportion of receptors that was engaged in dimerization. The clinical relevance of our findings was suggested by evidence that anti- VpreB Fabs sensitized BCP-ALL cells to low-dose chemotherapy. To complete our studies of pre-BCR oligomerization, we also evaluated receptor behavior on cells treated with the pre-BCR–crosslinking agent galectin-1. In addition to its well-known carbohydrate-binding properties (34), galectin-1 binds to the

unique region of λ5 (35) and serves as a pre-BCR ligand (36). There is intense interest in galectin-mediated signaling in the leukemia microenvironment (37), in which galectin-1 can crosslink the pre-BCR with integrins and other glycoproteins at stromal–blast cell synapses (38). In addition to being produced by stromal cells, galectin-1 is secreted by BCP-ALL blasts for which it may be a soluble or cell-bound ligand for the pre-BCR (39).

We showed that short-lived autonomous signals from the pre-BCR were important to regulate BCL6 abundance, as a downstream readout of pre-BCR activity. BCL6 protein abundance was decreased after treatment with inhibitors that target the pre-BCR signaling partners Lyn, Syk, and SHIP-1 (SH2 domain-containing Inositol 5'-Phosphatase). The Janus-activated kinase (Jak) inhibitor tofacitinib enhanced accumulation of BCL6 protein, confirming reports that signal transducer and activator of transcription (STAT) actively represses BCL6 transcription in BCPALL(40). Completed and ongoing clinical trials for Jak inhibitors in BCP-ALL (NCT01914484, NCT01251965, and NCT01164163) provide motivation for further studies to evaluate whether de-repression of BCL6 and other targets of the pre-BCR pathway offer potential escape mechanisms. Studies of pre-BCR cell lines and patient-derived leukemia blasts (26, 30, 40, 41) suggest that predicting the therapeutic responses of individual patients to targeted inhibitors of the pre-BCR and Jak-STAT pathways may require case-by-case evaluation, the development of reliable biomarkers, and a systems level approach to understanding the complex crosstalk between both pathways.

MATERIALS AND METHODS

Cell culture and treatments

Suspension cultures of BCP-ALL cell lines (697 and Nalm6) were cultured in RPMI 1640 with phenol red (Sigma-Aldrich, Saint Louis, MO), with 10% (v/v) heat-inactivated fetal bovine serum (HI FBS), 1% Penicillin/Streptomycin (Gibco, Gaithersburg, MD), and 2 mM LGlutamine. Patient samples were cultured in IMDM (Iscove's Modified Dulbecco's Medium), GlutaMAX (Gibco) supplemented with 20% (v/v) HI FBS, 1% Penicillin/Streptomycin, 1x Insulin, transferrin, and selenium (Gibco), 1 mM sodium

pyruvate (Gibco), and 55 μM 2- Mercaptoethanol (Gibco). Before experiments were performed, cells were washed twice with Tyrode's solution. Unless otherwise stated, cells were pretreated for 10 min with BAY61-3606 (1 μM), dasatinib (1 μM), tofacitinib (1 μM), anti-VpreB Fab (1 μM), or recombinant galectin-1 (10 μM) in the presence or absence of lactose in Tyrode's solution, 0.1% bovine serum albumin (BSA), and 20 mM glucose. For SPT experiments, galectin-1 was purchased from Peprotech (Rocky Hill, NJ). Inhibitors were purchased from Santa Cruz Biotechnology (Dallas, TX), Selleck Chemicals (Houston, TX), and Echelon Biosciences (Salt Lake City, UT).

Recombinant anti-VpreB antibody screening and production

The Contextual Combinatorial Immune Repertoire (ConCIRT) Synthetic Library (87), consisting of 56 billion synthetically constructed human antibodies arrayed in over 100 phage-displayed sub-libraries, was screened against recombinant "surrobodies." Surrobodies consist of a functional human IgG1 heavy chain isolated from an anti-influenza H5N1 hemagglutinin antibody and paired with either surrogate light chain components (VpreB1, λ5) or a chimeric polypeptide that is a product of the fusion of human VpreB1 and λ5. Phage bound to surrobodies coated on a 96-well microtiter plate were eluted and amplified for use in a subsequent round of screening. After four rounds of phage screening, individual clones from enriched pools were analyzed for specific binding by ELISA. Testing for binding specificity to VpreB1 was performed on ELISA plates coated with a chimeric VpreB1-λ5 polypeptide. Detection was quantified with HRP-conjugated anti-myc antibodies, which was followed by ELISA-based hit identification. After positive identification, 16 phage-derived clones with an affinity for VpreB in
the range 0.85 to 250 nM were sequenced. Clone 2460B04 was selected for integration into a mammalian expression plasmid, which was followed by transient transfection of HEK 293-F cells for the production of recombinant IgG antibodies. Intact IgG was reduced with 2MEA (2- mercaptoethylamine-HCl) to produce anti-VpreB1 Fab fragments. The reactivity of anti-VpreB1 Fabs against live 697 cells was evaluated by flow cytometry (fig. S7).

Anti-CD79b IgG purification

CB3-1 hybridoma cells (generously provided by Dr. Max D. Cooper, Emory University) were cultured in RPMI 1640 with phenol red (Sigma-Aldrich) containing 10% (v/v) HI FBS, 1% Penicillin/Streptomycin (ThermoFisher Scientific), 2 mM L-Glutamine (Gibco) and 1x β- mercaptoethanol (Gibco). Flask cultures were expanded by 2-week culture in 250 ml in RPMI media without FBS, which was followed by media collection, clarification by centrifugation at 560g, and filtration through a 0.22-μm vacuum filter. The culture medium was circulated overnight (4ºC) on a protein A/G affinity column and the IgG was eluted with glycine buffer (pH 2.5 to 3.0). Eluted 1-ml fractions were neutralized with 1 M TRIS buffer (pH 9.0).

Fab' generation, biotin conjugation, and QD labeling

Fab'-biotin probes were prepared as previously described (42). IgG derived from the CB3-1 hybridoma or anti-IgM (Jackson Immuno Research, West Grove, PA) was dialyzed into sodium acetate solution (pH 4.5) to prepare for addition to pepsin-conjugated agarose (ThermoFisher Scientific, Waltham, MA) according to the manufacturer's instructions. IgG digestion was performed for 5 h at 37ºC, and the eluate was dialyzed at 4ºC into 100 mM phosphate, 5 mM EDTA, (pH 6.0) to prepare for reduction of the interchain disulfides of F(ab')2 by 2- mercaptoethylamine (2-MEA, ThermoFisher Scientific). The sample was incubated in 2-MEA (50 mM) for 90 min at 37ºC and then dialyzed into storage buffer [100 mM phosphate, 5 mM EDTA, (pH 6.5 to 7.0)] for 4 hours at 4ºC, exchanging buffer multiple times. The exposed thiol groups, generated from the reduction of interchain disulfides, were selectively conjugated to biotin with the EZ-Link Maleimide-PEG2-Biotin (ThermoFisher Scientific) and resolved by SDS-PAGE. To remove higher molecular weight bands (F(ab')2 and undigested IgG, digested fragments were recovered at room temperature by FPLC size-exclusion chromatography with Superdex 75 10/300 column (GE Healthcare Life Sciences, Marlborough, MA) at a flow rate of 0.5 ml/min in phosphate-buffered saline (PBS) (fig. S1A). Residual intact Fc fragments were removed by batch processing with protein A/G agarose beads (ThermoFisher Scientific). The purity of the anti-CD79b Fab'-maleimide biotin conjugates was determined by Coomassie stain and Western blotting analysis (fig. S1, B and C) after the samples were resolved by SDS-PAGE under nonreducing conditions. The biotin to Fab' molar ratio was determined with

the FluoReporter biotective green reagent (ThermoFisher Scientific) with a reported mean biotin:Fab
molar ratio of 1:1. Anti-CD79b Fab'-Biotin or Anti-IgM Fab'-Biotin were mixed at a 1:1 ratio with Qdot655-strepavidin or Qdot585-streptavidin in PBS containing 1% (w/v) BSA to generate stock solutions.

QD labeling of live cells

Lab-Tek imaging chambers were coated with poly-l-lysine hydrobromide (Sigma-Aldrich) at 1mg/ml in sterile water for 20 min at room temperature, which was followed by three washes with water. BCP-ALL cells were serum-starved in RPMI 1640 without FBS for 2 hours before being added to coated wells and incubated for 15 min at 37°C. QD-Fab'-CD79b or QD-Fab'-IgM were added at a final concentration of 100 pM in Tyrodes's solution with 0.1% (w/v) BSA and 20 mM glucose and were incubated for 10 to 15 min at 37°C.

Single particle tracking and analysis

All corresponding GPU SPT and track elongation, squared displacement, mean square displacement, correlated motion, fiducial data acquisition and image registration, and three-state hidden Markov Model used in this study were described in detail previously (43).

Galectin-1 cloning, expression, and purification

MGC human galectin-1–encoding cDNA (LGALS1, accession# BC001693) was PCR-amplified with the CACC forward primer (FWD: 5'- CAC CAT GGC TTG TGG TCT GG -3') and reverse primer (REV: 5'- TCA GTC AAA GGC CAC ACA TTT GAT CT -3'). The amplified product was subcloned into pET101 by directional TOPO expression. The cloned product was transformed into One SHOT TOP10 Escherichia coli by heat-shock. Cells were grown overnight on ampicillin. Resistant cultures were selected and were used for DNA isolation. BL21 StarTM One Shot cells were transformed with the pET101 vector with LGALS1 by heat-shock, brief outgrowth in SOC medium, followed by transfer to 10 ml of LB containing ampicillin, and the cultures were grown overnight at 37ºC while

shaking. The next day, 50 ml of LB containing ampicillin was inoculated with 1 ml of the overnight culture. The culture was grown at 37ºC with shaking (225 to 250 rpm) for 2 to 3 hours. IPTG (1 mM) was added to induce the expression of galectin-1 for 3 to 4 hours. The cells were then harvested by centrifugation at 3000g for 10 min at 4ºC. The cells were purified by α-lactose/agarose (Sigma-Aldrich) as detailed previously (88).

Western blotting

After the cells were incubated in the presence or absence of the appropriate inhibitors or crosslinking agents, they were washed with ice-cold PBS and incubated for 15 min on ice in Tris-based lysis buffer containing 1% NP-40 and protease and phosphatase inhibitors (Thermo Scientific). To examine the effects of inhibitors on BCL6 abundance, treatments were performed for 24 hours. Cell lysates were clarified by centrifugation at 14,000g for 10 min at 4°C and then were added to Laemmli's Reducing buffer (final 2x). Proteins were resolved by SDS-PAGE and transferred to nitrocellulose membranes. After the blots were blocked with Tris-buffered saline containing 5% BSA, they were incubated with antibodies specific for pCD79a-Tyr182 (CST, Danver, MA), pSyk-Tyr348 (Novus Biologicals, Littleton, CO), pSyk-Tyr348 (Abcam, Cambridge, MA), pSyk-Tyr352 (CST), or BCL6 (Santa Cruz Biotechnology). Antibody specific for β-actin (Sigma-Aldrich) was used to confirm equivalent loading of gels.

Pervanadate treatment

The use of pervanadate to enhance signaling in various cell types has been reported previously (89-91). Here, all BCP-ALL cells were treated with freshly prepared pervanadate solution (0.2 mM sodium orthovanadate and 1 mM hydrogen peroxide) in the presence or absence of inhibitors and then treated for the times indicated in the figure legends.

Chemosensitization

To establish an effective concentration range for the potential synergy of targeted inhibitors with vincristine, 697 cells (50,000 cells per condition) were incubated for 3 days at 37oC with a range of concentrations of vincristine (0.1 to 100.0 ng/ml) (Sigma-Aldrich). Controls

are indicated in the figures, including vincristine alone and vehicle at the highest DMSO concentration used (0.2%). Curves were fit with a sigmoidal dose-response curve with the curve fitting toolbox of MATLAB.

Flow cytometry assays

Leukemia cell apoptosis was determined based on measurement of the binding of Annexin-V-FITC (BioLegend, San Diego, CA) or Pacific Blue Annexin-V (BioLegend), whereas loss of cell viability was measured by 7-AAD labeling (BioLegend), according to the manufacturer's procedures. For receptor-binding experiments, cells were incubated under saturating conditions for 1.5 hours on ice in PBS with anti-CD79b-APC antibody (BioLegend) or anti-VpreB-PE antibody (BioLegend). Flow cytometry data were calibrated with QuantumTM Simply Cellular beads (Bangs Laboratories, Fishers, IN) with anti-mouse Fc antibody according to the manufacturer's instructions. Dissociation constants were estimated with nonlinear regression analysis under KD-controlled conditions as described previously (92). All flow cytometry data collection was conducted on HyperCyt (93) or BD LSRFortessa flow cytometers and analyzed with the FlowJo Software Suite (Tree Star, Ashland, OR).

RT-PCR mRNA sequence analysis

Total RNA was extracted from the 697 and Nalm6 cell lines and from patient samples #238 and #280 with NucleoSpin RNA XS (Macherey-Nagel, Duren, Germany). cDNA synthesis was performed with both random hexamers and d(T)20 primers with SuperScript First-Strand Synthesis System (ThermoFisher Scientific). Primers were designed for the 5'-UTR (FWD: 5'- GAGCTCTGCATGTCTGCACC-3') and 3'-UTR (REV: 5'- CGTGCCTCTGCTGTCTTCAG- 3') based upon the sequence of the reference VPREB1 mRNA (NM_007128.3) sequence. PCR reactions used the Platinum PCR SuperMix (ThermoFisher Scientific). The Thermo Cycler setup was as follows: 94°C for 2 min to denature the DNA and activate the enzyme; 35 cycles of PCR amplification followed by 30 s at 94°C, 30 s at 55°C, and 72°C for 1 min. All PCR amplicons were agarose gel–purified (Macherey-Nagel) and subcloned into the pCR-BluntIITOPO vector according to the guidelines of the Zero Blunt TOPO PCR cloning kit (ThermoFisher Scientific). One

Shot Competent E. coli were then transformed with the plasmids, and 10 to 20 colonies were selected on LB plates with kanamycin (50 μg/ml) and grown in 5 ml of LB containing kanamycin overnight. Plasmids were purified with the NucleoSpin Plasmid Miniprep (Macherey-Nagel). Purified plasmids were sequenced (Genewiz, Cambridge, Massachusetts) using their predefined Sp6 and T7 primers. Only sequences that passed Genewiz quality control were analyzed. Each DNA sequence was compared to the reference sequence (NM_007128.3) by NCBI BLAST search. All multiple protein sequence alignments were performed with the MUSCLE server (94) and were compared to the reference sequence (UniProt #P12018). Prediction of the N-glycosylation of the reference and variant sequences was assessed with the NetNGlyc 1.0 Server.

Composite 3D model of preBCR Fab-like arms and Fcμ

Because the Fab-like X-Ray crystal structure of the preBCR (PDB: 2H32) does not contain the unique region, we used the MODELLER software suite (95) to build a homology model including the surrogate light chain unique region (UR) components. These surrogate light chain λ5-UR and VpreB-UR structural components were derived from the NMR solution structure (PDB: 2LKQ) and de novo peptide design PEP-FOLD online server (96), respectively. The composite 3D model shows the Fab-like arms extended from the Fcμ region derived from NMR and X-Ray structures (PDB: 4JVU, 4BA8, and 4JVW). Residues implicated in polymorphism were analyzed and highlighted with the VMD software package (97).

RESULTS

SPT captures serial pre-BCR engagements

The first step in the experimental plan to track pre-BCR self-association dynamics was the design and production of monovalent Quantum Dot (QD) probes. We base our probes on the CB3-1 antibody to the Igβ (CD79b). As a positive control, we also generated probes based upon antibodies that recognize the Fc portion of the membrane-bound pre-BCR heavy chain (mIgμ). Both reagents have the advantage of not recognizing the VpreB and λ5 moieties of the surrogate light chain, which are proposed to mediate pre-

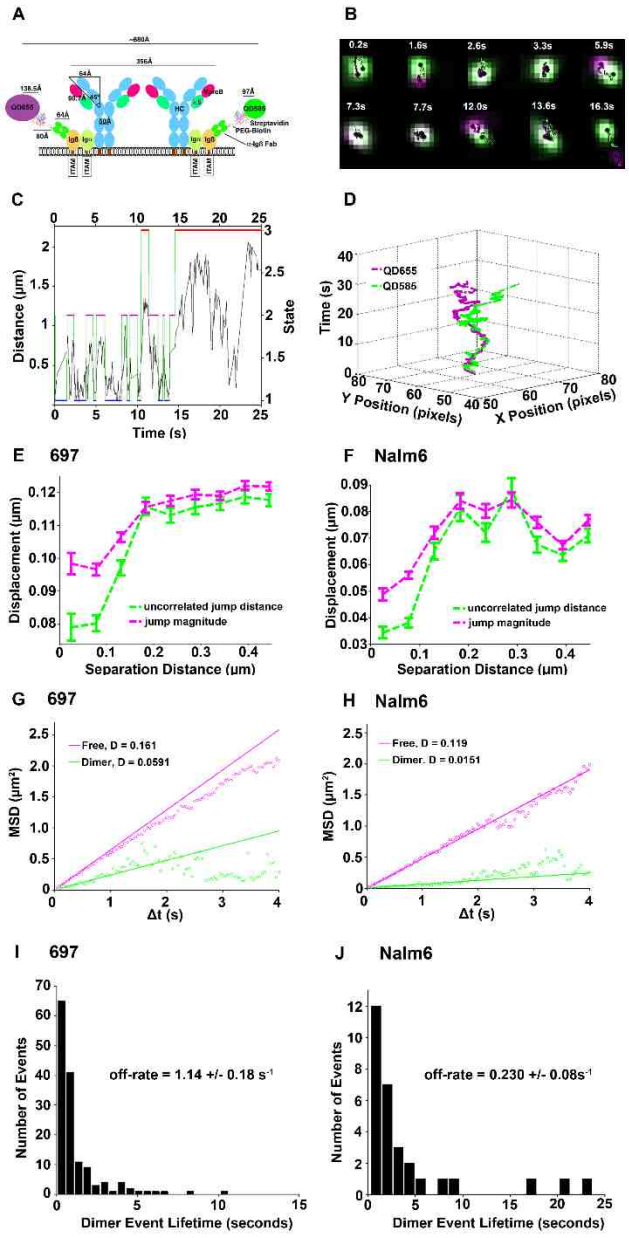

Fig. 1. Direct evidence of pre-BCR dimerization on the surface of BCP-ALL cells. (A) Experimental model with estimation of the interaction distance based upon the pre-BCR crystal structure (PDB ID: 2H32), streptavidin (PDB ID: 1STP), and the estimated QD radii. (B) Timelapse imaging (20 frames/s) of a single cell under resting conditions. (C) Viterbi plot of the most likely state (dimer, domain, and free) between two QD interactions as derived from hidden Markov model (HMM) with separation distance as the observed parameter. (D) Two-channel 3D trajectory of anti-Igβ Fab'-QD655 (magenta) and Fab'-

QD585 (green) bound to two receptors that serially engaged repeatedly over 14.5 s, with several instances of correlated motion before separating toward the end of acquisition. Data are representative of 35 independent experiments with 697 cells. (E and F) Analysis of displacement (magenta, jump magnitude) and degree of uncorrelated motion (green) as a function of separation distance (between 150 to 200 nm),observed with both 697 cells (E) and Nalm6 cells (F) . (G and H) Diffusion by state, as determined by HMM analysis. (I and J) Distribution of dimer lifetimes in 697 and Nalm6 cells, with estimated off-rates as predicted by HMM analysis. Interaction distances in the HMM were set to 100 and 300 nm, respectively. Data in (E) to (J) represent 26,447 trajectories in 697 cells and 2,800 trajectories in Nalm6 cells.

BCR homotypic interactions (18). In brief, intact IgG antibodies were collected from hybridoma culture supernatants, which was followed by controlled pepsin cleavage to initially produce F(ab')2 fragments. Anti-Igβ Fabs' with exposed thiol groups (42) were generated by incubation in 2-mercaptoethylamine (MEA) containing EDTA, followed by covalent, maleimide-based coupling of the free cysteines to PEG2-biotin. Protein G beads were used to remove any contaminating intact IgG or Fc fragments. Monovalent Fab'-PEG2-biotin was purified by FPLC (Fast Protein Liquid Chromatography) and then mixed 1:1 with avidin-conjugated QD585 or QD655 for dual-color SPT. We then characterized the anti-Igβ Fab' probe (fig. S1).

Our strategy for observing pre-BCR dimers by SPT involved tagging each multi-subunit pre-BCR with a different color of QD (QD585 or QD655) (Fig. 1A). Although there is limited structural information for the entire pre-BCR complex, if we assume a side-by-side orientation of all subunits, there would be approximately 80 to 100 nm between the two bound Fab'-QD probes in a dimer. Consistent with this, we found a best fit dimer distance between the QD probes of 100 nm with the Hidden Markov Model (HMM) to analyze large sets of two-color tracking data (43). Through SPT imaging (Fig. 1B), we captured pre-BCR dimerization in real time on the surface of live 697 cells [a cell line derived from a BCP-ALL patient (44)]. The two diffusing anti-Igß Fab'-QD probes were distinguished by pseudo-coloring them as green or magenta dots throughout a 25-s time series. At 2.6 to 3.3 s into image acquisition, the dots were clearly overlaid, indicating the presence of dimers. The pair became segregated at 5.9 s, which was followed by two rebinding events (at 7.3 and 13.6 s) (Fig. 1B). The Viterbi plot (45) reported the state-specific transitions of these two receptors over time (Fig. 1C), using rate constants determined by the HMM as previously described in detail (43). The HMM distinguished three states for mobile receptors: (i) dimers; (ii) pairs that are transiently co-confined in the same region; and (iiii) pairs of receptors that are widely segregated ("free"). The two receptors cycled between dimer and co-confined states over a ~14.5-s time window, after which diffusion resulted in their separation by a distance of > 1 μm (Fig. 1C). For this pair, homotypic interaction lifetimes were short (<3 s).

Our three-dimensional (3D) view of the same pre-BCR dimer pair (Fig. 1D) illustrated the relative X and Y positions of each anti-Igß Fab'-QD probe over time. Based upon their close proximity and correlated motion, the two pre-BCRs became dimerized at the beginning of the imaging. Their dissociation at 5.9 s was readily apparent, which was followed by a short reengagement period and then dissociation and diffusion in separate directions toward the end of the image acquisition period. Additional examples of pre-BCR dimer events were analyzed (fig. S2 and movie S1). We applied two other criteria to evaluate dimerization (Fig. 1, E and F), which examine whether pairs of molecules in the entire data set move independently ("uncorrelated motion", with dissimilar jump magnitudes) or together (correlated motion with similar jump magnitudes). These plots show characteristic drops in pre-BCR uncorrelated motion (green lines) and jump magnitude (magenta lines) that were a function of close separation distances, an expected requirement for interactions. These analyses were performed for 697 cells (Fig. 1E), as well as for Nalm6 cells (46) (Fig. 1F). These data provide statistically rigorous validation that pre-BCR dimerization occurred frequently on the surface of two distinct BCPALL cell lines. Analysis of the cytogenetics and the cell surface expression of BCP-ALL markers for both cell lines was also performed (table S1).

We then compared the relative mobilities of pre-BCR monomers and dimers on the surface of both cell lines (Fig. 1, G and H). In the free state, pre-BCRs had a relatively fast diffusion coefficient (0.16 and 0.12 μm2/s on 697 cells and Nalm6 cells, respectively). By comparison, the diffusion rates for interacting pairs of pre-BCRs (representing jump distributions only during the intervals when the receptors were identified as being dimerized) were markedly slower at 0.06 and 0.015 μm2/s on 697 cells and Nalm6 cells, respectively. When considering the whole population of receptors (that is, not state-specific), the ensemble Mean Square Displacement (MSD) plots for pre-BCRs on these cells were similar when either the anti-Igβ or the anti-mIgμ QD probes were used (fig. S3). The mean diffusion coefficients for the pre-BCR on the surfaces of 697 and Nalm6 cells were 0.13 and 0.09 μm2/s, respectively (table S2). We also summarized the number of trajectories tracked under each experimental condition in this work (table S2).

The dissociation of individual receptors from dimers was previously shown to be a stochastic process, resulting in a characteristic range of dimer lifetimes that represent all of the binding and unbinding events within a data set (43, 47). For 697 cells, most (84%) of lifetimes of the 146 bound events were less than 2 s, with an off-rate of 1.14 +/- 0.18/s calculated by the HMM (Fig 1I, fig. S4, and table S3). Homotypic interactions of the pre-BCR were slightly more stable on Nalm6 cells, as evidenced by a higher percentage of longer lifetime binding events (43% > 2 s) and an off-rate of 0.230 +/- 0.08/s (Fig 1J, fig. S4, and table S3). Note the correlation between the slower overall diffusion rate of the pre-BCR in Nalm6 cells and the slower off-rates for homotypic interactions.

Because lateral diffusion can be restricted by barriers and protein-protein interactions in a nonlinear fashion (48), the observation of slower pre-BCR diffusion rates on Nalm6 cells may reflect intrinsic differences in the cortical cytoskeleton, the increased size of pre-BCR complexes and their associated adaptor proteins, or both. The possibility of self-associated pre-BCR aggregates has been suggested previously (18, 19); their side-by-side

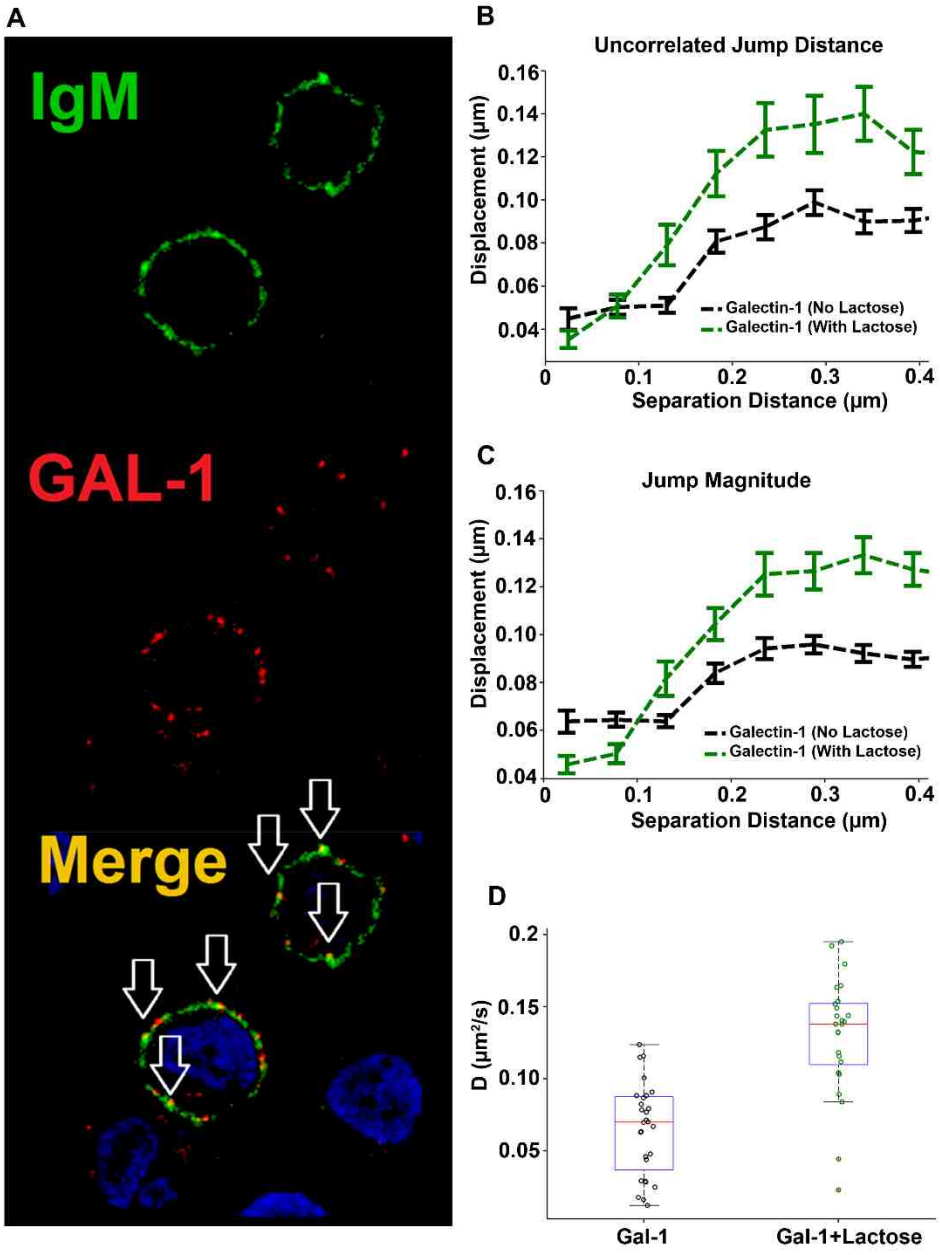

Fig. 2. Galectin-1 stabilizes receptor dimerization and promotes the formation of higher order complexes. (A) Analysis of the binding of labeled galectin-1 (red) to the pre-BCR (green) in 697 cells. Arrows indicate cluster formation and the colocalization of galectin-1 with the pre- BCR. Images are representative of three experiments. (B and C) Blocking the carbohydratebinding domain of galectin-1 with 10 mM lactose revealed differences in displacements for the uncorrelated jump distance and the jump magnitude of

distinct anti-Igβ probes at different separation distances. (D) Analysis of the diffusion of the pre-BCR in 697 cells treated with galectin-1 (GAL-1) in the absence or presence of 10 mM lactose. Plots represent cumulative data from 1491 (galectin) and 1560 (galectin + lactose) trajectories tracked over five independent experiments.

alignment would orient them in the form of chains. A potential outcome of the five-fold slower off-rate (Fig. 1J and fig. S4) for selfengaged pre-BCRs on Nalm6 cells, compared to that of pre-BCRs on 697 cells, may be the greater likelihood of them forming pre-BCR oligomers larger than dimers. We captured a pair of QD probes undergoing correlated motion on the surface of Nalm6 cells that were further apart than the 80 to 100 nm theoretical distance consistent with receptor dimers and their probes (movie S2). We interpret this movie as evidence for the diffusion of homotypic pre-BCR trimers or tetramers with the two Igβ Fab'-QD probes bound to the ends. We found that a median distance of 227 nm was maintained by the two probes undergoing correlated motion before blinking of the QD655 occurred (fig. S5, magenta).

Galectin leads to the formation of complex pre-BCR–glycoprotein aggregates with slow diffusion rates

Galectin-1 binds to λ5 with high specificity (Ka =2 x 106 M-1) (36). We next evaluated the effects of exogenous galectin-1 on the diffusion and aggregation dynamics of pre-BCRs. We first verified the purity of the protein used in our experiments (fig. S6A) and took note of a structural model for monomeric galectin-1 (fig. S6B). Incubation of 697 cells with Alexa 555–conjugated galectin-1 (red) led to the marked clustering of the pre-BCR (Fig. 2A, green) within 5 min. The merged image shows substantial colocalization (Fig. 2A, yellow) of galectin-1 and the pre-BCR in these clusters. For these experiments, we used 10 μM galectin-1, a concentration at which soluble galectin-1 should be >90% dimerized (49).

We performed SPT with the anti-Igβ Fab'-QD probes to evaluate the effects of galectin-1 on pre-BCR diffusion. We observed a marked decrease in both jump magnitude and uncorrelated motion for pre-BCRs on the surface of galectin-1–treated 697 cells (Fig. 2, B and C). A large fraction of pre-BCR essentially became immobile (Fig. 2D and movie S3), which is best explained by the formation of complex aggregates containing pre-BCR, galectin-1, and other cell surface glycoproteins. To provide evidence that the marked slowdown of the pre-BCR bound to galectin-1 could be attributed in part to carbohydrate-mediated lattices with other glycoproteins (37), we also performed experiments in the

presence of excess lactose (10 mM) to block the lectin-binding site of galectin-1 (fig. S6B). Under these conditions, we observed larger overall jump distributions for diffusing receptors and a shorter interaction distance for the onset of correlated motion (Fig. 2, B and C, green dashed lines). The overall diffusion rate of galectin-1– crosslinked pre-BCRs was markedly faster in the presence of lactose (Fig. 2D), approachingvalues for pre-BCRs under autonomous signaling conditions (table S2). Note that controls were performed with lactose alone (see fig. S6C) to ensure that the addition of lactose in the absence of galectin-1 did not alter the average diffusion behavior of the pre-BCR. Additional controls included the treatment of cells with 2 μM galectin-1, a concentration at which galectin-1 monomers predominate, which failed to markedly slow the diffusion rate of the pre-BCR (fig. S6D). Thus, these data suggest that soluble galectin-1 dimers are required to provide a bivalent ligand that binds to λ5 and promotes the aggregation of cell surface pre-BCRs (36).

Fabs against VpreB block the self-association of pre-BCRs

Our next goal was to test the effects of dimer-disrupting and dimer-stabilizing reagents upon the overall diffusive behavior of pre-BCRs. We reasoned that monovalent antibody fragments specific for the surrogate light chains of the pre-BCR would have potential as dimer-disrupting reagents. As described in the Materials and Methods, we screened the ConCIRT Synthetic Library to identify 16 phage-displayed clones that bound to recombinant VpreB1 polypeptide. A high-affinity clone was selected for the production of recombinant human IgG, and we then prepared anti-VpreB1 Fabs. The parent IgG bound to the pre-BCR on the surface of 697 cells with subnanomolar affinity (fig. S7).

We then generated MSD plots (Fig. 3A) for the pre-BCR in the absence and presence of a saturating concentration of anti-VpreB1 Fabs (1 μM). In these experiments, Fabs were added to 697 cells for 10 min at 37°C before we performed SPT. We observed that targeting the pre-BCR with these monovalent blocking reagents markedly increased the overall diffusion rate of the pre-BCR. The overall diffusion coefficient for the pre-BCR on untreated 697 cells was 0.129 μm2/s, which was slower than the rate of 0.172 μm2/s that was observed when anti-VpreB Fabs blocked pre-BCR self-association (Fig. 3B and table S2). For comparison, we also plotted the values for pre-BCR diffusion in 697 cells after

treatment with galectin-1 (Fig. 3A, black lines). After crosslinking with galectin-1, a greater percentage of pre-BCRs approached an immobile state, with an ensemble MSD-derived diffusion coefficient of 0.069 μm2/s (table S2 and movie S3). We also performed an overall comparison of the changes in jump magnitude (Fig. 3C) and uncorrelated motion (Fig. 3D) for pairs of pre-BCRs tracked on the surface of untreated cells (red lines; autonomous signaling) compared to those of cells treated with the anti-VpreB Fabs (blue lines) or galectin-1 (black lines). These data underscore our observations that pre-BCR self-association was prevented by monovalent blocking antibodies specific for the surrogate light chain and that galectin-1 induced the formation of large-scale pre-BCR aggregates.

Other studies suggest that early B cells are governed by a balance of finely tuned thresholds that govern early B cell checkpoints on self-reactivity and survival (40, 41, 50). We investigated the abundance of BCL6 protein as a readout of pre-BCR signaling under cell autonomous and galectin-mediated crosslinking conditions. We found that BCL6 protein abundance in 697 cells was greatest under autonomous signaling conditions (Fig. 3, E and F, left lanes). BCL6 abundance was decreased after overnight treatment with anti-VpreB Fabs, which inhibited homotypic interactions (Fig. 3E, right lane). Galectin-1–mediated crosslinking of the pre-BCR, in the absence, but not presence, of lactose, led to substantially reduced amounts of BCL6 (Fig. 3F).

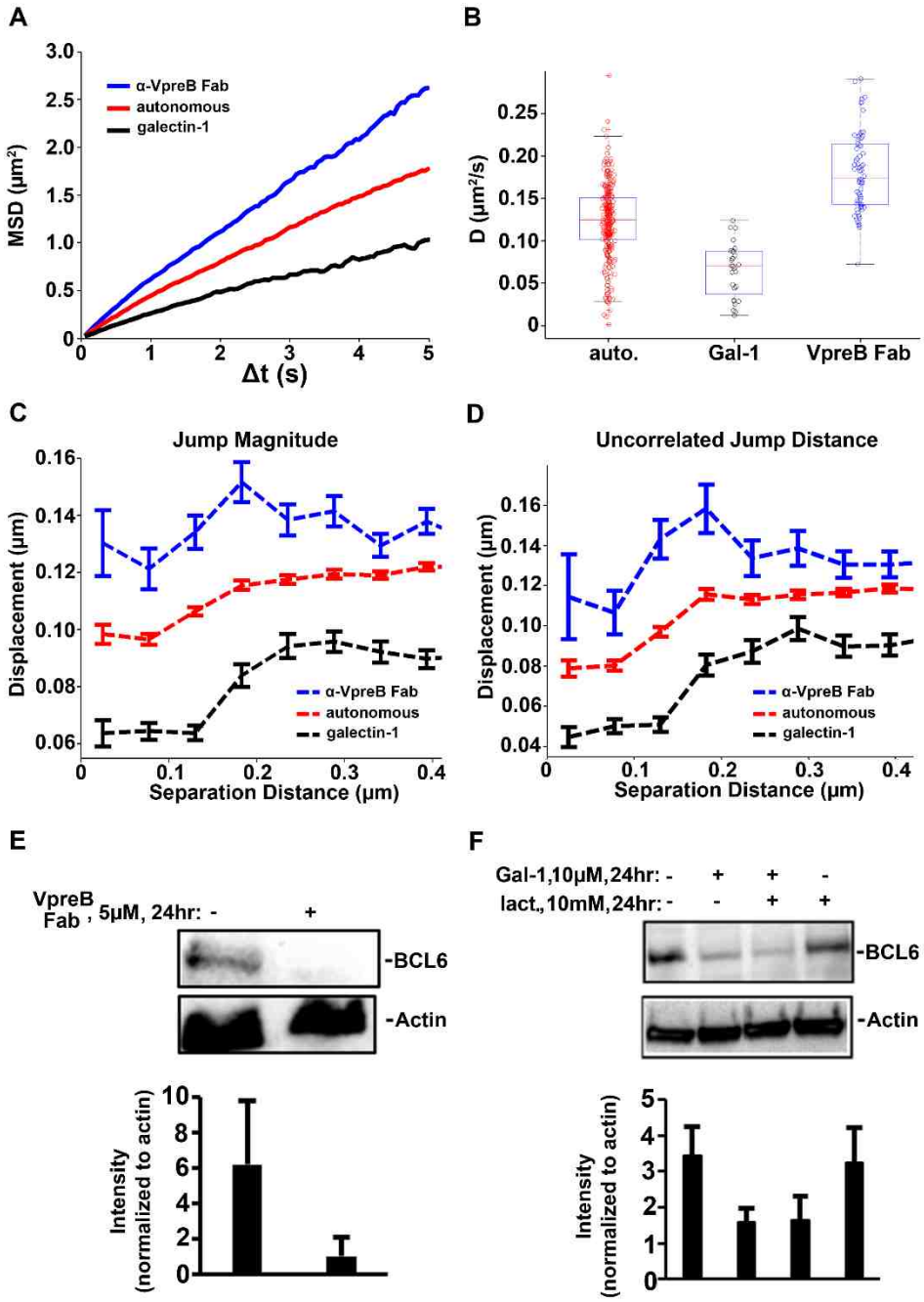

Fig. 3. Comparison of the effects of VpreB Fabs and galectin-1 on pre-BCR diffusion and dimerization. (A and B) Ensemble MSD values (A) and diffusion coefficients (B) revealed changes in pre-BCRs after 10 min of treatment with anti-VpreB Fabs (1 μM, blue) or galectin-1 (10 μM, black). The two-tailed t test from MATLAB was used to confirm statistical significance (see table S2). (C and D) Changes in uncorrelated jump distance and jump magnitude after 10 min of treatment with either 1 μM anti-VpreB Fab (blue dotted

lines) or 10 μM galectin-1 (black dotted lines). (E and F) 697 cells were left untreated or were treated for 24 hours with 5 μM anti-VpreB Fab (E) or with 10 μM galectin-1 in the presence or absence of 10 mM lactose (F) before being subjected to Western blotting analysis with antibodies against the indicated proteins. Each blot is representative of three or more independent experiments. Bar graphs report total densitometry data for the abundances of the indicated proteins normalized to the abundance of actin.

Tyrosine phosphorylation and leukemia cell survival are finely tuned by autonomous pre-BCR Signaling

We next evaluated the extent of Syk and CD79a phosphorylation under each of these experimental conditions (Fig. 4). We found that Syk phosphorylation at Tyr348 was detectable in lysates prepared from 3 x 107 Nalm6 cells under autonomous signaling conditions (Fig. 4A, left lane). Furthermore, treatment of cells for 30 min with anti-VpreB Fabs reduced the amount of Syk phosphorylated at Tyr348 by 40%. In addition, cells were treated for 5 min with galectin-1 either alone or in combination with lactose to block the carbohydrate-binding site of galectin-1. Addition of galectin-1 alone decreased the amount of Syk phosphorylated at Tyr348 (Fig. 4A), whereas crosslinking in the presence of lactose led to enhanced Syk phosphorylation on this site. This finding suggests that the inclusion of other glycoproteins and their signaling partners in the galectin-1–pre-BCR aggregate rapidly inhibits Syk-mediated signaling. Because the surface of BCP-ALL blasts is rich with ITIM-containing inhibitory receptors (50), co-aggregation of pre- BCRs with these glycoproteins might explain the reduced phosphorylation of Syk in response to galectin-1 alone. In our hands, detection of phosphorylated Syk (pSyk) under autonomous signaling conditions often required the overexposure of Western blots. Wienands et al. previously showed that treatment of B cells with the pan phosphatase inhibitor pervanadate reveals kinase activity that is constitutively opposed by phosphatase activity (51). We found a ~7-fold enhancement in the phosphorylation of Syk at Tyr348 after a 30-min treatment of Nalm6 cells with pervanadate (Fig. 4A).

Because phosphorylation detection under basal conditions required large quantities of cells, we took advantage of pervanadate to enhance the amounts of phosphorylated Igα

(CD79a) ITAM and pSyk (Y182, Y352) (Fig. 4, B to D). We interpreted the presence of two or more bands corresponding to phosphorylated CD79a (Fig. 4C, lane 2) as differential mobility caused by the unequal phosphorylation of tyrosine residues in the cytoplasmic tail of CD79a. Treatment of cells with the combination of pervanadate and anti-VpreB Fabs resulted in the near-complete ablation of phosphorylation of both Syk Tyr182 and CD79a. Thus, the increased phosphorylation of these proteins, revealed by inhibiting phosphatase activity, was completely dependent on homotypic pre-BCR interactions that stimulated autonomous signaling. Receptor phosphorylation by the Src family kinase Lyn precedes the recruitment and activation of Syk in the canonical ITAM signaling pathway (19). There is also evidence that once Syk is recruited to the receptor, it also participates in the phosphorylation of ITAMs (52).

We next evaluated these early steps in the autonomous pre-BCR signaling pathway in experiments with kinase-selective, cell-permeable inhibitors. Dasitinib is a cell-permeable inhibitor of the tyrosine kinases Src and Abl (53). Consistent with our earlier findings and those of others (26), we found that the addition of dasatinib to pervanadate-treated 697 cells blocked the Lyn-mediated phosphorylation of the pre-BCR, as detected by anti-CD79a-pY182 antibodies (Fig. 4D). The combination of the Syk inhibitor BAY61-3606 and dasatinib abolished the accumulation of phosphorylated CD79a during phosphatase inhibition, suggesting that trans-phosphorylation by Syk combined with Lyn activity was required for the robust phosphorylation of CD79a. The Syk inhibitor also resulted in a 20% reduction in the amount of pSyk phosphorylated at Tyr352, consistent with this tyrosine residue being a substrate of both Lyn and Syk (2). Treatment of 697 cells with the Jak inhibitor tofacitinib (54) did not substantially alter Syk phosphorylation in the presence of pervanadate (Fig. 4E).

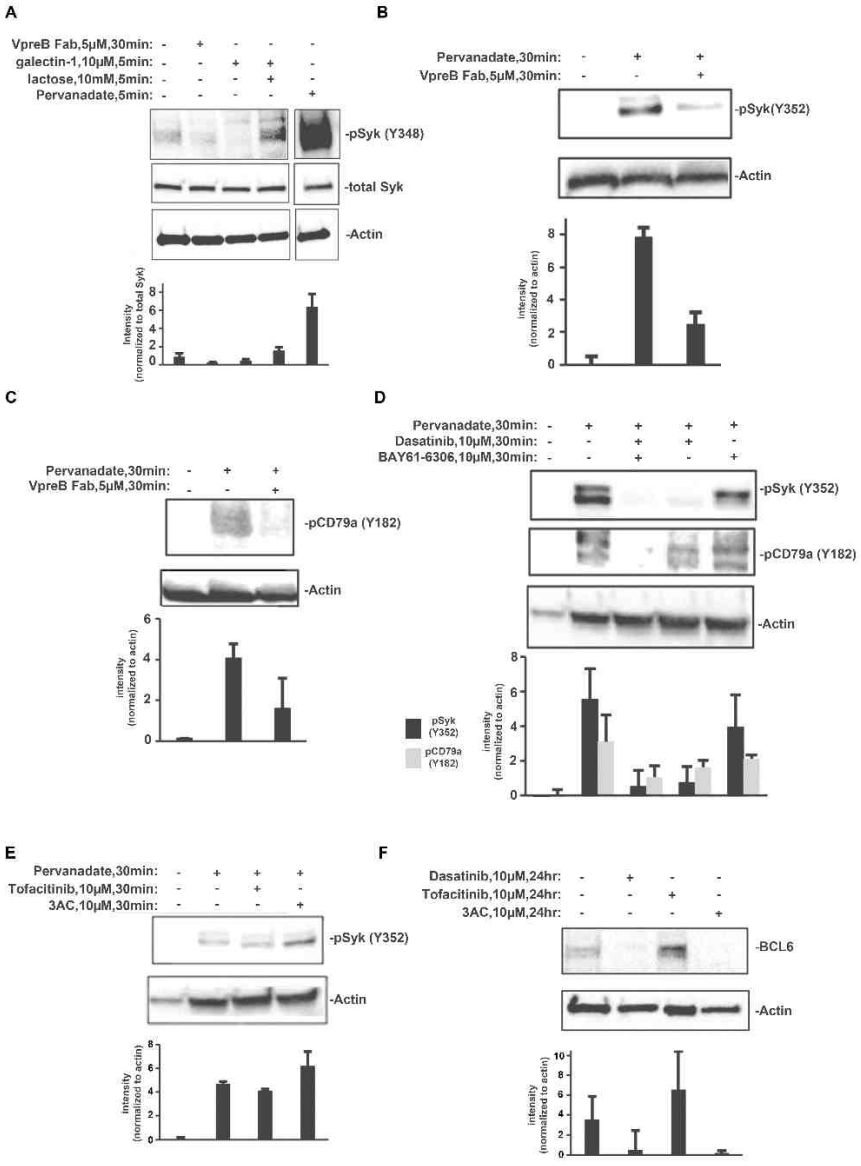

Fig. 4. Western blotting analysis of pre-BCR signaling. (A) Western blotting analysis of Nalm6 cell lysates (3 x 107cells) for Syk phosphorylation at Tyr348 (pSyk Y348) after the indicated treatments. Blots were stripped and incubated with antibodies against total Syk and actin. Note that the pervanadate lane is shown after gray scale adjustment of the digital image, to adjust for the intensity of the signal for pSykY348 compared to that in resting cells and after treatment with inhibitors. (B and C) Western blotting analysis of 697 cells (1.0 x 106) with antibodies specific for pSyk and pCD79a (Igα) after the cells were treated for 30 min with anti-VpreB Fab in the presence of pervanadate. (D) Western blotting analysis of 697 cells (1.0 x 106)with antibodies against pSyk and pCD79a (Igα) after the

cells were treatment with BAY61-3606 (Syk inhibitor) or dasatinib (Lyn and Abl inhibitor) in the presence of pervanadate. (E) Western blotting analysis of 697 cells (1.0 x 106) with antibody specific for pSyk after the cells were treated for 30 min with 3AC (SHIP inhibitor) or tofacitinib (Jak inhibitor) in the presence of pervanadate. (F) Western blotting analysis of 697 cells (1.0 x 106) with antibody specific for total BCL6 protein after the cells were treated for 24 hours with dasatinib, tofacitinib, or 3AC. All blots are representative of three or more independent experiments. Accompanying bar graphs report total densitometry data for all experiments for a given condition, with the abundance of the protein of interest normalized to that of actin or total Syk.

We also demonstrated the contribution of the pre-BCR–Lyn-Syk axis in autonomous signaling to BCL6 production, because treating 697 cells overnight with dasatinib resulted in reduced BCL6 abundance (Fig. 4F). Overnight treatment of 697 cells with tofacitinib increased the abundance of BCL6 protein, which we attributed to relief from a Jak-STAT pathway that represses BCL6 transcription (Fig. 4F) (26, 55). Genetic deletion of SH2-containing inositol-5 phosphatase-1 (SHIP1, also known as INPP5D) or inhibition of its phosphatase activity with the small molecule inhibitor 3AC (3-a-aminocholestane) leads to cell death in BCR-ABL1+ acute lymphoblastic leukemia cells (50). We also evaluated the effects of 3AC on 697 cells. As reported previously (50), 3AC slightly increased Syk phosphorylation in these cells (here performed in the presence of pervanadate) (Fig. 4E). In addition, overnight treatment with 3AC alone resulted in a decrease in BCL6 protein abundance (Fig. 4F).

Inhibitors of tyrosine kinases and inositol phosphatases differentially affect the survival of BCP-ALL cells

We next evaluated whether anti-VpreB Fabs or our panel of pharmacologic inhibitors could induce apoptosis in 697 cells, either alone or in combination with low concentrations of the chemotherapeutic agent vincristine. Overnight incubation of the cells with VpreB Fabs slightly enhanced the labeling of the cells with both 7-AAD and Annexin-V (14.9% compared to 8.5% of untreated cells, Fig. 5A). The combination of VpreB Fabs with vincristine (10 ng/ml) also slightly enhanced apoptosis (81.4% apoptotic cells compared to 69.9% for vincristine alone). At least for 697 cells, which lack Jak mutations known to be present in a minor subset of BCP-ALL cases (56), treatment with tofacitinib did not directly induce apoptosis (Fig. 5B). By comparison, both dasatinib (a Lyn inhibitor) and

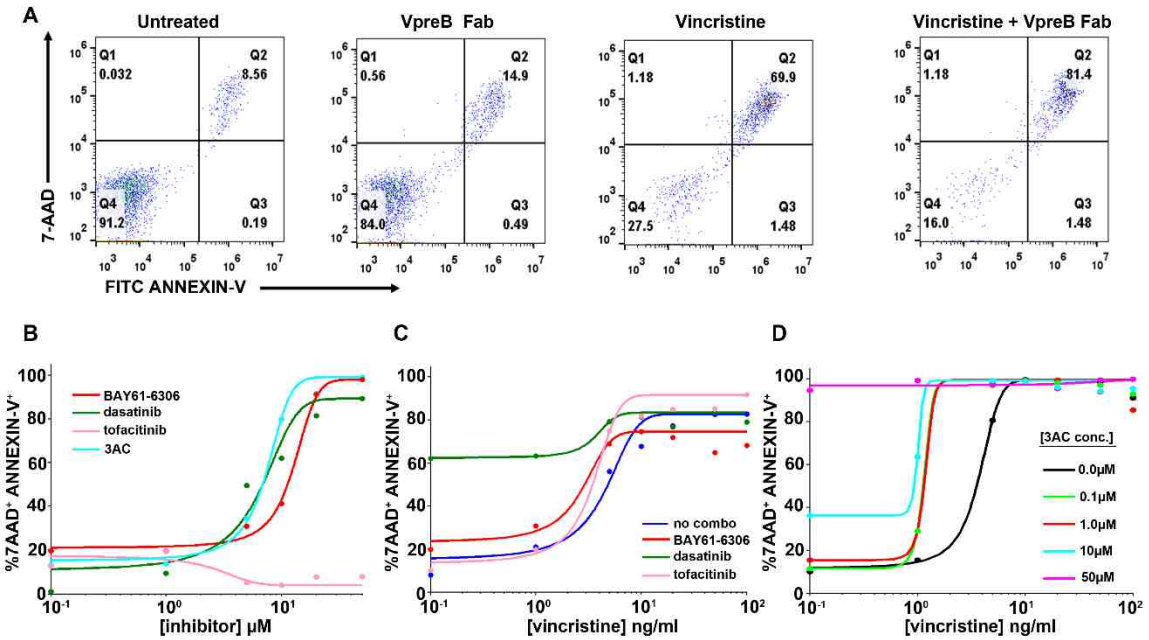

Fig. 5. Analysis of apoptosis and viability in BCP-ALL cell lines after treatment with pre-BCR pathway inhibitors. (A) Annexin V (FITC-conjugated) and 7-AAD labeling of 697 cells after 3 days of culture in the absence (autonomous) and presence of anti-VpreB Fabs or vincristine, as indicated. (B) 7-AAD and Annexin-V labeling of 697 cells treated for 3 days with a range of concentrations (0.1 to 100 µM) of tyrosine kinase inhibitors (BAY61-6306, dasatinib, tofacitinib) or inositol phosphatase (3AC). (C) 7-AAD and Annexin-V labeling of 697 cells treated for 3 days with or without a single dose (10 µM) of tyrosine kinase inhibitors (BAY61- 6306, dasatinib, tofacitinib) in combination with increasing concentrations (0.1 to 100 ng/ml) of vincristine. (D) 7-AAD and Annexin-V labeling of 697 cells incubated for 3 days with or without 3AC (0.1 to 50 µM) in combination with increasing doses of vincristine (0.1 to 100 ng/ml). In all plots, the percentage of cells that were 7AAD+Annexin-V+ is plotted against increasing concentrations of vincristine or inhibitor and fit with a sigmoidal dose-response curve. All data were acquired by flow cytometric analysis of at least 10,000 events for each condition and are representative of xxx independent experiments.

BAY61-3606 (a Syk inhibitor) resulted in increased 7-AAD labeling of non-viable cells (Fig. 5B). All three inhibitors (tofacitinib, dasatinib, and BAY61- 3606; each at 10 μM) modestly potentiated apoptosis in 697 cells treated with vincristine over a range of 0.1 to 2 ng/ml (Fig. 5C). When used at 1 μM, 3AC sensitized cells to low concentrations of vincristine (0.1 to 2 ng/ml) (Fig. 5D). Higher concentrations of 3AC (10 to 50μM) were required to induce direct killing of 697 cells, as determined by analysis of 7-AAD labeling (Fig. 5D and figs. S8 to S10).

Tracking of pre-BCRs in primary cells reveals differential effects of anti-VpreB Fabs and Lyn inhibition

The pre-BCR is absent from BCR-ABL1+ acute lymphoblastic leukemia cells (50); however, its presence in other BCP-ALL subsets likely defines those patients for which therapies that target autonomous signaling are of potential value (26). We identified two distinct BCP-ALL patient samples (#280 and #238) that had measurable amounts of pre-BCR on the cell surface (Fig. 6). To enable repeated measurements to be made of primary cells to validate pre-BCR diffusion and drug sensitivity studies, the patient samples were cryopreserved on the day of acquisition and then were either placed in tissue culture immediately after thawing or were passaged through Nod-SCID-γ2–deficient mice (a necessary step to expand primary leukemia blasts, which have a limited lifespan in culture). The cell surface abundance of the pre-BCR, based on quantitative binding of anti-VpreB antibodies (fig. S11), for these two patient samples ranged from ~4000 to 15,000 copies per cell, with average values of 6000 to 7000 (Fig. 6A). These values were very similar to those determined from experiments with Nalm6 cells and are equivalent to about half of the abundance of the pre-BCR on 697 cells. The pre-BCR complex is commonly assumed to have a uniform stoichiometry of two mIgμ:VpreB:λ5 complexes to one Igα−Igβ heterodimer; however, our flow cytometry–based quantitative measurements suggest that both sets of patient cells had an average of 4000 Igβ molecules, whereas there were ~6500 copies of Igβ on Nalm6 cells and ~8000 copies on Igβ on 697 cells. We found that there were slightly differing ratios (0.7 to 1.1) of mIgμ:Igβ for each cell type (Fig. 6B). We speculate that this variability may be explained by some of the pre-BCRs being composed of homodimers of Igβ or Igα.

We next performed SPT with the anti-Igβ Fab'-QD probes to evaluate the diffusion of pre-BCRs on untreated primary cells. We found that the overall diffusion coefficient for pre-BCRs on the plasma membrane of B cells from patient #238 was similar to that of 697 cells (Fig. 6C). The range of the observed values, as well as the overall diffusion coefficient for pre-BCRs on cells from patient #280, matched well with the diffusion characteristics of pre-BCRs on Nalm6 cells. As an extension of the drug profiling reported earlier, we also treated 697 cells with each of the three tyrosine kinase inhibitors and performed SPT experiments. Treatment of 697 cells with the Lyn and Syk inhibitors (dasatinib and BAY61-3606, respectively) increased pre-BCR mobility (Fig. 6D), as was expected given that ITAM phosphorylation generates docking sites for signaling partners that slow receptor diffusion. Incubation of B cells from patient #280 with either anti-VpreB Fab or dasatinib resulted in a marked increase in pre-BCR mobility (Fig. 6E). In contrast, there was little change in pre-BCR diffusion in cells from patient #238 after either treatment (Fig. 6F).

Together, our earlier findings related to the diffusion and dimerization properties of pre-BCRs (Figs. 3 and 6) suggest that these receptors fall into at least two distinct categories. To address potential explanations for these observations, we isolated mRNA from each of the two cell lines, as well as from the two patient samples. After RT-PCR amplification, we performed sequencing analysis for comparison to the reference sequence for VpreB (UniProt #P12018). We found that a substantial fraction of VpreB sequences expressed in each cell source differed from the reference sequence (fig. S12). Furthermore, the two groups with distinct diffusion profiles also sorted together based upon single nucleotide polymorphisms (SNPs). For 697 cells and those from patient #238, which had the fastest pre-BCR diffusion rates, we documented substitutions of lysine for glutamic acid at position 132 and glutamic acid for lysine at position 77. For Nalm6 cells and those from patient #280, which showed the slowest overall pre-BCR diffusion rates, we found either a 33 or 80% frequency, respectively, in substitution of asparagine for the aspartic acid at position 76. This latter change results in a putative N-linked glycosylation site, which is worth pursuing further because there are no N-linked glycosylation sites in the other forms

of VpreB. With the exception of the K77E variant, all of these variants are listed on the UniProt site as natural variants.

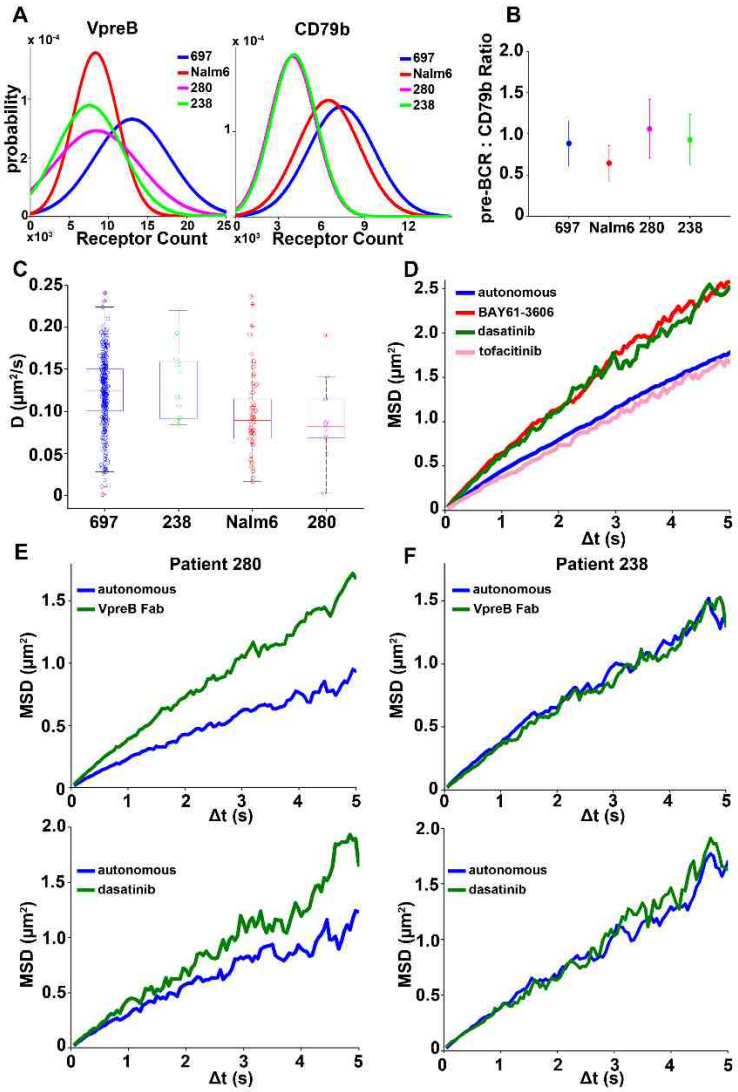

Fig. 6. Expression profile and single particle tracking of pre-BCRs on different primary BCP-ALL cells. (A) Comparison of the cell surface abundances of VpreB and CD79b (Igβ) on 697 cells, Nalm6 cells, and blasts from patients #238 and #280, as a readout of pre-BCR on the membrane of BCP-ALL cells. Cells were incubated with saturating concentrations of labeled fluorophore-conjugated anti-VpreB or anti-CD79b

antibodies and binding values were quantified by flow cytometry. Results were calibrated by saturation binding of each antibody to Simply Cellular anti-mouse IgG microspheres. Data are representative of at least three independent experiments. (B) Comparison of the mean fluorescent values after anti-VpreB and anti-CD79b labeling of the indicated cell types, plotted as a ratio of pre-BCR (2 VpreB = 1 pre-BCR) to CD79b. (C) Comparison of the diffusion coefficient (μm2/s) of the pre-BCR in 697 cells (n = 26,447 trajectories) and Nalm6 cells (n = 3,573 trajectories) to primary cells from patient 238 (304 trajectories) and patient 280 (353 trajectories); single particle tracking was performed onuntreated cells in all cases and performed over multiple days. (D) Ensemble MSD plots derived from SPT of the pre-BCR on 697 cells with or without a 10-min treatment with the indicated tyrosine kinase inhibitors. (E) Ensemble MSD plots derived from SPT of the pre-BCR on the surface of primary cells from patient 280 with and without a 10-min treatment with dasatinib (1μM) or anti-VpreB Fabs (1 μM). (F) Ensemble MSD plots derived from SPT of the pre-BCR on the surface of primary cells from patient 238 with and without a 10-min treatment with dasatinib (1 μM) or anti-VpreB Fabs (1 μM). Data in (D) to (F) are representative of xxx independentexperiments.

Primary BCP-ALL cells show differential sensitivity to blockade of autonomous pre-BCR signaling.

Given our observations that BCP-ALL cells fall into at least two distinct classes with respect to pre-BCR mobility and their possible linkage to VpreB polymorphisms, we evaluated whether blockade of homotypic pre-BCR self-associations might differentially sensitize the two primary patient samples to vincristine. We found that incubation of cells from patient #280 with anti- VpreB Fabs enhanced apoptosis, whether administered alone or in combination with a low concentration of vincristine (Fig. 7A). Blasts from patient #280 were also very sensitive to dasatinib as a single agent; 80% of cells were strained with 7-AAD and Annexin-V after 24 hours of culture. Longer incubations were not feasible, because the cells from this patient were 40% 7-AAD–positive when incubated with no drug or in the presence of up to 5 ng/ml vincristinel (Fig. 7A, blue line).

Blasts from patient #238, which is a high-risk case with MLL-rearrangement (table S1), were relatively resistant to vincristine alone up to concentrations of 10 ng/ml (Fig. 7B). Anti-VpreB Fabs did not potentiate low-dose vincristine treatment of cells from patient #238; however, we observed a ~50% increase in 7-AAD labeling of patient #238 cells when dasatinib was added over a range of concentrations of vincristine (1 to 100 ng/ml). Thus, the combination of dasatinib and vincristine was effective in killing cells from both patients, but higher concentrations of dasatinib were required to kill the cells from patient #238. Finally, basal amounts of BCL6 protein were slightly greater in patient #280 cells compared to those in cells from patient #238 (Fig. 7C). The addition of VpreB Fab to block autonomous signaling decreased the abundance of BCL6 only in the cells from patient #280 (Fig. 7C). Furthermore, BCL6 abundance was reduced or became undetectable in cells from either patient when treated with either dasatinib or 3AC (Fig. 7D). Because the cells from patient #238 cells harbor an MLL-AF4 fusion, they fall into a category of BCP-ALL that is not frequently associated with the "Ph-like" transcriptional signature (57). Nevertheless, based upon the inhibitor studies, the basal activities of Lyn and SHIP (and possibly Abl) apparently contributed to the survival of the cells from patient #238. As for 697 cells (Fig. 4D), BCL6 abundance in both sets of primary cells was markedly increased in response to the Jak inhibitor tofacitinib, which suggests that BCL6 expression was repressed by the Jak-STAT pathway. Together, our results suggest that agents targeting the pre-BCR or its downstream partners lead to lymphoblast killing in vitro. However, the extent to which this will apply in a clinical setting will require further evaluation, including analysis of surrogate light chain polymorphisms as well as of the abnormal activation of alternative tyrosine kinase signaling pathways linked to specific mutations in non-pre-BCR pathways.

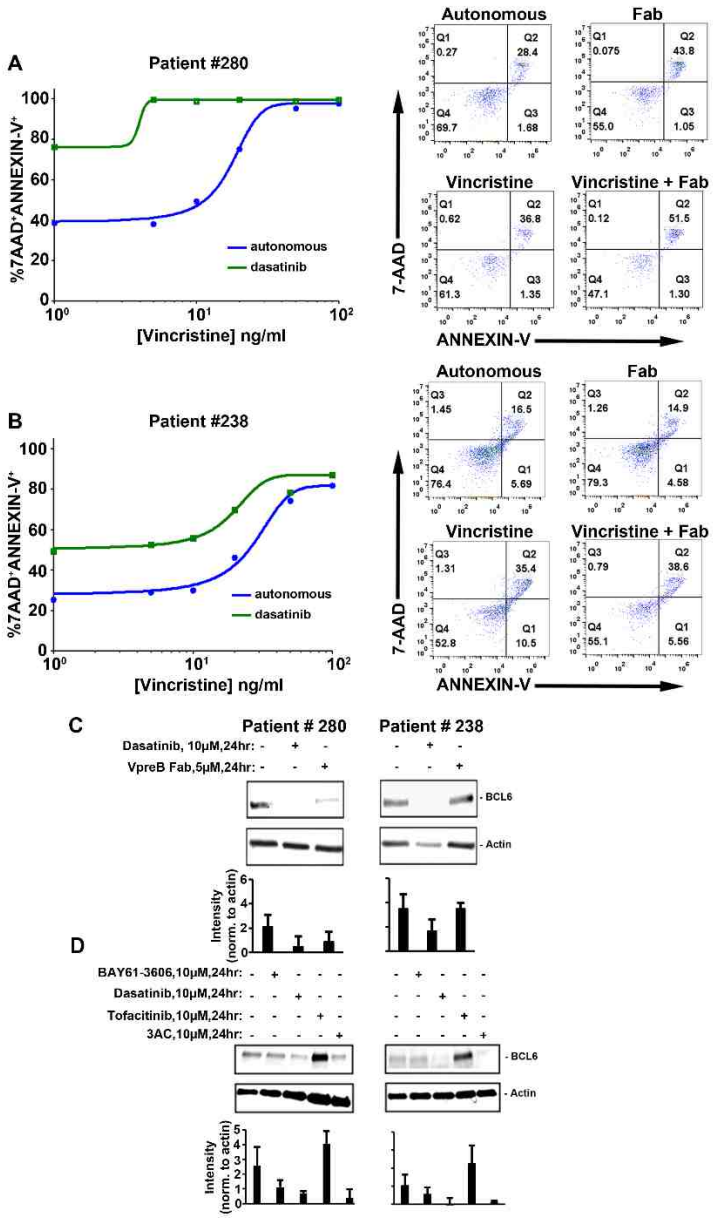

Fig. 7. Flow cytometric and Western blot analyses of primary BCP-ALL cells after treatment with tyrosine kinase inhibitors or anti-VpreB Fab. (A and B) Left: Plots show Annexin V (FITC-conjugated) and 7-AAD labeling of primary cells from patient #280 (A) and patient #238 (B) after 24 hours of culture with or without anti-VPreB Fabs (5 μM) or vincristine (1 to 100 ng/ml) as indicated. Right: Scatter plots report flow-based measurements of primary cells from patient 280 (A) and patient 238 (B) that were double labeled for 7-AAD and Annexin- V after 24 hours of culture with or without a single dose of anti-VpreB Fab (5 μM), vincristine (10 ng/ml), or both, as indicated. All data in (A) and

(B) were acquired by flow cytometric analysis of at least 10,000 events for each condition and are representative of xxx independent experiments. (C) Western blotting analysis of cell lysates (1.0 x 106 primary cells each) for patients 280 or 238 to compare the relative abundance of BCL6 protein after the cells were treated for 24 hours with dasatinib (10 μM) or anti-VpreB Fab (5 μM). (D) Western blotting analysis of cell lysates (1.0 x 106 cells) from patients 280 and 238 to compare the relative abundance of BCL6 protein after the cells were treated for 24 hours with BAY61-6306, dasatinib, tofacitinib, or 3AC. Each blot is representative of three or more independent experiments. Bar graphs show total densitometry data for all experiments for a given condition, with the abundance of the protein of interest normalized to that of actin.

DISCUSSION

Seminal studies over 20 years ago led to the discovery of the surrogate light chain components, VpreB and λ5, which proved to be critical for the cell surface expression of the μH chain in early B cells (58). The assembly of Igμ with surrogate light chain components generates a functional cell surface receptor that signals the successful recombination of the heavy chain, initiates a burst of pre-B-cell proliferation, and then sets the stage for cell cycle arrest and the recombination of light chain–encoding genes (59). Reviews have covered critical aspects of the pre-B cell checkpoint, including the proximal events associated with pre-BCR signaling (19) and complicated transcriptional regulation, which are important to control B cell development and avoid autoreactivity (60). These checkpoints are often overridden in the pre-B leukemia setting (25).

We chose to study the pre-BCR in the context of BCP-ALL, which is one of the most prevalent neoplasms in children (61) and an aggressive cancer in adolescents and adults (62). Although therapies have markedly increased the number of relapse-free patients in the past 40 years, there remain inherent concerns with existing treatments (63). Among these include the association of early chemotherapeutic administration with serious effects that alter early and late life stages (64). Considering these factors and the fact that high-risk leukemia outcome appears to have generally plateaued with conventional therapy (65),

a push for new therapeutic approaches and agents is of rising importance. Based on success in mature B cell neoplasms (66-68), the pre-BCR and its signaling partners (31) may also offer new promise for targeted therapy in BCP-ALL.

We focused here on the earliest events in pre-BCR signaling: the homo-oligomerization that drives autonomous signaling. We applied state-of-the-art imaging techniques to demonstrate the highly transient nature of homotypical pre-BCR interactions. These interactions influence pre- BCR diffusion in the plasma membrane of early lineage B cells. We found that pre-BCRdiffusion in 697 cells and blasts from patient #238 was relatively fast at ~0.12 μm2/s (table S2 and Fig. 6C). HMM analysis of >50,000 trajectories in 697 cells enabled these trajectories to be further divided into 2 groups: The fast group, traveling at 0.16 μm2/s, were considered "free" QD-tagged receptors and assumed to be mostly monomers, with the caveat that interactions with dark receptors cannot be captured under these SPT imaging conditions. The slow group, traveling at 0.059 μm2/s, represents QD-tagged pairs during the intervals in which they are engaged in homotypic interactions (Fig. 1G). It is likely that the slow population also reflects the transient residency of the pre-BCR in protein islands, which is already described as a mechanism to cluster the TCR and BCR in lymphocyte membranes (69, 70). Our results, which capture repeated interactions between the same pair of pre-BCRs (Fig. 1C), are consistent with the transient co-confinement of pre-BCRs in these specialized membrane microdomains and within cytoskeletal corrals.

Diffusion of the pre-BCR in the plasma membranes of Nalm6 cells and patient #280 blasts was slightly slower overall at ~0.09 μm2/s, with values of 0.12 μm2/s for free receptors and 0.015 μm2/s for receptors engaged in homotypic interactions. The slower diffusion rates for Nalm6 receptors in the bound state might reflect the five-fold slower off-rate for pre-BCR in Nalm6 compared to 697 cells (Fig. 1J and fig. S4), and therefore a greater propensity to form slow-moving, higher-order oligomers. We observed several instances in Nalm6 cells in which interacting pre-BCR pairs had an interaction distance >100 nm (fig. S5 and movie S2). Similarly, single-molecule imaging studies of the BCR demonstrated that higher affinity interactions support an enhanced ability of the receptor

to oligomerize (71). We do not currently have a definitive explanation for the two distinct off-rates that we observed for the homotypic pre-BCR interactions on different BCP-ALL cells, but we speculate that it could be because of the observed VpreB SNPs that we documented for this group (fig. S12A). Of particular interest is the SNP variant that introduces a putative N-glycosylation site (substitution of asparagine for aspartic acid at position 76). A 3D structural model based upon the solved NMR and X-ray crystal structures of the pre-BCR (fig. S12B) reveals that this amino acid (and any putative posttranslational modification) is at a protein surface that is exposed to be solvent. Differential N-glycosylation of Asn46 of the pre-BCR heavy chain was previously noted to have a major influence on pre-BCR autonomous signaling, possibly by neutralizing an inhibitory influence imposed by the arginine-rich λ5 tail of the surrogate light chain (15). The substitution of lysine for glutamic acid at position 132, seen in those 697 cells with a faster off-rate for pre-BCR homotypic interactions, could also reflect the change in charge near the putative VpreB dimerization site (17).

The BCRs of naïve and mature B cells have been the subject of impactful, high-resolution imaging studies (22, 70-73) that provide a context for the current work. BCR diffusion rates in the absence of ligand are generally slower than those of the pre-BCR, with variability amongst B cell sources and across imaging conditions. For example, BCR diffusion in J558L B cells was measured in TIRF mode on antigen-free lipid bilayers to have a range from 0.039 to 0.069 μm2/s (71). Up to 20% of BCRs are immobile under those conditions ($D < 0.01$ μm2/s). On the surface of A20 B cells, wild-type IgM BCR travels at an average rate of 0.031 μm2/s, with the caveat that those IgM BCRs that are outside actin-rich regions diffuse at a faster rate (0.108 μm2/s) than that of BCRs within actin-rich membrane (0.039 μm2/s) (22). The heavy chain moiety of BCR is very influential, because the IgD BCR exhibits very slow diffusion (0.005 μm2/s) (22). The cellular context also matters, particularly the influence of the actin cortical cytoskeleton, which forms corrals to restrict receptor motion (24). The BCR undergoes faster diffusion in B cells treated with latrunculin A (22) or in cells stimulated with ligands for Toll-like receptors, which induce cofilin-mediated severing of actin filaments (73). We speculate that variability in the cortical actin cytoskeleton of Nalm6 and 697 cells and in cells from

the two primary patients could contribute to our observed differences in pre-BCR diffusion rates.

Our experimental design was inspired by mutagenesis and structural studies that implicate the unique regions of λ5 in pre-BCR homotypic oligomerization for ligand-independent signaling (17, 18). We reasoned that Fabs directed at the VpreB component of the surrogate light chain would sterically block λ5-mediated homodimerization. This strategy was successful, because incubation with these monomeric antibody fragments resulted in faster pre-BCR diffusion rates and a marked reduction in observed dimerization events. Furthermore, the Fabs also blocked the accumulation of pCD79a and pSyk in the presence of pervanadate and H2O2, a strategy that reveals the close control of autonomous signaling by phosphatases (51). Kinetic proofreading is proposed as a generalized schema by which the number of receptors occupied and the duration of receptor occupancy translate into functional signals (74). In the absence of high-affinity interactions, frequent rebinding events associated with spatial confinement appear to provide the TCR a mechanism to propagate even weak signals (75). We speculate that frequent, low-affinity rebinding events also provide exactly the right threshold needed for the pre-BCR to maintain the narrow window for early B survival.

Galectin-1 binds to the λ5-UR domain of the pre-BCR (35) and, although this interaction is independent of the glycan-binding site of galectin, engagement with the pre-BCR induces local conformational changes that alter the affinity of galectin-1 for carbohydrates (37). Thus, it was important to evaluate the behavior of pre-BCRs that were crosslinked with soluble, dimeric galectin-1 in the presence and absence of lactose to distinguish "lattice-like" complexes, which include other cell-surface glycans, from dimers and chains of pre-BCRs and galectin-1 alone. We showed that the pre-BCR rapidly became immobile after the addition of galectin-1 alone (Fig. 3B and movie S3), forming clusters that were large enough to observe by standard epifluorescence techniques (Fig. 2A). Inclusion of lactose during galectin-1–mediated crosslinking disrupted complex, glycan-mediated aggregation, which was observed as a substantial change in the values for uncorrelated jump distance (Fig. 2B) and jump magnitude (Fig. 2C), as well as in overall diffusion (Fig.

2D). It is remarkable that galectin-mediated crosslinking in either context did not support accumulation of BCL6 protein. The need for a perfectly tuned autonomous pre-BCR signal was previously described as the “Goldilocks” threshold that optimally supports the PI3K-Akt pro-survival pathway (76, 77). The role for galectin-1–mediated crosslinking of the pre-BCR in ALL deserves further study. There may be a difference between galectin-1–mediated pre-BCR signaling when galectin-1 is produced as a soluble autocrine factor (a notable feature of MLL-rearranged BCP-ALL cells) (39) versus galectin presentation on the surface of stromal cells (78). It has been proposed that early B cells occupy different bone marrow niches as they progress from dependency on IL-7 to stromal presentation of galectin (16).

One challenge will be to identify those BCP-ALL patients for which pre-BCR targeted therapy is appropriate, because there are multiple mechanisms that enable leukemia cells to bypass the pre- BCR checkpoint (25). A recent study of 830 cases from four clinical trials identified 13.5% of patients as being particularly reliant on autonomous pre-BCR signaling (26). On face value, the two patient samples (#280 and #238) that we studied here would fall within this class, because they expressed pre-BCR on the cell surface and were sensitive to dasatinib (Fig. 7). However, only one patient sample (#280) exhibited faster diffusion of the pre-BCR after exposure to anti- VpreB Fabs, which was accompanied by an increase in the fraction of apoptotic cells. This indicates that the cell surface expression of the pre-BCR alone does not predict reliance on autonomous signaling for survival.

Important BCP-ALL subsets rely on aberrant Abl or Jak signaling pathways, indicating that they are arrested very early in the B cell developmental process. Twenty-five percent of BCP-ALL cases express BCR-ABL because of a 9:22 translocation (Philadelphia chromosome, Ph+), and their responses to BCR-ABL kinase inhibitors can be short-lived (79). A “Ph-like” transcriptional signature has been linked to poor outcome in 10% of childhood ALL and 27% of adult ALL cases; the novel translocations and activating mutations associated with Ph-like ALL involve a number of cytokine receptors (FTL3, IL-7R, CRLF2, EPOR, PDGFRB, TSLF) and their associated signaling partners (kinases of the Jak and Abl families) (80). It appears that the ITAM-Syk and the ITIM-phosphatase

are operating in the background of these oncogenic signaling pathways, because inhibitors of both pathways can stimulate pre-existing B cell programs for cell death (50). ITIM-bearing receptors (including, PECAM1, CD300A, LAIR1, and CD22/SIGLEC-2) are expressed in BCP-ALL cells, where they serve critical roles in recruiting the tyrosine and inositol phosphatases SHP1 (PTPN6) and SHIP-1 (INPP5D), respectively (50, 81). Whereas SHIP-1 acts as a mediator of negative signaling from ITIM-bearing receptors in immune cells, SHIP-1 is important in negative regulatory loops downstream of the BCR (82). SHIP-1 can be engaged under conditions that promote the incomplete phosphorylation of Igα and Igβ ITAMs, which favors the recruitment of single SH2 domain– bearing phosphatases over the recruitment of the dual SH2 domain–bearing kinase Syk (83). The Lyn–SHIP-1–PTEN–SHP1 negative regulatory axis is an essential and constitutively engagedregulator of the BCR, particularly in the context of anergy (83, 84).

The complexities of the pre-BCR and its downstream partners (Syk, SLP65, and BCL6) alternatively serving as oncogenes or tumor suppressors have been reviewed (25). Central to understanding this complexity will be accurate maps of the stage-specific transcription factor network, which normally coordinates B lymphoid progression, and how disruption at key checkpoints leads to oncogenesis (85). We expect that improved understanding of pre-BCR dynamics and signaling outcomes, begun here with the current study, will be particularly important as tyrosine kinase inhibitors are incorporated into BCP-ALL therapy. Because of complex regulatory feed-forward and feed-back loops in early B cell development (26, 41, 85), it is critical to understand if low-level pre-BCR signaling events offer potential sources of drug resistance when the strongly proliferative signals from BCR-ABL and mutant Jak-STAT signaling pathways are suppressed. The exquisite sensitivity of BCP-ALL cells to inhibitors of Lyn, Syk, and SHIP-1, as shown here, underscores that a substantial number of BCP-ALL cases are likely to benefit when chemotherapy and kinase inhibitors are administered in combination This concept has already been demonstrated in an animal model of Ph+ ALL, combining dasatinib (which inhibits Abl and Lyn) with ruxolitinib (which inhibits Jak) (86). Serial administration or immunotherapy may be possible if toxicity is a barrier when chemotherapeutics and kinase

inhibitors are co-administered.

CHAPTER 3

Molecular Dynamic Simulations of Galectin-1 with Carbohydrates: Influence of Binding to pre-BCR λ5-UR

M. Frank Erasmus[1], César A López[2], Bridget S. Wilson[1] and S. Gnanakaran[2]

[1]Department of Pathology, University of New Mexico, Albuquerque, New Mexico
[2]Theoretical Biology and Biophysics Group, Los Alamos National Laboratory, Los Alamos, New Mexico

ABSTRACT

Early B cell development requires functional expression of the pre-B cell receptor (pre-BCR) composed of the Igμ heavy chain associated with surrogate light chain components, λ5 and VpreB. Precursor B cells pass the first critical development checkpoint based upon appropriate survival signals mediated through the pre-BCR. This autonomous signal is initiated through transient pre-BCR/pre-BCR homodimers and is important in both B cell development and malignancies. In contrast, the binding of Galectin-1, a known pre-BCR ligand, promotes the formation of complex higher order oligomers. This complex modulates important signals required in early B cell development and may also have an important role in leukemia progression through crosstalk with stromal cells in the bone marrow microenvironment. Galectin-1 is known for its glycan-binding properties, which promotes cell-to-cell contacts between precursor B cells and bone marrow stromal cells and forms a galectin-1 dependent signaling niche. Upon binding the pre-BCR's λ5 subunit, galectin-1 undergoes a conformational change within its carbohydrate-binding site (CBS) altering its affinity for N-acetyllactosamines (LacNAc) on the stromal surface in favor of glycoreceptors on the precursor B cell membrane. This remodeling of the galectin binding preference can potential lead to differential crosslinking of the pre-BCR with cell surface glycoproteins and glycolipids, modifying signaling outcomes downstream of the pre-BCR.

Here we use molecular dynamics (MD) simulations to study how the pre-BCR λ5/galectin-1 protein-protein interaction modifies the carbohydrate binding properties of galectin-1. The MD results support recent experimental findings that implicate critical conformational changes within galectin-1's conserved binding core. These structural modifications disrupt the hydrogen bonding network and aromatic stacking interactions that are central to galectin-1/carbohydrate interactions. Computational calculations of binding free energies exhibit a distinct reduction in the affinity for LacNAc molecules induced by pre-BCR binding. Our results also suggest that the pre-BCR λ5/galectin-1 interaction also influences galectin-1's dimer/monomer equilibrium.

INTRODUCTION

Functional expression of the pre-B cell receptor (pre-BCR) is an essential checkpoint in the early stages of normal B cell development. The first step in pre-BCR expression is the successful rearrangement of the immunoglobulin heavy chain (HC or Igμ), which is then co-expressed with the λ5 and VpreB components of the surrogate light chain (SLC)(*1*). Igμ and SLC assemble with Igα and Igβ signaling subunits in the endoplasmic reticulum soon after synthesis (*2*), then traffic as an oligomeric pre-BCR to the cell surface. Once resident at the plasma membrane, pre-BCRs diffuse in the membrane and undergo transient homo-dimerization events that propagate weak, ligand-independent signaling (*3*). Referred to as autonomous or "tonic" signaling (*4, 5*) transient pre-BCR homo-oligomerization engages the src family kinase, Lyn, for phosphorylation of Igα and Igβ immunoreceptor tyrosine-based activation motifs (ITAMs) (*6*). Dually phosphorylated ITAMs serve as docking sites for the Src homology 2 (SH2) domains of spleen tyrosine kinase (Syk), the critical kinase responsible for driving healthy B cell development. Dysregulated pre-BCR signaling pathway is emerging as an important contributor to early stage B cell malignancies (*7*). Recently, it has been shown that autonomous signals mediated through the pre-BCR leads to increased BCL6 expression in B cell precursor acute leukemia (BCP-ALL) (*8*), driving a positive feedback loop that results in worse clinical outcome in subpopulations of leukemia patients. While targeting the homo-dimerization interface with monovalent Fabs has shown promising results *in vitro (3),* evidence suggests that alternative mechanisms can drive pre-BCR signaling following interactions with extracellular proteins within the bone marrow.

Galectin-1, expressed in wide variety of tissues including bone marrow (*9*), is a pre-BCR ligand (*10*). Galectin-1 mediates cell-to-cell contacts between the pre-B cell and stromal cells, through both carbohydrate/protein and protein/protein interactions (*10-12*). Upon galectin-1 binding on stromal cells, the pre-BCR redistributes to one pole to form a "developmental synapse" at the cell-cell interface and initiate robust downstream phosphorylation (*12, 13*). This interaction likely plays an important role in early healthy precursor B cell development, as these cells migrate from an IL-7+-dependent niche to a galectin-

1+ niche within the bone marrow (*13*, *14*). The galectin-1+ signaling niche also has an important role contributing to B cell survival (*14*, *15*).

Galectin-1 is a member of the large family of β-galactoside binding lectins, each with a highly conserved carbohydrate recognition domain (CRD) (*16*). Galectin-1 is a homodimer in solution composed of two identical 14.5kDa monomers. Galectin-1 folds into a β sandwich topology with two antiparallel β-sheets forming a concave and convex side. The concave side creates a groove composed of five subsites (A-E) that are responsible for carbohydrate binding. Subsites C and D represent the conserved core responsible for β-galactoside interactions. This includes an electrostatic interactions mediated through a hydrogen bonding network from hydroxyl groups within the carbohydrate and key residues within galectin-1 (His-44, Asn-46, His-52, His-54, Arg-48, Trp-68, Glu-71, and Arg-73) and detailed previously (*17*). This also includes a key hydrophobic aromatic stacking interaction mediated through the galactosyl of the carbohydrate and six-membered ring of Trp-68 in galectin-1. Though each CBS appears structurally independent, evidence suggests that binding of a saccharide within one CBS results in increased conformational entropy that drives negative cooperativity of binding in the CBS of adjacent site when binding to the same carbohydrate (*18*).

Recent NMR data has shown that galectin-1/pre-BCR binds directly to the λ5 subunit of the pre-BCR surrogate light chain, targeting the N-terminal unique region termed "λ5-UR" (*11*). This protein/protein interaction interface is in close proximity to amino acid residues contributing to carbohydrate affinity and has been shown to alter galectin-1's carbohydrate binding affinity (*19*). A plausible model (*19*) proposes that, in the bone marrow, galectin-1 is initially bound to N-acetylgalactosamine (LacNAc)-glycosylated receptors on stromal surfaces. Upon pre-BCR engagement, galectin-1 then undergoes a conformational change that alters its carbohydrate affinity. This frees the carbohydrate-binding site (CBS) of galectin-1, which now has differential preference for select saccharides, altering the crosslinking complexity of galectin-1 and the pre-BCR with glycolipids and glycoproteins in the microenvironment. It is important to note that the affinity of galectin binding to the pre-BCR is not changed by the presence or absence of the carbohydrate (*11*). We recently showed that inhibiting the

lectin-binding properties of galectin-1 with saturating concentration of lactose modulates the downstream signaling profile in pre-BCR+ leukemic B cells to galectin challenge (*3*).

Prior experimental and computational methods have raised many questions regarding galectin-1 regulation (*17, 18, 20*). The accommodation of different sugars in the carbohydrate binding pocket suggests considerable flexibility, but fails to provide detailed explanations for galectin-1's enhanced affinity for select sugars. A recent report made the intriguing observation that pre-BCR/galectin-1 engagement alters galectin-1 affinity for specific saccharides (*19*). Here, we employ molecular dynamics simulations to evaluate how carbohydrate binding properties of galectin-1 are altered in presence and absence of λ5-UR of the pre-BCR. We also explore the impact of carbohydrate or λ5-UR binding on galectin-1 dimerization. MD simulations are useful in studying allosteric effects because the enhanced level of molecular detail at both spatial and temporal scales and can be used to incorporate specific perturbations into the biomolecular system (*21*). Allostery has shown as an important for regulation of protein function and MD simulations have enabled scientists to elucidate function in variety of biological processes including immunological escapes (*22*), drug-design (*23*), and protein engineering (*24*). Mechanistically, we note galectin-1 in complex with the pre-BCR undergoes a significant alteration of the hydrogen bonding network, resulting in increased overall fluctuation and destablization of the conserved carbohydrate-binding core. Our simulations support recent findings (*19*) that show binding of λ5-UR to galectin-1 induces structural changes within subsite D of the CBS that disrupts key interactions to specific glycans., We also observed a significant shift in aromatic stacking interactions between Trp68 of galactin-1 and the galactosyl ring, which can modulate between more favorable or less favorable distributions dependent on the carbohydrate docked in the CBS. We are the first to report that pre-BCR engagement might also impact galectin-1 dimer stability.

METHODS

Systems Set-Up

Carbohydrate construction

The complete galectin-1 homodimer was used as a structural framework for these studies. Four different galectin-1 X-Ray structures bound to different carbohydates were obtained from the protein data bank**.** Sugars used in this study are detailed in **Figure 1**. These include **sugar 1A,** (gal(β1→4)glcNAc) (pdb id:4Y1U); **sugar 1B (**gal(β1→4)(6CO2)glcNAc) (pdb id: 4Y1Z), **sugar 2A (**gal(β1→3)glcNAc) (pdb id: 4Y1V); **sugar 4A** (neu5Ac(α2→3)gal(β1→4)glc) (pdb id: 4Y20). We used galectin-1 X-Ray structure (pdb id: 1GZW) for the unbound structure. The coordinates of the sugar neu5Ac(α2→3)gal(β1→4)glc, **sugar 4A**, bound to galectin-1 were copied and moved to a separate file. We added an N-acetyl group to the 3'-carbon using Marvin Sketch and validated with the 3D structure check tool (*25*). This sugar (see **sugar 4B**, **Figure 1**) was named neu5Ac(α2→3)gal(β1→4)glcNAc throughout text. Neu5Ac(α2→3)-gal(β1→4)glcNAc was superimposed to equivalent carbons within neu5Ac(α2→3)gal(β1→4)glc bound to galectin-1. LactoNNeotetraose (gal(β1→4)glcNAc(β1→3)gal(β1→4)glc) (see **sugar 3A,B, Figure 1**) was constructed using the GLYCAM Carbohydrate Builder Online Software tool (*26*). The carbons (C1-C6) of non-terminal and terminal gal(β1→4)glcNAc and gal(β1→4)glc groups of the gal(β1→4)glcNAc(β1→3)gal(β1→4)glc (**see red outline, Figure1 - sugar 3A,B**) were superimposed within gal(β1→4)glcNAc and gal(β1→4)glc , respectively, using the Chimera Software suite (*27*).

Docking of λ5-unique region to galectin-1

The pre-BCR λ5-unique region (λ5-UR) that interacts directly with galectin-1 was recently solved by ^{1}H TOCSY and two-dimensional ^{1}H NOESY experiments (*11*)**.** CD measurements confirmed a low level α-helical secondary structure (*19*). The coordinates of this 24-mer peptide λ5-UR$^{22-45}$ were obtained from the protein data bank (pdb id 2lkq). The λ5-UR (renumbered 1-22) was docked to galectin-1 (pdb id: 4Y20) chain A using the online ZDock server (*28*). This method incorporates shape complementarity, desolvation free energy and electrostatic scoring functions into the docking algorithm. Shape complementarity involves the explicit rotation (15° increments around each Cartesian angle) and translation

of the ligand with respect to a fixed receptor. For each rotational transformation, a Fast Fourier Transform (FFT) algorithm scans the translational space. Two shape complementarity functions for the receptor and ligand R_{SC} and L_{SC} are used to describe the geometric characteristics of the receptor (i.e. galectin-1) and ligand (λ5-peptide), respectively. An N x N x N grid is established with 1.2Å spacing, with N sufficiently large to cover maximal spans of receptor and ligand. The surface and core of the protein are identified by computing solvent accessible area with a water probe radius set to 1.4Å. Core grid points are set to predefined penalty scores as detailed (*28*). Shape complementarity scores could then be calculated using a correlation function between functions R_{SC} and L_{SC}. Surface grid point contacts contributed to positive correlation (with 1.0 being optimal), while core-core contacts contribute to a large negative penalty. Surface-core contacts results in a milder penalty compared to core-core contacts. A discrete Fourier Transform (DFT) and Inverse Fourier Transform (IFT) function are used to calculate the correlation between the two separate R_{SC} and L_{SC} functions. The next phase of the ZDock algorithm incorporates desolvation free energy which implements atomic contact energy (ACE) developed by *Zhang et al (29)*. These desolvation energies are the free energies associated with replacing a protein-atom/water contact with a protein-atom/protein atom contact. Finally, Z-Dock also uses electrostatics, which uses the Coulombic formula and partial charges derived from the CHARMM19 (*30*). Each of these criteria are combined whereby top prediction models are produced. ZDock reduces the overall search space by setting restraints to the receptor and ligand binding partners and/or through the exclusion of residues not implicated in the binding interaction. We set initial binding restraints to conserve the key electrostatic and hydrophobic interactions. Electrostatic interactions include Arg-6 and Arg-8 of λ5-UR to Asp-102 and Glu-74 of galectin-1, respectively. Hydrophobic interactions include Trp9 of the λ5-UR buried within Val76, Tyr104 and Phe106 of galectin-1.

Solvating galectin-1 for MD simulations

This galectin-1/λ5-UR model was equilibrated in a cubic box and solvated with ~18,000 TIP3P water molecules, with 150mM of Na and Cl ions. Counter ions were added to the system to maintain neutrality. Periodic boundary conditions were applied in x, y and z directions. All system set-up, equilibration and

simulations were conducted using the GROMACS package (*31*, *32*), version 5.1 and run on linux supercomputer cluster using multiple CPU nodes coupled with GPU acceleration.

Homology model of carbohydrates to galectin-1/λ5-UR

After energy minimization and equilibration a 1ns production MD simulations was conducted on the galectin-1/λ5-UR complex (see MD Computational Details for additional information). The final frame was collected and analyzed to ensure key galectin-1/pre-BCR interactions were maintained (i.e. Tpr-9 of λ5-UR buried within galectin-1 pocket). This equilibrated structure was used to construct a homology model of each galectin-1/carbohydrate complex. This was achieved using the MODELLER software package (*33*) using multiple template alignment. The carbohydrate-binding site of chain A was modeled by aligning residues 1 to 73 with galectin-1 bound to carbohydrate (without λ5-UR). Residues 74 to 134 of chain A were aligned to mimic the galectin-1/λ5-UR binding region. All chain B residues (with no sugar or λ5-UR) were aligned using averaging of both template structures. Five models were generated and the top structure for each sugar was selected based upon best DOPE score (*34*). All structures were analyzed using RMSD whereby protein residues showed < 0.1nm RMSD deviation from X-Ray structure and the carbohydrates were aligned with an identical starting orientation.

Topology generation using ACPYPE tool

The 3D coordinates from each carbohydrate docked into galectin-1's CBS were processed separately to prepare them with appropriate parameters for use in MD simulations. Hydrogens were added using the AddH function in Chimera software (*35*). Protonated structures were output with the mol2 format and used as input for ACPYPE, which was used to generate carbohydrate topologies and parameters for MD simulations compatible with AMBER99SB force field in GROMACS. The AnteChamber Python Parser (ACPYPE) (*36*) interface is a wrapper script for use with the ANTECHAMBER software (*37*).

MD Computational Details

Parameters from the AMBER99SB parameter set (*38*) were applied and short-range non-bonded interactions were cut off at 1.0nm. Long-range electrostatics were calculated using the Particle Mesh Ewald (PME) algorithm (*39*) and the model was energy minimized using steepest descent algorithm (*40*). Position restraints were applied to the heavy atoms and a constant volume (NVT) ensemble simulation was conducted for 100ps. During NVT (and NPT) equilibration, the protein/sugar and non-protein atoms were coupled to separate temperature baths and maintained at 310K using the V-rescale scheme (*41*) to maintain pressure isotropically at 1.0bar for 100ps. Next, constant pressure (NPT) equilibration was conducted with Parrinello-Rahman barostat (*42, 43*) to maintain pressure isotropically at 1.0bar for 100ns. For NVT and NPT equilibration, temperature, density and pressures were plotted over time to ensure the values converged. Preliminary production MD simulations were conducted without restraints for 30ns, unless otherwise stated, whereby the V-rescale thermostat and Parinello-Rahman barostat were applied.

MD Analysis

Dihedral Angle and Aromatic Stacking Measurements

For dihedral angle calculation for the carbohydrate molecule we used the interglycosidic linkage between the β-galactosyl ring and the glucosyl ring within galectin-1's conserved binding core (subsite C and D). The dihedral Φ/Ψ torsion angles were defined by (O_5-C_1-O_1-C_n' and C_1-O_1-C_n'-C_{n-1}') for the β1→3 and β1→4 interglycosidic linkages as detailed previously (*44, 45*).

Two criteria fulfill the aromatic stacking interaction: 1) stacking angle between planar rings and 2) centroid distance between the COM of the different rings (*17*). By taking the normal vectors projecting from the centroid of the aromatic ring of Trp68 and pyranose ring of galactosyl group of the carbohydrate, we can measure the stacking angle between these two groups. If two aromatic rings sit parallel to one another the angle would have a value of 180º. For the second criterion, the distance (R) from the centroids of the galactosyl ring of the carbohydrate and aromatic ring of Trp-68. Again we only consider the galactosyl ring bound to conserved galectin-1 C/D subsite.

Principal Component Analysis

We used principal component (PCA) analysis to gain insight into internal fluctuations of galectin-1 in presence of pre-BCR relative to unbound state. An in-depth mathematical formalism for principal component analysis (PCA) is found elsewhere (*46*). In brief, the center-of-mass of each configuration of galectin-1 bound to λ5-UR (Cα-carbons of galectin-1 only) were translated to the origin. Atoms are then subject to rotational least squares fit to a reference (i.e. galectin-1 unbound to λ5-UR). Diagonalization of a variance-covariance matrix of positional fluctuations is performed using an orthogonal coordinate transformation. This transforms the symmetric covariance matrix, which contains the eigenvalues (λ). Each column of the diagnolized matrix contains the eigenvector or principal component. The mean square positional fluctuation along a given eigenvector is represented by each eigenvalue, which represents the contribution of each principal component to the total fluctuation. It has been shown that the first 10-20 eigenvectors contribute to 90% of the total fluctuations of the protein (*47*). The RMSF of the first 10 eigenvectors of the PCA are plotted. The covariance and matrix and rmsf values were extrapolated using the covar and anaeig tools in GROMACS.

Iterative Linear Interaction Calculations

We applied a slightly altered method proposed by (*48*) that employed an iterative LIE method to exclude configurational transitions and applying weighted factor to the LIE equation (*49*).

$$\boldsymbol{W_i} = \frac{e^{\frac{-\Delta G_{calc,i}}{k_B T}}}{\sum_i^N e^{\frac{-\Delta G_{calc,i}}{k_B T}}} \quad (1)$$

where W_i is the weighted factor used below in equation 2. W_i depends on the free energy of binding that is determined from each respective simulation ($\Delta G_{calc,i}$). T is the temperature (Kelvin) and k_B is the Boltzmann constant. Each simulation

(i) is run over total N number of simulations. This weighted factor is then incorporated into a weighted LIE equation proposed previously (*50*).

$$\Delta G_{calc} =$$

$$\alpha \sum_i^N W_i\left(\langle V_{lig-surr}^{vdW}\rangle_{bound} - \langle V_{lig-surr}^{vdW}\rangle_{free}\right) + \beta \sum_i^N W_i\left(\langle V_{lig-surr}^{elec}\rangle_{bound} - \langle V_{lig-surr}^{elec}\rangle_{free}\right) \quad (2)$$

With the scaling parameters α and β for the van der Waals and electrostatic contributions, respectively. The bracketed terms represent the van der Waals or electrostatic interaction of ligand and its surroundings. A key assumption is that each simulation covers different parts of the configurational space with minimal overlap. The inclusion of major transitions within simulation may result in inaccuracies within ensemble averages of vdW or coloumbic contributions. We identify these transitional changes within local parts of the conformational space by employing a method proposed previously(*48*) We then include these local parts that occur after or before a given transition as different conformational states that can be weighted according to equation 1. In brief, the method proposed by (*48*) and adapted for our purpose collects the trajectories from each sugar bound pose. These are filtered with a discrete Fourier transformation filter to exclude high-frequency fluctuations associated with thermal fluctuations. A univariate spline is applied to the filtered Fourier set and gradients are evaluated. If the gradient exceeds a given cut-off value, the change in configuration is identified (**Fig 5A**). The ranges that are below the gradient cut-off can be used for subsequent simulations and the weighted LIE (equation 2) can then be applied to obtain the ΔG_{calc}. The training set of LIE parameters of α β were derived from experimental data detailed in (*19*, *51*). These parameters were developed using two-parameter linear regression model with values of α and β 0.18 and 0.06, respectively. The free ligand estimates were conducted for each sugar in the absence of ligand, using the same conditions as proposed above.

Umbrella Sampling

The protein and the terminal lactnoneotetraose complex were extracted after 10ns and moved into umbrella sampling procedures. For each carbohydrate complex, the sugar molecule was placed at different center-of-mass (COM) distances from the CBS. To ensure equivalent pull direction in x,y, and z Cartesian space, we defined a pull vector that was normal to a plane defined by three Cα residues (44,50 and 62) lying within the CBS. Not only does this ensure a uniform pull direction among each galectin-1/carbohydrate complex but also these coordinates were implicated in conserved binding region of galecitn-1's CBS. Each molecule was placed in a cubic box with dimensions 8.1 x 8.1 x 8.1nm with center of the galectin-1 offset to allow the carbohydrate with enough space to be pulled in direction of the pull vector. There was at least 1.2nm spacing from the box edge to the protein. For each complex, all restraints were removed except to chain B to allow free molecular fluctuation of chain A and the carbohydrate. Each umbrella sampling window was defined at 0.1nm spacing from 0 to 1.0nm from the binding pocket. We used a spring constant of 1807.5kJmol^{-1}nm^{-2} (300.15pN/Å), used previously with lactose (*52*), for each umbrella sampling window. A harmonic restraint was placed at the COM of each carbohydrate within the defined window at different distances away from the CBS. Each window consisted of 20ns of simulation time for a total simulation time of 160-200ns. A potential of mean force (PMF) was calculated with the weighted histogram analysis method (WHAM) (*53*) with error estimates using bootstrapping using GROMACS wham tool.

RESULTS

We set out to determine the allosteric impact of the pre-BCR on galectin-1 bound to variety of sugars (**Fig. 1**). Before determining how each carbohydrate was altered within galectin-1' binding pocket, we first looked at the effect of pre-BCR on galectin-1's CBS without any carbohydrate bound (**Fig. 2A).** Our simulations were initialized with the dimeric form of galectin-1.

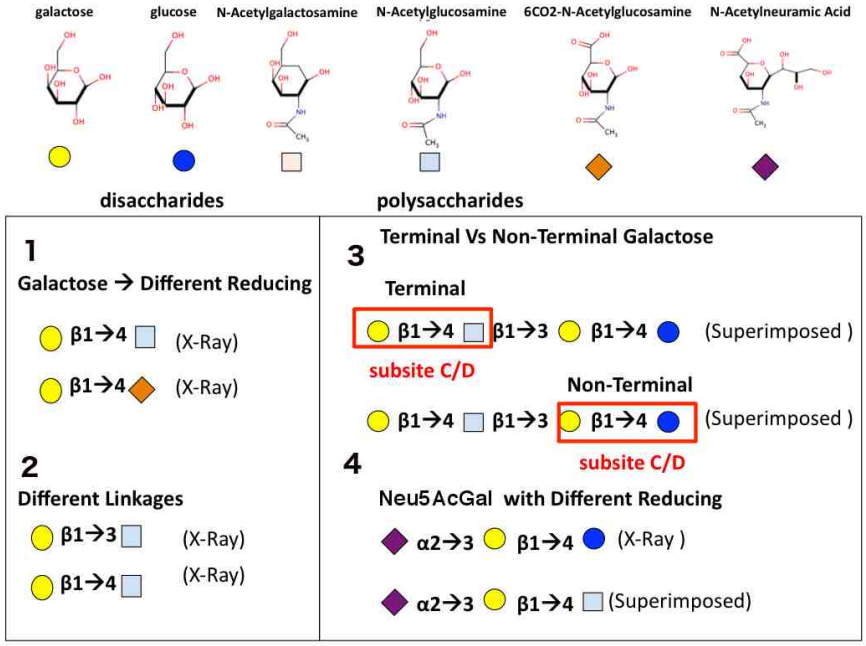

Figure 1. Illustration of structures featured in this study. A). The galectin-1 heterodimer is composed of A and B monomeric subunits (pdb 1GZWs) B). Carbohydrates used in this study are illustrated, along with colored symbols used to represent each monosaccharide unit in subsequent figures. Disaccharides and polysaccharides with different molecular properties were modeled. This includes 1) galaactosyl groups attached to different reducing sugars at the reducing end (glcNAc versus 6CO2-glcNAc), 2) LacNAc with different interglycosidic linkages (β1→4 vs β1→3), 3) lactonneotetraose (LNN-gal(β1→4)glc(β1→3)gal(β1→4)glcNAc), and 4) Neu5Acetylneuramic acid (α3S - neu5Ac(α2→3)gal(β1→4)glc) attached to different reducing sugars (glcNAc vs glc).

Relative Fluctuations by Subsites of Galectin-1 at the CBS in presence of pre-BCR λ5-UR

Since prior evidence has suggested negative cooperativity of binding in the adjacent chain when lactose is bound to one monomeric unit (*18*), our first goal was to assess whether binding of the pre-BCR λ5-UR$^{22-45}$ also induced notable molecular changes in a bound monomer or the adjacent chain. The final model is shown in **Fig. 2A**. Highlighted in pink are the hydrophobic (dark) and electrostatic (light) residues of galectin-1 at the N-terminal region of the peptide; subsites A-E are color-coded. Subsites C and D represent the conserved binding core of galectin-1 with the core galactosyl-glucosyl moieties of the carbohydrate. Subsites A, B, and E confer specificity for different carbohydrate groups. The dimerization interface of galectin-1 is found at the N- and C-terminal regions of each monomer.

To determine how pre-BCR binding impacts galectin-1 in the absence of carbohydrate, we conducted MD simulations in explicit solvent. The system was heated to 310K and equilibrated. During the production MD simulation, all restraints were removed. Root-mean-square deviation (RMSD) of Cα atoms were calculated across individual frames of MD trajectories and are shown in **Fig. 2B (**red, orange). Subsites A and B exhibited minimal change in RMSD over the 10ns time period between two states. There was an increased RMSD in subsite C and D (**Fig 2B**, green, purple), which is the conserved binding core of the CBS. Subsite E, responsible for carbohydrate specificity, explores a conformational space with decreased RMSD before transitioning back to RMSD values that correspond to unbound galectin-1 **(Fig 2B**, yellow). To assess the relative fluctuations by residue across chain A and B, we monitored the root-mean-square fluctuations by residue. We collected the RMSF from chain A to chain B during same trajectory in the pre-BCR λ5-UR bound and unbound state. We then subtracted the RMSF from pre-BCR λ5-UR bound (preBCR(-)) from pre-BCR λ5-UR bound (pre-BCR(+)) state (**Fig. 2C**). This allows us to extrapolate where the largest fluctuations occur when bound to pre-BCR λ5-UR. We note a relative increase in RMSF across residues 51-54 (subsite C,D) and 100-102 (pre-BCR binding region) when bound to the pre-BCR (**Fig. 2C**, negative values). In contrast, there is a relatively large reduction in RMSF in residues 61-70 (subsites

C,D, and E), 76-77 (pre-BCR, hydrophobic), 92-94 (adjacent to preBCR binding region), 108-111 (near pre-BCR λ5-UR binding region) and 133 (dimer interface) (**Fig. 2C**, positive values). This analysis of RMSD and RMSF showed increased fluctuations at the CBS, especially within regions C and D, which is associated with the conserved β-galactoside binding core.

To evaluate potential allosteric effects of pre-BCR λ5-UR /galectin-1 on proximal or distal regions, we employed principal component analysis (PCA). We project the eigenvectors onto the reference structure (galectin-1 without λ5-UR bound) to visualize the regions that exhibit a higher degree of change (**Fig 2D, residues listed**). By monitoring RMSF across each of these eigenvectors, we note large fluctuations localized to subsite C, D and around the pre-BCR λ5-UR binding site (**Fig 2E, top panel**). Interestingly, an apparently large fluctuation can be seen across multiple eigenvectors within the N-terminal region of the adjacent chain B (**Fig 2E, bottom panel).** Essential dynamics revealed increased fluctuations at within select regions within the CBS in addition in addition to increased fluctuations at the N-terminal region of chain B in galectin-1.

Pre-BCR λ5 Binding Impacts Solvent Accessible Surface Areas in Galectin-1 and its Hydrogen Bonding Network

With evidence suggesting that the pre-BCR λ5-UR impacts residues within galectin-1's CBS, we next laid out a strategy to understand how different carbohydrate subgroups impact buried surface and the hydrogen bonding network. The X-ray crystal structures of galectin-1 bound to different sugars reveals a network of hydrogen bonds contributing to carbohydrate affinity. Within the galactosyl ring, His-44, Trp-68 and Asn-46 (subsite C) form a hydrogen bond with the 4'-hydroxyl group of the galactose ring with remarkably short and stable interatomic distances. The hydroxyl groups within the glucosyl ring form hydrogen bond contacts with residues His-52, Asp-54 and Arg-73 (subsite C/D). Lastly, residues Glu-71 (subsite D) and Arg-48 (subsite C) form contacts with both galactosyl and glucosyl rings. Using preset cutoffs for the angle donor-acceptor and the distance donor-acceptor, we calculated the number of hydrogen bonds over the course of a given trajectory. We compared these

results with distribution profiles of solvent accessible solvent area (SASA), to provide insight into the relative buried surface area of the carbohydrate.

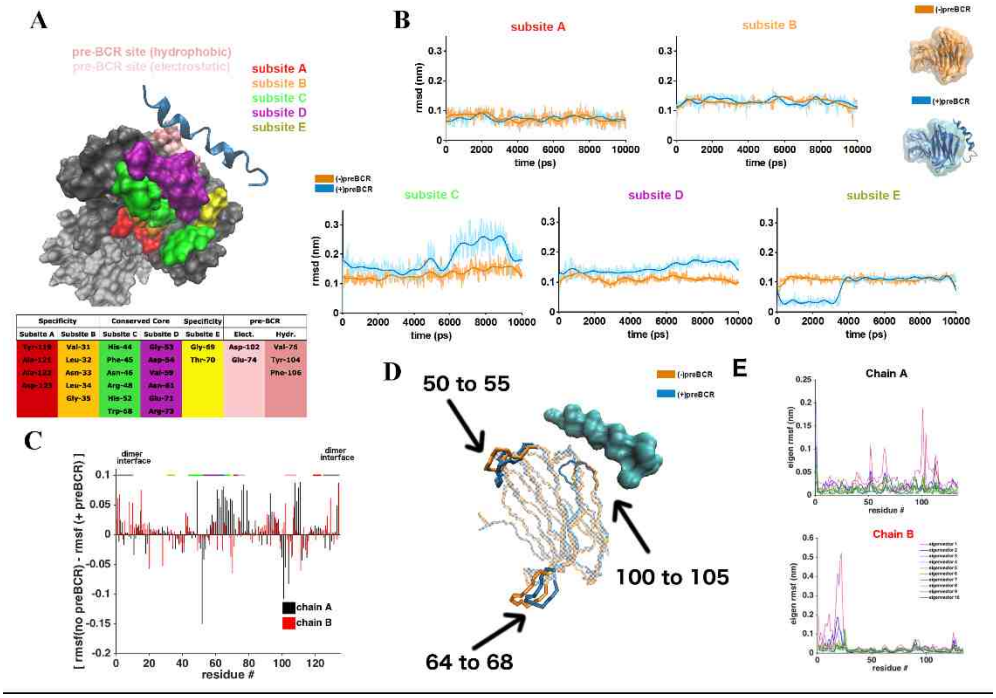

Figure 2. Binding of galectin-1 by pre-BCR modifies relative fluctuations CBS subsites. A) Model of galectin-1 bound to pre-BCR (λ5-UR). Key electrostatic interactions occur between Glu-74 and Asp-102 with Arg-6 and Arg-8 of the N-terminal region of the peptide (blue). Trp-9 of the λ5-UR is buried within Val-76, Tyr-104 and Phe-106 forming an essential hydrophobic interaction (dark pink). Subsite residues A-E are color-coated, with corresponding residues displayed in chart below**. B)** Root-mean-square deviation (RMSD) of subsite residues A-E.in presence (blue) and absence (orange) of pre-BCR **C)** Root-mean-square fluctuation (RMSF) difference between pre-BCR unbound and bound ($RMSF_{unbound=} - RMSF_{bound}$) state by residue within chain A (black) and chain B (red) of the galectin-1 homodimer. Dimer interface is at the N- and C-terminal segment of each monomer unit. **D)** Principal component analysis (PCA) of galectin-1 bound to pre-BCR relative to reference structure (unbound state). **E)** PCA derived RMSF for the first 10 eigenvectors for each residue within chain A and chain B with galectin-1 in presence of pre-BCR.

We compared different LacNAc molecules comprised of different linkages (β1→4 versus β1→3) (**Fig. 1B, group 2**). Our results suggest β1→3 linkages correspond to an enhanced hydrogen bonding profile (**Fig. 3A**). There is a notable drop in H bond number 22000ps into the simulation for the β1→4 linkage, which was not observed in galectin-1 model bound to the pre-BCR (**Fig. 3A**). There is on overall increase in the solvent accessible area within β1→4 suggesting a decreased buried surface area relative to β1→3 linkage.

Attachment of 6'-CO2 group to glucosyl ring of reducing sugar (**Fig. 1B, group 1**) results in an increased number of hydrogen bonds relative to the LacNAc (**Fig. 3B**). This corresponded with a decreased SASA. Similar to β1→3 linkage, the SASA and H bond are not significantly altered when galectin-1 is bound to the λ5-UR peptide (**Fig. 3B)**.

Clear differences in galectin-1 affinity have been reported between polysaccharides with terminal versus non-terminal galactosyl groups, with a binding preference for the former over the latter (*54*). We next determined the binding properties of LNN (galβ1→4glcNAcβ1→3-galβ1→4glc) molecules with either the terminal or non-terminal galactoysl ring engaged with galectin-1's conserved subsite C/D (**Fig. 1B, group 3)**. Measuring SASA between terminal (conserved C/D subsite bound to galactosyl end, **Fig. 2**) and non-terminal bound LNN exhibits minimal differences in the SASA, with a modest increase in the latter. In contrast, we note a large disparity in the H Bond network (**Fig. 3C)** when the non-terminal versus terminal galactosyl is engaged to the conserved galectin-1 binding core. The terminal LNN pose shows large fluctuations early in the simulation before transitioning to a conformation showing an enhanced H bond network relative to the non-terminal pose. Introduction of the pre-BCR λ5-UR significantly destabilizes the H bond network of both terminal and non-terminal LNN at 100ps and 17ns for the non-terminal and terminal LNN.

Addition of N-Acetyl functional group to 3'position of reducing sugar attached to the Neu5AcGal polysaccharide (**Fig. 1B, group 4**) exhibits a difference in the SASA profile (**Fig. 3D, upper panel**). In both Neu5AcGal groups attached to

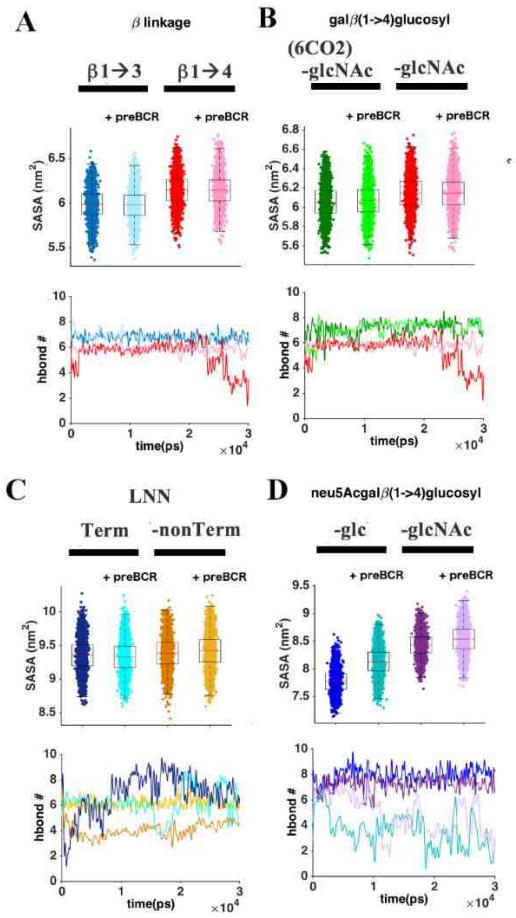

Figure 3. pre-BCR impact on SASA and H bond network within CBS. A) SASA (upper panel) and H Bond (lower panel) calculation of galactosyl-glcNAc sugars containing different interglyosidic linkages (β1→3 vs β1→4) in pre-BCR bound and unbound state. **B)** SASA (upper panel) and H Bond (lower panel) calculation of LacNAc with carboxylic acid attached at 6' positon of the sugar (galβ1→4(6CO2)glcNAc) in pre-BCR bound and unbound state. **C)** SASA (upper panel) and H Bond (lower panel calculation of polysaccharide (galβ1→4glcNAcβ1→3galβ1→4glc) in pre-BCR bound and unbound state. The poses differ by whether the glcNAc (non-Term) or glucose (term) are docked within galectin-1's conserved subsite C/D. **D)** SASA (upper panel) and H Bond (lower panel) calculation of neu5AcGal(β1→4) moieties with either glucose or glcNAc attached at reducing end.

different reducing sugars, we observe an increased median SASA value upon pre-BCR engagement (**Fig. 3D, upper panel**). In the absence of the pre-BCR λ5-UR, the H bond network between the two different polysaccharides remains relatively stable and similar through the course of the simulation (**Fig. 3D, lower panel**). Interestingly, addition of the pre-BCR λ5-UR substantially disrupts the H Bond network of both Neu5AcGalβ1→4glc and Neu5AcGalβ1→4glcNAc (**Fig. 3D, lower panel**). Overall, polysaccharides bound to galectin-1 show have a substantial disruption in the interaction network with the λ5-UR bound.

Pre-BCR λ5-UR affects structure of sugars in binding site.

Glycosidic torsion angles are a measure of the relative stability of the carbohydrate within the galectin-1 binding pocket. All interglycosidic β-linkage considered are between the galactosyl and glucosyl bound to conserved C/D subsite of the CBS. The median Φ/Ψ angles for the β1→3 and β1→4 are -72.4±7.3º/-94.9±7.2º and -75.6º ±7.9/137.7±16.2º, respectively (**Fig. 4A,B**). When the pre-BCR is bound the Φ/Ψ angle of β1→3 and β1→4 linkage slightly changed to -81.0±8.4º/-97.8±7.4º and -75.7 ±7.9º/142.9±7.0º, respectively **(Fig 4A,B**). The variance of the Ψ angle for the β1→4 linkage decreased when bound. The addition of carboxylic acid group to the glcNAc residue at the 6'-position of the glucosyl ring showed similar median Φ/Ψ angle of -76.98± 8.5º/138.3±6.7º to glcNAc in unbound state. This value showed modest change Φ/Ψ angle, -80.5±9.0º/136.0±6.7º, in presence of the pre-BCR λ5-UR (**Fig. 4C**). We obtained a Φ/Ψ angle of -72.8±8.1º/138.6±7.2º and -78.3º±17.0/133.7±20.5 for the terminal and non-terminal LNN, respectively (**Fig. 4D,E**) When the λ5-UR bound to galectin-1, the terminal LNN shows a significant shift in the Φ/Ψ angle and increased variance -73.7±11.3º /140.6±56.4º (**Fig. 4D**). Similarly galectin-1 bound to non-terminal galactosyl of LNN with λ5-UR boudn shows a significant change in Φ/Ψ angle plot with values of -102.6±23.7/95.4±18.7º (**Fig. 4E**). Neu5Ac-Glc and Neu5Ac-GlcNAc exhibit β1→4 linkage Φ/Ψ dihedral angles of -83.7 ±9.9/134.1±9.4 and -84.9±9.3/142.8±7.2, respectively (**Fig. 4D,E**). We noted a change in these angles when bound to the pre-BCR (**Fig. 4F,G**) with measured Φ/Ψ dihedral angles of -74.7±8.3º/129.5±11.0º and -

80.4±11.4/121.1±16.3, respectively (**Fig. 4D**). In contrast to the 6' carboxylic acid or β1→3 linked dissacharide, β1→4 linked N-acetylglucosamines with no additional attachments to glucosyl ring display a clear disruption the Φ/Ψ angles, likely altering the sugars stability within the CBS pocket.

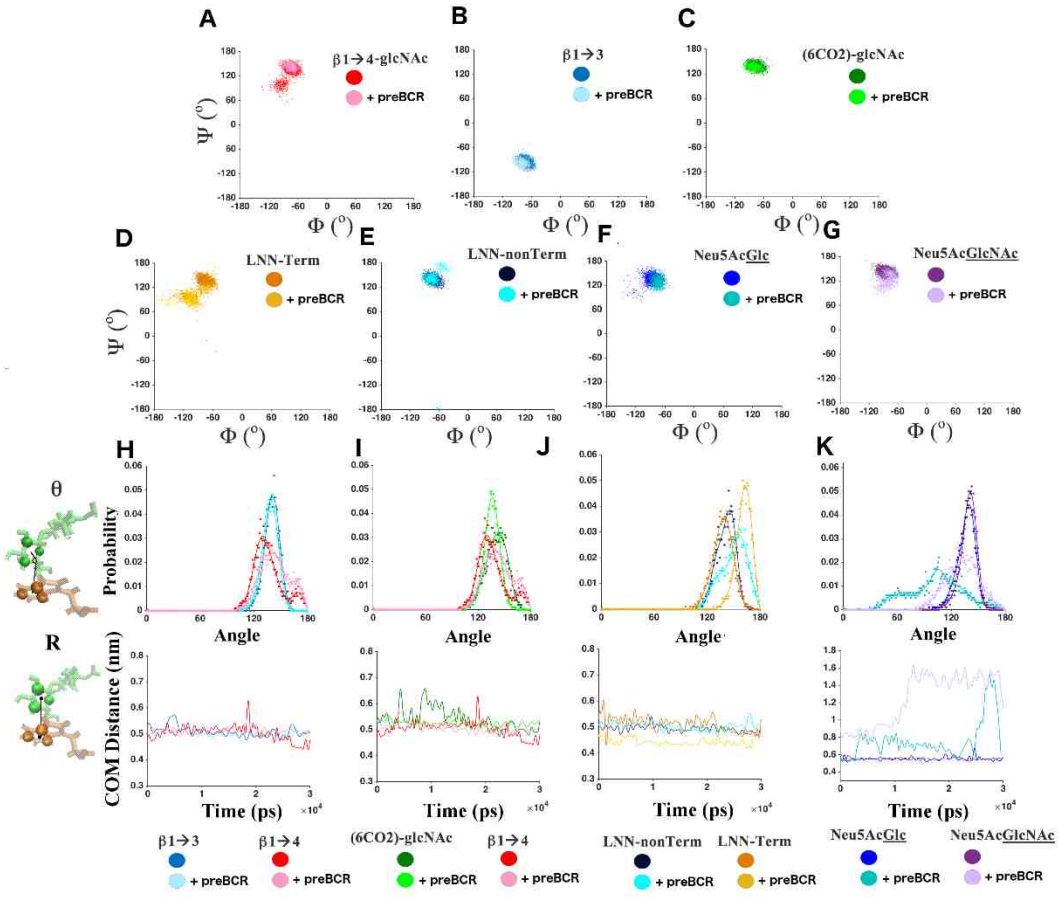

Figure 4. Dihedral angle and aromatic stacking angle distribution in pre-BCR bound vs. unbound state. A-G) Phi (ϕ) and psi (φ) dihedral angle of the interglycosidic linkage between glucosyl and glycosyl groups within subsite C/D for listed carbohydrates in pre-BCR bound versus unbound state. **E-K)** Aromatic stacking angle (top panel) and centroid ring distance (lower panel) between Trp-68 of galectin-1 and galactosyl ring within conserved subsite C/D within the CBS for listed carbohydrates in pre-BCR bound versus unbound state.

Aromatic Stacking Interactions Significantly Altered with pre-BCR engagement

In addition to electrostatic interactions, key hydrophobic interactions occur between the carbohydrate rings and aromatic side chains, particularly tryptophan. The schematic for the calculation of aromatic stacking angle (θ) and distance (R) is shown (**Fig. 4H, left of graph**) and detailed in methods. X-Ray data exhibits a stacking angle around 142º for the LacNAc carbohydrate and a measured distance between two centroids of 0.51nm. The stacking angle of the β1→3 LacNAc in pre-BCR λ5-UR bound versus unbound state was calculated at 137.9±8.9º (bound) versus 139.8±8.6º and the mean centroid distance at 0.5085±0.0352nm (bound) versus 0.4975±0.0285nm (**Fig. 4H**,blue). The carbohydrate with β1→4 linkage exhibits a bimodal distribution (**Fig. 4H**, red) shifting to more favorable angle through the course of the simulation. The mean stacking angle of the β1→4 LacNAc were in pre-BCR λ5-UR bound versus unbound state were calculated at 143.1±16.4(bound) versus 135.8±16.2º in the unbound state. The measured centroid distance was 0.5063±0.0618nm for pre-BCR bound and 0.5036±0.0453nm pre-BCR λ5-UR unbound state (**Fig 4H,** red and pink). Addition of the carboxylic acid to the reducing sugar also showed a slightly more unfavorable downward shift of the aromatic stacking angle when bound to the pre-BCR λ5-UR (**Fig 4I**, **light green**) We calculated values of 135.6±8.8º (bound) and 140.43±12.2º (unbound) with measured distance of 0.5212±0.0356 (bound) and 0.5394nm±0.0610 (unbound).

The LNN polysaccharide displayed a rightward (more favorable) shift in the distribution of the stacking angle in presence of the pre-BCR λ5-UR. Within the pre-BCR λ5-UR unbound state the terminal and non-terminal galactosyl bound LNN had mean aromatic stacking angles of 141.1±10.3º and 137.52±11.5º, respectively. This corresponds to a calculated mean centroid distance of the terminal and non-terminal LNN poses were 0.4935±0.0319nm and 0.5119±0.0415nm, respectively. When bound to the pre-BCR λ5-UR, the aromatic angle shifts upward to 149.7±`14.7º for terminal LNN and 161.3±8.6º for the non-terminal LNN pose. This corresponded to a distance of

0.5001±0.0423nm and 0.4424±0.0218nm for the non-terminal and terminal poses, respectively.

We note a significant disruption of the aromatic stacking angle with both poses of N-acetylneuramic acid attached to the LacNAc moiety (**Fig 4J**). This corresponded to distance values of 0.5518±0.0382 0.5537±0.0333 in unbound pre-BCR λ5-UR state for the glc and glcNAc sugar attached at the reducing end, respectively. The calculated aromatic stacking angle was 136.5± 10.0 and 139.0±9.0º in the unbound pre-BCR λ5-UR state for the glc and glcNAc sugar attached at the reducing end, respectively. The corresponding distances changed dramatically through course of simulation as can be seen (**Fig 4K**, **lower panel**). Clearly N-Acetylneuramic acid and both non-terminal and terminal lactonneotreatose polysaccharides exhibit clear disruption in the aromatic stacking angle when the λ5-UR is bound to galectin-1.

Galectin-1 subsite D residue Arg-73 undergoes large conformation change altering interaction distance

Because Arg-73 displayed the greatest decrease in chemical shift variations (*19*) and is located at the intersection between the CBS and the pre-BCR binding site, we looked at the minimum distance of this residue relative to the sugar. All residues containing β1→4 linkages and coupled to glcNAc showed drastic shifts when bound to the pre-BCR (**Fig. 5A,D-G**). In contrast, the β1→3 linkage or when a carboxylic acid is attached at the 6' position of the β1→4, there was a minimal impact on this minimum distance calculation (**Fig. 5B-C**). When the pre-BCR is bound Arg-73 undergoes a side-chain reorientation whereby Arg-73 faces away from the CBS toward the λ5-peptide. This event subsequently destabilizes critical hydrogen bonding interactions at this site and may be indicative of the loss of carbohydrate affinity for select sugars. Interestingly, this appears dependent on the type of sugar within the binding pocket, with 6-CO2 attachment or β1→3 linkage both showing relatively constant distances in the presence and absence of λ5-UR.

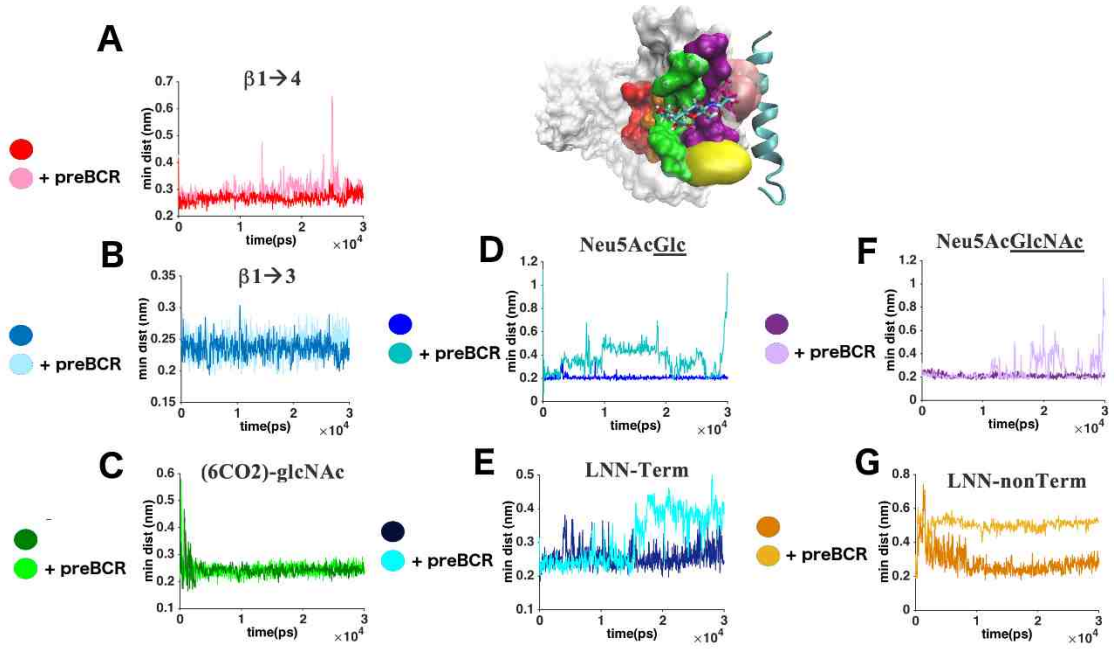

Figure 5. Minimum distance between carbohydrate and Arg-73. A-G) Minimum distance (nm) measurement between the carbohydrate and Arg-73 of the galectin-1 along the trajectory.

Linear interaction energy calculations of the carbohydrate in presence / absence of the pre-BCR

To estimate the binding free energy of the carbohydrate to galectin-1 in the presence and absence of the pre-BCR λ5-UR, we incorporated the improved LIE method as detailed in Methods that includes both **Equation 1** and **Equation 2**. The Weighted factor (W_i) in addition to α and β are was obtained using iterative scheme described previously (*48*) and detailed in methods above. Data shows the different vdW and electrostatic energies derived from Neu5AcNGlc MD simulation, for which a filtered Fourier Transform series was fit. Fitting a cubic spline to the filtered set and calculating the gradient, we plot the absolute value of the gradient as shown in (**Fig. 6A**). From this particular simulation, we note three different local conformational spaces (1-3000ps 6000-18000ps and 1750-30000ps) corresponding with two transitions as exhibited with increased gradient (**Fig. 6A**, **top panel**). When gradient value exceeds a set value (**Fig. 6A, red line, upper panel**), it is flagged and excluded from the analysis. For ΔG_{bind} evaluated for this set, all non-transitional states were weighted according to **Equation 1** and subject to the weighted LIE (**equation 2**). ΔG_{bind} was calculated for each carbohydrate (**Fig. 6B**). We note a decreased affinity between galectin-1 for most of the polysaccharides tested when the pre-BCR was bound. We did observe a more favorable binding energy when the pre-BCR was bound between galectin-1 and LacNAc bearing the β1→3 linkage or when the carboxylic acid was attached at the 6' position of the glcNAc moiety.

A

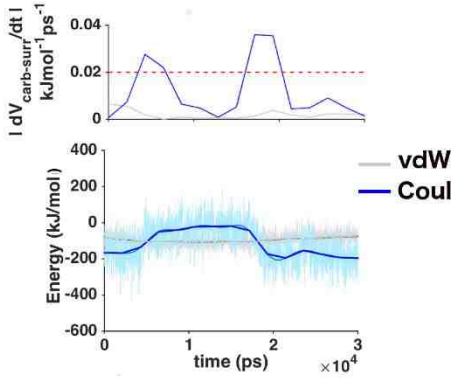

B

	Ref	CARBOHYDRATE	ΔG exp (kJ/moL)	ΔG lie (kJ/moL)
1	1	gal(β1->4)glcNAc	-22.84±0.17	-23.30±0.21
2	**1**	**gal(β1->4)glcNAc + λ5-UR**	**-22.30±0.21**	**-22.40±0.19**
3	2	gal(β1->3)glcNAc	-24.23	-24.13±0.12
4	**-**	**gal(β1->3)glcNAc + λ5-UR**	**ND**	**-29.49±0.16**
5	-	galbeta(1->4)_6CO2	ND	-21.37±0.17
6	**-**	**galbeta(1->4)_6CO2 + λ5-UR**	**ND**	**-23.87±0.18**
7	1	gal(β1->4)glcNAc(β1->3)gal(β1->4)glcNAc	-24.48±0.29	-23.65±0.24
8	**1**	**gal(β1->4)glcNAc(β1->3)gal(β1->4)glcNAc (+ λ5-UR)**	**-22.18±0.21**	**-8.29±0.23**
9	-	gal(β1->4)glcNAc(β1->3)gal(β1->4)glcNAc	ND	-29.09±0.26
10	**-**	**gal(β1->4)glcNAc(β1->3)gal(β1->4)glcNAc (+ λ5-UR)**	**ND**	**7.80±0.21**
11	-	neu5Ac(α2->3)gal((β1->4)glc	ND	-36.94±0.25
12	**-**	**neu5Ac(α2->3)gal((β1->4)glc + λ5-UR**	**ND**	**-19.39±0.25**
13	1	neu5Ac(α2->3)gal((β1->4)glcNAc	-20.67±0.17	-36.43±0.24
14	**1**	**neu5Ac(α2->3)gal((β1->4)glcNAc + λ5-UR**	**-26.28±0.21**	**-13.46±0.26**

1 - *Bonzi et al*, 2015 (see Ref 19)
2 - *Echeverria et al*, 2011 (see Ref 34)

Figure 6. Free energy of binding by different carbohydrates with galectin-1 in pre-BCR λ5 bound versus unbound state using improved LIE method. A) The electrostatic (light blue) and vdW (grey) contributions of carbohydrate binding in presence of Neu5AcLacNAc bound to galectin-1. Each data set are filtered with discrete fourier transform filter and splines are fit to filtered data. Gradients are calculated from these spline fits and plotted (upper panel). A transitional state is determined when the absolute value of the gradient is greater than a set cut-off point (i.e. 0.02kJmol^{-1}ps^{-1}). **B)** Experimental data and LIE calculated from 30ns simulations are shown in table..

Umbrella Sampling Simulations

We incorporated umbrella sampling and the weighted histogram analysis procedure to construct a potential of mean force (PMF) curve for the terminal lactoNNeotetraose (**Figure 1, sugar 3**) in presence and absence of the pre-BCR λ5-UR. The reaction coordinate was defined as the COM distance from the normal unit vector that protrudes from the CBS. Each sampling window was spaced at 0.1nm intervals that extended along this vector, whereby a harmonic restraint is on the COM of the carbohydrate. The PMF was plotted as a function of COM distance (**Fig. 7A**), with errors evaluated using block averaging of 5ns segments through that stretched through each umbrella sampling window. The PMF shows clear differences in the energy landscape with a deeper basin when pre-BCR is not engaged to galectin-1. The structural insets reveal the hydrogen bonds are clearly disrupted between the Arg-73 and sugar. This breakage occurs at shorter timescales when pre-BCR was bound. There is a more notable change in the in electrostatic interactions, as revealed from Lennard-Jones and Coulombic energy differences across each US window **(Fig. 7B**). It is clear that the overall impact on affinity when the pre-BCR is bound is likely dictated through electrostatic hydrogen bonds between galectin-1.

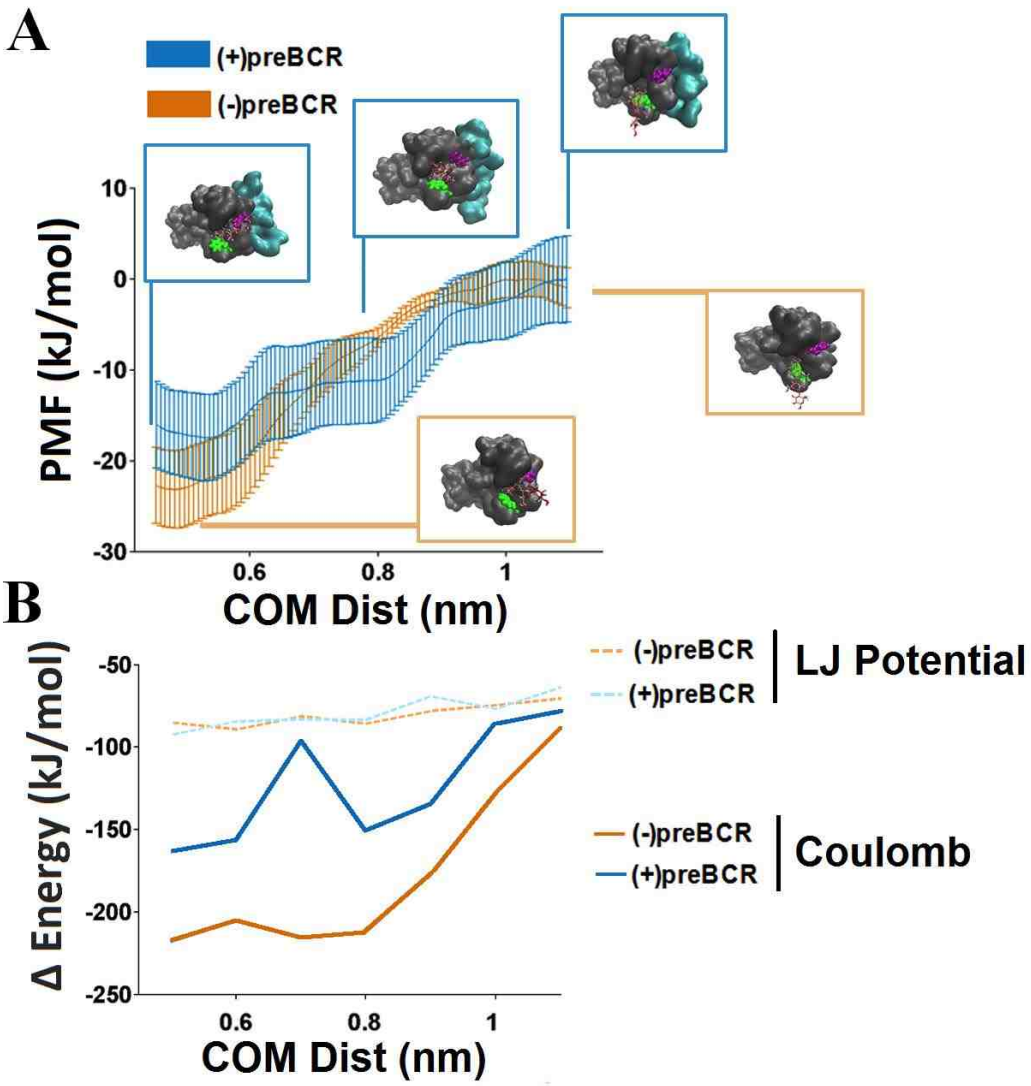

Figure 7. Potential of mean force (PMF) of Neu5AcLacNAc bound to galectin-1. A) The weighted histogram analysis method (WHAM) was used to calculate the Potential of Mean Force as a function of the distributions of COM umbrella sampling windows for the terminal lactoNNeotetraose sugar molecule (**Figure 1, sugar 3**) in presence and absence of pre-BCR. **B)** The mean Lennard-Jones and Coulomb energy differences were calculated from each US window

DISCUSSION

Recent evidence has provided definitive evidence that galectin-1 binds the pre-BCR's surrogate light chain subunit λ5 (*11*). When presented on the surface of stromal cells, galectin-1 engagement with the pre-BCR leads to stable cell-cell contacts and a synapse-like redistribution of pre-BCR on precursor B cells to the contact sites (*11*). Binding of soluble galectin-1 dimers leads to pre-BCR aggregates with markedly reduced diffusion (*3, 11*). We recently showed that incubation of precursor B leukemia cells with galectin-1 plus saturating doses of lactose (galβ1→4glc) restored pre-BCR diffusion to pre-BCR-galectin complexes (*3*) interpreted as evidence that monosaccaride binding prevents galectin-mediated crosslinking of the pre-BCR to other cell surface glycoproteins and glycolipids. Importantly, the addition of lactose also amplified the downstream signaling response of pre-BCRs after galectin-1 binding. These results suggest that the complex aggregates formed by galectin-1 binding to both the pre-BCR and glycoreceptors actively attenuate signaling. Galectin-1 has been shown to interact with a variety of negative regulatory membrane glycoproteins, including the tyrosine phosphatase CD45. Thus, different glycosylation patterns on surface of stromal cells and/or precursor B cells may drive different signaling profiles dependent on the composition of glycoproteins that are co-crosslinked with the pre-BCR/galectin-1 complex. These concepts strongly motivate detailed explorations of the galectin-1 carbohydrate binding characteristics in the presence of the pre-BCR.

In agreement with NMR data (*19*), we have demonstrated that binding of the pre-BCR λ5-UR impacts the flexibility of residues within galectin-1 CBS, particularly in subsites C and D (**Fig 2**). Interestingly, we note a decreased RMSD profile within subsite D with addition of pre-BCR that may impact interactions within this subsite. Using PCA derived RMSF across the first 10 eigenvectors, we noted a substantial RMSF within the N-terminal region of chain B of galectin-1 homodimer. This suggests that pre-BCR binding may impact dimer/monomer equilibrium. Experimental data shows that lactose binding leads to a shift in the homodimer equilibrium and factors the dimeric state compared to when galecitn-1 is not bound to any carbohydrate (*55*). Galectin-1 dimers can then protect

galectin-1 from oxidative inactivation, a process of disulfide bond formation that significantly decreases galectin-1's for carbohydrates (*56*). In future experimental work, it would be interesting to test the prediction that pre-BCR engagement modifies the galectin-1 dimer/monomer equilibrium and thus alter the lifetime of dimer bonds that drive oligomerization.

We noted a disruption of the H-Bond network for all residues with β1→4 linkages containing a glcNAc or glucose reducing end (**Fig 3.B-D**). Attachment of a 6'-COO group or LacNAc with a β1→3 did not disrupt the H Bond network. Interestingly, these results directly correlate with data on the minimum distance profile of the sugar molecule to Arg-73 of galectin-1 (**Fig. 5**). The Arg-73 residue lies within subsite D, which rests at the intersection between the λ5-UR binding region and the carbohydrate binding site. In fact, like the hydrogen bonding network profile, all carbohydrates with the β1→4 linkages (excepting those with a 6'-glucosyl attachment) are impacted by the shifted movement of this residue away from the CBS toward the λ5-UR binding region. It has been shown that addition of anionic moieties at different positions (i.e. 3' or 6') drastically impacted the relative affinity of given sugars to galectin-1 (*57*). We see here that attachment of a 6'-carboxylic acid on the glucosyl ring still retains Arg-73 binding through the course of the simulation. Similarly, the β1→3 also does not lose this critical electrostatic interaction upon pre-BCR engagement. A look at the molecular structure reveals that, within the β1→4 linkage, the glcNac functional group is in direct contact with the Arg-73 residue and the glcNAc is attached via the β1→3.

In general we observed a more substantial impact of pre-BCR λ5 binding on galectin-1's affinity for polysaccharides, relative to the disaccharides tested. Altered affinity is more readily apparent as the polysaccharide length is increased (**Figs 3-6**). We noted an overall increase in binding affinity when the non-terminal galactosyl group when bound to conserved binding core. This increased affinity is driven through interactions within subsites A/B. While binding energies of galactose-terminating and non-galactose terminating carbohydates rates have been measured (*54, 58, 59*) it had been proposed that four LacNAc

units can be accommodated by galectin-1; non-terminal galactosyl residues were not required for binding. Experiments in CHO cells reveal teat terminal galactosyl residues are not required for binding (*60*). Our data corroborate this finding and actually show that sufficient binding energy may occur to to non-galactose terminating carbohydrates.

In summary, we employed molecular dynamics simulations to extrapolate additional detail about the pre-BCR/galectin-1 interaction with molecular-level. This work provides an example of how MD simulations can be utilized to understand the impact of allostery in molecular function, as has been shown in a variety of other studies (*61-63*). Galectin-1 has been directly implicated in BCP-ALL, where niches that normally support the pre-BII population of developing B cells have the undesired effect of promotng enhanced overall survival of leukemia blasts. Due to the diverse nature of glycoreceptors on the surface of precursor B cells, as well as stromal cells, understanding these interactions in greater detail is important to understand how changing carbohydrate binding may effectively shift the composition of bystander glycoproteins recruited to galectin-1/pre-BCR heterocomplexes. Of particular interest is the impact on co-crosslinking of the pre-BCR with negative regulatory signaling partners, such as CD45 and other phosphatases. Differential recruiting of positive or signaling co-receptors is expected to lead to altered signaling profile and opposing cell-fate decisions. In addition, galectin-1 has been considered as a potential therapeutic target (*19, 64*). Understanding how these protein/protein interactions alter galectin-1's CBS will aid in the design process of key inhibitors that may specifically exploit disease processes, including precursor B neoplasms and inflammatory processes that are specific to galectin-1 when engaged with the pre-BCR.

CHAPTER 4

Preclinical characterization of a chimeric antigen receptor T cell therapy targeting the pre-B cell receptor

M. Frank Erasmus[1,2], Ichiko Kinjyo[1,2], Stuart S. Winter[2,3], Michael Horowitz[4], and Bridget S. Wilson[1,2]

[1]Department of Pathology, University of New Mexico, Albuquerque, New Mexico
[2]UNM Comprehensive Cancer Center, Albuquerque, New Mexico
[3]Department of Pediatrics, UNM Health Sciences Center, Albuquerque, New Mexico
[4]Sea Lane Biotechnologies, Mountain View, CA

ABSTRACT

Current immunotherapy options in B cell precursor acute lymphoblastic leukemia (BCP-ALL) are primarily based on antibodies targeting CD19, CD20 or CD22. Recent successes in clinical trials include T cells engineered to express anti-CD19 chimeric antigen receptors (CAR). Because CD19 is widely expressed on mature B cell lineages, anti-CD19 CAR T cell therapy impacts the patient's entire existing B cell repertoire. We focus here on targeting the pre-BCR, which is expressed only at the precursor B cell stage of normal development and represents a highly specific target for subsets of BCP-ALL patients with poor prognosis. The pre-BCR is distinguished from the mature BCR, based upon substitution of the surrogate light chain (SLC) for □ or □ light chain. The SLC is comprised of λ5 and VpreB subunits, which show no sequence homology to any other expressed gene within the human genome. In normal B cell development, the SLC assembles with successfully rearranged Igμ for expression of the pre-BCR. Autonomous pre-BCR signaling then enables the immature B cells to pass a critical checkpoint. In this study, we

design a CAR T cell therapy against the pre-BCR SLC with the aid of computational antibody design. We demonstrate high affinity binding of recombinant scFv to pre-BCR expressing cells, forming the basis of the lentivirus construct for expression of a novel anti-pre-BCR CAR. We present evidence that CD8+ T cells expressing the anti-pre-BCR CAR bind and kill target leukemia cells. The anti-pre-BCR CAR T cells form robust synapses with pre-BCR expressing leukemia cells, leading to polarization of CAR T receptors to the cell-cell interface. Cytolytic granules subsequently redistribute to synapse, leading to fusion and killing of pre-BCR+ BCP-ALL cell lines and patient samples. CAR density and target density are shown to be important factors in the robustness of killing. These CAR T cells can expanded *in vitro* for preclinical studies in a human xenograft model of BCP-ALL in immunocompromised mice. This study sets the stage to utilize mouse models to study T cell-mediated killing of both target and off-target B cell lineages, as well as T cell exhaustion, focusing on potential advantages of the pre-BCR CAR T cells versus the pan-B cell CAR T cells that target CD19+ normal and neoplastic cells.

INTRODUCTION

Acute lymphoblastic leukemia (ALL) is the most prevalent neoplasm in children (*1*) and an aggressive cancer in adults (*2*). Treatment of patients with intensive combination chemotherapy is often considered a modern success story, with relapse-free survival rates approaching 90% in children (*3*). Unfortunately, high-risk cases of ALL remain incurable (*4*) and there are inherent concerns with toxicity and long-lasting side effects of existing treatments (*5*).

ALL arises from both early B cell (BCP-ALL) and T (T-ALL) cell lineages. There is considerable interest in developing more targeted therapies for these diseases, based upon advances that have identified mutations and genetic alterations associated with specific ALL subsets (*6*). For example, ALL patients expressing oncogenic forms of specific cytokine receptors exhibit sensitivity to tyrosine kinase inhibitors (TKIs) such as dasatinib, ruxolitinib and crizotinib (*7, 8*). The high risk group termed "Ph+ ALL" was coined based upon transcriptional profiles with similarity to BCR-ABL+ cases; these cases may respond to TKIs, which are typically delivered in combination with multi-agent induction, post-remission and maintenance chemotherapy (*9*). Yet, even in the advent of improved outcomes of BCP-ALL patients treated with TKIs, relapse is still common (*9*). Targeted therapy options may also include antibody-based approaches that support antibody-dependent cytotoxicity (ADCC) and phagocytosis (ADCP) (*10, 11*), antibody-dependent toxin delivery (*12*) or establishment of T cell-mediated immunity based on adoptive transfer of genetically modified immune effector cells (*13, 14*). Recent, highly successful clinical trials based on the latter approach have led to intense efforts to improve cell-based therapies, as well as to limit the considerable risks during treatment (*15*).

CD19 is a B-cell surface marker that is expressed throughout the different stages of B cell development. To date, this receptor is the most common target used for T cell-mediated cell therapies in ALL and B cell malignancies (*16*). In brief, the approach is based upon genetic modification of the patient's effector T cells to enable the expression of recombinant, chimeric antigen receptor (CAR) that targets CD19 on the surface of

leukemia target cells. The original CAR was a fusion protein comprised of an extracellular domain bearing the antigen recognition domain of an anti-CD19 antibody, in the form of a single-chain fragment variable (scFv), together with a transmembrane domain and the intracellular ITAM-bearing tail of the CD3-ζ chain (*17, 18*). Poor response rates in early clinical trials were linked to limited *in vivo* expansion and rapid disappearance of CAR+ T cells upon infusion (*19, 20*). This led to the design of "second generation" CARs that incorporated costimulatory domains (4-1BB, CD28) into the receptor cytoplasmic tail and enhanced antitumor activity relative to CARs composed only of the CD3-ζ C-terminus (*21, 22*). Use of these costimulatory domains results in enhanced *in vivo* expansion of T cells, persistence of anti-target effector function for months to years after injection, and expression of a memory-like phenotype (*23*).

Anti-CD19 CAR therapies can ablate both healthy and malignant B-cells. Although B cell aplasia has been reported to be highly tolerable in patient populations (*24*), we propose that there may be advantages for developing novel CAR T approaches that avoid loss of existing B cell adaptive immunity. In addition, several cases of relapse have still reported due to loss of CD19 expression (*25*) or reduced CART cell efficacy (reduced CAR T expression or increased T cell exhaustion) even when CD19+ leukemic cells are still detectable in the blood (*26*). The desire for co-infusion of CAR T's that target multiple targets on the surface of ALL blasts has been proposed (*25, 26*).

Our focus here is on the pre-BCR as a therapeutic target, as proposed recently based on its supportive role in leukemogenesis of CD179+ BCP-ALL (*27, 28*). It is noteworthy that targeted therapies against the BCR in mature B-cell neoplasms are already well advanced in clinical trials (*29*). Unique structural and developmental properties of the pre-BCR makes for a highly desirable target for pre-BCR(+) cases. In normal B cell ontogeny, up to 10 million pre-B cells are produced daily (*30*). The majority of these are destroyed due to failure to pass the pre-BCR checkpoint (*31*), which occurs at the pro-B to pre-B cell junction after successful recombination of Ig heavy chain (IgH) genes (*32*). Two identical, covalently linked IgH chains each associate with the surrogate light chain (SLC) and signaling subunits Igα and Igβ (*32*). A weak, autonomous ("tonic") signal is propagated

via transient pre-BCR homodimers at the extracellular surface (*28*), mediated through homotypic interactions of surrogate light chain components (*33*). Distinct from light chain (LCs) found on B cell receptors at later stages during B cell development, the SLC is composed of two unique polypeptides known as λ5 and VpreB that are non-polymorphic. The C- and N-terminal regions of the VpreB and λ5 subunits each contain non-Ig unique regions (UR) that do not show sequence homologies to any other genes (*31, 34*). Similar to healthy B cells, many of the pre-BCR(+) leukemias are trapped at this particular stage of development and undergo constitutive pre-BCR signaling. A recent report, covering four clinical trials and 830 patients, showed that BCP-ALL can be divided into different subtypes dependent on pre-BCR function with pre-BCR(+) exhibiting worse outcome (*35*). Targeting the pre-BCR pathway in these pre-BCR(+) leukemias with small molecule inhibitors (*35*) or with an anti-VpreB Fab (*28*) significantly impacted leukemia cell survival.

We describe the pre-clinical development of a precursor B cell-specific, 2nd generational CAR T cell therapy. We began with an anti-VpreB murine antibody selected using high-throughput phage display screening (*28*). Applying computational design principals for antibody engineering, we generated a scFv that retained the specificity and subnanomolar binding affinity of the parent antibody. This scFv was incorporated into a lentiviral expression vector, creating an anti-pre-BCR CAR with a CD28 juxtamembrane domain and C-terminal derived from the CD3ζ cytoplasmic tail. Human CAR T cells were produced and shown to be effective at killing pre-BCR+ BCP-ALL cell lines, as well as patient blasts passaged through immunocompromised mice. Fluorescence imaging was employed to characterize CAR T synapses with target leukemia cells. Since the pre-BCR is bivalent, to our knowledge this is the first reported CAR directed at a multivalent antigen. This novel feature of anti-pre-BCR CAR T cells may offer advantages for amplification of signaling by CARs, motivating future studies of the impact of target antigen valency on signaling competency of CAR T cells.

MATERIALS AND METHODS

Computational Design of the scFv

Antibody design was based upon the sequence of the complementary determining region (CDR) of the parent mouse $IgG_1\kappa$ anti-VpreB antibody, as previously described (*28*). The Rosetta structure prediction tool was used to develop a high quality antibody Fv homology model. The RosettaAntibody protocol has been described in detail (*36*) with an improvement to the VL-VH orientation (*37*). In brief, V_L and V_H framework and non-H3 complementarity determining region (CDR) loops regions use the BLAST (Altschul SF, Gish: Basic Local Alignment Tool) algorithm with BLOSOM and PAM30 scoring matrices used for each, respectively. The bit score is used to identify best match across the antibody sequence and structure database for each region. Each V_L and V_H framework is superimposed on the barrel of the template with greatest sequence similarity and non-H3 CDR loops are superimposed of backbone atoms of two root residues on either side of the loop. CDR H is modeled using Rosetta loop modeling and Kinematic Closure to close the loops. All atoms are refined with VL-VH rigid-body minimization with CDR H3 is restrained. The H3 region is then minimized within the surrounding environment. Average RMSDs of templates for each model tested relative to experimentally determined template were sub-Ångstrom for the framework regions and non-H3 CDRs.

Construction of the HC/LC scFv in *E. coli*

Plasmid DNA (PTT5-2460BO4) bearing the HC and LC of the parent anti-VpreB antibody was transformed into NEBα competent *E. coli* (New England Biolabs, Ipswich, MA). Framework regions (CDR, constant region) were defined using RosettaAntibody bioinformatics tool. We applied a two fragment assembly as laid out previously (*38*). Based upon the information from computational modeling, we designed a 20mer Gly4Ser linker with the HC-linker-LC orientation. In brief, the VH and VL domains were PCR-amplified from the PTT5 vector. Primers were designed to be compatible with a pET101/TOPO vector that contains C-terminal His-Tag. We used a CACC-HC forward primer (5'-CACCATGGAGGTGCAGCTGGTCG-AGTC-3') and the LC-Reverse without a Stop Codon (5'-GGTCCGCTTGATCTCCA-CCT-3'). Primers for the HC-20mer linker-

reverse complement (5'-GGAGCCGCCGCCGCCAGAACCACCACCACCAGAACCA-CCACCACCggacacggtgaccag-3') and LC-20mer-Linker(fwd)(5'GGTTCTGGCGGCG-GCGGCTCCGGTGGTGGTGGATCCgacatc-cagctgacccagag-3'). For fusion of each segment, we used the protocol established previously (*38*). PCR conditions were 5min at 95ºC, then 25 cycles of 1min at 95ºC, 1 min at 57ºC, 30s at 72ºC and 5min at 72ºC. Primer for the 3'region of VH was extended to convert the linear region and 5' end of VL was extend to cover the other amino acids. The first round PCR products were amplified individually. Band were excised from agarose cells and purified products were joined by overlapping extension PCR, resulting in a scFv with the correct linker sequence. For this PCR, 5µL of each purified VH and VL template were joined without the addition of primers by cycling seven times: 30s at 95ºC, 1min at 50ºC and 30s at 72ºC. 50pmol of the forward primer for VH and VL-reverse primer were added at 95ºC, then cycling was continued 25 times: 1min at 95ºC, 1min at 50ºC and 1min at 72ºC and finally 5min at 72ºC. The PCR product was then run on 1.2% agarose gel and the band excised (757bp). The fusion product was cloned into a pET101/TOPO vector using the (ThermoFisher Scientific, Waltham, MA) according to manufacturer's instructions. After 1hr incubation in SOC media at 37ºC with shaking, 200µL of bacterial culture was spread on a pre-warmed LB-Agar plate with ampicillin selection antibiotic and incubated overnight. A BamHI-HiEfficiency and EcoRI-HiEfficiency (New England BioLabs, Ipswich, MA) restriction digest was performed to check for proper insertion. Bands were excised and purified; sequencing results showed 100% sequence identity with the 6x-His tag encoded in frame at the C-terminal end.

The pET101/TOPO vector containing the scFv construct was transformed into BL21 Star ^{TM}(DE3) OneShot® (ThermoFisher Scientific) according to the manufacturer's instructions. In brief, transformed *E. coli* were cultured in 10ml of LB media containing the ampicillin antibiotic, then grown overnight at 37ºC with shaking. Bacteria were then transferred to LB media containing antibiotic; after 3 hr culture at 37ºC with shaking, mM IPTG was added to induce expression and cultures were expanded for an additional 4 hours. Proteins were purified from bacterial lysates using the ProBond® Ni-NTA purification procedure as described by the manufacturer (ThermoFisher Scientific).

Binding Affinity and Specificity Measurement of the scFv

To detect binding of scFv to BCR-ALL cell surfaces, purified scFv-HisTag was diluted to 100µM in HANKS buffer and serially diluted. Cultured 697 cells were resuspended in 90µl buffer, followed by additions of varying dilutions of purified scFv and incubation for 1 hr at 4ºC. Cells were washed 3x with ice-cold PBS, then incubated on ice for 30 min with anti-His(PE) antibody (BioLegend, San Diego, CA) according to manufacturer's instructions. After washing, cells were re-suspended in 500µl PBS for flow cytometry analysis. Data was collected on the LSR Fortessa (BDBioscience, San Jose, CA) and analyzed using the FlowJo® software (FlowJo, LLC, Ashland, OR). Dose response curves calculate the apparent K_D and hill coefficient given two vectors, plotted on a semilog graph and fitted with the Hill Equation sigmoid using MATLAB's nonlinear fit statistics toolbox.

For specificity of the scFv for the VpreB target, we competed the scFv with the parent antibody (anti-VpreB mouse IgG_1). The parent VpreB antibody was prepared at different concentrations ranging from .001 to 500nM. The scFv-His was incubated at saturating conditions >20xK_D(100nM) with 697 cells ($1.0x10^5$). After 1hr incubation at 4ºC, cells were washed 3x in ice-cold PBS. Each dose from the parent antibody was added in separate conditions to each saturated scFv condition for 1-hr on ice. After the incubation period, cells were washed 3x and incubated with anti-His(PE) antibody (BioLegend) for 30min on ice. Cells were washed 3x with 1xPBS and spun down at 300xg for 5min at each wash. Cells resuspended in 500µL of 1xPBS for flow cytometry analysis. Data was collected on the LSR Fortessa (BDBioscience, San Jose, Ca) and analyzed using the FlowJo® software (FlowJo, LLC, Ashland, OR). Dose response curves calculate the IC_{50} using competitive binding curve equation after conversion of the responses to %total binding:

$$Y = Nonspecific + \frac{(Total - Nonspecific)}{1 + 10^{\log[parentAb] - \log(IC_{50})}}$$

Y represents the total binding, log[parentAb] is the logarithm of the concentration of the parent antibody plotted along the X axis. Nonspecific binding is defined as binding in

presence of saturating conditions of parent antibody and total binding as binding in absence of parent antibody. Fits were conducted using MATLAB's nonlinear fit statistics toolbox.

Construction of the CAR T cell cassette

To generate the lentiviral vector containing the scFv, XbaI and EcoRI, the scFv-His sequence was prepared to include EcoRI and XbaI restriction sites. The HC-linker-LC-HisTag fragment was ligated into second XbaI and EcoRI-digested fragment that encoded the retroviral backbone and extracellular portions of CD28, the entire transmembrane and cytoplasmic portions of human CD28 and the cytoplasmic portion of the human TCR-CD3 using services of Promab, Inc (Richmond, CA).

Culture Media

T cells were cultured in T cell medium: AIMV medium (ThermoFisher Scientific, Walham, MA) plus 5% AB (blood type AB) (Gemini Bioproducts, Woodland, CA), 100U/mL penicillin, 100µg/mL streptomycin and 1.25µg/mL amphotericin B) (*39*). During culture, T cell media was supplemented with 300IU/mL IL-2 (Peprotech, Rocky Hill, NJ). PBMCs were cultured in 1640 medium plus 5% FBS, 100U/mL penicillin, 100µg/mL streptomycin and 2mM L-glutamine.

Peripheral blood mononuclear cells (PBMCs) isolation

Fresh blood was obtained from United Blood Services (Albuquerque, NM). Donor blood was added to 5 separate 50mL collection tubes to aliquot into 20 separate SepMate^{TM} tubes (STEMCELL^{TM} Technologies, Cambridge, MA) according to manufacturer's instruction. Whole blood (12.5ml) blood was added to equal volume of RPMI and mixed. 25ml of the Blood/RPMI mixture was added to top of SepMate^{TM} tube containing 15ml Ficoll-Paque Plus^{TM} (GE Healthcare, Little Chalfront, UK). Tubes were centrifuged at 1200xg for 10 min at RT. The mononuclear layer (middle layer) of cells were collected, then re-suspended in 5ml RPMI for cell count. Cells were diluted in RPMI to a final concentration of $2.0x10^6$cells/ml.

$CD8^+$ T cell Enrichment from PBMC population

Solutions of PBMCs were combined for a total of at least $50x10^7$cells for CD8+ enrichment. After washing, cells were resuspended in 1ml sterile PBS, 0.1% BSA, 2mM EDTA and 2% FBS. $50x10^7$cells/ml were added to 5ml polystyrene round bottom tubes. An enrichment cocktail (50□l) of STEMCELL, Inc., EasySep™ $CD8^+$ negative selection kit (STEMCELL™ Technologies, Cambridge, MA) was added, followed by gentle mixing and incubation at RT for 10 min. Meanwhile, magnetic particles were vortexed (30s) and 150µl added to the tubes. After gentle mixing, tubes were incubated at RT for 5 min before addition of 5 ml PBS, 0.1% BSA, 2mM EDTA. Tube were placed into magnet holders and incubated for >1 min before removing fluid. Magnetic bead-bound cells enumerated to evaluate CD8+ yield and re-suspended in $2.0x10^6$cells/ml T cell media, supplemented with 300IU/ml IL-2.

CD3/CD28 Activation/Expansion Beads

After $CD8^+$ enrichment and every 7-8 days thereafter, cells were activated with CD3/CD28 beads (Promab, Inc., Richmond, CA) according to manufacturer's instructions. Cell densities were maintained at $2.0x10^6$ cells/ml and 25µl of the activation macrobeads were used per $1.0x10^6$ T cells/well.

RetroNectin Coating for Prior to Viral Transduction

Following two day stimulation with CD3/CD28 macrobeads, activated $CD8^+$ T cells were combined and diluted to $2.0x10^6$cells/ml. Wells of a 24h well plate were coated with 38.0µg/ml of retronectin (Clontech/Takara, Mountain View, CA) that had been resuspended in 500□l sterile PBS. Plates were incubated for 2 hr at RT, followed by aspiration and addition of 500µl blocking solution (0.1µM filtered PBS, 3%BSA) to each well. Plates were blocked for 30 min at FT, then wash sterile HANKS buffer. Plates were either used immediately or stored at 4ºC for up to a week prior to use.

Transduction of $CD8^+$ T cells

Lentiviral products were supplied at 3.23E8 IFU/ml. CD8+ T cells ($1.0x10^6$) were transduced with a multiplicity of infection (MOI) of 10. To prepare for lentiviral transduction, lentiviral particles were diluted in T cell media, with 300IU/mL of IL-2). The

viral particle solution was added to retronectin-coated plates, followed by centrifugation of plates (2000xg, 2hrs at 32ºC). 500µL of the media was kept in well and 500µl of CD8+ (CD3/CD28 beads removed) within T cell media (supplemented with 300IU/ml of IL-2) were added to the plates for a final concentration of cells at $1.0x10^6$cells/ml. Untransduced T cells were added to the plates that only contained retronectin. After cell addition, plates were centrifuged for 10 minutes (200xg) and then cultured at 37º for 24 hr before a second round of transduction.

Expansion Protocol

Following transduction, cells were maintained in culture at an average density of $1.0x10^6$/ml. For expansion, the CD3/CD28 macrobeads were added at 25µl/ml and cultured for 3-days. If cells exceeded $2.0x10^6$cells/well they were split into fresh wells of a 24-well plate to optimize density. CD3/CD28 beads were added every 7-8 days.

FACS Analysis of Intracellular and Extracellular Receptors

Extracellular staining protocol was conducted as follows, unless otherwise stated. Primary conjugated antibodies were used to detect extracellular receptors: anti-CD69-AF488 (Biolegend, San Diego, CA), anti-IgM-PacificBlue (Biolegend), anti-GranzymeB-APC (Biolegend), anti-IFNγ-AF488 (Biolegend), Anti-His-AF555(ThermoFisher Scientific), anti-CD45-FITC (Biolegend), anti-CD8-PacificBlue(Biolegend), anti-PD1-FITC, anti-TIM3-APC (Biolegend). Cells were incubated with manufacturer's recommended antibody volume prepared for 100µl of cells at $1.0x10^6$cells/ml in PBS and typically held for 30-45min on ice. Between steps, cells were routinely washed 3x and recovered by centrifugation (300xg, 5min), then re-suspended in 500µl of PBS and moved to LSR Fortessa for data collection. If intracellular staining procedure was conducted, the cells were fixed with 4% paraformaldehyde in PBS for 15 min at RT, permeabilized with 1%Triton-X in PBS for 30min at 37ºC, followed by 10 min incubation at RT with primary antibodies. All data was processed with FlowJo Software. Where so noted, flow cytometry data were calibrated sing the Quantum Simply Cellular beads (Bang Laboratories) with anti-mouse Fc antibodies according to the manufacturer's instructions.

Induced Stimulation of T cells with Ionomycin/PMA treatment for FACS

In stimulated wells, phorbal myristate acetate (PMA) was added at final concentration of 20ng/mL and ionomycin (1µg/mL), with 1:1000 dilution of BD Golgi stop solution. After 4 hr, cells were labeled with surface and/or intracellular staining protocols.

Immunofluorescence Staining Protocol for Confocal Microscopy

For confocal microscopy imaging, CAR T and 697 were co-incubated for 24 hour time period in 96-well round bottom plate at 2:1 CAR T:697 ratio. Cells were transferred to poly-l-lysine coated well for 30 minutes at 37ºC. Cells rincesed with PBS and fixed with 1% paraformaldehyde in PBS for 15min at RT. Cells rinsed with PBS and blocked for 60min (PBS, 3%BSA). Cells were incubated with primary antibody for 1-hr at RT using dilutions recommended by manufacturer. For the intracellular staining protocol, cells were permeabilized with 1% Triton-X in PBS prior to incubation with primary antibodies for 2 hrs at RT. After final washes, Prolong gold® (ThermoFisher Scientific) was applied to coverslips and samples were cured overnight at RT in the dark.

Cytotoxicity measurement to assess CAR T target efficacy

Target cell death was measured using the non-radioactive cytotoxicity assay, cytotox 96® (Promega, Madison, WI). Controls included spontaneous release of target cell line (697 or Nalm6 alone), max LDH release (target cell line with lysis buffer added), effector cell spontaneous release (CAR T alone), culture medium background. For the LDH release assay, the CAR T:target cell ratio was 5:1. Alternatively, cytotoxicity was measured in 697 and Nalm6 cell lines stably expressing GFP, varying CAR T:target cell ratios at 4:1, 2:1, 1:1, 0.5:1, 0.25:1,0.125:1 and 0.0625:1. Effector and target cells were incubated for 3 days, followed by labeling with anti-CD19 or anti-IgM FITC-conjugated antibodies. Cytotoxicity was measured as a loss of target cell fluorescence.

Epitope Prediction using MD simulations

The structural coordinates from the pre-BCR Fab-like region were downloaded from the protein data bank (pdb id: 2H32) and used to build a homology model. To dock the anti-VpreB to the scFv, we used a blind prediction of the binding site limited the solvent-

exposed regions. We coupled a soft docking approach using ZDock followed by a refined model using RosettaDock. ZDock is an inistial stage unbound docking algorithm that uses minimal assumptions of the binding site. We localize binding region to the CDR regions within the scFv using the Kabat Chothia, and Rosetta protocols. For docking to the VpreB region, we excluded the HC and λ5 regions from the search criteria. The mathematical formalism and algorithm have been described in detail previously (*40*). In brief, the scFv and VpreB solvent exposed regions and the core atoms are identified using solvent-accessible solvent area (SASA) and a penalty grid to identify the geometric characteristics of the of each receptor and ligand. These functions are then fed into 1) shape complementarity 2) desolvation free energy, 3) and electrostatic calculations, which are later combined to find the top predicted scores. Each group was clustered according to their RMSD before each model was refined using the RosettaDock Algorithm(*36*). Output scores were generated from Rosetta Dock and top refined structures from each group were moved forward into MD simulations in explicit solvent.

Epitope Mapping Rupture Force from Steered Molecular Dynamics

To predict the top docked pose from the selected output from the ZDock and RosettaDock algorithms, we used steered molecular dynamics (SMD) using the GROMACS package, version 5.1. A recent study showed that there is a linear correlation for umbrella sampling (US) and rupture force calculation derived from SMD allowing for fast free energy predictions (*41*). We applied this approach to estimate relative binding energies among the different poses. First we measured the radius of gyration of the anti-VpreB scFv to gain an idea of the spacing required for SMD pull calculation. The system was set with 2.0Å spacing on either side of the VpreB/scFv complex. The principal axis was determined from the first complex for the scFv and the entire complex was aligned. Each scFv was superimposed onto the scFv so in subsequent SMD pull simulations the same pull force would be applied equally to the scFv in the same direction. The pull distance was estimated as the diameter (2 x radius of gyration) x 3 diameter lengths as depicted in **Figure 2**. Each complex parameter from the GROMOS96 53A6 parameter set (*42*) were used. Short-range non-bonded interactions were cut off at 1.4nm and the particle mesh Ewald (PME) algorithm used for long-range electrostatics. We used periodic boundary conditions in all

directions. Starting structures were equilibrated in the predefined box as detailed above and filled with SPC water molecules. We added 100mM NaCl and neutralizing counterions. We performed energy minimization using steepest descents. Equilibration was conducted over two 100ps periods with position restraints applied to heavy atoms for both protein units. The initial phase of equilibration was conducted for 100ps using an NVT ensemble. All protein and non-protein atoms were coupled to separate temperature coupling baths and maintained at 310K with the Berendsen weak coupling method. An NPT ensemble was conducted for 100ps to maintain pressure at 1.0bar. Equilibrations used as starting configurations the SMD simulations, as detailed above. We performed 10 SMD simulations over 500ps using a range of spring constants of 200, 400, 600, 800, 1000, 1500, 2000, 2500, 3000, 4000kJ/mol/nm^2. Each all heavy atoms of the pre-BCR were restrained while all restraints were removed from the scFv. Each scFv was pulled along the single x-coordinate. Rupture force was calculated as the max pull force when all the bonds broken between the scFv and pre-BCR. After comparing each group derived from the initial docking, the best scored pose was then subjected to screening alanine mutagenesis to predict the epitope on the surface of the VpreB region.

RESULTS

Design of the scFv for functional surface expression

ScFv are composed ~25-30kDa fragments comprised of VH and VL domains. In practice, each of the domains are linked together by established Gly-Ser linkers of varying sizes. It is well established that the scFv have characteristic problems with self-aggregation, lack of binding specificity, loss of binding affinity to target, and improper orientation. These problems arise from the inherent sequence of the scFv (framework and CDR regions), whereby some fragments simply do not orient properly to retain appropriate efficacy. Other problems are associated with the linker region. Due to these inherent problems with scFv, and before proceeding with subcloning the scFv into a lentiviral vector, we incorporated advances in antibody computation methods to design the scFv. This included selection of an antibody fragment with the appropriate binding orientation and linker region that would confer binding affinity to the VpreB target.

Table 1. RosettaAntibody Algorithm output. Each region of the scFv (CDR-L1, CDR-H1, etc.) show information for each region. Resolution is the experimental structure resolution. % identity is the percent sequence identity. The E-Value and Bit-Score are relative measures of the probabilities associated with given matches.

MODEL REGION	RESOLUTION	%-IDENTITY	E-VALUE	BIT-SCORE
CDR-L1	2.5	81.8	0.02	18.9
CDR-L2	2.5	100.00	0.49	14.2
CDR-L3	1.2	77.80	0.04	17.6
CDR-H1	2.0	60.00	0.02	19.3
CDR-H2	2.0	68.80	0.00	25.2
CDR-H3	2.5	80.00	3.70	11.2
FR-LC	2.7	100.00	4.00E-38	117.0
FR-HC	2.20	98.40	**3.00E-43**	**130.0**
GRAFTING SCORE:	**-209**			
RELAXATION SCORE:	**-277**			
H3 LOOP SCORE	**-288**			

Computational Construction of scFv Homology using RosettaAntibody Algorithm

The RosettaAntibody algorithm is composed of two main steps with recent improvements on VH-VL orientation. The first step involves the selection of an appropriate template and grafting from known structures to construct a coarse-grained model. The second step incorporates Monte Carlo sequence disruptions and minimization of the CDR-H3 loop followed by further refinement of the remaining CDR loops and redocking of the VL and VH domains. The first step utilizes the BLAST algorithm with the BLOSUM and PAM30 scoring matrices to identify sequence homology with a curated database of solved antibody structures with resolution ≤ 3.0Å. The output from the initial RosettaAntibody score is shown in **Table 1**, with a good match for our protein sequence and those within the RosettaAntibody database. For instance, the framework regions of the heavy and light chain of the scFv showed % sequence similarity of 100% and 98.4% for the framework region of the light chain (FR-LC) and heavy chain (FR-HC), respectively. The low E-value and high Bit-Score values show the framework regions could be grafted to backbone atoms with high predictability. The non-CDR regions exhibited sequence similarity of 60-100% with acceptable E-value/Bit-Scores. The best predicted model was selected and moved forward into MD simulations.

MD Simulations Provide Insight into Optimal Sequence Orientation

Next we used MD simulations to predict which scFv orientation, Nterm-VL-linker-VH-Cterm versus Nterm-VH-linker-VL-Cterm, would confer a more stable linker connection and evaluate the impact on the CDR binding region of the model. The output RosettaAntibody homology model displayed inherent differences between the N-term end of the VL region and C-terminal end of the VH region and vice versa (**Fig1A**). If the VL-linker-VH sequence was utilized, this would entail VL-Cterm would couple to the VH-Nterm region with a linker. There was a spatial distance distribution of this orientation ranging from 35-44Å, which is on average 13Å greater than the distance between VH-Nterm coupled to VL-Cterm (**Fig 1A**). Before the computational incorporation of the flexible glycine-serine (Gly4Ser) linker, we wanted to see the inherent stability of the Nterm and Cterm region at the framework regions within the VH (aka HC) and VL (aka

LC) regions. We note larger over root-mean-square deviations (RMSD) compared to initial conformation at time = 0ps. This measure allows us to predict the relative flexibility of each region. The RMSD of the Cterm-LC and Nterm-HC (LC-linker-HC orientation) show a larger overall RMSD relative to the Cterm-HC and Nterm-LC (HC-linker-LC orientation) (**Fig 1B**).

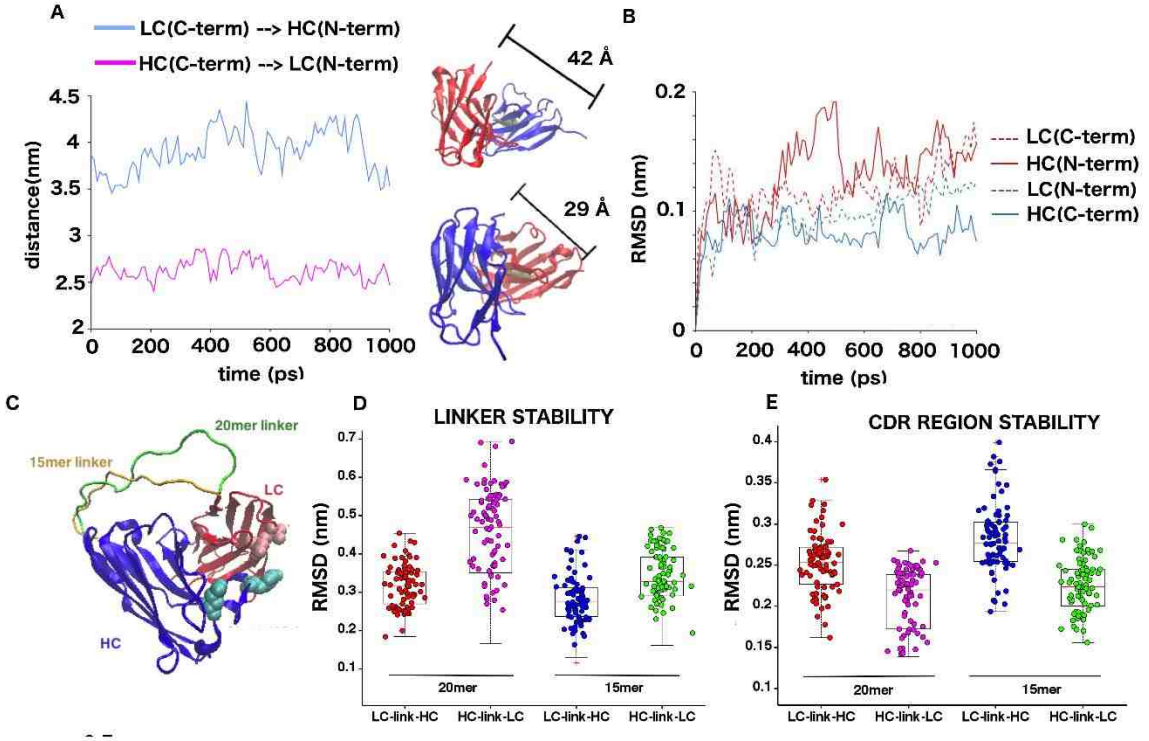

Figure 1. Computational modeling of scFv for optimal orientation and linker length. A, Minimum distance measurement of the N-terminal and C-terminal regions of the VH (LC) and VL (HC) domains to which the linker would be attached. B, Comparison of the RMSD (nm) of the different N-terminal and C-terminal regions of the VH and VL domains. C, Output homology model of the scFv attached to a 20mer and 15mer linker in the HC-linker-LC orientation. D) Relative linker stability using RMSD over the course of a 1ns MD simulation for different orientations and linker lengths E) Relative complemenarity determining region (CDR) stability with different orientations and linker lengths.

Next, we built a homology model of the scFv containing the 15mer or 20mer linker, attached between either the Cterm-LC and Nterm-HC (LC-linker-HC orientation) or Cterm-HC and Nterm-LC (HC-linker-LC orientation). The scFv model generated (without linker region) by the Rosetta algorithm served as the template and the missing Gly4Ser 15mer or 20mer linkers were "filled-in" using the MODELLER software package. Because the glycine-serine is flexible and disordered with minimal secondary structure (*43*), we set out to determine how this flexible linker would impact the CDR regions of the antibody allosterically. The top predicted model from MODELLER is shown in **Figure 1C,** with the 15mer and 20mer linker attached between the LC-Cterm and HC-Nterm regions for the HC-linker-LC orientation. As expected there was an increase in the RMSD of the 20mer linker relative to 15mer linker in both orientations (**Fig 1D**). Interestingly, even with higher amount of flexibility within the linker region itself, we noted a significant decrease in the RMSD of residues within the CDR region when using the longer (20mer) relative to the shorter (15mer) linker (**Fig 1E**). In both cases the HC-linker-LC showed decreased RMSD values in the CDR region.

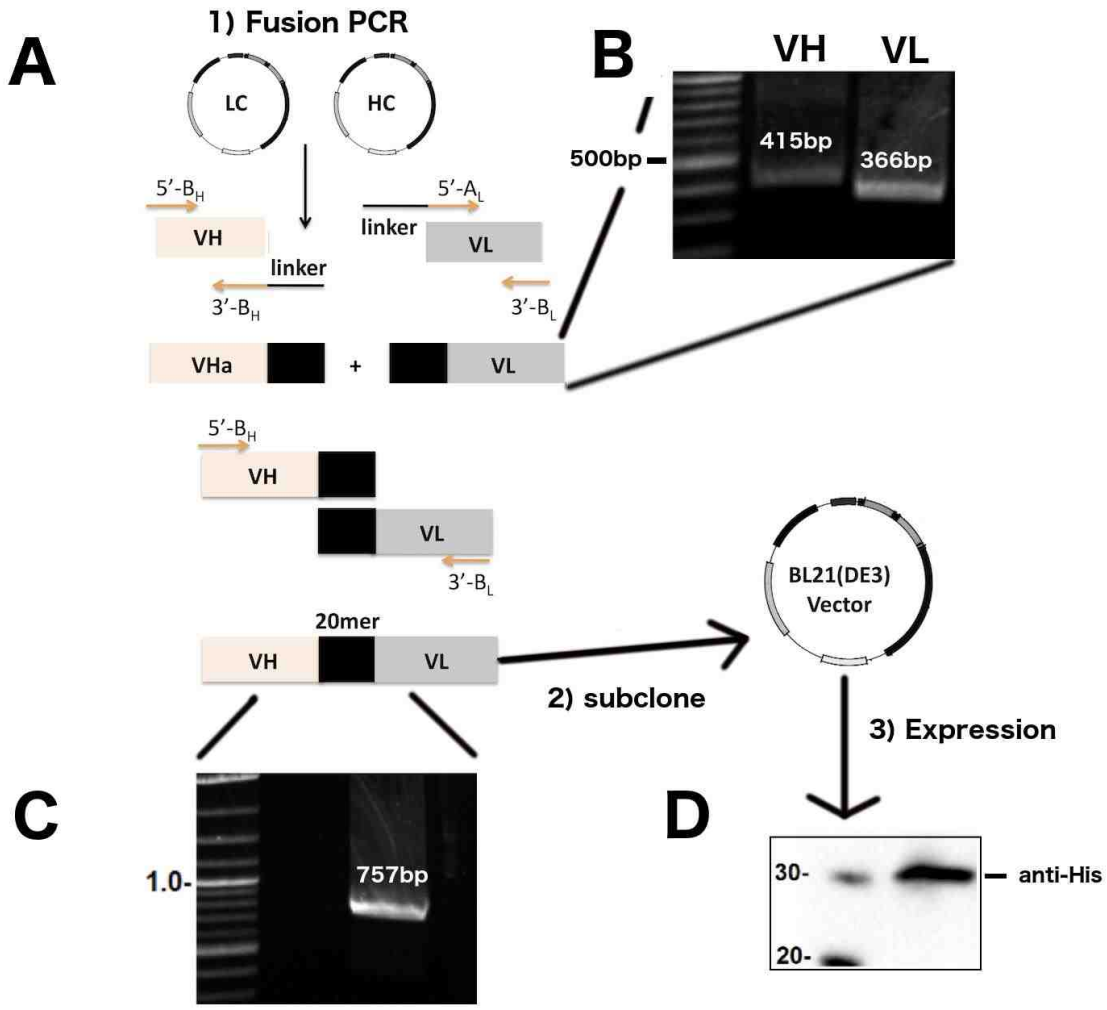

Figure 2. Cloning and Expression of the scFv in E. coli. A, General schematic of the fusion PCR approach. B, VH and VL PCR products that are excised and brought forward for fusion PCR. C, Fusion PCR product of the full-length scFv DNA. D, Detection of purified anti-VpreB-scFv-6xHis via Western blotting.

Production of anti-VpreB1 scFv

From our computational prediction above, we selected the HC-linker-LC orientation with at 20mer linker for scFv fragment engineering. A soluble version of His-tagged, anti-VpreB scFv was produced in *E. coli* to ensure the engineered monomeric antibody retained appropriate affinity and specificity. The steps in the production of recombinant scFv are shown in **Figure 2A**; details are described in Materials and Methods. Results at specific steps are illustrated in **Fig 2B-D**, showing a yield of appropriate-sized fragments for the VH and VL regions (**2B**), PCR-mediated fusion and amplification of VH-linker and linker-VL regions using the HC-forward and LC-reverse primers to yield a product at the predicted size (**2C**). After subcloning into a BL21(DE3) compatible vector, cell lysates were collected from IPTG-induced bacterial cultures. The scFv was purified by nickel chromatography, detected by western blotting (**2D**), and stored at a concentration of 500μM.

scFv binds with subnanomolar binding affinity to VpreB

To ensure the purified scFv detects the VpreB component of the pre-BCR on the surface of leukemic pre-B cells, we used the 697 BCP-ALL cell line as a model system. Tubes bearing cultured suspensions of 697 cells ($1x10^5$) were incubated with recombinant scFv, followed by incubation with PE-conjugated anti-6xHis antibodies. Results in **Fig 3A** show strong binding of the scFv to 697 (blue histogram), compared to an isotype-control (pink histogram). To estimate the binding affinity, cells were incubated with serially diluted scFv over a range of concentrations. Based upon a nonlinear regression fit to the sigmoid Hill equation, the scFv bound to 697 cells with subnanomolar binding affinity (K_D= 0.63nM; **Fig 3B**). **Fig. 3C** show results of a competitive binding assay performed in the presence of increasing concentrations of unlabeled, anti-VpreB IgG. The effective competition with whole (dark) IgG antibodies confirmed that the engineered scFv retains the same specificity as the parental antibodies.

Transduction of CAR T Construct into PBMCs

Our next step was to cloning of the scFv antibody fragment into a CAR T lentiviral vector. As illustrated in **Figure 4A**, the construct orients an N-terminal scFv-6xHis in frame with

a CD28 hinge/transmembrane/cytosolic region. Following the cytosolic CD28 costimulatory domain is the CD3ζ cytoplasmic tail.

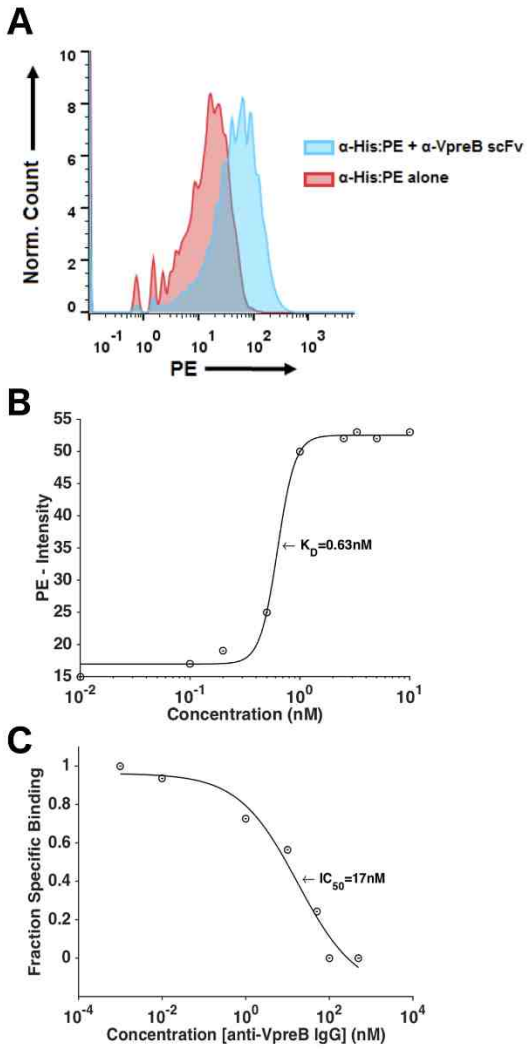

Figure 3. Binding affinity and specificity measurements to live BCP-ALL cell lines. A, Binding of the scFv at saturating conditions. B, Binding curve with increasing concentrations of the scFv-6xHis fit to sigmoidal Hill equation. C, Competitive binding assay of the scFv-6x with parent antibody. Increasing partent antibody are added after saturating receptor with anti-VpreB scFv.

For the production of pre-BCR specific CAR T cells, we modified published protocols for lentivirus transduction using RetroNectin-coated 24-well plates. RetroNectin utilizes a heparin-binding domain (H-domain), cell-binding domain (C-domain), and CS-1 sequence. Virus particles bind to the H-domain, while integrin receptors VLA-5 and VLA-4 bind the C-domain and CS-1, respectively. The first round of transduction was attempted with freshly-isolated PBMCs, without specific steps to enrich for CD8+ cytotoxic T cells. As shown in **Fig. 4B**, this resulted in a marked uptake of the virus by non-CD8+ T cells. Although these cells would be activated with PMA/ionomycin treatment (**Fig. 4C**), this pool was not a productive source of cytotoxic CAR T cells and represented an apparent sink for viral particles.

We next elected to add negative selection, using CD8+ enrichment kit (EasySep), to the protocol prior to RetroNectin-mediated lentiviral transduction of peripheral blood T cells. As shown in **Fig. 4D**, this resulted in successful CD8 enrichment. Results in **Fig. 4E**, we achieved a higher transduction efficiency of CD8+ T cells (left panel, 4E), which also had marked expression of the T cell activation marker, CD69+ (right panel, 4E).

CAR T Forms Synapse with BCP-ALL Blasts and Exhibits Cytotoxic Activity

When subjected to a single round of RetroNectin transduction, CAR T+ cells exhibited a broad distribution of chimeric receptor expression, as shown in the typical example in **Fig. 5A**. Based upon calibration of these results using anti-HisTag antibodies and Simply Cellular Bead standards (**Fig. 5B**), CAR expression levels ranged from 4600 to ~300,000 receptors/cell, with a median of ~71,000 receptors/cell. We found that a double transduction protocol (see Methods) resulted in more consistent and increased receptor expression in transduced CD8+ T cells (**Fig. 5C**) and adopted the two-transduction method for all subsequent work.

We observed a strong correlation between the number of CAR expressed on the CD8 T cell surface and the level of killing activity against target leukemia cells (**Fig. 5D**). Here,

the HI category was defined to be as a count of >30,000 CAR per T cell, while the LO category was defined to be cells displaying 10,000 receptors. The CAR T HI population exhibited much more potent activity against 697-GFP and Nalm6-GFP BCP-ALL lines (**Fig 5E**). Note that, while 697 cells express slightly higher pre-BCR binding sites than Nalm6 cells (22,000 vs 18,000), there was no appreciable difference in leukemia cell depletion after incubation with CAR T-Hi cells.

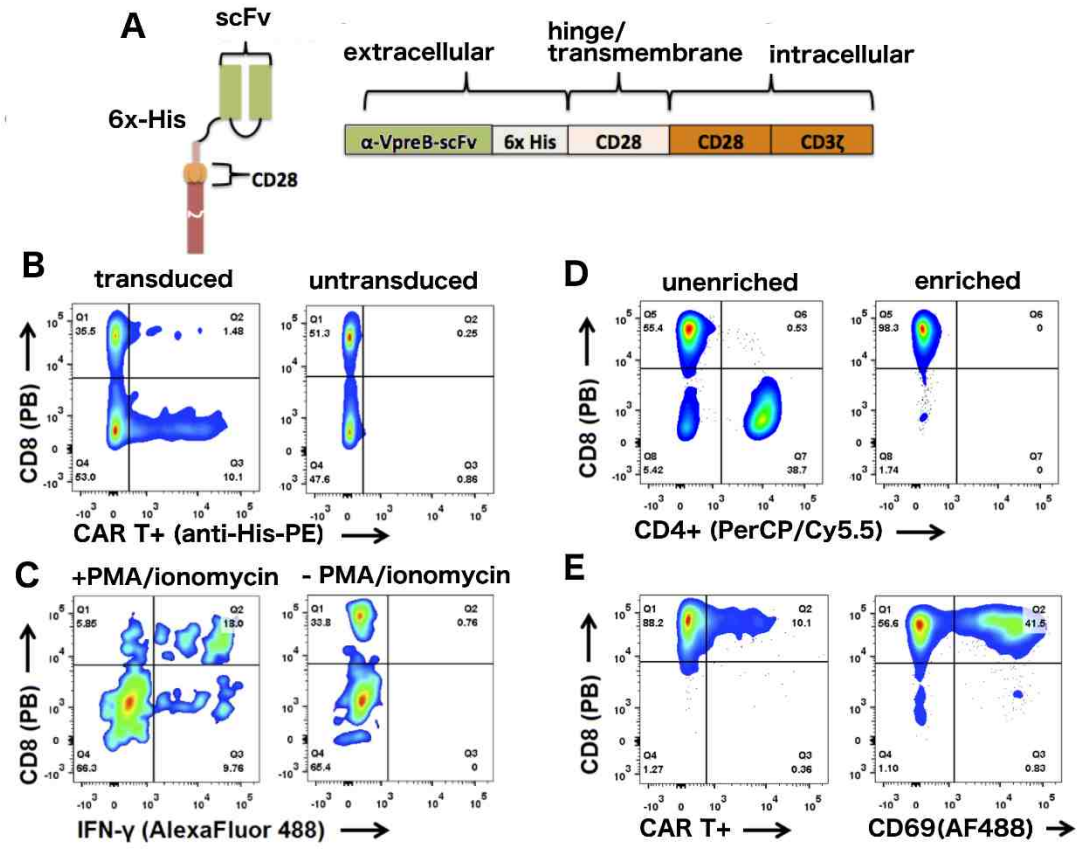

Figure 4. CAR T Detection and Activation status of T cells. A, Schematic of the anti-VpreB scFv incorporated into the CAR T lentiviral cassette containing the CD28 (hinge/tm/cytosolic) and CD3ξ signaling subunit. B, Initial round of transduction of entire population of PBMC. C, Activation of PBMC with PMA/ionomycin exhibits IFNγ signaling. D, Negative selection enrichment of CD8+ T cells for new round of

transductions. E, Increased transduction efficiency of CAR T lentiviral vector into CD8+ T cells, which exhibits expression of early activation marker CD69.

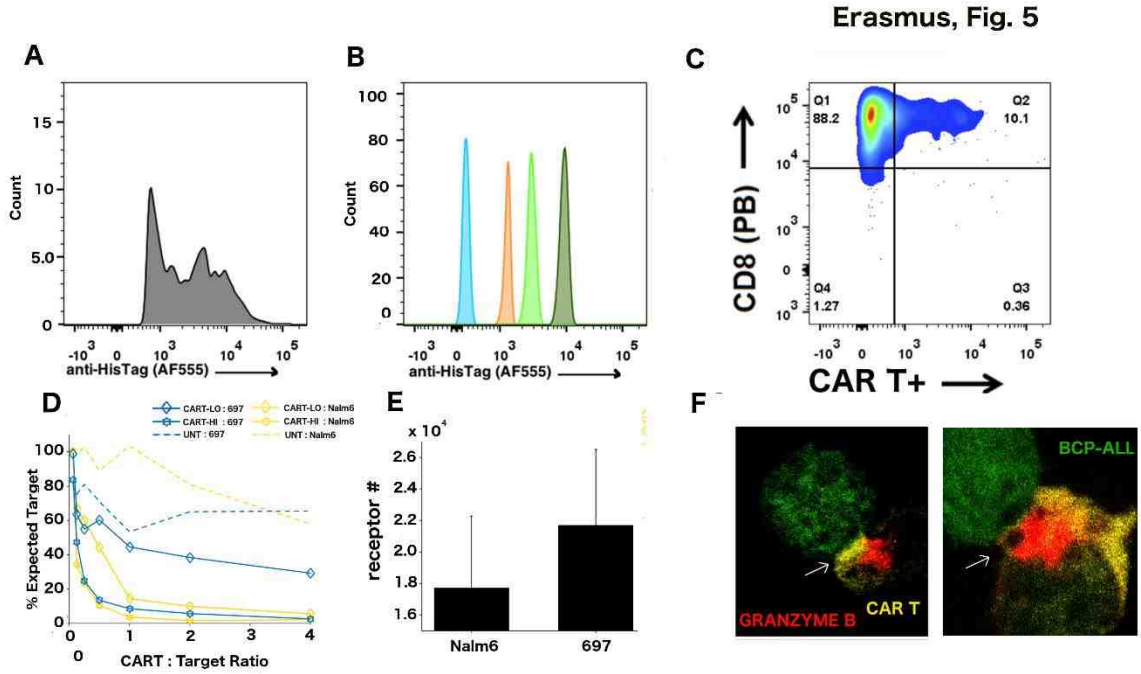

Figure 5. Confocal imaging of CAR T / preBCR synapse and in vitro cytotoxicity. A, Anti-6xHis(AF555) antibody is used for calibrating the beads and for detection of receptor on the surface of live CAR T cells. B, Calibration curve of the anti-6xHis(AF555) antibody bound to the calibration beads with known number of binding sites. C, Transduction efficiency of CAR T lentivival vector into CD8+ T cells. D, Cytotoxicity assay detects decreasing numbers of target 697-GFP or Nalm6-GFP after 3-day co-incubation with different ratios of the CART : Target. E, Quantification of receptors on surface of different BCP-ALL cell lines.F, Confocal imaging of the CAR T (yellow) binding to 697 (GFP, green) and accumulation of granzyme B (red) at the synapse (white arrow).

We also evaluated the interactions of CAR T cells with leukemia target cells by fluorescence microscopy. After co-incubation of CAR T cells with BCP-ALL cell line (697), we observed the formation of a synapse between CARs on surface of T cells with leukemic B cells labeled with cytosolic GFP (**Fig 5F,** white arrows). This engagement resulted in relocalization of the CARs to the point of contact at the synapse (**Fig 5F,** yellow). The T cell serine protease, granzyme B, accumulates at the synapse (**Fig 5F,** red).

Epitope Mapping for Structural Insight of the pre-BCR/CAR T Synapse

The antigen epitope is likely to have an important role in CAR T cell triggering. To gain a more detailed understanding of the VpreB epitope in this study, we employed protein/protein docking protocols and steered-molecular dynamics (SMD) to predict the VpreB epitope. We first applied a soft, blind-docking approach of the scFv to the VpreB region, given limited knowledge of the binding epitope. We utilized the ZDock algorithm and set a restrictive criteria to limit the search area to solvent-exposed regions of the VpreB. The top 10 poses from the soft-docking were output and we compared the relative orientation of the CDR regions of the anti-VpreB scFv after superimposition of the preBCR. Heat map analysis of CDR RMSD (**Fig 6A, top**) revealed the clustering of receptor to four distinct binding poses (**Fig 6A**, **bottom**). Each of the top scoring subgroups were then subject to the RosettaDock algorithm for further docking refinement. After refinement, hundreds to thousands of different poses were generated and scored. We selected the top poses based off the RosettaDock's interface and total scores (**Table 2**). Top scoring poses that were associated to groups identified from soft-docking protocol were selected and moved into SMD simulations.

A linear correlation had been established between the SMD derived rupture force as a function of pull constants and the derived ΔG_{bind} derived from umbrella sampling (US), so we used this to rank our different poses. SMD simulations are comparable experimental data derived from atomic force microscopy (AFM). In this case our scFv is attached to a virtual spring whereby a constant force or velocity is applied to the center-of-mass to pull the protein from the binding pocket (**Fig 6B**). As the COM distance increases between the

scFv and the pre-BCR, a force builds up to a max point (rupture force) until critical interactions are disrupted. By changing the pull force constant, we obtain different pull force profiles (**Fig. 6C**). By plotting the rupture force versus the pull constant for the

Table 2. RosettaDock Refinement Output. Post-clustering refinement of scFv docked to VpreB that determines outputs top performing scores based upon the interface and total score. Grayed are the models used for input into SMD simulations for relative affinity comparison.

Group	Interface Score	Total Score
1	**-4.4**	**-505.8**
2	-4.5	-516.9
2	**-5.5**	**-516.9**
2	**-4.7**	**-516.8**
2	-4.5	-516.9
3	**-5.5**	**-519.4**
3	**-5.4**	**-502.8**
2	-4.3	-504.8
3	-4.3	-503.1
1	-2.4	
3	-3.0	-502.7
4	**-4.9**	**-505.8**
4	-4.3	-503.8
4	-3.7	-503.5
4	-3.4	-503.3

different poses, we arrive at a ranking between the different groups in the order of 3, 4, 2, 1 (**Fig 6D**). We selected pose 3 and performed longer simulations to identify critical interactions between the CDR region and VpreB. Using a series of minimum distance , H bond, and RMSF calculations we identified the top residues within the VpreB region. We next performed screening alanine mutagenesis among several residues to determine whether this would impact affinity in our SMD simulations. Mutation of several of the identified residues showed a dramatic impact on apparent binding affinity, particularly serine 11 (**Fig 6E**). The top five potential binding sites identified between scFv and VpreB are shown (**Fig 6F-G**).

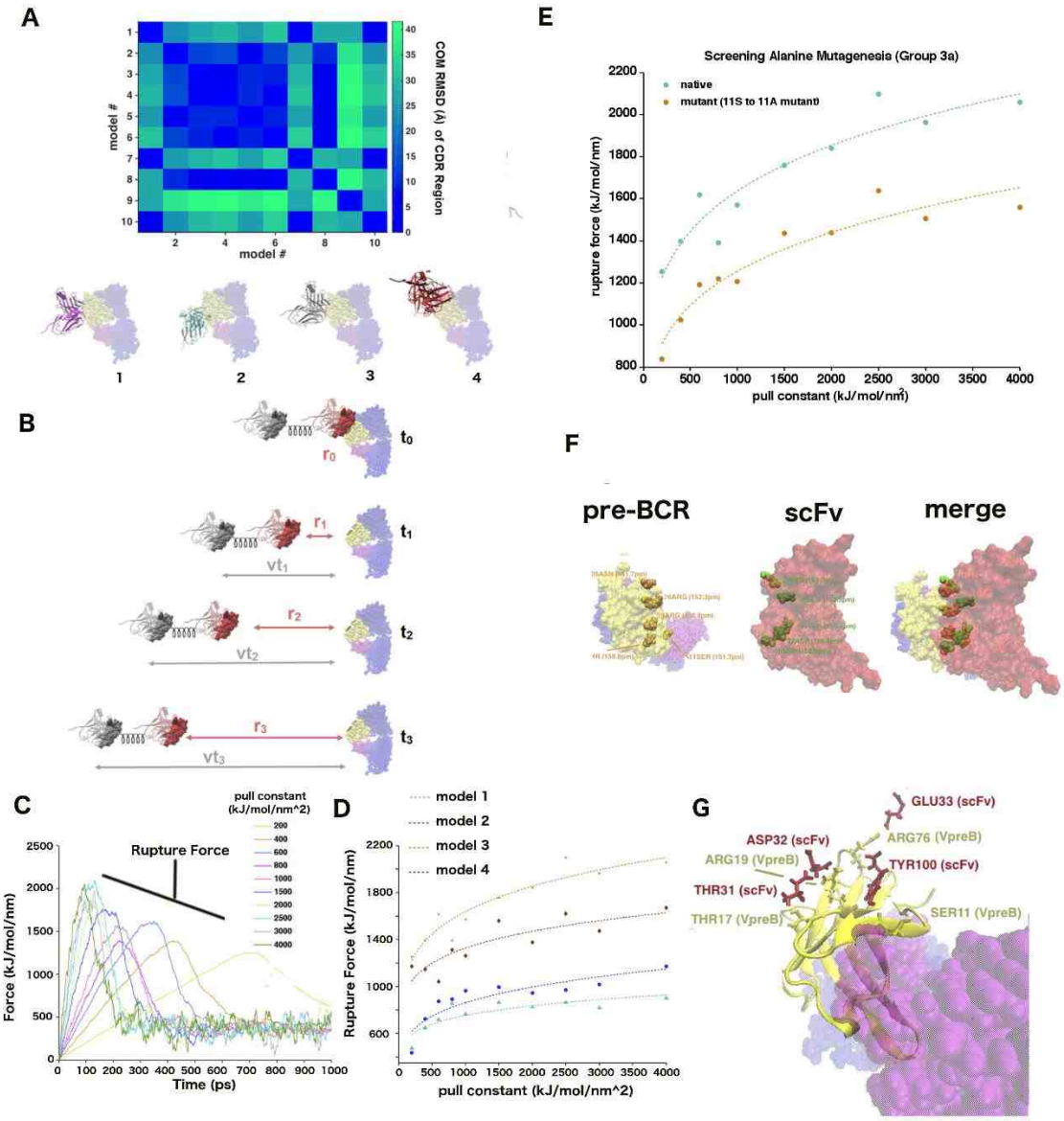

Figure 6. Epitope mapping of the scFv binding site on surface of VpreB. A, Heat map of that clusters different groups based off RMSD of the different CDR regions after superimposition of the VpreB structure among the different models. B, Schematic showing the basic premise of steered molecular dynamic simulations. C, Pull force curve at varying pull force constants (kJ/mol/nm^2). Rupture force (kJ/mol/nm) is the max point of the pull curve before key interactions are broken. D) Plot of rupture force (kJ/mol/nm) as a function of the pull force constant (kJ/mol/nm^2) of the different model outputs. E) Plot of rupture force (kJ/mol/nm) as function of the pull force constants (kJ/mol/nm^2) after performing screening alanine mutagenesis of key residues within implicated in top predicted model.

F-G) Best predicted model with top 5 key residues within the scFv (red) and VpreB (yellow) highlighted.

DISCUSSION

In contrast to the anti-CD19 CAR T therapy that has already been tested and validated in clinical trials (*15, 26, 44*), we characterized a new target (*28*) that can utilize this therapy in BCP-ALL. Recent evidence suggests that certain biophysical properties of the CAR itself (epitope location (*45-47*), valency (*48*)) and/or upon the target cell (i.e. receptor density (*49, 50*)) play an important role in dictating T cell efficacy. We speculate that the bivalency of the pre-BCR with two equal binding sites (*51*) may impact CAR T signaling efficiency. The pre-BCR, like the BCR (*52*), is already structurally optimized to form an immunological synapse (*52-54*). The CD3ζ is a signaling subunit of the TCR that relies on appropriate synapse formation to trigger activation (*55, 56*). Therefore we hypothesize that the structural features of the pre-BCR, which have been shown to form synapses to different cells (*53, 54, 57*), are well-suited to facilitate binding in a trans-fashion to the CAR on surface of cytotoxic T lymphocytes, forming robust synapses that can trigger activation. Recent literature provides ample evidence that suggest differentially engineered CARs [see review (*58*)] with different structural features (*46, 58*), such as 4-1BB versus CD28 co-stimulatory domains (*59*), exhibit changes in signaling that alter the T cell efficacy when honing in on the same target (i.e.CD19). We are currently looking to determine whether certain CAR T design principles still hold true when comparing CARs that are made to target the pre-BCR with unique structural properties.

In this study, we observe that CAR T transduction generated a wide distribution of receptor counts on the target cells (**Fig. 5A**). We showed that there were clear differences in efficacy that depended upon the levels of expression on the surface of both CAR T and BCP-ALL cells (**Fig. 5D**). Thus, it is not only important to understand how the threshold of signaling for CARTs (*50*) with different signaling domains (i.e. 4-1BB versus CD28) (*59*) impacts efficacy but also how the downstream signaling profile changes when we alter the antibody binding specificity. Quantifying the receptor density, scFv/target affinity, synapse profiles, downstream signaling and epitope mapping have been shown to be (*50, 60, 61*) important to CAR T potentcy. We have already observed a clear polarization of the CAR T and formation of granules at the synapse (**Fig. 5F**). It is well known that polarization of

cytotoxic T cells leads to directed secretion of perforins and granzymes that is triggered by cytoplasmic Ca2+ elevation (*55*). As a future direction, we will incorporate ratiometric imaging to study the robustness of our CAR/pre-BCR synapse in activating signaling (*62*). We are currently establishing whether synaptic exclusion of critical negative regulatory receptors (PD-1, CD45, Tim-3) (*63*) might serve as a predictive measure for T cell exhaustion (*64*). This will continue to be important in order to understand activation and long-term duration of the CAR T cells when exposed to different targets. It has already been established that the target epitope (*65*) and receptor density (*66*) are important properties in fine-tuning the signaling threshold required for CAR T cell activation.

Incorporation of theoretical modeling (*67*), including MD simulations (*41*), advanced docking protocols (*40, 68*), and rule-based modeling (*69*), can aid in our understanding of these CAR T signaling thresholds and provide insight into the CAR T/target receptor relationship. Our ability to utilize recent advances in antibody modeling coupled with large-scale computational resources enables us to make better 3D predictions of our scFv poses in binding to the target (**Fig 6A-G**). This structural input will allow us to apply these substructure predictions to different spatial and temporal formats such as coarse grain simulations (*70*). This can be used to make predictions about intermembrane spacing distribution and/or how extracellular engagement might influence the interactions between the cytoplasmic ITAM domain and the lipid bilayer (*71*). Further, predictions of the binding pose can be compared to low-resolution TEM images (*72*), whereby we can establish how different orientations influence the synapse. Use of computational methods in small molecule therapy development has been accepted almost ubiquitously in the pharmaceutical industry to optimize pharmacoketic profiles. Computational approaches are applied to aid the experimental set-up whereby they can help generate testable hypotheses and provide insight into experimental hurdles (*73*). The use of computational design to guide experiments are just beginning to make headway in antibody-based therapies. Improvements of algorithms and enlarging antibody databases are rapidly improving our ability to predict 3D structure of antibody fragments (*36*). To this end we have used computational modeling protocols to aid in the engineering of an anti-VpreB scFv that retains pre-BCR specificity and exhibits high affinity (**Fig 1-3**).

We propose that the pre-BCR is a unique target for subsets of BCP-ALL patients, since it is expressed only at a specific stage during B cell development (*74*). Unlike CAR T and antibody therapies that target the CD19 extracellular target (*75-77*), or TKI drugs for that matter(*78*), treatment of pre-BCR+ leukemias with anti-preBCR CAR T should protect the mature population of B cells that are essential to the adaptive immune response. The λ5 and VpreB (*79*) are unique with no sequence homology to any other gene, which should limit off-target effects. Further, we showed the pre-BCR is critical for survival in certain subsets of leukemias (*28*). In plasma cell malignancies, groups showed that BCMA was essential to the proliferation of these particular cells(*80, 81*).These data show the importance of BCMA in the survival of plasma cells may prevent the outgrowth of a resistant subpopulation. Also, in contrast to ROR1 (another proposed target in BCP-ALL), which has been shown to be expressed on pancreatic and lung tissue in some models (*82, 83*), the pre-BCR's restriction to B cells should minimize 'on-target, off-tumor' toxicity. We still anticipate that our anti-VpreB CAR T will ablate both healthy and leukemic precursor B cells alike, but anticipate, due to the narrow window that the pre-BCR is expressed during B cell development, an large proportion of mature B cells should remain intact. Other important things to consider include the loss of CAR T function via tumor-mediated immunosuppression (*84*) or chronic T cell activation that leads to the upregulation of inhibitory ligands (*85*). These factor are worth considering and will be a main point of focus in our studies to further characterize our anti-VpreB CAR T.

This upregulation of negative regulatory receptors is also known as T cell exhaustion (*86*). Overstimulation of CAR T signaling receptor leads to increased expression of inhibitory receptors (PD-1, TIM-3, LAG-3) reduced cytokine production and proliferative capacity, and increased rates of apoptosis(*59, 64*). Different groups are employing alternative strategies to minimize these deleterious aspect of overstimulated T cells. Incorporation of the 4-1BB costimulatory domain showed reduced T cell exhaustion in anti-CD19 CAR T constructs compared to the CD28 costimulatory domain (*59*). The 4-1BB signaling unit corresponded with longer persistence beyond two years (*24*) which far exceeded the CD28 costimulatory domain, which exhibited a max persistence time of 68 days (*44*). These

results show that the incorporation of certain costimulatory domains (4-1BB and CD28) were important in regulating T cell activity when the CAR was honed in on a similar epitope (i.e. CD19). However, a question still remains as to whether target specificity (CD19 versus preBCR) might impact CAR T activation status and/or expression of exhaustion markers when they have the same co-stimulatory domain (i.e. CD28). Many groups have provided evidence to suggest that spatial organization of the epitope has an important role in CAR T cell efficacy (*45, 47, 65, 87, 88*). Further, it was shown by (*89*) that analogous receptors to anti-CD19 CARs engaged with their target on Raji B-cells and exhibited a highly convoluted membrane surface that was remarkably different from those interacting via TCR-pMHC. These data suggest that this engagement may impact CAR T potency. Like the TCR-pMHC complex the structural properties of the pre-BCR(*53, 54*) makes it optimally designed to engage antigen of a variety of forms to trigger the formation of an immunological synapse. This might suggests that the pre-BCR may represent more well-suited target in its capacity to form an appropriate signaling synapse compared to the CD19 receptor in pre-BCR(+) leukemias.

This study points to the need to carefully optimize conditions for transduction and expansion of CD8+ T Cells, and is an area that is of active attention (*58*). After cloning our scFv into lentiviral vector, we showed robust activation and efficient surface expression (**Fig 4**) of the CAR on the surface of CD8+ T cells. We determined it was advantageous to remove non-CD8+ PBMCs to enable better transduction efficiency of the CAR T into the CD8+ population. However, it will be important to further establish *in vivo* whether the CD8+ is more optimal alone or when co-injected with CD4+ CAR T cells. It has recently been shown that these CD4+/CD8+ ratios) may be important in for *in vivo* efficacy (*90, 91*).

Concluding Remarks

Approximately 13.5% (112 cases) exhibited tonic pre-BCR signaling that drove BCL6 expression, a positive feedback regulator of the pre-BCR pathway(*35*). In the majority of leukemia subsets that did not contain a functional pre-BCR pathway there was active

repression of BCL6 expression (*35*). Interestingly, targeting Ph+ ALL with tyrosine kinase inhibitors (TKIs) revealed a novel mechanism of drug resistance through increased BCL6 expression (*92*). This suggests that in ALL subsets that exhibit a pre-BCR(-) profile and treated with TKIs targeting the cytokine receptor pathway should be monitored at later stages to ensure there is no upregulation of pre-BCR signaling products. In the event that the cells do express pre-BCR products, it may necessitate the use of therapies to target the pre-BCR pathway. Targeting pre-BCR highly desirable, regardless if it is expressed early on or at later stages of assessment.

CHAPTER 5: DISCUSSION

This dissertation focuses on validating the pre-BCR self-oligomerization model on the surface of leukemic blasts and the design of novel therapeutics against this target. While there has been intense interest to understand the pre-BCR signal initiating mechanism (*1-4*), this work provided the first direct evidence for receptor homotypic interactions on live cells. Further, to our knowledge no reports have explored the dimer interface of the pre-BCR as a putative target in BCP-ALL. Through the use of advanced imaging modalities (*5, 6*) and theoretical modeling (*7, 8*) , we showed that oligomerization of the pre-BCR occurs through both homotypic and galectin1-mediated mechanisms. We were the first to show that we can directly target the dimer interface with inhibitory monovalent antibodies, which demonstrably impacts the survival of leukemia blasts *in vitro* (*9*). Further, we make a compelling case for the pre-BCR as a target for chimeric antigen receptor (CAR) T cell therapy.

Validating the pre-BCR Oligomerization Model in Different BCP-ALL

Through the use of cutting-edge imaging techniques, we were able to capture brief, repeated homodimerization on the surface of live leukemic B cells (**Chapter 2, Fig. 1B-D**). Using SPT, we showed that pre-BCR dimer events were characterized by correlated motion at short separation distances. Using the hidden Markov Model (HMM), we could distinguish between tagged-preBCRs in the "dimer-state" and the "free-state". The dimer state exhibited characteristic slower diffusion (**Chapter 2, Fig. 1G-H**). This is consistent with slowed diffusion of dimers and their signaling partners, but may also be influenced by transient residency of pre-BCR within protein islands that have been implicated in TCR and BCR clustering (*10, 11*). Our observations of repeated interactions between pairs of pre-BCRs is likely due to their transient co-confinement within these specialized microdomains as well as corrals created by the dynamic cortical cytoskeleton (*12, 13*).

We noted differences in dimer lifetimes and diffusion profiles of the pre-BCR on the surface of two distinct BCP-ALL cell lines, 697 and Nalm6, which are characterized by distinct genetic lesions (*14*, *15*). Nalm6 cells showed slower diffusion rates that correlated with a fivefold slower off-rate relative to 697 cells. These data suggest that the pre-BCR in Nalm6 has a higher tendency to form slow-moving, higher-order oligomers. One possible explanation is that this may be the result of specific VpreB single nucleotide polymorphisms (SNPs) (*9*). We noted that a polymorphism in the VpreB was more prevalent in Nalm6 cells, resulting in an asparagine introduction within the VpreB protein. It is intriguing that this results in a putative N-glycosylation site, since prior work by others linked N-glycosylation of the μHC (membrane heavy chain) to autonomous signals from the pre-BCR (*16*). Further, addition of an N-glycosylation site into δ-HC receptors, which does not contain this specific post-translational modification, was sufficient to activate autonomous pre-BCR signaling (*16*). In contrast, a VpreB-UR SNP within the 697 cell lines substituted lysine for glutamic acid. It has been suggested that acidic residues within VpreB-UR are involved in salt bridge formations with positively charged λ5-UR and may affect the ability of the λ5-tail to interact with specific ligands. Thus, a change in molecular charge within the VpreB region might subsequently alter λ5's binding capacity. We also showed that patient samples with unique cytogenetic profiles could be subdivided into one of two diffusion patterns associated with either Nalm6 or 697 cells (**Chapter 2, Fig. 6C**). Previous studies have shown that disruption of the actin cytoskeletal network with latrunculin A (*17*) or through cofilin-mediated severing via Toll-like receptor ligands (*18*) increased BCR diffusion. We do not rule out that the observed differences in diffusion might also be associated with variations within the cortical actin cytoskeleton.

Galectin-1 Mediates Large Aggregation Through Different Binding Modes

In contrast to the frequent, serially engaging rebinding events characteristic of pre-BCR dimerization, galectin-1 binds to pre-BCR to form larger, more stable aggregates. The study of the glycan network and glycan-binding proteins adds an important feature to membrane dynamics. Glycans are central to extracellular matrix and cell membrane due to their ubiquitous presence on glycoproteins and glycolipids (*19*). Further, the multivalent

nature of glycan-binding proteins have been shown to form higher-order oligomers resulting in a glycan network (*20, 21*). While a large portion of studies have focused on the functionality of lectins, many groups are now turning to advanced imaging techniques (*9, 22*) to study how these proteins influence membrane dynamics. We looked into how lectin-binding proteins and glycan networks might influence the pre-BCR interaction network. Recent studies revealed that galectin-1 acts as an intermediary protein between the pre-BCR and glycoreceptors on both the pre-B cell surface and stromal cells (*3, 4*). It has been postulated that galectin-1 is presented at the extracellular surface of stromal cells attached to N-acetyllactosamines (LacNAc) on integrins at the stromal cell surface (*23*). In the context of the bone marrow microenvironment, precursor B cells bearing a functional pre-BCR could bind to galectin-1 on stroma and induce a local conformational change in galectin that alters its carbohydrate-binding preference (*23*). In one model, pre-BCR-galectin binding could mediate the release of trans-dominant pre-BCR/glycoreceptor interactions between pre-B cells and stromal cells, in favor of cis- dominant interactions between receptors on surface of pre-B cells. Introduction of galectin-1 in the absence of stromal cells resulted in the formation of large clusters at the membrane surface (**Chapter 2, Fig. 2A)** and caused a dramatic slowdown of the pre-BCR (**Chapter 2, Fig 3B**). We showed increased correlated motion of 2-color tagged pre-BCRs at greater separation distances when galectin-1 was added (**Chapter 2, Fig. 2B-C**). When we blocked galectin-1's lectin-binding properties with saturating concentrations of lactose, we noted increased pre-BCR mobility and correlated motion at shorter pre-BCR separation distances that were similar to pre-BCR diffusion under tonic signaling conditions (**Chapter 2, Fig 2B-D**). These results show that even in a cis- setting (absence of stromal cell binding) glycan-mediated interactions influences the pre-BCR membrane dynamics. We anticipate that this remodeling of pre-BCR from trans- to cis- hetero-interactions could drive differential pre-BCR signals as the pre-B cells escape the stromal-cell+ signaling niche (*24*). To understand how pre-BCR dynamics in presence of galectin-1 influence downstream signaling we turned to biochemical assays.

Galectin-1 +/- Lectin Binding Properties Influences Differential Signals

Prior data revealed that formation of cell-cell contacts ("synapses") between stromal and precursor B cells leads to robust phosphorylation associated with pre-B cell activation (*3*, *25*). Galectin-glycan lattices have been shown to be involved in a wide variety of cellular processes from immune system and anti-tumor immunity responses (*26*, *27*). We incubated precursor B cells with soluble, dimeric galectin-1 in the absence of stromal cells, a condition which would be more representative of cis- mediated galectin-1 interactions after stromal cell release, and noted a significant reduction in pre-BCR proximal activation profiles (**Chapter 2, Figure 4A**). These data suggest that galectin-1 mediated interactions, either in the presence or absence of the stromal cells, may lead to drastically different proximal activation profiles in pre-B cells. Interestingly, we noted that galectin-1 binding in the presence of lactose led to increased Syk activity (pY352) above tonic signaling conditions (**Chapter 2, Fig 4A**). This would suggest that, within these cis-dominant conditions, the pre-BCR's downstream signaling profile could be readily altered by differential glycoreceptor aggregation. In one scenario (CBS exposed) galectin-1 binds the pre-BCR through its protein-protein interaction and likely recruits other glycoreceptors forming large heterocomplexes. Since galectin-1 has been shown to directly bind to negative regulatory glycoreceptors such as CD45 (*28*), with intrinsic phosphatase activity, this may explain the attenuated signal we observed (**Chapter 2, Fig. 4A**). In the other scenario, (CBS blocked) galectin-1 enhances the ability for two pre-BCR to co-aggregate, leading to enhanced proximal activation. Without the ability to bind glycoreceptors, galectin-1 binding would be expected to stabilize homotypic interactions between diffusing pre-BCRs, resulting in dimers, chains and complex aggregates. Galectin-1 with or without carbohydrate leads to increased and decreased proximal activation, respectively. In both of these cases, we noted a significant reduction of BCL6 expression. It would be interesting to assess how the stromal cell signaling niche (*24*) may select for B cells that exhibit an optimized signaling threshold, balanced through appropriate expression profiles that balance critical feedforward and feedback loops.

Allosteric Control of Galectin-1 through Pre-BCR Binding Interactions

Our theoretical work revealed that pre-BCR/galectin-1 interactions decrease galectin-1's affinity for N-acetyllactosamine residues (**Chapter 3, Figure 6-7**) by destabilizing the sugar in the binding pocket (**Chapter 3, Figure 4A-D**). This work is another example of how MD simulations can be used to study allosteric impacts in macromolecular structures (*29-31*). These simulations corroborated the finding that pre-BCR binding alters critical intermolecular interactions between Arg-73 and the carbohydrate (*23*). They also revealed that the aromatic stacking interactions (*32, 33*) between the sugar and Trp-68 of galectin-1 (**Chapter 3, Figure 4F-H)** can be modified by pre-BCR binding**.** Together, these experimental and theoretical findings raise new questions that can be validated at the bench. It would be interesting to test whether galectin-1/pre-BCR interactions alter galectin-1's binding preference for negative (i.e. CD45 or ITIM-containing) or positive coregulatory receptors (i.e. CD19) at the plasma membrane. Further, principal component analysis (*34, 35*) of our MD trajectories revealed that pre-BCR/galectin-1 interactions increased root-mean-square fluctuations across several different eigenvectors at the N-terminal dimer interface region on adjacent monomer of the galectin-1 homodimer **Chapter 3, Figure 2D**). This data may implicate that pre-BCR binding may destabilize the dimer region and shift galectin-1's monomer/dimer equilibrium in favor of monomers. Allosteric control of dimerization has been reported before using MD simulations (*36*). Further, experimental evidence suggests allostery to also be involved in galectin-1 binding whereby it was shown through gel filtration studies that galectin-1 exists in a reversible monomer-dimer equilibrium and carbohydrate binding shifted the equilibrium toward dimer formation (*37*). This disruption in dimer/monomer stability would offer an alternate explanation to the decreased phosphorylation of Syk at phospho-acceptor site 352 (C**hapter 1, Fig 4A**).

Targeting pre-BCR Dimerization Impacts Survival

We designed Fabs against the VpreB region of the surrogate light chain to address how homotypic pre-BCR interactions support leukemia blast survival. We reasoned that a monovalent antibody fragment against the VpreB component would sterically hinder λ5-mediated homodimers. Indeed, incubation of live BCP-ALL cells with this Fab for 10-

15min inhibited pre-BCR homointeractions, seen as the significant loss of correlated motion at short separation distances between distinctly labeled pre-BCRs (**Chapter 2, Fig. 3C-D**). Based on single particle tracking, we also observed that the inhibitory Fabs decreased the incidence of slower diffusing pre-BCRs (**Chapter 2, Fig. 3A-B**) and increased dimer off-rates (*9*). Using phosphorylated ITAMs and phospho-activation sites on Syk as readouts; we showed that Fabs targeting the pre-BCR dimer blocked proximal pre-BCR signaling (**Chapter 2, Fig. 4A**). Overnight Fab treatment abrogated BCL6 expression (**Chapter 2, Fig. 3E**), an important readout of constitutive pre-BCR signaling (*38*). Just as inhibition of pre-BCR pathway kinases or BCL6 expression mitigated the survival potential of leukemia cells (*38*), we showed that our Fab could also induce apoptosis, especially in the presence of low-dose chemotherapy (**Chapter 2, Fig. 5A & 7A)**. We expect that the likely mechanism that leads to apoptosis is regulated through central B cell tolerance (*39*). Further, patient samples that were shown have different diffusion patterns of the pre-BCR (**Chapter 2, Fig. 6C**) were more or less susceptible to killing. Blasts that showed a significant disruption of pre-BCR mobility upon treatment with the anti-VpreB Fab (**Chapter 2, Fig. 6E**) were more readily killed with lower doses of chemotherapy (**Chapter 2, Fig 7A**). Although these observations suggest potential biomarkers for classifying risk on leukemia, it is difficult to imagine that our methods could be implemented in a clinical setting. The weak induction of killing of the anti-VpreB Fab as a monoreagent had us speculate as to whether targeting the λ5-UR (*1*) with immunotherapy might display more robust and durable responses in leukemic B cells.

Small Molecule Inhibition Alters pre-BCR Dynamics and Survival

Evidence for pre-BCR+ signaling through tyrosine kinase and PI3 kinase pathways suggest that subclasses of BCP-ALL patients may benefit from targeted therapy, including cell-permeable small molecule inhibitors (*40-42*). First, treatment of 697 cells for 10-15 minutes with Lyn (dasatinib) and Syk (BAY61-3606) caused a significant increase in pre-BCR diffusion (**Chapter 2, Fig 6D**). Due to the fact that treatment disrupted ITAM and Syk phosphorylation (**Chapter 2, Fig. 4D**, we speculate that this increased diffusion is an effect caused by a lower density of docking partners localized at the cell membrane, which

might remove the population of slower diffusing pre-BCR particles. It has been suggested that the docking of LAT to TCR clusters increases the number of interactions among TCR-associated kinases and an extensive LAT cytoplasmic domain, which may be important for the compartmentalization of signaling (*43*). Extended treatment for 24 hours with these Lyn and Syk inhibitors led to a significant reduction in BCL6 expression (**Chapter 2, Fig. 4F**) that correlated with a strong induction of cell death as monoreagants (**Chapter 2, Fig 5B)** or in conjunction with low-dose chemotherapy (**Chapter 2, Fig. 5C**). Just as precursor B cells are eliminated if they lack autonomous pre-BCR signals (*44*), leukemic B cells are also rejected if these critical signals are not received.

Small Molecule Hyperactivation Alters pre-BCR Dynamics and Survival

Most efforts to improve treatment options in leukemia are directed at development of potent tyrosine kinase inhibitors aimed at keeping oncogenic signaling to a bare minimum (*45*). At a first glance, this concept is pretty straightforward and appealing based upon targeted suppression of pathways (i.e. Ras, Myc, $BRAF^{V600E}$) that drive rapid cell proliferation (*46*, *47*). However, the situation is more complex since negative feedback molecules can operate to keep the system in check (*48*). Leukemic B cells may be addicted to negative regulation (*49*), which apparently counterbalances hyperactive pathways to maintain a finely-tuned signaling threshold for survival. Further, leukemic B cells retain many features that are characteristic of healthy lymphoid progenitors and are subject to the controls that regulate central B cell tolerance. A series of important papers revealed that hyperactivation of Erk (*49*) or Syk (*50*) pathways in pre-B leukemia cells offers a new therapeutic strategy to combat acute leukemias. While most of these studies showed that hyperactivation of select pathways lead to high rates of killing, these findings were only conducted in Ph+ leukemias that have been classified as pre-BCR(-) (*38*). We recently corroborated this finding (*9*) and showed that hyperactivation also rapidly killed pre-BCR+ leukemias (**Chapter 2, Fig. 5B,D**). One of the intriguing findings in this dissertation is that modulation of the pre-BCR signal upward or downward in pre-BCR+ leukemia always led to the downregulation of BCL6 expression. For instance, upon incubation of potent SHIP-1 inhibitor (3AC) (*51*), we noted hyperactivation of Syk (**Chapter 2, Fig4E)** and

significant downregulation of BCL6 (**Chapter 2, Fig. 4F**). This reduced BCL6 expression was also shown with the introduction of exogenous galectin-1 (see above) whereby proximal pre-BCR signals could be modulated up or down based upon the presence or absence of lactose, respectively. Nonetheless, the downregulation of BCL6 with 3AC treatment corresponding in a potent induction of apoptosis to a much greater extent than seen with Syk-specific and SFK-specific inhibitors (**Chapter 2, Fig. 5A**).

Other Important Therapeutic Options in Leukemia

Biologic agents, such as therapeutic antibodies, are also options for targeted treatment in BCP-ALL. These leukemic blasts have been shown to express a list of membrane antigens on the surface with therapeutic potential (*52*). An idealistic target would be expressed in all leukemic cells, exhibit little/no expression on healthy populations and should remain stable (except those that internalize rapidly - see below) upon challenge with directed therapy (*53*). Unfortunately, all of the targets currently proposed for use in BCP-ALL treatment have a wide expression profile in both healthy and malignant cells (*54*). Monoclonal antibody treatment toward these targets come in three predominant forms: 1) naked antibodies, 2) T-cell engaging bispecific single-chain (BiTE®) antibodies, and 3) toxin conjugated (*54*). Naked antibodies rely on their opsinizing capacity whereby the Fc-region of the IgG can recruit effector cells of the immune responses to trigger cell-mediated phagocytosis (ADCP) and/or cytotoxicity (ADCC) (*55*, *56*) or complement-dependent killing (*54*). If the target of interest is known to internalize quickly, antibodies can be used as delivery vehicles for toxic payloads (*57*). Each of these antibody forms have been or are currently being tested in human trials, including B cell cancers such as Burkitt lymphoma and Ph+/Ph- BCP-ALL (*53*). The most common targets studied for monoclonal antibody use in BCP-ALL include CD19 (*58*), CD20 (*59*), CD22 (*52*), and CD52 (*60*). Therapeutic antibodies directed at common B cell antigens have exhibited clinical responses in BCP-ALL (*61-63*) but rarely lead to durable responses or cures. Rituximab, an anti-CD20 antibody that induces killing by ADCC/ADCP or complement-activating pathways (*64*), has been recently used to treat CD20+ BCP-ALL (*61, 62*). Rituximab was well tolerated (*61*) with improved 5-year survival rates relative to standard induction and consolidated

chemotherapy (*62*). Several therapy options have been used for CD19, with a bispecific T-cell engaging antibody, blinatumomab (*63*) showing promise in the clinic. This includes a recent trial involving patients with active systemic ALL relapse (*65, 66*). The overall response rate in this study approached 70% with median survival at 9.8 months for these patients. Moxetumomab is an anti-CD22 immunotoxin that consists of a fragment variable derived from the antibody fused to a 38-kDa fragment of *Pseudomona aeruginosa* exotoxin A (*67*). In recent refractory ALL Phase I trial (*68*). Of the 17 patients that could be evaluated, 24% achieved complete remission, 6% showed partial response and 47% exhibited hematologic improvement. While most of these monoclonal antibody treatments are being used for ALL salvage, it has been suggested that incorporation of these therapies as frontline options may improve overall efficacy (*54*).

Rationalization of anti-VpreB CAR T cell Therapy for BCP-ALL

Above, we discussed the limitations of monovalent Fab's directed at the pre-BCR dimer interface, which weakly sensitized leukemic B cells to killing. Further we showed, that while targeted therapy options through tyrosine kinase inhibitors and monoclonal antibodies are good options, alternative approaches are necessary to more readily wipe out the malignancy. An even more promising strategy is the use of CAR T cell therapy to target BCP-ALL where many of the antigenic targets explored for monoclonal antibody treatment are being tested (*69, 70*). Several different institutions are testing CD19-specific CAR Ts in clinical trials [review (*71*)]. Results from these studies have been promising with complete response (CR) rates from 70 to 91%, even in the relapsed or refractory B-ALL setting (*69*). For instance, in the first published clinical trials (*72*) at Memorial Sloan Kettering Cancer Center in New York, of the 32 patients receiving CAR T cell therapy, all achieved minimum residual disease (MRD)-negative complete remission (*73*). In a recent follow-up study the complete responses achieved 91% (*74*). Other malignancies apart from BCP-ALL for CAR T therapy are being tested. These include CLL, multiple myeloma, Hodgkin's lymphoma, non-Hodgkin's lymphoma, myeloid malignancies, and solid tumors. For an extensive review of current targets that extend beyond BCP-ALL see (*69*).

Though clinical data reveal the promising potential of CAR T cell therapy, especially in the refractory/relapse BCP-ALL setting, there are still some inherent treatment concerns. Similar to monoclonal antibody drugs, B cell specific CAR Ts target the same receptors that are expressed (CD19, CD22, CD20) throughout the different developmental stages. Thus, recent studies continue to report 'on-target, off-tumor' destruction of non-malignant B cell leading to B cell aplasia (*73, 75-78*). However, B cell aplasia is not the only toxicity associated with CAR T therapy. Other reports have described the onset of cytokine release syndrome (CRS), acute anaphylaxis (*77*), cross-reaction to normal tissues (*79, 80*) and neurological disorders (*74*). CRS is a byproduct of rapid and enhanced activation of the transferred CAR T cells that results in a general disruption of the immune system including release of proinflammatory cytokines such as TNF-alpha and IL-6 (*70, 78*). Incorporation of IL-6 blockade with tocilizumab has been suggested to minimize effects caused by "cytokine storms" (*81*). These factors are important to consider as groups continue to advance the design of CAR T's that can minimize these effects (*82*) or by being used in conjunction with other therapeutic strategies (*83*).

CAR T Design: Minimizing Off-Target Effects

Another hindrance to CAR T cell therapy in clinical trials involving BCP-ALL is antigenic escape (*71, 84, 85*). One particular mechanism of escape is through the loss of CD19 expression (*86*). Current strategies to overcome this limitation include the generation of CAR+ T cells that can recognize multiple antigens (*87, 88*). However, the purported targets for these multivalent CAR Ts include the CD20 (*89*) and CD22 (*90*), which would ablate the B cell immune response. The non-polymorphic and high sequence similarity of splice variants in VpreB may minimize the frequency of antigenic escape as has been observed with anti-CD19 CAR T therapies (*86*). The unique regions found within λ5 and VpreB (*91*) do not exhibit sequence similarity within the proteome and should limit off-target effects. It is also important to consider the importance of the this target to the survival of pre-BCR+ leukemias as we have shown previously (*9*). Similar to BCMA in plasma cell malignancies (*92, 93*) and ROR1 in both ALL and CLL (*94, 95*), the pre-BCR is important to survival of the leukemia blasts. This would entail that downregulation of the pre-BCR

(a common escape mechanism when targeting CD19) would mitigate the survival capacity of the blasts and minimize potential pathways of resistance. Unlike ROR1, with evidence to suggest expression on pancreatic and lung tissue (*96, 97*) the pre-BCR specificity to B cells should also minimize 'on-target, off-tumor' toxicity. While we would expect our anti-VpreB CAR T to continue to target both healthy and leukemic precursor B cells alike, we expect that this approach should sustain a higher proportion of mature B cells. Lastly, other proposed mechanisms of escape are associated with the loss of efficacy of the CAR T either through tumor-mediated immunosuppression (*98*) or chronic T cell activation leading to induction of inhibitory ligands, called T cell exhaustion (*99*). These detrimental factors may be alleviated through an understanding of CAR T signaling profiles and structural constructions of the CAR itself.

CAR T Design: Threshold Considerations

CAR T cells, like T cells (*100*), must be optimally tuned for killing efficiency and long-term persistence (*101*). Several factors are important in modulating the CAR T cell signaling threshold that includes epitope location (*102*), scFv affinity (*103*), target density (*104*), and length of the spacer region (*103, 105, 106*). It has recently been shown that an improved binding affinity does not always correlate with CAR T efficacy (*103, 107-109*). A study involving a CAR against ROR1 in mantle cell lymphoma revealed improved efficacy correlated with enhanced binding affinity (*103*). In contrast, several other studies show that there was an avidity threshold for CARs whereby an improved binding constant did not boost the CAR T's therapeutic efficacy (*107-109*) and in some cases may even be augment long-term survival (*101*). By tuning the affinity of a CAR, some groups showed that CAR T's could be made to discriminate between tumor cells and normal cells that express lower or normal levels of the same antigen (*110, 111*). We have shown that expression levels of the anti-VpreB CAR on the surface of effector T cells and/or relative expression of the receptor on BCP-ALL impact the killing efficiency (**Chapter 4, Fig 5D**). Quantitation of CAR numbers on surface of the T cells showed a broad distribution of receptors (**Chapter 4, Fig 5A)** from few thousand to over 100,000. Understanding the receptor density and affinity on CAR Ts may be an important consideration in order to

optimize signaling thresholds that will maximize both T cell persistence and killing capacity. In a recent study, an anti-CD20 CAR T showed that only about 200 CD20 molecules were required to induce killing; however, a 10-fold higher expression was necessary for select cytokine production (*104*). It may be important to utilize the large library of data describing TCR signaling thresholds. For instance, studies have revealed that co-stimulatory receptors can lower the threshold for TCRs and inclusion of the stimulatory CD28 domains into the TCR signaling complex lowered the total number of TCR-pMHC interactions required to trigger activation (*112*). This information has been used to enhance CAR T activity whereby most CAR designs include co-stimulatory domains (i.e. CD28, 4-1BB) (*102, 113, 114*). In fact, it has been shown by *Long et al* that addition of different co-stimulatory domains can augment or ameliorate T cell exhaustion (*113*).

CAR T Design: Using Computational Modeling to Aid in CAR T Engineering

In Chapter 4, we described the first steps in developing an alternative chimeric antigen receptor (CAR) therapy for pre-BCR+ cases of BCP-ALL. This chapter outlined our stepwise strategy to create and test scFv derived from an intact anti-VpreB IgG. When expressed outside their typical context, recombinant antibody-based fragments can display disappointing physicochemical and structural issues (*115*). Many reports have shown the susceptibility of Ig domains to lose binding specificity or to be unstable due to structural alterations such unfolding or aggregation (*115*). Loss of stability for small, recombinant antibody fragments (i.e scFv versus Fabs) can be an additive effect. This may be due to the loss of complementation or disulfide bonds along the quaternary structure (*116*). To overcome a potential loss in structural integrity, scFv's are typically designed to incorporate a flexible peptide linker that is resistant to endopeptidases (*117, 118*). Even with a flexible linker, scFv still have a tendency to unfold and a phenomenon called "domain swapping" may occur. This effect, usually due to the length of the peptide linker, results in the interaction of Ig domains of adjacent scFv causing them to oligomerize (*119*). Further, another source of instability for the scFv are associated with the CDR loops (*120*). To optimize our scFv design, we employed advances in antibody modeling tools (*121*) to

construct several different 3D models. We then evaluated these structures using MD simulations. Our homology models showed that the VL-linker-VH versus VH-linker-VL orientation exhibited different intermolecular distances (**Chapter4, Fig. 1A**). Different framework regions at the N- and C-terminal ends showed characteristic differences in the root-mean-square deviations (**Chapter4, Fig. 1B**). These data suggest that upon attachment of the inter-framework linker the VH-linker-VL orientation would minimize both the intermolecular distance and residual fluctuations. This would help to minimize allosteric impacts at the CDR region (**Chapter 4, Fig. 1A-B**). Our MD simulations revealed that there was less of an impact at the CDR binding region with the VH-linker-VL orientation and 20mer linker model (**Chapter 4, Fig. 1D-E)**. This information was then applied to in engineering phase of our anti-VpreB Fab (**Chapter 4, Fig. 2**). We showed that the soluble form of our 20mer scFv in the HC-linker-LC orientation retained specificity and high affinity for the surrogate light chain on live leukemic B cells (**Chapter 4, Fig. 2-3**). This construct was then incorporated into a lentiviral vector, expressed on surface of CD8+ T cells (**Chapter 4, Fig. 5C**) and displayed T cell activation markers (**Chapter 4, Fig. 4C,E**). Importantly, these CAR Ts displayed *in vitro* cytotoxicity (**Chapter 4, Fig. 5D**) and synapse formation (**Chapter 4, Fig. 5F**) to BCP-ALL cell lines. With the generation of a CAR T with *in vitro* efficacy, we could now turn to other important studies to further characterize the anti-VpreB CAR T and its interaction with the novel BCP-ALL target.

We employed protein/protein docking algorithms (*122, 123*) and molecular dynamics simulations (*124*) to map out probable binding domains within the VpreB region (**Chapter 4, Fig 6A-G**). Computational approaches have been used to make *in silico* modifications to the CDR region to engineer antibodies (*125*). These alterations can be incorporated into the CAR's scFv binding region in order to modify binding to oncogenic mutations that may occur within the target and/or modulate the affinity threshold that would corresponds most optimally with efficacy. Information about the binding site can also serve as the theoretical framework to determine how intermembrane spacing, epitope proximity to membrane, multivalency, interaction to different extracellular receptors, or synaptic exclusion may influence CAR T signaling efficiency (*76, 126*). We can also use electron or confocal

microscopy experiments to assess, synaptic size, recruitment of granzyme B, and synaptic exclusion of negative regulatory receptors (PD-1, TIM-3, CD45). We showed that the synapse formed between the anti-VpreB CAR T and BCP-ALL cell lines (**Chapter 4, Fig 5F**) results in polarization and accumulation of granzyme B at the contact zone (**Chapter 4, Fig 5F**). Data presented in (48) suggested that when anti-CD19 CARs engaged their cognate receptor on Raji B-cells they exhibited a convoluted membrane that differed markedly from the more "natural" TCR-pMHC synapse. We plan to assess whether anti-VpreB CARTs exhibit a more optimal synapse formation due to the multivalent features of the pre-BCR and its ability to form "development synapses" with other cells (*24*) Further, it is known that accumulation of granules at the polarization zone derives from elevated levels of Ca^{2+} levels (*127*). Through the use of ratiometric imaging we can quantitatively measure differences of CAR T signaling to determine if anti-VpeB CARTs display any signaling advantage relative to existing anti-CD19 CAR Ts. It is apparent that a case-by-case testing will be required to optimize CAR T design.

The infusion of specific CAR T cell subsets at defined ratios may be important for enhanced *in vivo* potency against tumors (*128, 129*). Due to the high uptake of our CAR T into non-CD8+ (**Chapter 4, Figure 4B**) populations, we opted to enrich for CD8+ populations from PBMC populations to improve transduction efficiency of this particular subset. We noted a significant improvement in the CD8+ transduction efficiency (**Chapter 4, Fig. 4E**), with high rates of *in vitro* efficacy (**Chapter 4, Fig. 5D**). However, early *in vivo* testing in a BCP-ALL xenograft model exhibited a marked reduction of effector T cells in the blood after 28 days (**data not shown**). We suspect this may be due in part to lower proliferative capacity of CD8+ *in vivo* without signals received from PBMCs or T_H (CD4+) populations. Studies revealed that infusion of CD4+ and CD8+ T CAR+ T cell at 1:1 ratio exhibited a remarkable improvement in tumor reduction and long-term persistence in the blood (*128, 129*) Thus, it might be important to selectively transduce both CD4+ and CD8+ T cells with our CAR construct. We can then combine these two populations and inject into the mice to compare how this combination fares relative to each population on their own.

CONCLUDING REMARKS

This dissertation set to improve our understanding of pre-BCR dynamics and their corresponding signaling outcomes in the context of leukemia. As specific therapies continue to be incorporated into BCP-ALL it is essential to understanding the complexities of the pre-BCR signaling network. Our data revealed that similar to healthy B cell populations, the pre-BCR continues to be a highly regulated process even in the context of leukemia. Thus, as *Mucshen* and colleagues have suggested through a series of important papers, hyperactivation or inhibition of the pre-BCR signaling network may confer novel therapeutic benefits. While the pre-BCR+ leukemia subset represents a smaller population of BCP-ALL patients (10-15%)(*38*), evidence suggests that tyrosine kinase inhibition of the JAK/STAT pathway led to the upregulation of the feedforward pre-BCR pathway regulator, BCL6 (*130*). It is worth considering how long-term treatment of the IL7R/JAK/STAT pathway may influence expression profiles in BCP-ALL cases that are initially diagnosed as pre-BCR(-). This factor may substantiate the need to target the pre-BCR pathway even in these pre-BCR(-) leukemic populations to reduce potential of all possible escape routes.

REFERENCES

CHAPTER 1: INTRODUCTION

1. N. J. Winick, W. L. Carroll, S. P. Hunger, Childhood leukemia--new advances and challenges. *The New England journal of medicine* **351**, 601-603 (2004).
2. D. Douer, Adult acute lymphoblastic leukemia: a cancer with no standard of care. *Acta Haematol* **130**, 196-198 (2013).
3. P. S. Gaynon *et al.*, Long-term results of the children's cancer group studies for childhood acute lymphoblastic leukemia 1983-2002: a Children's Oncology Group Report. *Leukemia* **24**, 285-297 (2010).
4. S. Asner, R. A. Ammann, H. Ozsahin, M. Beck-Popovic, N. X. von der Weid, Obesity in long-term survivors of childhood acute lymphoblastic leukemia. *Pediatric blood & cancer* **51**, 118-122 (2008).
5. S. S. Winter, Pediatric acute leukemia therapies informed by molecular analysis of high-risk disease. *Hematology Am Soc Hematol Educ Program* **2011**, 366-373 (2011).
6. F. Babor *et al.*, Invasive aspergillosis in pediatric oncology patients: a rare event with poor prognosis--case analysis to plan better targeted prophylactic or therapeutic measurement. *Klin Padiatr* **224**, 160-165 (2012).
7. B. Lund *et al.*, Risk factors for treatment related mortality in childhood acute lymphoblastic leukaemia. *Pediatric blood & cancer* **56**, 551-559 (2011).
8. J. A. Irving *et al.*, Integration of genetic and clinical risk factors improves prognostication in relapsed childhood B-cell precursor acute lymphoblastic leukemia. *Blood* **128**, 911-922 (2016).
9. H. Geng *et al.*, Self-enforcing feedback activation between BCL6 and pre-B cell receptor signaling defines a distinct subtype of acute lymphoblastic leukemia. *Cancer cell* **27**, 409-425 (2015).
10. E. Lengline *et al.*, Successful tyrosine kinase inhibitor therapy in a refractory B-cell precursor acute lymphoblastic leukemia with EBF1-PDGFRB fusion. *Haematologica* **98**, e146-148 (2013).

11. J. S. Woo, M. O. Alberti, C. A. Tirado, Childhood B-acute lymphoblastic leukemia: a genetic update. *Exp Hematol Oncol* **3**, 16 (2014).
12. J. M. Ribera, A. Ferrer, J. Ribera, E. Genesca, Profile of blinatumomab and its potential in the treatment of relapsed/refractory acute lymphoblastic leukemia. *Onco Targets Ther* **8**, 1567-1574 (2015).
13. E. Maino *et al.*, Modern immunotherapy of adult B-lineage acute lymphoblastic leukemia with monoclonal antibodies and chimeric antigen receptor modified T cells. *Mediterr J Hematol Infect Dis* **7**, e2015001 (2015).
14. D. W. Lee *et al.*, T cells expressing CD19 chimeric antigen receptors for acute lymphoblastic leukaemia in children and young adults: a phase 1 dose-escalation trial. *Lancet* **385**, 517-528 (2015).
15. R. J. Brentjens *et al.*, CD19-targeted T cells rapidly induce molecular remissions in adults with chemotherapy-refractory acute lymphoblastic leukemia. *Sci Transl Med* **5**, 177ra138 (2013).
16. M. Zhang, G. Srivastava, L. Lu, The pre-B cell receptor and its function during B cell development. *Cell Mol Immunol* **1**, 89-94 (2004).
17. M. R. Clark, M. Mandal, K. Ochiai, H. Singh, Orchestrating B cell lymphopoiesis through interplay of IL-7 receptor and pre-B cell receptor signalling. *Nature reviews. Immunology* **14**, 69-80 (2014).
18. F. Melchers, Checkpoints that control B cell development. *The Journal of clinical investigation* **125**, 2203-2210 (2015).
19. T. Tsubata, M. Reth, The products of pre-B cell-specific genes (lambda 5 and VpreB) and the immunoglobulin mu chain form a complex that is transported onto the cell surface. *The Journal of experimental medicine* **172**, 973-976 (1990).
20. M. F. Erasmus *et al.*, Dynamic pre-BCR homodimers fine-tune autonomous survival signals in B cell precursor acute lymphoblastic leukemia. *Sci Signal* **9**, ra116 (2016).
21. K. Ohnishi, F. Melchers, The nonimmunoglobulin portion of lambda5 mediates cell-autonomous pre-B cell receptor signaling. *Nat Immunol* **4**, 849-856 (2003).
22. J. G. Monroe, ITAM-mediated tonic signalling through pre-BCR and BCR complexes. *Nat Rev Immunol* **6**, 283-294 (2006).

23. I. L. Martensson, N. Almqvist, O. Grimsholm, A. I. Bernardi, The pre-B cell receptor checkpoint. *FEBS Lett* **584**, 2572-2579 (2010).
24. R. Nahar *et al.*, Pre-B cell receptor-mediated activation of BCL6 induces pre-B cell quiescence through transcriptional repression of MYC. *Blood* **118**, 4174-4178 (2011).
25. M. Mandal *et al.*, Ras orchestrates exit from the cell cycle and light-chain recombination during early B cell development. *Nat Immunol* **10**, 1110-1117 (2009).
26. R. Stadhouders *et al.*, Pre-B cell receptor signaling induces immunoglobulin kappa locus accessibility by functional redistribution of enhancer-mediated chromatin interactions. *PLoS Biol* **12**, e1001791 (2014).
27. W. Schuh, S. Meister, K. Herrmann, H. Bradl, H. M. Jack, Transcriptome analysis in primary B lymphoid precursors following induction of the pre-B cell receptor. *Mol Immunol* **45**, 362-375 (2008).
28. K. Anbazhagan *et al.*, Human pre-B cell receptor signal transduction: evidence for distinct roles of PI3kinase and MAP-kinase signalling pathways. *Immun Inflamm Dis* **1**, 26-36 (2013).
29. N. Almqvist, I. L. Martensson, The pre-B cell receptor; selecting for or against autoreactivity. *Scand J Immunol* **76**, 256-262 (2012).
30. M. Zouali, Transcriptional and metabolic pre-B cell receptor-mediated checkpoints: implications for autoimmune diseases. *Mol Immunol* **62**, 315-320 (2014).
31. O. Grimsholm *et al.*, Absence of surrogate light chain results in spontaneous autoreactive germinal centres expanding V(H)81X-expressing B cells. *Nat Commun* **6**, 7077 (2015).
32. D. G. Osmond, Proliferation kinetics and the lifespan of B cells in central and peripheral lymphoid organs. *Curr Opin Immunol* **3**, 179-185 (1991).
33. N. Sakaguchi, F. Melchers, Lambda 5, a new light-chain-related locus selectively expressed in pre-B lymphocytes. *Nature* **324**, 579-582 (1986).

34. R. Kersseboom *et al.*, Bruton's tyrosine kinase cooperates with the B cell linker protein SLP-65 as a tumor suppressor in Pre-B cells. *The Journal of experimental medicine* **198**, 91-98 (2003).
35. B. H. Ye *et al.*, Alterations of a zinc finger-encoding gene, BCL-6, in diffuse large-cell lymphoma. *Science (New York, N.Y.)* **262**, 747-750 (1993).
36. C. Duy *et al.*, BCL6 enables Ph+ acute lymphoblastic leukaemia cells to survive BCR-ABL1 kinase inhibition. *Nature* **473**, 384-388 (2011).
37. Z. Chen *et al.*, Signalling thresholds and negative B-cell selection in acute lymphoblastic leukaemia. *Nature* **521**, 357-361 (2015).
38. S. Shojaee *et al.*, Erk Negative Feedback Control Enables Pre-B Cell Transformation and Represents a Therapeutic Target in Acute Lymphoblastic Leukemia. *Cancer cell* **28**, 114-128 (2015).
39. R. C. Rickert, New insights into pre-BCR and BCR signalling with relevance to B cell malignancies. *Nature reviews. Immunology* **13**, 578-591 (2013).
40. J. E. Cortes *et al.*, Ponatinib in refractory Philadelphia chromosome-positive leukemias. *The New England journal of medicine* **367**, 2075-2088 (2012).
41. A. J. Bankovich *et al.*, Structural insight into pre-B cell receptor function. *Science* **316**, 291-294 (2007).
42. R. Ubelhart *et al.*, N-linked glycosylation selectively regulates autonomous precursor BCR function. *Nat Immunol* **11**, 759-765 (2010).
43. L. Gauthier, B. Rossi, F. Roux, E. Termine, C. Schiff, Galectin-1 is a stromal cell ligand of the pre-B cell receptor (BCR) implicated in synapse formation between pre-B and stromal cells and in pre-BCR triggering. *Proceedings of the National Academy of Sciences of the United States of America* **99**, 13014-13019 (2002).
44. J. Lippincott-Schwartz, N. Altan-Bonnet, G. H. Patterson, Photobleaching and photoactivation: following protein dynamics in living cells. *Nature cell biology* **Suppl**, S7-14 (2003).
45. E. A. Reits, J. J. Neefjes, From fixed to FRAP: measuring protein mobility and activity in living cells. *Nature cell biology* **3**, E145-147 (2001).
46. K. Bacia, S. A. Kim, P. Schwille, Fluorescence cross-correlation spectroscopy in living cells. *Nature methods* **3**, 83-89 (2006).

47. E. Haustein, P. Schwille, Fluorescence correlation spectroscopy: novel variations of an established technique. *Annual review of biophysics and biomolecular structure* **36**, 151-169 (2007).
48. C. Manzo, M. F. Garcia-Parajo, A review of progress in single particle tracking: from methods to biophysical insights. *Rep Prog Phys* **78**, 124601 (2015).
49. M. J. Saxton, K. Jacobson, Single-particle tracking: applications to membrane dynamics. *Annu Rev Biophys Biomol Struct* **26**, 373-399 (1997).
50. H. Geerts *et al.*, Nanovid tracking: a new automatic method for the study of mobility in living cells based on colloidal gold and video microscopy. *Biophysical journal* **52**, 775-782 (1987).
51. M. De Brabander, R. Nuydens, H. Geerts, C. R. Hopkins, Dynamic behavior of the transferrin receptor followed in living epidermoid carcinoma (A431) cells with nanovid microscopy. *Cell Motil Cytoskeleton* **9**, 30-47 (1988).
52. T. Fujiwara, K. Ritchie, H. Murakoshi, K. Jacobson, A. Kusumi, Phospholipids undergo hop diffusion in compartmentalized cell membrane. *The Journal of cell biology* **157**, 1071-1081 (2002).
53. M. P. Clausen, B. C. Lagerholm, The probe rules in single particle tracking. *Curr Protein Pept Sci* **12**, 699-713 (2011).
54. A. Kusumi *et al.*, Paradigm shift of the plasma membrane concept from the two-dimensional continuum fluid to the partitioned fluid: high-speed single-molecule tracking of membrane molecules. *Annual review of biophysics and biomolecular structure* **34**, 351-378 (2005).
55. E. Betzig, R. J. Chichester, Single molecules observed by near-field scanning optical microscopy. *Science (New York, N.Y.)* **262**, 1422-1425 (1993).
56. T. Schmidt, G. J. Schutz, W. Baumgartner, H. J. Gruber, H. Schindler, Imaging of single molecule diffusion. *Proceedings of the National Academy of Sciences of the United States of America* **93**, 2926-2929 (1996).
57. Y. Sako, S. Minoghchi, T. Yanagida, Single-molecule imaging of EGFR signalling on the surface of living cells. *Nat Cell Biol* **2**, 168-172 (2000).

58. G. T. Dempsey, J. C. Vaughan, K. H. Chen, M. Bates, X. Zhuang, Evaluation of fluorophores for optimal performance in localization-based super-resolution imaging. *Nature methods* **8**, 1027-1036 (2011).

59. M. Bruchez, Jr., M. Moronne, P. Gin, S. Weiss, A. P. Alivisatos, Semiconductor nanocrystals as fluorescent biological labels. *Science (New York, N.Y.)* **281**, 2013-2016 (1998).

60. W. C. Chan, S. Nie, Quantum dot bioconjugates for ultrasensitive nonisotopic detection. *Science (New York, N.Y.)* **281**, 2016-2018 (1998).

61. T. Q. Vu, W. Y. Lam, E. W. Hatch, D. S. Lidke, Quantum dots for quantitative imaging: from single molecules to tissue. *Cell Tissue Res* **360**, 71-86 (2015).

62. S. T. Low-Nam *et al.*, ErbB1 dimerization is promoted by domain co-confinement and stabilized by ligand binding. *Nat Struct Mol Biol* **18**, 1244-1249 (2011).

63. M. P. Steinkamp *et al.*, ErbB3 is an active tyrosine kinase capable of homo- and hetero-interactions. *Mol Cell Biol*, (2013).

64. F. Pinaud, S. Clarke, A. Sittner, M. Dahan, Probing cellular events, one quantum dot at a time. *Nature methods* **7**, 275-285 (2010).

65. M. Howarth *et al.*, Monovalent, reduced-size quantum dots for imaging receptors on living cells. *Nature methods* **5**, 397-399 (2008).

66. M. Kuno, Fromm, D.P., Hamann, H.F., Gallagher, A. and Nesbitt D.J., Nonexponential "blinking" kinetics of single CdSe quantum dots: A universal power law behavior. *The Journal of Chemical Physics* **112**, 3117 (2000).

67. G. Margolin, V. Protasenko, M. Kuno, E. Barkai, Photon counting statistics for blinking CdSe-ZnS quantum dots: a Levy walk process. *J Phys Chem B* **110**, 19053-19060 (2006).

68. B. Mahler *et al.*, Towards non-blinking colloidal quantum dots. *Nat Mater* **7**, 659-664 (2008).

69. A. Serge, N. Bertaux, H. Rigneault, D. Marguet, Dynamic multiple-target tracing to probe spatiotemporal cartography of cell membranes. *Nature methods* **5**, 687-694 (2008).

70. P. J. Cutler *et al.*, Multi-color quantum dot tracking using a high-speed hyperspectral line-scanning microscope. *PLoS One* **8**, e64320 (2013).

71. D. Alcor, G. Gouzer, A. Triller, Single-particle tracking methods for the study of membrane receptors dynamics. *Eur J Neurosci* **30**, 987-997 (2009).

72. A. Kusumi, T. A. Tsunoyama, K. M. Hirosawa, R. S. Kasai, T. K. Fujiwara, Tracking single molecules at work in living cells. *Nature chemical biology* **10**, 524-532 (2014).

73. J. Torreno-Pina, Manzo, C and Garcia-Parajo, MF, Uncovering homo-and hetero-interactions on the cell membrane using single particle tracking approaches. *J. Phys. D: Appl. Phys.* **49**, pp12 (2016).

74. M. J. Saxton, Single-particle tracking: connecting the dots. *Nat Methods* **5**, 671-672 (2008).

75. H. Deschout *et al.*, Precisely and accurately localizing single emitters in fluorescence microscopy. *Nat Methods* **11**, 253-266 (2014).

76. W. J. Godinez *et al.*, Deterministic and probabilistic approaches for tracking virus particles in time-lapse fluorescence microscopy image sequences. *Med Image Anal* **13**, 325-342 (2009).

77. N. L. Andrews *et al.*, Actin restricts FcepsilonRI diffusion and facilitates antigen-induced receptor immobilization. *Nature cell biology* **10**, 955-963 (2008).

78. N. L. Andrews *et al.*, Small, mobile FcepsilonRI receptor aggregates are signaling competent. *Immunity* **31**, 469-479 (2009).

79. L. D. Frye, M. Edidin, The rapid intermixing of cell surface antigens after formation of mouse-human heterokaryons. *J Cell Sci* **7**, 319-335 (1970).

80. M. F. Garcia-Parajo, A. Cambi, J. A. Torreno-Pina, N. Thompson, K. Jacobson, Nanoclustering as a dominant feature of plasma membrane organization. *J Cell Sci* **127**, 4995-5005 (2014).

81. M. Cebecauer, M. Spitaler, A. Serge, A. I. Magee, Signalling complexes and clusters: functional advantages and methodological hurdles. *J Cell Sci* **123**, 309-320 (2010).

82. A. S. Harding, J. F. Hancock, Using plasma membrane nanoclusters to build better signaling circuits. *Trends Cell Biol* **18**, 364-371 (2008).

83. T. Tian *et al.*, Plasma membrane nanoswitches generate high-fidelity Ras signal transduction. *Nat Cell Biol* **9**, 905-914 (2007).

84. J. A. Torreno-Pina *et al.*, Enhanced receptor-clathrin interactions induced by N-glycan-mediated membrane micropatterning. *Proceedings of the National Academy of Sciences of the United States of America* **111**, 11037-11042 (2014).

85. D. S. Lidke, K. A. Lidke, B. Rieger, T. M. Jovin, D. J. Arndt-Jovin, Reaching out for signals: filopodia sense EGF and respond by directed retrograde transport of activated receptors. *J Cell Biol* **170**, 619-626 (2005).

86. V. Roullier *et al.*, High-affinity labeling and tracking of individual histidine-tagged proteins in live cells using Ni2+ tris-nitrilotriacetic acid quantum dot conjugates. *Nano letters* **9**, 1228-1234 (2009).

87. I. Camby, M. Le Mercier, F. Lefranc, R. Kiss, Galectin-1: a small protein with major functions. *Glycobiology* **16**, 137R-157R (2006).

88. D. Gupta, M. Cho, R. D. Cummings, C. F. Brewer, Thermodynamics of carbohydrate binding to galectin-1 from Chinese hamster ovary cells and two mutants. A comparison with four galactose-specific plant lectins. *Biochemistry* **35**, 15236-15243 (1996).

89. M. Cho, R. D. Cummings, Galectin-1, a beta-galactoside-binding lectin in Chinese hamster ovary cells. I. Physical and chemical characterization. *The Journal of biological chemistry* **270**, 5198-5206 (1995).

90. M. C. Miller, I. V. Nesmelova, D. Platt, A. Klyosov, K. H. Mayo, The carbohydrate-binding domain on galectin-1 is more extensive for a complex glycan than for simple saccharides: implications for galectin-glycan interactions at the cell surface. *Biochem J* **421**, 211-221 (2009).

91. G. A. Rabinovich, N. Rubinstein, M. A. Toscano, Role of galectins in inflammatory and immunomodulatory processes. *Biochimica et biophysica acta* **1572**, 274-284 (2002).

92. G. A. Rabinovich *et al.*, Galectins and their ligands: amplifiers, silencers or tuners of the inflammatory response? *Trends Immunol* **23**, 313-320 (2002).

93. H. Leffler, S. Carlsson, M. Hedlund, Y. Qian, F. Poirier, Introduction to galectins. *Glycoconj J* **19**, 433-440 (2004).

94. A. Symons, D. N. Cooper, A. N. Barclay, Characterization of the interaction between galectin-1 and lymphocyte glycoproteins CD45 and Thy-1. *Glycobiology* **10**, 559-563 (2000).

95. J. C. Sacchettini, L. G. Baum, C. F. Brewer, Multivalent protein-carbohydrate interactions. A new paradigm for supermolecular assembly and signal transduction. *Biochemistry* **40**, 3009-3015 (2001).

96. L. Elantak *et al.*, Structural basis for galectin-1-dependent pre-B cell receptor (pre-BCR) activation. *J Biol Chem* **287**, 44703-44713 (2012).

97. J. Bonzi *et al.*, Pre-B cell receptor binding to galectin-1 modifies galectin-1/carbohydrate affinity to modulate specific galectin-1/glycan lattice interactions. *Nat Commun* **6**, 6194 (2015).

98. F. Mourcin *et al.*, Galectin-1-expressing stromal cells constitute a specific niche for pre-BII cell development in mouse bone marrow. *Blood* **117**, 6552-6561 (2011).

99. V. Makrynikola, K. F. Bradstock, Adhesion of precursor-B acute lymphoblastic leukaemia cells to bone marrow stromal proteins. *Leukemia* **7**, 86-92 (1993).

100. F. Fei *et al.*, B-cell precursor acute lymphoblastic leukemia and stromal cells communicate through Galectin-3. *Oncotarget* **6**, 11378-11394 (2015).

101. W. Luo *et al.*, Identification of galectin-1 as a novel mediator for chemoresistance in chronic myeloid leukemia cells. *Oncotarget* **7**, 26709-26723 (2016).

102. C. Pena *et al.*, Galectins as therapeutic targets for hematological malignancies: a hopeful sweetness. *Ann Transl Med* **2**, 87 (2014).

103. L. Ingrassia *et al.*, Anti-galectin compounds as potential anti-cancer drugs. *Curr Med Chem* **13**, 3513-3527 (2006).

104. H. Bradl, J. Wittmann, D. Milius, C. Vettermann, H. M. Jack, Interaction of murine precursor B cell receptor with stroma cells is controlled by the unique tail of lambda 5 and stroma cell-associated heparan sulfate. *J Immunol* **171**, 2338-2348 (2003).

105. C. Vettermann *et al.*, A unique role for the lambda5 nonimmunoglobulin tail in early B lymphocyte development. *Journal of immunology* **181**, 3232-3242 (2008).

106. B. Rossi, M. Espeli, C. Schiff, L. Gauthier, Clustering of pre-B cell integrins induces galectin-1-dependent pre-B cell receptor relocalization and activation. *J Immunol* **177**, 796-803 (2006).

107. G. G. Dodson, D. P. Lane, C. S. Verma, Molecular simulations of protein dynamics: new windows on mechanisms in biology. *EMBO Rep* **9**, 144-150 (2008).

108. J. R. Perilla *et al.*, Molecular dynamics simulations of large macromolecular complexes. *Curr Opin Struct Biol* **31**, 64-74 (2015).

109. A. Hospital, J. R. Goni, M. Orozco, J. L. Gelpi, Molecular dynamics simulations: advances and applications. *Adv Appl Bioinform Chem* **8**, 37-47 (2015).

110. G. H. Snyder, R. Rowan, 3rd, S. Karplus, B. D. Sykes, Complete tyrosine assignments in the high field 1H nuclear magnetic resonance spectrum of the bovine pancreatic trypsin inhibitor. *Biochemistry* **14**, 3765-3777 (1975).

111. K. Wuthrich, G. Wagner, NMR investigations of the dynamics of the aromatic amino acid residues in the basic pancreatic trypsin inhibitor. *FEBS Lett* **50**, 265-268 (1975).

112. J. A. McCammon, B. R. Gelin, M. Karplus, Dynamics of folded proteins. *Nature* **267**, 585-590 (1977).

113. M. Karplus, J. A. McCammon, Molecular dynamics simulations of biomolecules. *Nat Struct Biol* **9**, 646-652 (2002).

114. H. Larsson P, B, Lindahl, E, Algorithm improvements for molecular dynamics simulations. *Wiley INterdisciplinary Reviews: Computational Molecular Science* **1**, (2011).

115. W. F. Van Gunsteren, H. J. Berendsen, R. G. Geurtsen, H. R. Zwinderman, A molecular dynamics computer simulation of an eight-base-pair DNA fragment in aqueous solution: comparison with experimental two-dimensional NMR data. *Ann N Y Acad Sci* **482**, 287-303 (1986).

116. T. Hansson, C. Oostenbrink, W. van Gunsteren, Molecular dynamics simulations. *Curr Opin Struct Biol* **12**, 190-196 (2002).

117. S. a. K. Weiner, PA, An All Atom Force Field for Simulations of Proteins and Nucleic Acids. *Journal of Computational Chemistry* **7**, 230-252 (1986).

118. R. Brooks, Bruccoleri, RE, Olafson, BD, States, DJ, Swaminathan, S., and Karplus, M., CHARMM: A Program for Macromolecular Energy, Minimization, and Dynamics Calculations. *Journal of Computational Chemistry* **4**, (2004).

119. T. A. Soares, X. Daura, C. Oostenbrink, L. J. Smith, W. F. van Gunsteren, Validation of the GROMOS force-field parameter set 45Alpha3 against nuclear magnetic resonance data of hen egg lysozyme. *J Biomol NMR* **30**, 407-422 (2004).

120. W. L. Jorgensen, J. Tirado-Rives, The OPLS [optimized potentials for liquid simulations] potential functions for proteins, energy minimizations for crystals of cyclic peptides and crambin. *J Am Chem Soc* **110**, 1657-1666 (1988).

121. S. Hertig, N. R. Latorraca, R. O. Dror, Revealing Atomic-Level Mechanisms of Protein Allostery with Molecular Dynamics Simulations. *PLoS Comput Biol* **12**, e1004746 (2016).

122. D. Kern, E. R. Zuiderweg, The role of dynamics in allosteric regulation. *Curr Opin Struct Biol* **13**, 748-757 (2003).

123. V. J. Hilser, Biochemistry. An ensemble view of allostery. *Science* **327**, 653-654 (2010).

124. A. Sethi, J. Tian, C. A. Derdeyn, B. Korber, S. Gnanakaran, A mechanistic understanding of allosteric immune escape pathways in the HIV-1 envelope glycoprotein. *PLoS Comput Biol* **9**, e1003046 (2013).

125. R. Nussinov, C. J. Tsai, Allostery in disease and in drug discovery. *Cell* **153**, 293-305 (2013).

126. S. Raman, N. Taylor, N. Genuth, S. Fields, G. M. Church, Engineering allostery. *Trends Genet* **30**, 521-528 (2014).

127. Y. Shan, Kim, ET, Eastwood, MP, Dror, RO, Seeliger, MA,and Shaw, DE, How Does a Drug Molecule Find Its Binding Site? . *J. Am. Chem. Soc.* **133**, 9181-9183 (2011).

128. R. O. Dror *et al.*, Pathway and mechanism of drug binding to G-protein-coupled receptors. *Proceedings of the National Academy of Sciences of the United States of America* **108**, 13118-13123 (2011).

129. J. D. Durrant, J. A. McCammon, Molecular dynamics simulations and drug discovery. *BMC Biol* **9**, 71 (2011).

130. S. E. Nichols, R. V. Swift, R. E. Amaro, Rational prediction with molecular dynamics for hit identification. *Curr Top Med Chem* **12**, 2002-2012 (2012).

131. V. A. Feher, J. D. Durrant, A. T. Van Wart, R. E. Amaro, Computational approaches to mapping allosteric pathways. *Curr Opin Struct Biol* **25**, 98-103 (2014).

132. S. W. Lockless, R. Ranganathan, Evolutionarily conserved pathways of energetic connectivity in protein families. *Science* **286**, 295-299 (1999).

133. M. D. Daily, T. J. Upadhyaya, J. J. Gray, Contact rearrangements form coupled networks from local motions in allosteric proteins. *Proteins* **71**, 455-466 (2008).

134. N. Kannan, S. Vishveshwara, Identification of side-chain clusters in protein structures by a graph spectral method. *J Mol Biol* **292**, 441-464 (1999).

135. Y. Kong, M. Karplus, Signaling pathways of PDZ2 domain: a molecular dynamics interaction correlation analysis. *Proteins* **74**, 145-154 (2009).

136. A. Sethi, J. Eargle, A. A. Black, Z. Luthey-Schulten, Dynamical networks in tRNA:protein complexes. *Proceedings of the National Academy of Sciences of the United States of America* **106**, 6620-6625 (2009).

137. A. E. Garcia, Large-amplitude nonlinear motions in proteins. *Phys Rev Lett* **68**, 2696-2699 (1992).

138. A. Amadei, A. B. Linssen, H. J. Berendsen, Essential dynamics of proteins. *Proteins* **17**, 412-425 (1993).

139. J. Wereszczynski, J. A. McCammon, Statistical mechanics and molecular dynamics in evaluating thermodynamic properties of biomolecular recognition. *Q Rev Biophys* **45**, 1-25 (2012).

140. D. L. Beveridge, F. M. DiCapua, Free energy via molecular simulation: applications to chemical and biomolecular systems. *Annu Rev Biophys Biophys Chem* **18**, 431-492 (1989).

141. B. Kuhn, P. Gerber, T. Schulz-Gasch, M. Stahl, Validation and use of the MM-PBSA approach for drug discovery. *Journal of medicinal chemistry* **48**, 4040-4048 (2005).

142. T. Hansson, J. Marelius, J. Aqvist, Ligand binding affinity prediction by linear interaction energy methods. *Journal of computer-aided molecular design* **12**, 27-35 (1998).

143. A. Laio, M. Parrinello, Escaping free-energy minima. *Proceedings of the National Academy of Sciences of the United States of America* **99**, 12562-12566 (2002).

144. H. Kokubo, T. Tanaka, Y. Okamoto, Ab initio prediction of protein-ligand binding structures by replica-exchange umbrella sampling simulations. *Journal of computational chemistry* **32**, 2810-2821 (2011).

145. V. J. Torrie GM, Nonphysical sampling distributions in Monte carlo free-energy estimation: umbrella sampling. *J Comput Phys* **23**, 187-199 (1977).

146. C. R. Vosmeer *et al.*, Improving the iterative Linear Interaction Energy approach using automated recognition of configurational transitions. *J Mol Model* **22**, 31 (2016).

147. O. J. D'Cruz, F. M. Uckun, Novel Bruton's tyrosine kinase inhibitors currently in development. *Onco Targets Ther* **6**, 161-176 (2013).

148. S. Fernandez de Mattos *et al.*, FoxO3a and BCR-ABL regulate cyclin D2 transcription through a STAT5/BCL6-dependent mechanism. *Molecular and cellular biology* **24**, 10058-10071 (2004).

149. V. T. Bicocca *et al.*, Crosstalk between ROR1 and the Pre-B cell receptor promotes survival of t(1;19) acute lymphoblastic leukemia. *Cancer cell* **22**, 656-667 (2012).

150. R. C. Harvey *et al.*, Identification of novel cluster groups in pediatric high-risk B-precursor acute lymphoblastic leukemia with gene expression profiling: correlation with genome-wide DNA copy number alterations, clinical characteristics, and outcome. *Blood* **116**, 4874-4884 (2010).

151. C. M. Lindqvist *et al.*, The mutational landscape in pediatric acute lymphoblastic leukemia deciphered by whole genome sequencing. *Human mutation* **36**, 118-128 (2015).

152. J. Wu, J. Fu, M. Zhang, D. Liu, Blinatumomab: a bispecific T cell engager (BiTE) antibody against CD19/CD3 for refractory acute lymphoid leukemia. *J Hematol Oncol* **8**, 104 (2015).

153. E. Jabbour, S. O'Brien, F. Ravandi, H. Kantarjian, Monoclonal antibodies in acute lymphoblastic leukemia. *Blood* **125**, 4010-4016 (2015).

154. N. Daver, S. O'Brien, Novel therapeutic strategies in adult acute lymphoblastic leukemia--a focus on emerging monoclonal antibodies. *Current hematologic malignancy reports* **8**, 123-131 (2013).

155. L. Sullivan-Chang, R. T. O'Donnell, J. M. Tuscano, Targeting CD22 in B-cell malignancies: current status and clinical outlook. *BioDrugs* **27**, 293-304 (2013).

156. M. Sadelain, I. Riviere, R. Brentjens, Targeting tumours with genetically enhanced T lymphocytes. *Nat Rev Cancer* **3**, 35-45 (2003).

157. W. Y. Ho, J. N. Blattman, M. L. Dossett, C. Yee, P. D. Greenberg, Adoptive immunotherapy: engineering T cell responses as biologic weapons for tumor mass destruction. *Cancer cell* **3**, 431-437 (2003).

158. R. E. Billingham, L. Brent, P. B. Medawar, Quantitative studies on tissue transplantation immunity. II. The origin, strength and duration of actively and adoptively acquired immunity. *Proc R Soc Lond B Biol Sci* **143**, 58-80 (1954).

159. C. Yee *et al.*, Adoptive T cell therapy using antigen-specific CD8+ T cell clones for the treatment of patients with metastatic melanoma: in vivo persistence, migration, and antitumor effect of transferred T cells. *Proceedings of the National Academy of Sciences of the United States of America* **99**, 16168-16173 (2002).

160. A. Mackensen *et al.*, Phase I study of adoptive T-cell therapy using antigen-specific CD8+ T cells for the treatment of patients with metastatic melanoma. *J Clin Oncol* **24**, 5060-5069 (2006).

161. M. E. Dudley *et al.*, Adoptive transfer of cloned melanoma-reactive T lymphocytes for the treatment of patients with metastatic melanoma. *J Immunother* **24**, 363-373 (2001).

162. I. Algarra, T. Cabrera, F. Garrido, The HLA crossroad in tumor immunology. *Hum Immunol* **61**, 65-73 (2000).

163. G. Gross, T. Waks, Z. Eshhar, Expression of immunoglobulin-T-cell receptor chimeric molecules as functional receptors with antibody-type specificity. *Proceedings of the National Academy of Sciences of the United States of America* **86**, 10024-10028 (1989).

164. B. A. Irving, A. Weiss, The cytoplasmic domain of the T cell receptor zeta chain is sufficient to couple to receptor-associated signal transduction pathways. *Cell* **64**, 891-901 (1991).

165. B. Jena, G. Dotti, L. J. Cooper, Redirecting T-cell specificity by introducing a tumor-specific chimeric antigen receptor. *Blood* **116**, 1035-1044 (2010).

166. M. Sadelain, R. Brentjens, I. Riviere, The promise and potential pitfalls of chimeric antigen receptors. *Curr Opin Immunol* **21**, 215-223 (2009).

167. M. C. Milone *et al.*, Chimeric receptors containing CD137 signal transduction domains mediate enhanced survival of T cells and increased antileukemic efficacy in vivo. *Mol Ther* **17**, 1453-1464 (2009).

168. C. Carpenito *et al.*, Control of large, established tumor xenografts with genetically retargeted human T cells containing CD28 and CD137 domains. *Proceedings of the National Academy of Sciences of the United States of America* **106**, 3360-3365 (2009).

169. D. L. Porter *et al.*, Chimeric antigen receptor T cells persist and induce sustained remissions in relapsed refractory chronic lymphocytic leukemia. *Science translational medicine* **7**, 303ra139 (2015).

170. M. L. Davila *et al.*, Efficacy and toxicity management of 19-28z CAR T cell therapy in B cell acute lymphoblastic leukemia. *Sci Transl Med* **6**, 224ra225 (2014).

171. S. A. Grupp *et al.*, Chimeric antigen receptor-modified T cells for acute lymphoid leukemia. *The New England journal of medicine* **368**, 1509-1518 (2013).

172. A. D. Fesnak, C. H. June, B. L. Levine, Engineered T cells: the promise and challenges of cancer immunotherapy. *Nat Rev Cancer* **16**, 566-581 (2016).

173. P. F. Robbins *et al.*, Tumor regression in patients with metastatic synovial cell sarcoma and melanoma using genetically engineered lymphocytes reactive with NY-ESO-1. *Journal of clinical oncology : official journal of the American Society of Clinical Oncology* **29**, 917-924 (2011).

174. A. P. Rapoport *et al.*, NY-ESO-1-specific TCR-engineered T cells mediate sustained antigen-specific antitumor effects in myeloma. *Nat Med* **21**, 914-921 (2015).

175. M. B. Geyer, R. J. Brentjens, Review: Current clinical applications of chimeric antigen receptor (CAR) modified T cells. *Cytotherapy* **18**, 1393-1409 (2016).

176. W. Yang *et al.*, Diminished expression of CD19 in B-cell lymphomas. *Cytometry B Clin Cytom* **63**, 28-35 (2005).

177. E. Sotillo *et al.*, Convergence of Acquired Mutations and Alternative Splicing of CD19 Enables Resistance to CART-19 Immunotherapy. *Cancer Discov* **5**, 1282-1295 (2015).

178. B. G. Till *et al.*, CD20-specific adoptive immunotherapy for lymphoma using a chimeric antigen receptor with both CD28 and 4-1BB domains: pilot clinical trial results. *Blood* **119**, 3940-3950 (2012).

179. L. E. Budde *et al.*, Combining a CD20 chimeric antigen receptor and an inducible caspase 9 suicide switch to improve the efficacy and safety of T cell adoptive immunotherapy for lymphoma. *PLoS One* **8**, e82742 (2013).

180. W. Haso *et al.*, Anti-CD22-chimeric antigen receptors targeting B-cell precursor acute lymphoblastic leukemia. *Blood* **121**, 1165-1174 (2013).

181. B. G. Till *et al.*, Adoptive immunotherapy for indolent non-Hodgkin lymphoma and mantle cell lymphoma using genetically modified autologous CD20-specific T cells. *Blood* **112**, 2261-2271 (2008).

182. M. Ruella *et al.*, Dual CD19 and CD123 targeting prevents antigen-loss relapses after CD19-directed immunotherapies. *J Clin Invest* **126**, 3814-3826 (2016).

183. A. Kudo, F. Melchers, A second gene, VpreB in the lambda 5 locus of the mouse, which appears to be selectively expressed in pre-B lymphocytes. *EMBO J* **6**, 2267-2272 (1987).

184. D. T. Avery *et al.*, BAFF selectively enhances the survival of plasmablasts generated from human memory B cells. *J Clin Invest* **112**, 286-297 (2003).

185. B. P. O'Connor *et al.*, BCMA is essential for the survival of long-lived bone marrow plasma cells. *J Exp Med* **199**, 91-98 (2004).

186. A. Choudhury *et al.*, Silencing of ROR1 and FMOD with siRNA results in apoptosis of CLL cells. *Br J Haematol* **151**, 327-335 (2010).

187. M. A. Kay, State-of-the-art gene-based therapies: the road ahead. *Nat Rev Genet* **12**, 316-328 (2011).

188. M. De Palma *et al.*, Promoter trapping reveals significant differences in integration site selection between MLV and HIV vectors in primary hematopoietic cells. *Blood* **105**, 2307-2315 (2005).

189. S. J. Howe *et al.*, Insertional mutagenesis combined with acquired somatic mutations causes leukemogenesis following gene therapy of SCID-X1 patients. *J Clin Invest* **118**, 3143-3150 (2008).

190. H. Singh *et al.*, Manufacture of clinical-grade CD19-specific T cells stably expressing chimeric antigen receptor using Sleeping Beauty system and artificial antigen presenting cells. *PloS one* **8**, e64138 (2013).

191. E. E. Perez *et al.*, Establishment of HIV-1 resistance in CD4+ T cells by genome editing using zinc-finger nucleases. *Nature biotechnology* **26**, 808-816 (2008).

192. L. Poirot *et al.*, Multiplex Genome-Edited T-cell Manufacturing Platform for "Off-the-Shelf" Adoptive T-cell Immunotherapies. *Cancer research* **75**, 3853-3864 (2015).

193. W. Qasim *et al.*, Molecular remission of infant B-ALL after infusion of universal TALEN gene-edited CAR T cells. *Science translational medicine* **9**, (2017).

194. J. Ren *et al.*, Multiplex Genome Editing to Generate Universal CAR T Cells Resistant to PD1 Inhibition. *Clin Cancer Res*, (2016).

195. K. Schumann *et al.*, Generation of knock-in primary human T cells using Cas9 ribonucleoproteins. *Proceedings of the National Academy of Sciences of the United States of America* **112**, 10437-10442 (2015).

196. P. Tebas *et al.*, Gene editing of CCR5 in autologous CD4 T cells of persons infected with HIV. *The New England journal of medicine* **370**, 901-910 (2014).

197. M. C. Jensen *et al.*, Antitransgene rejection responses contribute to attenuated persistence of adoptively transferred CD20/CD19-specific chimeric antigen receptor redirected T cells in humans. *Biol Blood Marrow Transplant* **16**, 1245-1256 (2010).

198. T. Gargett, M. P. Brown, The inducible caspase-9 suicide gene system as a "safety switch" to limit on-target, off-tumor toxicities of chimeric antigen receptor T cells. *Front Pharmacol* **5**, 235 (2014).

199. D. T. Rodgers *et al.*, Switch-mediated activation and retargeting of CAR-T cells for B-cell malignancies. *Proceedings of the National Academy of Sciences of the United States of America* **113**, E459-468 (2016).

200. C. Y. Wu, K. T. Roybal, E. M. Puchner, J. Onuffer, W. A. Lim, Remote control of therapeutic T cells through a small molecule-gated chimeric receptor. *Science (New York, N.Y.)* **350**, aab4077 (2015).

201. J. A. Craddock *et al.*, Enhanced tumor trafficking of GD2 chimeric antigen receptor T cells by expression of the chemokine receptor CCR2b. *J Immunother* **33**, 780-788 (2010).

202. J. G. Gaultney, W. K. Redekop, P. Sonneveld, C. A. Uyl-de Groot, Novel anticancer agents for multiple myeloma: a review of the evidence for their therapeutic and economic value. *Expert Rev Anticancer Ther* **12**, 839-854 (2012).

203. D. M. Pardoll, The blockade of immune checkpoints in cancer immunotherapy. *Nat Rev Cancer* **12**, 252-264 (2012).

204. C. J. Saret *et al.*, Value of innovation in hematologic malignancies: a systematic review of published cost-effectiveness analyses. *Blood* **125**, 1866-1869 (2015).

205. J. A. Fraietta *et al.*, Ibrutinib enhances chimeric antigen receptor T-cell engraftment and efficacy in leukemia. *Blood* **127**, 1117-1127 (2016).

206. L. B. John, M. H. Kershaw, P. K. Darcy, Blockade of PD-1 immunosuppression boosts CAR T-cell therapy. *Oncoimmunology* **2**, e26286 (2013).

207. Y. Yang, E. Jacoby, T. J. Fry, Challenges and opportunities of allogeneic donor-derived CAR T cells. *Current opinion in hematology* **22**, 509-515 (2015).

CHAPTER 2: Dynamic pre-BCR homodimers fine-tune autonomous survival signals in B cell precursor acute lymphoblastic leukemia

1. Bannish, G., E. M. Fuentes-Panana, J. C. Cambier, W. S. Pear, and J. G. Monroe. 2001. Ligandindependent signaling functions for the B lymphocyte antigen receptor and their role in positive selection during B lymphopoiesis. The Journal of experimental medicine 194: 1583-1596.
2. Geahlen, R. L. 2009. Syk and pTyr'd: Signaling through the B cell antigen receptor. Biochim Biophys Acta 1793: 1115-1127.
3. Kurosaki, T., S. A. Johnson, L. Pao, K. Sada, H. Yamamura, and J. C. Cambier. 1995. Role of the Syk autophosphorylation site and SH2 domains in B cell antigen receptor signaling. J Exp Med 182:1815-1823.
4. Nahar, R., P. Ramezani-Rad, M. Mossner, C. Duy, L. Cerchietti, H. Geng, S. Dovat, H. Jumaa, B. H. Ye, A. Melnick, and M. Muschen. 2011. Pre-B cell receptor-mediated activation of BCL6 induces pre-B cell quiescence through transcriptional repression of MYC. Blood 118: 4174-4178.
5. Mandal, M., S. E. Powers, K. Ochiai, K. Georgopoulos, B. L. Kee, H. Singh, and M. R. Clark. 2009. Ras orchestrates exit from the cell cycle and light-chain recombination during early B cell development. Nat Immunol 10: 1110-1117.
6. Stadhouders, R., M. J. de Bruijn, M. B. Rother, S. Yuvaraj, C. Ribeiro de Almeida, P. Kolovos, M. C. Van Zelm, W. van Ijcken, F. Grosveld, E. Soler, and R. W. Hendriks. 2014. Pre-B cell receptor signaling induces immunoglobulin kappa locus accessibility by functional redistribution of enhancer-mediated chromatin interactions. PLoS Biol 12: e1001791.
7. Schuh, W., S. Meister, K. Herrmann, H. Bradl, and H. M. Jack. 2008. Transcriptome analysis in primary B lymphoid precursors following induction of the pre-B cell receptor. Mol Immunol 45:362-375.
8. Anbazhagan, K., A. Rabbind Singh, P. Isabelle, I. Stella, A. D. Celine, E. Bissac, B. Bertrand, N. Remy, T. Naomi, F. Vincent, J. Rochette, and K. Lassoued. 2013. Human pre-B cell receptor signal transduction: evidence for distinct roles of PI3kinase and MAP-kinase signalling pathways. Immun Inflamm Dis 1: 26-36.

9. Kawano, Y., S. Yoshikawa, Y. Minegishi, and H. Karasuyama. 2006. Pre-B cell receptor assesses the quality of IgH chains and tunes the pre-B cell repertoire by delivering differential signals. J Immunol 177: 2242-2249.
10. Almqvist, N., and I. L. Martensson. 2012. The pre-B cell receptor; selecting for or against autoreactivity. Scand J Immunol 76: 256-262.
11. Zouali, M. 2014. Transcriptional and metabolic pre-B cell receptor-mediated checkpoints: implications for autoimmune diseases. Mol Immunol 62: 315-320.
12. Grimsholm, O., W. Ren, A. I. Bernardi, H. Chen, G. Park, A. Camponeschi, D. Chen, B. Bergmann, N. Hook, S. Andersson, A. Stromberg, I. Gjertsson, S. Cardell, U. Yrlid, A. De Riva, and I. L. Martensson. 2015. Absence of surrogate light chain results in spontaneous autoreactive germinal centres expanding V(H)81X-expressing B cells. Nat Commun 6: 7077.
13. Fuentes-Panana, E. M., G. Bannish, N. Shah, and J. G. Monroe. 2004. Basal Igalpha/Igbeta signals trigger the coordinated initiation of pre-B cell antigen receptor-dependent processes. J Immunol 173: 1000-1011.
14. Kohler, F., E. Hug, C. Eschbach, S. Meixlsperger, E. Hobeika, J. Kofer, H. Wardemann, and H. Jumaa. 2008. Autoreactive B cell receptors mimic autonomous pre-B cell receptor signaling and induce proliferation of early B cells. Immunity 29: 912-921.
15. Ubelhart, R., M. P. Bach, C. Eschbach, T. Wossning, M. Reth, and H. Jumaa. 2010. N-linked glycosylation selectively regulates autonomous precursor BCR function. Nat Immunol 11: 759-765.
16. Mourcin, F., C. Breton, J. Tellier, P. Narang, L. Chasson, A. Jorquera, M. Coles, C. Schiff, and S. J. Mancini. 2011. Galectin-1-expressing stromal cells constitute a specific niche for pre-BII cell development in mouse bone marrow. Blood 117: 6552-6561.
17. Ohnishi, K., and F. Melchers. 2003. The nonimmunoglobulin portion of lambda5 mediates cellautonomous pre-B cell receptor signaling. Nat Immunol 4: 849-856.
18. Bankovich, A. J., S. Raunser, Z. S. Juo, T. Walz, M. M. Davis, and K. C. Garcia. 2007. Structural insight into pre-B cell receptor function. Science 316: 291-294.

19. Monroe, J. G. 2006. ITAM-mediated tonic signalling through pre-BCR and BCR complexes. Nat Rev Immunol 6: 283-294.

20. Tsourkas, P. K., W. Liu, S. C. Das, S. K. Pierce, and S. Raychaudhuri. 2012. Discrimination of membrane antigen affinity by B cells requires dominance of kinetic proofreading over serial engagement. Cell Mol Immunol 9: 62-74.

21. Tolar, P., and T. Meckel. 2009. Imaging B-cell receptor signaling by single-molecule techniques. Methods Mol Biol 571: 437-453.

22. Treanor, B., D. Depoil, A. Gonzalez-Granja, P. Barral, M. Weber, O. Dushek, A. Bruckbauer, and F. D. Batista. 2010. The membrane skeleton controls diffusion dynamics and signaling through the B cell receptor. Immunity 32: 187-199.

23. Andrews, N. L., J. R. Pfeiffer, A. M. Martinez, D. M. Haaland, R. W. Davis, T. Kawakami, J. M. Oliver, B. S. Wilson, and D. S. Lidke. 2009. Small, mobile FcepsilonRI receptor aggregates are signaling competent. Immunity 31: 469-479.

24. Andrews, N. L., K. A. Lidke, J. R. Pfeiffer, A. R. Burns, B. S. Wilson, J. M. Oliver, and D. S. Lidke. 2008. Actin restricts FcepsilonRI diffusion and facilitates antigen-induced receptor immobilization. Nat Cell Biol 10: 955-963.

25. Eswaran, J., P. Sinclair, O. Heidenreich, J. Irving, L. J. Russell, A. Hall, D. P. Calado, C. J. Harrison, and J. Vormoor. 2015. The pre-B-cell receptor checkpoint in acute lymphoblastic leukaemia. Leukemia 29: 1623-1631.

26. Geng, H., C. Hurtz, K. B. Lenz, Z. Chen, D. Baumjohann, S. Thompson, N. A. Goloviznina, W. Y. Chen, J. Huan, D. LaTocha, E. Ballabio, G. Xiao, J. W. Lee, A. Deucher, Z. Qi, E. Park, C. Huang, R. Nahar, S. M. Kweon, S. Shojaee, L. N. Chan, J. Yu, S. M. Kornblau, J. J. Bijl, B. H. Ye, K. M. Ansel, E. Paietta, A. Melnick, S. P. Hunger, P. Kurre, J. W. Tyner, M. L. Loh, R. G. Roeder, B. J. Druker, J. A. Burger, T. A. Milne, B. H. Chang, and M. Muschen. 2015. Self-enforcing feedback activation between BCL6 and pre-B cell receptor signaling defines a distinct subtype of acute lymphoblastic leukemia. Cancer cell 27: 409-425.

27. Davis, R. E., V. N. Ngo, G. Lenz, P. Tolar, R. M. Young, P. B. Romesser, H. Kohlhammer, L. Lamy, H. Zhao, Y. Yang, W. Xu, A. L. Shaffer, G. Wright, W. Xiao, J. Powell, J. K. Jiang, C. J. Thomas, A.

Rosenwald, G. Ott, H. K. Muller-Hermelink, R. D. Gascoyne, J. M. Connors, N. A. Johnson, L. M. Rimsza, E. Campo, E. S. Jaffe, W. H. Wilson, J. Delabie, E. B. Smeland, R. I. Fisher, R. M. Braziel, R. R. Tubbs, J. R. Cook, D. D. Weisenburger, W. C. Chan, S. K. Pierce, and L. M. Staudt. 2010. Chronic active B-cell-receptor signalling in diffuse large B-cell lymphoma. Nature 463: 88-92.

28. Stevenson, F. K., S. Krysov, A. J. Davies, A. J. Steele, and G. Packham. 2011. B-cell receptor signaling in chronic lymphocytic leukemia. Blood 118: 4313-4320.
29. Niemann, C. U., and A. Wiestner. 2013. B-cell receptor signaling as a driver of lymphoma development and evolution. Semin Cancer Biol 23: 410-421.
30. Bicocca, V. T., B. H. Chang, B. K. Masouleh, M. Muschen, M. M. Loriaux, B. J. Druker, and J. W. Tyner. 2012. Crosstalk between ROR1 and the Pre-B cell receptor promotes survival of t(1;19) acute lymphoblastic leukemia. Cancer cell 22: 656-667.
31. Perova, T., I. Grandal, L. M. Nutter, E. Papp, I. R. Matei, J. Beyene, P. E. Kowalski, J. K. Hitzler, M D. Minden, C. J. Guidos, and J. S. Danska. 2014. Therapeutic potential of spleen tyrosine kinase inhibition for treating high-risk precursor B cell acute lymphoblastic leukemia. Sci Transl Med 6:236ra262.
32. Muschen, M. 2015. Rationale for targeting the pre-B-cell receptor signaling pathway in acute lymphoblastic leukemia. Blood 125: 3688-3693.
33. Ubelhart, R., and H. Jumaa. 2015. Autoreactivity and the positive selection of B cells. European journal of immunology.
34. Barondes, S. H., D. N. Cooper, M. A. Gitt, and H. Leffler. 1994. Galectins. Structure and function of a large family of animal lectins. J Biol Chem 269: 20807-20810. 35. Elantak, L., M. Espeli, A. Boned, O. Bornet, J. Bonzi, L. Gauthier, M. Feracci, P. Roche, F. Guerlesquin, and C. Schiff. 2012. Structural basis for galectin-1-dependent pre-B cell receptor (pre-BCR) activation. J Biol Chem 287: 44703-44713.
36. Gauthier, L., B. Rossi, F. Roux, E. Termine, and C. Schiff. 2002. Galectin-1 is a stromal cell ligand of the pre-B cell receptor (BCR) implicated in synapse formation between pre-B and stromal cells and in pre-BCR triggering. Proceedings

of the National Academy of Sciences of the United States of America 99: 13014-13019.

37. Bonzi, J., O. Bornet, S. Betzi, B. T. Kasper, L. K. Mahal, S. J. Mancini, C. Schiff, C. Sebban-Kreuzer, F. Guerlesquin, and L. Elantak. 2015. Pre-B cell receptor binding to galectin-1 modifies galectin-1/carbohydrate affinity to modulate specific galectin-1/glycan lattice interactions. Nat Commun 6: 6194.

38. Rossi, B., M. Espeli, C. Schiff, and L. Gauthier. 2006. Clustering of pre-B cell integrins inducesgalectin-1-dependent pre-B cell receptor relocalization and activation. J Immunol 177: 796-803.

39. Juszczynski, P., S. J. Rodig, J. Ouyang, E. O'Donnell, K. Takeyama, W. Mlynarski, K. Mycko, T. Szczepanski, A. Gaworczyk, A. Krivtsov, J. Faber, A. U. Sinha, G. A. Rabinovich, S. A. Armstrong, JL. Kutok, and M. A. Shipp. 2010. MLL-rearranged B lymphoblastic leukemias selectively express the immunoregulatory carbohydrate-binding protein galectin-1. Clinical cancer research : an official journal of the American Association for Cancer Research 16: 2122-2130.

40. Duy, C., C. Hurtz, S. Shojaee, L. Cerchietti, H. Geng, S. Swaminathan, L. Klemm, S. M. Kweon, R. Nahar, M. Braig, E. Park, Y. M. Kim, W. K. Hofmann, S. Herzog, H. Jumaa, H. P. Koeffler, J. J. Yu, N. Heisterkamp, T. G. Graeber, H. Wu, B. H. Ye, A. Melnick, and M. Muschen. 2011. BCL6 enables Ph+ acute lymphoblastic leukaemia cells to survive BCR-ABL1 kinase inhibition. Nature 473: 384-388.

41. Shojaee, S., R. Caeser, M. Buchner, E. Park, S. Swaminathan, C. Hurtz, H. Geng, L. N. Chan, L. Klemm, W. K. Hofmann, Y. H. Qiu, N. Zhang, K. R. Coombes, E. Paietta, J. Molkentin, H. P. Koeffler, C. L. Willman, S. P. Hunger, A. Melnick, S. M. Kornblau, and M. Muschen. 2015. Erk Negative Feedback Control Enables Pre-B Cell Transformation and Represents a Therapeutic Target in Acute Lymphoblastic Leukemia. Cancer cell 28: 114-128.

42. Peluso, P., D. S. Wilson, D. Do, H. Tran, M. Venkatasubbaiah, D. Quincy, B. Heidecker, K. Poindexter, N. Tolani, M. Phelan, K. Witte, L. S. Jung, P. Wagner, and S. Nock. 2003. Optimizing antibody immobilization strategies for the construction of protein microarrays. Anal Biochem. 312: 113-124.

43. Low-Nam, S. T., K. A. Lidke, P. J. Cutler, R. C. Roovers, P. M. van Bergen en Henegouwen, B. S.Wilson, and D. S. Lidke. 2011. ErbB1 dimerization is promoted by domain co-confinement and stabilized by ligand binding. Nat Struct Mol Biol 18: 1244-1249.

44. Findley, H. W., Jr., M. D. Cooper, T. H. Kim, C. Alvarado, and A. H. Ragab. 1982. Two new acute lymphoblastic leukemia cell lines with early B-cell phenotypes. Blood 60: 1305-1309.

45. Forney, G. 1973. The Viterbi algorithm. Proc. IEEE 61: 268-278.

46. Hurwitz, R., J. Hozier, T. LeBien, J. Minowada, K. Gajl-Peczalska, I. Kubonishi, and J. Kersey. 1979. Characterization of a leukemic cell line of the pre-B phenotype. Int J Cancer 23: 174-180.

47. Steinkamp, M. P., S. T. Low-Nam, S. Yang, K. A. Lidke, D. S. Lidke, and B. S. Wilson. 2014. erbB3 Is an Active Tyrosine Kinase Capable of Homo- and Heterointeractions. Mol Cell Biol 34: 965-977.

48. Zhang, F., B. Crise, B. Su, Y. Hou, J. K. Rose, A. Bothwell, and K. Jacobson. 1991. Lateral diffusion of membrane-spanning and glycosylphosphatidylinositol-linked proteins: toward establishing rules governing the lateral mobility of membrane proteins. The Journal of cell biology 115: 75-84.

49. Stowell, S. R., M. Cho, C. L. Feasley, C. M. Arthur, X. Song, J. K. Colucci, S. Karmakar, P. Mehta, M. Dias-Baruffi, R. P. McEver, and R. D. Cummings. 2009. Ligand reduces galectin-1 sensitivity to oxidative inactivation by enhancing dimer formation. J Biol Chem 284: 4989-4999.

50. Chen, Z., S. Shojaee, M. Buchner, H. Geng, J. W. Lee, L. Klemm, B. Titz, T. G. Graeber, E. Park, Y. X. Tan, A. Satterthwaite, E. Paietta, S. P. Hunger, C. L. Willman, A. Melnick, M. L. Loh, J. U. Jung, J. E. Coligan, S. Bolland, T. W. Mak, A. Limnander, H. Jumaa, M. Reth, A. Weiss, C. A. Lowell, and M. Muschen. 2015. Signalling thresholds and negative B-cell selection in acute lymphoblastic leukaemia. Nature 521: 357-361.

51. Wienands, J., O. Larbolette, and M. Reth. 1996. Evidence for a preformed transducer complex organized by the B cell antigen receptor. Proceedings of the National Academy of Sciences of the United States of America 93: 7865-7870.

52. Rolli, V., M. Gallwitz, T. Wossning, A. Flemming, W. W. Schamel, C. Zurn, and M. Reth. 2002.Amplification of B cell antigen receptor signaling by a Syk/ITAM positive feedback loop. Mol Cell 10: 1057-1069.

53. Finn, R. S., J. Dering, C. Ginther, C. A. Wilson, P. Glaspy, N. Tchekmedyian, and D. J. Slamon. 2007. Dasatinib, an orally active small molecule inhibitor of both the src and abl kinases, selectively inhibits growth of basal-type/"triple-negative" breast cancer cell lines growing in vitro. Breast Cancer Res Treat 105: 319-326.

54. Degryse, S., and J. Cools. 2015. JAK kinase inhibitors for the treatment of acute lymphoblastic leukemia. Journal of hematology & oncology 8: 91.

55. Swaminathan, S., L. Klemm, E. Park, E. Papaemmanuil, A. Ford, S. M. Kweon, D. Trageser, B. Hasselfeld, N. Henke, J. Mooster, H. Geng, K. Schwarz, S. C. Kogan, R. Casellas, D. G. Schatz, M. R. Lieber, M. F. Greaves, and M. Muschen. 2015. Mechanisms of clonal evolution in childhood acute lymphoblastic leukemia. Nat Immunol 16: 766-774.

56. Zhang, J., C. G. Mullighan, R. C. Harvey, G. Wu, X. Chen, M. Edmonson, K. H. Buetow, W. L. Carroll, I. M. Chen, M. Devidas, D. S. Gerhard, M. L. Loh, G. H. Reaman, M. V. Relling, B. M.
Camitta, W. P. Bowman, M. A. Smith, C. L. Willman, J. R. Downing, and S. P. Hunger. 2011. Keypathways are frequently mutated in high-risk childhood acute lymphoblastic leukemia: a report from the Children's Oncology Group. Blood 118: 3080-3087.

57. van der Veer, A., E. Waanders, R. Pieters, M. E. Willemse, S. V. Van Reijmersdal, L. J. Russell, C. J. Harrison, W. E. Evans, V. H. van der Velden, P. M. Hoogerbrugge, F. Van Leeuwen, G. Escherich, M. A. Horstmann, L. Mohammadi Khankahdani, D. Rizopoulos, H. A. De Groot-Kruseman, E. Sonneveld, R. P. Kuiper, and M. L. Den Boer. 2013. Independent prognostic value of BCR-ABL1-like signature and IKZF1 deletion, but not high CRLF2 expression, in children with B-cell precursor ALL. Blood 122: 2622-2629.

58. Conley, M. E., and P. D. Burrows. 2010. Plugging the leaky pre-B cell receptor. J Immunol 184:1127-1129.

59. Herzog, S., M. Reth, and H. Jumaa. 2009. Regulation of B-cell proliferation and differentiation by pre-B-cell receptor signalling. Nat Rev Immunol 9: 195-205.

60. von Boehmer, H., and F. Melchers. 2010. Checkpoints in lymphocyte development and autoimmune disease. Nat Immunol 11: 14-20.

61. Winick, N. J., W. L. Carroll, and S. P. Hunger. 2004. Childhood leukemia--new advances and challenges. The New England journal of medicine 351: 601-603.

62. Douer, D. 2013. Adult acute lymphoblastic leukemia: a cancer with no standard of care. Acta Haematol 130: 196-198.

63. Gaynon, P. S., A. L. Angiolillo, W. L. Carroll, J. B. Nachman, M. E. Trigg, H. N. Sather, S. P. Hunger, and M. Devidas. 2010. Long-term results of the children's cancer group studies for childhood acute lymphoblastic leukemia 1983-2002: a Children's Oncology Group Report. Leukemia 24: 285-297.

64. Asner, S., R. A. Ammann, H. Ozsahin, M. Beck-Popovic, and N. X. von der Weid. 2008. Obesity in long-term survivors of childhood acute lymphoblastic leukemia. Pediatric blood & cancer 51:118-122.

65. Winter, S. S. 2011. Pediatric acute leukemia therapies informed by molecular analysis of high risk disease. Hematology Am Soc Hematol Educ Program 2011: 366-373.

66. Awan, F. T., and J. C. Byrd. 2014. New strategies in chronic lymphocytic leukemia: shifting treatment paradigms. Clinical cancer research : an official journal of the American Association for Cancer Research 20: 5869-5874.

67. Sharman, J., M. Hawkins, K. Kolibaba, M. Boxer, L. Klein, M. Wu, J. Hu, S. Abella, and C. Yasenchak. 2015. An open-label phase 2 trial of entospletinib (GS-9973), a selective spleen tyrosine kinase inhibitor, in chronic lymphocytic leukemia. Blood 125: 2336-2343.

68. Puri, K. D., J. A. Di Paolo, and M. R. Gold. 2013. B-cell receptor signaling inhibitors for treatment of autoimmune inflammatory diseases and B-cell malignancies. Int Rev Immunol 32: 397-427.

69. Lillemeier, B. F., J. R. Pfeiffer, Z. Surviladze, B. S. Wilson, and M. M. Davis. 2006. Plasma membrane-associated proteins are clustered into islands attached to the

cytoskeleton. Proceedings of the National Academy of Sciences of the United States of America 103: 18992-18997.

70. Maity, P. C., A. Blount, H. Jumaa, O. Ronneberger, B. F. Lillemeier, and M. Reth. 2015. B cell antigen receptors of the IgM and IgD classes are clustered in different protein islands that are altered during B cell activation. Sci Signal 8: ra93.

71. Sohn, H. W., P. Tolar, and S. K. Pierce. 2008. Membrane heterogeneities in the formation of B cell receptor-Lyn kinase microclusters and the immune synapse. J Cell Biol 182: 367-379.

72. Mattila, P. K., C. Feest, D. Depoil, B. Treanor, B. Montaner, K. L. Otipoby, R. Carter, L. B. Justement, A. Bruckbauer, and F. D. Batista. 2013. The actin and tetraspanin networks organize receptor nanoclusters to regulate B cell receptor-mediated signaling. Immunity 38: 461-474.

73. Freeman, S. A., V. Jaumouille, K. Choi, B. E. Hsu, H. S. Wong, L. Abraham, M. L. Graves, D. Coombs, C. D. Roskelley, R. Das, S. Grinstein, and M. R. Gold. 2015. Toll-like receptor ligands sensitize B-cell receptor signalling by reducing actin-dependent spatial confinement of the receptor. Nat Commun 6: 6168.

74. Hlavacek, W. S., A. Redondo, H. Metzger, C. Wofsy, and B. Goldstein. 2001. Kinetic proofreading models for cell signaling predict ways to escape kinetic proofreading. Proceedings of the National Academy of Sciences of the United States of America 98: 7295-7300.

75. Aleksic, M., O. Dushek, H. Zhang, E. Shenderov, J. L. Chen, V. Cerundolo, D. Coombs, and P. A. van der Merwe. 2010. Dependence of T cell antigen recognition on T cell receptor-peptide MHC confinement time. Immunity 32: 163-174.

76. McCarthy, N. 2016. Tumour suppressors: Turning a negative into a positive. Nat Rev Cancer 16: 272-273.

77. Shojaee, S., L. N. Chan, M. Buchner, V. Cazzaniga, K. N. Cosgun, H. Geng, Y. H. Qiu, M. D. von Minden, T. Ernst, A. Hochhaus, G. Cazzaniga, A. Melnick, S. M. Kornblau, T. G. Graeber, H. Wu, H. Jumaa, and M. Muschen. 2016. PTEN opposes negative selection and enables oncogenic transformation of pre-B cells. Nat Med 22: 379-387.

78. Fei, F., E. J. Joo, S. S. Tarighat, I. Schiffer, H. Paz, M. Fabbri, H. Abdel-Azim, J. Groffen, and N. Heisterkamp. 2015. B-cell precursor acute lymphoblastic leukemia and stromal cells communicate through Galectin-3. Oncotarget 6: 11378-11394.

79. Fielding, A. K., J. M. Rowe, G. Buck, L. Foroni, G. Gerrard, M. R. Litzow, H. Lazarus, S. M. Luger, D. I. Marks, A. K. McMillan, A. V. Moorman, B. Patel, E. Paietta, M. S. Tallman, and A. H. Goldstone. 2014. UKALLXII/ECOG2993: addition of imatinib to a standard treatment regimen enhances long-term outcomes in Philadelphia positive acute lymphoblastic leukemia. Blood 123: 843-850.

80. Roberts, K. G., Y. Li, D. Payne-Turner, R. C. Harvey, Y. L. Yang, D. Pei, K. McCastlain, L. Ding, C. Lu, G. Song, J. Ma, J. Becksfort, M. Rusch, S. C. Chen, J. Easton, J. Cheng, K. Boggs, N. Santiago-Morales, I. Iacobucci, R. S. Fulton, J. Wen, M. Valentine, C. Cheng, S. W. Paugh, M. Devidas, I. M. Chen, S. Reshmi, A. Smith, E. Hedlund, P. Gupta, P. Nagahawatte, G. Wu, X. Chen, D. Yergeau, B. Vadodaria, H. Mulder, N. J. Winick, E. C. Larsen, W. L. Carroll, N. A. Heerema, A. J. Carroll, G. Grayson, S. K. Tasian, A. S. Moore, F. Keller, M. Frei-Jones, J. A. Whitlock, E. A. Raetz, D. L. White, T. P. Hughes, J. M. Guidry Auvil, M. A. Smith, G. Marcucci, C. D. Bloomfield, K. Mrozek, J. Kohlschmidt, W. Stock, S. M. Kornblau, M. Konopleva, E. Paietta, C. H. Pui, S. Jeha, M. V. Relling, W. E. Evans, D. S. Gerhard, J. M. Gastier-Foster, E. Mardis, R. K. Wilson, M. L. Loh, J. R. Downing, S. P. Hunger, C. L. Willman, J. Zhang, and C. G. Mullighan. 2014. Targetable kinase-activating lesions in Ph-like acute lymphoblastic leukemia. The New England journal of medicine 371: 1005-1015.

81. Shah, N. N., M. S. Stevenson, C. M. Yuan, K. Richards, C. Delbrook, R. J. Kreitman, I. Pastan, and A. S. Wayne. 2015. Characterization of CD22 expression in acute lymphoblastic leukemia. Pediatric blood & cancer 62: 964-969.

82. Daeron, M., S. Jaeger, L. Du Pasquier, and E. Vivier. 2008. Immunoreceptor tyrosine-based inhibition motifs: a quest in the past and future. Immunological reviews 224: 11-43.

83. O'Neill, S. K., A. Getahun, S. B. Gauld, K. T. Merrell, I. Tamir, M. J. Smith, J. M. Dal Porto, Q. Z. Li, and J. C. Cambier. 2011. Monophosphorylation of CD79a and

CD79b ITAM motifs initiates a SHIP-1 phosphatase-mediated inhibitory signaling cascade required for B cell anergy. Immunity 35: 746-756.

84. Getahun, A., N. A. Beavers, S. R. Larson, M. J. Shlomchik, and J. C. Cambier. 2016. Continuous inhibitory signaling by both SHP-1 and SHIP-1 pathways is required to maintain unresponsiveness of anergic B cells. J Exp Med 213: 751-769.
85. Somasundaram, R., M. A. Prasad, J. Ungerback, and M. Sigvardsson. 2015. Transcription factor networks in B-cell differentiation link development to acute lymphoid leukemia. Blood 126: 144-152.
86. Appelmann, I., C. D. Rillahan, E. de Stanchina, G. Carbonetti, C. Chen, S. W. Lowe, and C. J. Sherr. 2015. Janus kinase inhibition by ruxolitinib extends dasatinib- and dexamethasone-induced remissions in a mouse model of Ph+ ALL. Blood 125: 1444-1451.
87. Xu, L., H. Yee, C. Chan, A. K. Kashyap, L. Horowitz, M. Horowitz, R. R. Bhatt, and R. A. Lerner. 2008. Combinatorial surrobody libraries. Proceedings of the National Academy of Sciences of the United States of America 105: 10756-10761.
88. Carlow, D. A., M. J. Williams, and H. J. Ziltener. 2003. Modulation of O-glycans and N-glycans on murine CD8 T cells fails to alter annexin V ligand induction by galectin 1. J Immunol 171: 5100-5106.
89. Imbert, V., J. F. Peyron, D. Farahi Far, B. Mari, P. Auberger, and B. Rossi. 1994. Induction of tyrosine phosphorylation and T-cell activation by vanadate peroxide, an inhibitor of protein tyrosine phosphatases. Biochem J 297 (Pt 1): 163-173.
90. Smrz, D., P. Lebduska, L. Draberova, J. Korb, and P. Draber. 2008. Engagement of phospholipid scramblase 1 in activated cells: implication for phosphatidylserine externalization and exocytosis. J Biol Chem 283: 10904-10918.
91. Klasener, K., P. C. Maity, E. Hobeika, J. Yang, and M. Reth. 2014. B cell activation involves nanoscale receptor reorganizations and inside-out signaling by Syk. Elife 3: e02069.
92. Drake, A. W., and S. L. Klakamp. 2007. A rigorous multiple independent binding site model for determining cell-based equilibrium dissociation constants. J Immunol Methods 318: 147-152.

93. Edwards, B. S., S. M. Young, I. Ivnitsky-Steele, R. D. Ye, E. R. Prossnitz, and L. A. Sklar. 2009. Highcontent screening: flow cytometry analysis. Methods Mol Biol 486: 151-165.

94. Edgar, R. C. 2004. MUSCLE: multiple sequence alignment with high accuracy and high throughput. Nucleic Acids Res 32: 1792-1797.

95. Sali, A., and T. L. Blundell. 1993. Comparative protein modelling by satisfaction of spatial restraints. J Mol Biol 234: 779-815.

96. Shen, Y., J. Maupetit, P. Derreumaux, and P. Tuffery. 2014. Improved PEP-FOLD Approach for Peptide and Miniprotein Structure Prediction. J Chem Theory Comput 10: 4745-4758.

97. Humphrey, W., A. Dalke, and K. Schulten. 1996. VMD: visual molecular dynamics. J Mol Graph 14: 33-38, 27-38.

Chapter 3 - Molecular Dynamic Simulations of Galectin-1 with Carbohydrates: Influence of Binding to pre-BCR λ5-UR

1. T. Tsubata, M. Reth, The products of pre-B cell-specific genes (lambda 5 and VpreB) and the immunoglobulin mu chain form a complex that is transported onto the cell surface. *J Exp Med* **172**, 973-976 (1990).
2. M. Reth, Antigen receptors on B lymphocytes. *Annu Rev Immunol* **10**, 97-121 (1992).
3. M. F. Erasmus *et al.*, Dynamic pre-BCR homodimers fine-tune autonomous survival signals in B cell precursor acute lymphoblastic leukemia. *Sci Signal* **9**, ra116 (2016).
4. K. Ohnishi, F. Melchers, The nonimmunoglobulin portion of lambda5 mediates cell-autonomous pre-B cell receptor signaling. *Nat Immunol* **4**, 849-856 (2003).
5. J. G. Monroe, ITAM-mediated tonic signalling through pre-BCR and BCR complexes. *Nat Rev Immunol* **6**, 283-294 (2006).
6. E. M. Fuentes-Panana, G. Bannish, J. G. Monroe, Basal B-cell receptor signaling in B lymphocytes: mechanisms of regulation and role in positive selection, differentiation, and peripheral survival. *Immunological reviews* **197**, 26-40 (2004).
7. R. Kersseboom *et al.*, Bruton's tyrosine kinase cooperates with the B cell linker protein SLP-65 as a tumor suppressor in Pre-B cells. *J Exp Med* **198**, 91-98 (2003).
8. H. Geng *et al.*, Self-enforcing feedback activation between BCL6 and pre-B cell receptor signaling defines a distinct subtype of acute lymphoblastic leukemia. *Cancer cell* **27**, 409-425 (2015).
9. L. Cindolo *et al.*, galectin-1 and galectin-3 expression in human bladder transitional-cell carcinomas. *Int J Cancer* **84**, 39-43 (1999).
10. L. Gauthier, B. Rossi, F. Roux, E. Termine, C. Schiff, Galectin-1 is a stromal cell ligand of the pre-B cell receptor (BCR) implicated in synapse formation between pre-B and stromal cells and in pre-BCR triggering. *Proceedings of the National Academy of Sciences of the United States of America* **99**, 13014-13019 (2002).
11. L. Elantak *et al.*, Structural basis for galectin-1-dependent pre-B cell receptor (pre-BCR) activation. *J Biol Chem* **287**, 44703-44713 (2012).

12. B. Rossi, M. Espeli, C. Schiff, L. Gauthier, Clustering of pre-B cell integrins induces galectin-1-dependent pre-B cell receptor relocalization and activation. *J Immunol* **177**, 796-803 (2006).
13. M. Espeli, S. J. Mancini, C. Breton, F. Poirier, C. Schiff, Impaired B-cell development at the pre-BII-cell stage in galectin-1-deficient mice due to inefficient pre-BII/stromal cell interactions. *Blood* **113**, 5878-5886 (2009).
14. F. Mourcin *et al.*, Galectin-1-expressing stromal cells constitute a specific niche for pre-BII cell development in mouse bone marrow. *Blood* **117**, 6552-6561 (2011).
15. V. Makrynikola, K. F. Bradstock, Adhesion of precursor-B acute lymphoblastic leukaemia cells to bone marrow stromal proteins. *Leukemia* **7**, 86-92 (1993).
16. I. Camby, M. Le Mercier, F. Lefranc, R. Kiss, Galectin-1: a small protein with major functions. *Glycobiology* **16**, 137R-157R (2006).
17. M. G. Ford, T. Weimar, T. Kohli, R. J. Woods, Molecular dynamics simulations of galectin-1-oligosaccharide complexes reveal the molecular basis for ligand diversity. *Proteins* **53**, 229-240 (2003).
18. I. V. Nesmelova *et al.*, Lactose binding to galectin-1 modulates structural dynamics, increases conformational entropy, and occurs with apparent negative cooperativity. *J Mol Biol* **397**, 1209-1230 (2010).
19. J. Bonzi *et al.*, Pre-B cell receptor binding to galectin-1 modifies galectin-1/carbohydrate affinity to modulate specific galectin-1/glycan lattice interactions. *Nat Commun* **6**, 6194 (2015).
20. C. Meynier *et al.*, NMR and MD investigations of human galectin-1/oligosaccharide complexes. *Biophys J* **97**, 3168-3177 (2009).
21. S. Hertig, N. R. Latorraca, R. O. Dror, Revealing Atomic-Level Mechanisms of Protein Allostery with Molecular Dynamics Simulations. *PLoS Comput Biol* **12**, e1004746 (2016).
22. A. Sethi, J. Tian, C. A. Derdeyn, B. Korber, S. Gnanakaran, A mechanistic understanding of allosteric immune escape pathways in the HIV-1 envelope glycoprotein. *PLoS Comput Biol* **9**, e1003046 (2013).
23. R. Nussinov, C. J. Tsai, Allostery in disease and in drug discovery. *Cell* **153**, 293-305 (2013).

24. S. Raman, N. Taylor, N. Genuth, S. Fields, G. M. Church, Engineering allostery. *Trends Genet* **30**, 521-528 (2014).
25. B. G. Pierce, Y. Hourai, Z. Weng, Accelerating protein docking in ZDOCK using an advanced 3D convolution library. *PLoS One* **6**, e24657 (2011).
26. V. Hornak *et al.*, Comparison of multiple Amber force fields and development of improved protein backbone parameters. *Proteins* **65**, 712-725 (2006).
27. T. A. Darden, L. G. Pedersen, Molecular modeling: an experimental tool. *Environ Health Perspect* **101**, 410-412 (1993).
28. A. Sali, T. L. Blundell, Comparative protein modelling by satisfaction of spatial restraints. *J Mol Biol* **234**, 779-815 (1993).
29. M. Y. Shen, A. Sali, Statistical potential for assessment and prediction of protein structures. *Protein Sci* **15**, 2507-2524 (2006).
30. E. F. Pettersen *et al.*, UCSF Chimera--a visualization system for exploratory research and analysis. *J Comput Chem* **25**, 1605-1612 (2004).
31. A. W. Sousa da Silva, W. F. Vranken, ACPYPE - AnteChamber PYthon Parser interfacE. *BMC Res Notes* **5**, 367 (2012).
32. J. Wang, W. Wang, P. A. Kollman, D. A. Case, Automatic atom type and bond type perception in molecular mechanical calculations. *J Mol Graph Model* **25**, 247-260 (2006).
33. A. Amadei, A. B. Linssen, H. J. Berendsen, Essential dynamics of proteins. *Proteins* **17**, 412-425 (1993).
34. L. Zanetti-Polzi, S. Corni, I. Daidone, A. Amadei, Extending the essential dynamics analysis to investigate molecular properties: application to the redox potential of proteins. *Phys Chem Chem Phys* **18**, 18450-18459 (2016).
35. C. R. Vosmeer *et al.*, Improving the iterative Linear Interaction Energy approach using automated recognition of configurational transitions. *J Mol Model* **22**, 31 (2016).
36. J. Aqvist, C. Medina, J. E. Samuelsson, A new method for predicting binding affinity in computer-aided drug design. *Protein Eng* **7**, 385-391 (1994).
37. E. Stjernschantz, C. Oostenbrink, Improved ligand-protein binding affinity predictions using multiple binding modes. *Biophys J* **98**, 2682-2691 (2010).

38. I. Echeverria, L. M. Amzel, Disaccharide binding to galectin-1: free energy calculations and molecular recognition mechanism. *Biophysical journal* **100**, 2283-2292 (2011).

39. M. O. Jensen, Y. Yin, E. Tajkhorshid, K. Schulten, Sugar transport across lactose permease probed by steered molecular dynamics. *Biophys J* **93**, 92-102 (2007).

40. H. Ahmed, H. J. Allen, A. Sharma, K. L. Matta, Human splenic galaptin: carbohydrate-binding specificity and characterization of the combining site. *Biochemistry* **29**, 5315-5319 (1990).

41. M. C. Miller, I. V. Nesmelova, D. Platt, A. Klyosov, K. H. Mayo, The carbohydrate-binding domain on galectin-1 is more extensive for a complex glycan than for simple saccharides: implications for galectin-glycan interactions at the cell surface. *Biochem J* **421**, 211-221 (2009).

42. C. M. Guardia *et al.*, Structural basis of redox-dependent modulation of galectin-1 dynamics and function. *Glycobiology* **24**, 428-441 (2014).

43. D. D. Roberts, V. Ginsburg, Sulfated glycolipids and cell adhesion. *Arch Biochem Biophys* **267**, 405-415 (1988).

44. D. Gupta, M. Cho, R. D. Cummings, C. F. Brewer, Thermodynamics of carbohydrate binding to galectin-1 from Chinese hamster ovary cells and two mutants. A comparison with four galactose-specific plant lectins. *Biochemistry* **35**, 15236-15243 (1996).

45. J. C. Solomon *et al.*, Studies of the binding specificity of the soluble 14,000-dalton bovine heart muscle lectin using immobilised glycolipids and neoglycolipids. *Carbohydr Res* **213**, 293-307 (1991).

46. Q. Zhou, R. D. Cummings, L-14 lectin recognition of laminin and its promotion of in vitro cell adhesion. *Arch Biochem Biophys* **300**, 6-17 (1993).

47. V. J. Hilser, Biochemistry. An ensemble view of allostery. *Science* **327**, 653-654 (2010).

48. A. Hospital, J. R. Goni, M. Orozco, J. L. Gelpi, Molecular dynamics simulations: advances and applications. *Adv Appl Bioinform Chem* **8**, 37-47 (2015).

49. D. Kern, E. R. Zuiderweg, The role of dynamics in allosteric regulation. *Curr Opin Struct Biol* **13**, 748-757 (2003).

50. L. Ingrassia *et al.*, Anti-galectin compounds as potential anti-cancer drugs. *Curr Med Chem* **13**, 3513-3527 (2006).

Chapter 4 - Preclinical characterization of a chimeric antigen receptor T cell therapy targeting the pre-B cell receptor

1. R. C. Harvey *et al.*, Identification of novel cluster groups in pediatric high-risk B-precursor acute lymphoblastic leukemia with gene expression profiling: correlation with genome-wide DNA copy number alterations, clinical characteristics, and outcome. *Blood* **116**, 4874-4884 (2010).
2. S. Larson, W. Stock, Progress in the treatment of adults with acute lymphoblastic leukemia. *Current opinion in hematology* **15**, 400-407 (2008).
3. M. Schrappe *et al.*, Outcomes after induction failure in childhood acute lymphoblastic leukemia. *The New England journal of medicine* **366**, 1371-1381 (2012).
4. R. Bassan, D. Hoelzer, Modern therapy of acute lymphoblastic leukemia. *Journal of clinical oncology : official journal of the American Society of Clinical Oncology* **29**, 532-543 (2011).
5. P. S. Gaynon *et al.*, Long-term results of the children's cancer group studies for childhood acute lymphoblastic leukemia 1983-2002: a Children's Oncology Group Report. *Leukemia* **24**, 285-297 (2010).
6. C. G. Mullighan, The molecular genetic makeup of acute lymphoblastic leukemia. *Hematology / the Education Program of the American Society of Hematology. American Society of Hematology. Education Program* **2012**, 389-396 (2012).
7. K. G. Roberts *et al.*, Outcomes of children with BCR-ABL1-like acute lymphoblastic leukemia treated with risk-directed therapy based on the levels of minimal residual disease. *Journal of clinical oncology : official journal of the American Society of Clinical Oncology* **32**, 3012-3020 (2014).
8. K. G. Roberts *et al.*, Targetable kinase-activating lesions in Ph-like acute lymphoblastic leukemia. *The New England journal of medicine* **371**, 1005-1015 (2014).
9. V. Leoni, A. Biondi, Tyrosine kinase inhibitors in BCR-ABL positive acute lymphoblastic leukemia. *Haematologica* **100**, 295-299 (2015).

10. H. M. Kantarjian *et al.*, Inotuzumab Ozogamicin versus Standard Therapy for Acute Lymphoblastic Leukemia. *The New England journal of medicine* **375**, 740-753 (2016).
11. J. Wu, J. Fu, M. Zhang, D. Liu, Blinatumomab: a bispecific T cell engager (BiTE) antibody against CD19/CD3 for refractory acute lymphoid leukemia. *J Hematol Oncol* **8**, 104 (2015).
12. R. J. Kreitman, I. Pastan, Antibody fusion proteins: anti-CD22 recombinant immunotoxin moxetumomab pasudotox. *Clin Cancer Res* **17**, 6398-6405 (2011).
13. M. Sadelain, I. Riviere, R. Brentjens, Targeting tumours with genetically enhanced T lymphocytes. *Nat Rev Cancer* **3**, 35-45 (2003).
14. W. Y. Ho, J. N. Blattman, M. L. Dossett, C. Yee, P. D. Greenberg, Adoptive immunotherapy: engineering T cell responses as biologic weapons for tumor mass destruction. *Cancer cell* **3**, 431-437 (2003).
15. H. J. Jackson, S. Rafiq, R. J. Brentjens, Driving CAR T-cells forward. *Nat Rev Clin Oncol* **13**, 370-383 (2016).
16. H. Almasbak, T. Aarvak, M. C. Vemuri, CAR T Cell Therapy: A Game Changer in Cancer Treatment. *J Immunol Res* **2016**, 5474602 (2016).
17. G. Gross, T. Waks, Z. Eshhar, Expression of immunoglobulin-T-cell receptor chimeric molecules as functional receptors with antibody-type specificity. *Proceedings of the National Academy of Sciences of the United States of America* **86**, 10024-10028 (1989).
18. B. A. Irving, A. Weiss, The cytoplasmic domain of the T cell receptor zeta chain is sufficient to couple to receptor-associated signal transduction pathways. *Cell* **64**, 891-901 (1991).
19. B. Jena, G. Dotti, L. J. Cooper, Redirecting T-cell specificity by introducing a tumor-specific chimeric antigen receptor. *Blood* **116**, 1035-1044 (2010).
20. M. Sadelain, R. Brentjens, I. Riviere, The promise and potential pitfalls of chimeric antigen receptors. *Curr Opin Immunol* **21**, 215-223 (2009).
21. M. C. Milone *et al.*, Chimeric receptors containing CD137 signal transduction domains mediate enhanced survival of T cells and increased antileukemic efficacy in vivo. *Mol Ther* **17**, 1453-1464 (2009).

22. C. Carpenito *et al.*, Control of large, established tumor xenografts with genetically retargeted human T cells containing CD28 and CD137 domains. *Proceedings of the National Academy of Sciences of the United States of America* **106**, 3360-3365 (2009).
23. M. Kalos *et al.*, T cells with chimeric antigen receptors have potent antitumor effects and can establish memory in patients with advanced leukemia. *Sci Transl Med* **3**, 95ra73 (2011).
24. S. L. Maude *et al.*, Chimeric antigen receptor T cells for sustained remissions in leukemia. *The New England journal of medicine* **371**, 1507-1517 (2014).
25. S. A. Grupp *et al.*, Chimeric antigen receptor-modified T cells for acute lymphoid leukemia. *The New England journal of medicine* **368**, 1509-1518 (2013).
26. S. L. Maude, D. T. Teachey, D. L. Porter, S. A. Grupp, CD19-targeted chimeric antigen receptor T-cell therapy for acute lymphoblastic leukemia. *Blood* **125**, 4017-4023 (2015).
27. M. Muschen, Rationale for targeting the pre-B-cell receptor signaling pathway in acute lymphoblastic leukemia. *Blood* **125**, 3688-3693 (2015).
28. M. F. Erasmus *et al.*, Dynamic pre-BCR homodimers fine-tune autonomous survival signals in B cell precursor acute lymphoblastic leukemia. *Sci Signal* **9**, ra116 (2016).
29. J. Worch, M. Rohde, B. Burkhardt, Mature B-cell lymphoma and leukemia in children and adolescents-review of standard chemotherapy regimen and perspectives. *Pediatr Hematol Oncol* **30**, 465-483 (2013).
30. D. G. Osmond, Proliferation kinetics and the lifespan of B cells in central and peripheral lymphoid organs. *Curr Opin Immunol* **3**, 179-185 (1991).
31. N. Sakaguchi, F. Melchers, Lambda 5, a new light-chain-related locus selectively expressed in pre-B lymphocytes. *Nature* **324**, 579-582 (1986).
32. M. Reth, Antigen receptors on B lymphocytes. *Annual review of immunology* **10**, 97-121 (1992).
33. K. Ohnishi, F. Melchers, The nonimmunoglobulin portion of lambda5 mediates cell-autonomous pre-B cell receptor signaling. *Nat Immunol* **4**, 849-856 (2003).

34. A. Kudo, F. Melchers, A second gene, VpreB in the lambda 5 locus of the mouse, which appears to be selectively expressed in pre-B lymphocytes. *EMBO J* **6**, 2267-2272 (1987).

35. H. Geng *et al.*, Self-enforcing feedback activation between BCL6 and pre-B cell receptor signaling defines a distinct subtype of acute lymphoblastic leukemia. *Cancer cell* **27**, 409-425 (2015).

36. B. D. Weitzner, D. Kuroda, N. Marze, J. Xu, J. J. Gray, Blind prediction performance of RosettaAntibody 3.0: grafting, relaxation, kinematic loop modeling, and full CDR optimization. *Proteins* **82**, 1611-1623 (2014).

37. N. A. Marze, S. Lyskov, J. J. Gray, Improved prediction of antibody VL-VH orientation. *Protein Eng Des Sel* **29**, 409-418 (2016).

38. A. Krebber *et al.*, Reliable cloning of functional antibody variable domains from hybridomas and spleen cell repertoires employing a reengineered phage display system. *J Immunol Methods* **201**, 35-55 (1997).

39. J. N. Kochenderfer *et al.*, Construction and preclinical evaluation of an anti-CD19 chimeric antigen receptor. *J Immunother* **32**, 689-702 (2009).

40. B. G. Pierce *et al.*, ZDOCK server: interactive docking prediction of protein-protein complexes and symmetric multimers. *Bioinformatics* **30**, 1771-1773 (2014).

41. J. K. Marzinek *et al.*, Free energy predictions of ligand binding to an alpha-helix using steered molecular dynamics and umbrella sampling simulations. *J Chem Inf Model* **54**, 2093-2104 (2014).

42. C. Oostenbrink, A. Villa, A. E. Mark, W. F. van Gunsteren, A biomolecular force field based on the free enthalpy of hydration and solvation: the GROMOS force-field parameter sets 53A5 and 53A6. *J Comput Chem* **25**, 1656-1676 (2004).

43. Z. Shen, H. Yan, Y. Zhang, R. L. Mernaugh, X. Zeng, Engineering peptide linkers for scFv immunosensors. *Anal Chem* **80**, 1910-1917 (2008).

44. D. W. Lee *et al.*, T cells expressing CD19 chimeric antigen receptors for acute lymphoblastic leukaemia in children and young adults: a phase 1 dose-escalation trial. *Lancet* **385**, 517-528 (2015).

45. R. D. Guest *et al.*, The role of extracellular spacer regions in the optimal design of chimeric immune receptors: evaluation of four different scFvs and antigens. *J Immunother* **28**, 203-211 (2005).
46. G. Dotti, S. Gottschalk, B. Savoldo, M. K. Brenner, Design and development of therapies using chimeric antigen receptor-expressing T cells. *Immunological reviews* **257**, 107-126 (2014).
47. W. Haso *et al.*, Anti-CD22-chimeric antigen receptors targeting B-cell precursor acute lymphoblastic leukemia. *Blood* **121**, 1165-1174 (2013).
48. A. Kunkele *et al.*, Functional Tuning of CARs Reveals Signaling Threshold above Which CD8+ CTL Antitumor Potency Is Attenuated due to Cell Fas-FasL-Dependent AICD. *Cancer Immunol Res* **3**, 368-379 (2015).
49. L. Ginaldi *et al.*, Levels of expression of CD19 and CD20 in chronic B cell leukaemias. *J Clin Pathol* **51**, 364-369 (1998).
50. K. Watanabe *et al.*, Target antigen density governs the efficacy of anti-CD20-CD28-CD3 zeta chimeric antigen receptor-modified effector CD8+ T cells. *Journal of immunology* **194**, 911-920 (2015).
51. A. J. Bankovich *et al.*, Structural insight into pre-B cell receptor function. *Science* **316**, 291-294 (2007).
52. P. Tolar, T. Meckel, Imaging B-cell receptor signaling by single-molecule techniques. *Methods Mol Biol* **571**, 437-453 (2009).
53. L. Gauthier, B. Rossi, F. Roux, E. Termine, C. Schiff, Galectin-1 is a stromal cell ligand of the pre-B cell receptor (BCR) implicated in synapse formation between pre-B and stromal cells and in pre-BCR triggering. *Proceedings of the National Academy of Sciences of the United States of America* **99**, 13014-13019 (2002).
54. B. Rossi, M. Espeli, C. Schiff, L. Gauthier, Clustering of pre-B cell integrins induces galectin-1-dependent pre-B cell receptor relocalization and activation. *J Immunol* **177**, 796-803 (2006).
55. D. R. Fooksman *et al.*, Functional anatomy of T cell activation and synapse formation. *Annu Rev Immunol* **28**, 79-105 (2010).
56. M. L. Dustin, D. Depoil, New insights into the T cell synapse from single molecule techniques. *Nat Rev Immunol* **11**, 672-684 (2011).

57. L. Elantak *et al.*, Structural basis for galectin-1-dependent pre-B cell receptor (pre-BCR) activation. *J Biol Chem* **287**, 44703-44713 (2012).

58. A. D. Fesnak, C. H. June, B. L. Levine, Engineered T cells: the promise and challenges of cancer immunotherapy. *Nat Rev Cancer* **16**, 566-581 (2016).

59. A. H. Long *et al.*, 4-1BB costimulation ameliorates T cell exhaustion induced by tonic signaling of chimeric antigen receptors. *Nat Med* **21**, 581-590 (2015).

60. R. Oren *et al.*, Functional comparison of engineered T cells carrying a native TCR versus TCR-like antibody-based chimeric antigen receptors indicates affinity/avidity thresholds. *J Immunol* **193**, 5733-5743 (2014).

61. M. Chmielewski, A. Hombach, C. Heuser, G. P. Adams, H. Abken, T cell activation by antibody-like immunoreceptors: increase in affinity of the single-chain fragment domain above threshold does not increase T cell activation against antigen-positive target cells but decreases selectivity. *J Immunol* **173**, 7647-7653 (2004).

62. A. Evstratova, K. Toth, Synaptically evoked Ca2+ release from intracellular stores is not influenced by vesicular zinc in CA3 hippocampal pyramidal neurones. *J Physiol* **589**, 5677-5689 (2011).

63. L. Cherkassky *et al.*, Human CAR T cells with cell-intrinsic PD-1 checkpoint blockade resist tumor-mediated inhibition. *J Clin Invest* **126**, 3130-3144 (2016).

64. X. Huang, Y. Yang, Driving an improved CAR for cancer immunotherapy. *J Clin Invest* **126**, 2795-2798 (2016).

65. A. A. Hombach *et al.*, T cell activation by antibody-like immunoreceptors: the position of the binding epitope within the target molecule determines the efficiency of activation of redirected T cells. *Journal of immunology* **178**, 4650-4657 (2007).

66. H. G. Caruso *et al.*, Tuning Sensitivity of CAR to EGFR Density Limits Recognition of Normal Tissue While Maintaining Potent Antitumor Activity. *Cancer Res* **75**, 3505-3518 (2015).

67. A. Sivasubramanian, A. Sircar, S. Chaudhury, J. J. Gray, Toward high-resolution homology modeling of antibody Fv regions and application to antibody-antigen docking. *Proteins* **74**, 497-514 (2009).

68. A. Tovchigrechko, I. A. Vakser, GRAMM-X public web server for protein-protein docking. *Nucleic Acids Res* **34**, W310-314 (2006).

69. M. Hwang, M. Garbey, S. A. Berceli, R. Tran-Son-Tay, Rule-Based Simulation of Multi-Cellular Biological Systems-A Review of Modeling Techniques. *Cell Mol Bioeng* **2**, 285-294 (2009).

70. C. A. Lopez *et al.*, MARTINI coarse-grained model for crystalline cellulose microfibers. *J Phys Chem B* **119**, 465-473 (2015).

71. C. A. Lopez, A. Sethi, B. Goldstein, B. S. Wilson, S. Gnanakaran, Membrane-mediated regulation of the intrinsically disordered CD3 cytoplasmic tail of the TCR. *Biophys J* **108**, 2481-2491 (2015).

72. M. McCabe Pryor *et al.*, Orchestration of ErbB3 signaling through heterointeractions and homointeractions. *Mol Biol Cell* **26**, 4109-4123 (2015).

73. D. Kuroda, H. Shirai, M. P. Jacobson, H. Nakamura, Computer-aided antibody design. *Protein Eng Des Sel* **25**, 507-521 (2012).

74. R. C. Rickert, New insights into pre-BCR and BCR signalling with relevance to B cell malignancies. *Nat Rev Immunol* **13**, 578-591 (2013).

75. M. S. Topp *et al.*, Phase II trial of the anti-CD19 bispecific T cell-engager blinatumomab shows hematologic and molecular remissions in patients with relapsed or refractory B-precursor acute lymphoblastic leukemia. *J Clin Oncol* **32**, 4134-4140 (2014).

76. D. Nagorsen, P. Kufer, P. A. Baeuerle, R. Bargou, Blinatumomab: a historical perspective. *Pharmacol Ther* **136**, 334-342 (2012).

77. D. L. Porter, B. L. Levine, M. Kalos, A. Bagg, C. H. June, Chimeric antigen receptor-modified T cells in chronic lymphoid leukemia. *The New England journal of medicine* **365**, 725-733 (2011).

78. C. H. Pui *et al.*, Childhood Acute Lymphoblastic Leukemia: Progress Through Collaboration. *J Clin Oncol* **33**, 2938-2948 (2015).

79. F. B. Guloglu, E. Bajor, B. P. Smith, C. A. Roman, The unique region of surrogate light chain component lambda5 is a heavy chain-specific regulator of precursor B cell receptor signaling. *J Immunol* **175**, 358-366 (2005).

80. B. P. O'Connor *et al.*, BCMA is essential for the survival of long-lived bone marrow plasma cells. *J Exp Med* **199**, 91-98 (2004).

81. D. T. Avery *et al.*, BAFF selectively enhances the survival of plasmablasts generated from human memory B cells. *J Clin Invest* **112**, 286-297 (2003).

82. R. Al-Shawi, S. V. Ashton, C. Underwood, J. P. Simons, Expression of the Ror1 and Ror2 receptor tyrosine kinase genes during mouse development. *Dev Genes Evol* **211**, 161-171 (2001).

83. M. Hudecek *et al.*, The B-cell tumor-associated antigen ROR1 can be targeted with T cells modified to express a ROR1-specific chimeric antigen receptor. *Blood* **116**, 4532-4541 (2010).

84. G. L. Beatty, E. K. Moon, Chimeric antigen receptor T cells are vulnerable to immunosuppressive mechanisms present within the tumor microenvironment. *Oncoimmunology* **3**, e970027 (2014).

85. D. M. Pardoll, The blockade of immune checkpoints in cancer immunotherapy. *Nat Rev Cancer* **12**, 252-264 (2012).

86. E. J. Wherry, T cell exhaustion. *Nature immunology* **12**, 492-499 (2011).

87. S. E. James *et al.*, Antigen sensitivity of CD22-specific chimeric TCR is modulated by target epitope distance from the cell membrane. *Journal of immunology* **180**, 7028-7038 (2008).

88. B. G. Till *et al.*, CD20-specific adoptive immunotherapy for lymphoma using a chimeric antigen receptor with both CD28 and 4-1BB domains: pilot clinical trial results. *Blood* **119**, 3940-3950 (2012).

89. J. R. James, R. D. Vale, Biophysical mechanism of T-cell receptor triggering in a reconstituted system. *Nature* **487**, 64-69 (2012).

90. C. J. Turtle *et al.*, CD19 CAR-T cells of defined CD4+:CD8+ composition in adult B cell ALL patients. *J Clin Invest* **126**, 2123-2138 (2016).

91. D. Sommermeyer *et al.*, Chimeric antigen receptor-modified T cells derived from defined CD8+ and CD4+ subsets confer superior antitumor reactivity in vivo. *Leukemia* **30**, 492-500 (2016).

92. C. Duy *et al.*, BCL6 enables Ph+ acute lymphoblastic leukaemia cells to survive BCR-ABL1 kinase inhibition. *Nature* **473**, 384-388 (2011).

CHAPTER 5: DISCUSSION

1. K. Ohnishi, F. Melchers, The nonimmunoglobulin portion of lambda5 mediates cell-autonomous pre-B cell receptor signaling. *Nature immunology* **4**, 849-856 (2003).
2. A. J. Bankovich *et al.*, Structural insight into pre-B cell receptor function. *Science (New York, N.Y.)* **316**, 291-294 (2007).
3. B. Rossi, M. Espeli, C. Schiff, L. Gauthier, Clustering of pre-B cell integrins induces galectin-1-dependent pre-B cell receptor relocalization and activation. *Journal of immunology* **177**, 796-803 (2006).
4. L. Gauthier, B. Rossi, F. Roux, E. Termine, C. Schiff, Galectin-1 is a stromal cell ligand of the pre-B cell receptor (BCR) implicated in synapse formation between pre-B and stromal cells and in pre-BCR triggering. *Proceedings of the National Academy of Sciences of the United States of America* **99**, 13014-13019 (2002).
5. T. Q. Vu, W. Y. Lam, E. W. Hatch, D. S. Lidke, Quantum dots for quantitative imaging: from single molecules to tissue. *Cell Tissue Res* **360**, 71-86 (2015).
6. C. Manzo, M. F. Garcia-Parajo, A review of progress in single particle tracking: from methods to biophysical insights. *Rep Prog Phys* **78**, 124601 (2015).
7. W. F. Van Gunsteren, H. J. Berendsen, R. G. Geurtsen, H. R. Zwinderman, A molecular dynamics computer simulation of an eight-base-pair DNA fragment in aqueous solution: comparison with experimental two-dimensional NMR data. *Ann N Y Acad Sci* **482**, 287-303 (1986).
8. T. Hansson, C. Oostenbrink, W. van Gunsteren, Molecular dynamics simulations. *Curr Opin Struct Biol* **12**, 190-196 (2002).
9. M. F. Erasmus *et al.*, Dynamic pre-BCR homodimers fine-tune autonomous survival signals in B cell precursor acute lymphoblastic leukemia. *Sci Signal* **9**, ra116 (2016).
10. B. F. Lillemeier, J. R. Pfeiffer, Z. Surviladze, B. S. Wilson, M. M. Davis, Plasma membrane-associated proteins are clustered into islands attached to the cytoskeleton. *Proceedings of the National Academy of Sciences of the United States of America* **103**, 18992-18997 (2006).

11. P. C. Maity *et al.*, B cell antigen receptors of the IgM and IgD classes are clustered in different protein islands that are altered during B cell activation. *Sci Signal* **8**, ra93 (2015).
12. N. L. Andrews *et al.*, Actin restricts FcepsilonRI diffusion and facilitates antigen-induced receptor immobilization. *Nature cell biology* **10**, 955-963 (2008).
13. N. L. Andrews *et al.*, Small, mobile FcepsilonRI receptor aggregates are signaling competent. *Immunity* **31**, 469-479 (2009).
14. H. W. Findley, Jr., M. D. Cooper, T. H. Kim, C. Alvarado, A. H. Ragab, Two new acute lymphoblastic leukemia cell lines with early B-cell phenotypes. *Blood* **60**, 1305-1309 (1982).
15. R. Hurwitz *et al.*, Characterization of a leukemic cell line of the pre-B phenotype. *International journal of cancer. Journal international du cancer* **23**, 174-180 (1979).
16. R. Ubelhart *et al.*, N-linked glycosylation selectively regulates autonomous precursor BCR function. *Nature immunology* **11**, 759-765 (2010).
17. B. Treanor *et al.*, The membrane skeleton controls diffusion dynamics and signaling through the B cell receptor. *Immunity* **32**, 187-199 (2010).
18. S. A. Freeman *et al.*, Toll-like receptor ligands sensitize B-cell receptor signalling by reducing actin-dependent spatial confinement of the receptor. *Nat Commun* **6**, 6168 (2015).
19. J. Torreno-Pina, Manzo, C and Garcia-Parajo, MF, Uncovering homo-and hetero-interactions on the cell membrane using single particle tracking approaches. *J. Phys. D: Appl. Phys.* **49**, pp12 (2016).
20. G. A. Rabinovich, M. A. Toscano, S. S. Jackson, G. R. Vasta, Functions of cell surface galectin-glycoprotein lattices. *Curr Opin Struct Biol* **17**, 513-520 (2007).
21. G. A. Rabinovich, M. A. Toscano, Turning 'sweet' on immunity: galectin-glycan interactions in immune tolerance and inflammation. *Nature reviews. Immunology* **9**, 338-352 (2009).
22. J. A. Torreno-Pina *et al.*, Enhanced receptor-clathrin interactions induced by N-glycan-mediated membrane micropatterning. *Proceedings of the*

National Academy of Sciences of the United States of America **111**, 11037-11042 (2014).

23. J. Bonzi *et al.*, Pre-B cell receptor binding to galectin-1 modifies galectin-1/carbohydrate affinity to modulate specific galectin-1/glycan lattice interactions. *Nat Commun* **6**, 6194 (2015).
24. F. Mourcin *et al.*, Galectin-1-expressing stromal cells constitute a specific niche for pre-BII cell development in mouse bone marrow. *Blood* **117**, 6552-6561 (2011).
25. L. Elantak *et al.*, Structural basis for galectin-1-dependent pre-B cell receptor (pre-BCR) activation. *The Journal of biological chemistry* **287**, 44703-44713 (2012).
26. F. Cedeno-Laurent, C. J. Dimitroff, Galectins and their ligands: negative regulators of anti-tumor immunity. *Glycoconj J* **29**, 619-625 (2012).
27. J. P. Cerliani *et al.*, Expanding the universe of cytokines and pattern recognition receptors: galectins and glycans in innate immunity. *J Clin Immunol* **31**, 10-21 (2011).
28. A. Symons, D. N. Cooper, A. N. Barclay, Characterization of the interaction between galectin-1 and lymphocyte glycoproteins CD45 and Thy-1. *Glycobiology* **10**, 559-563 (2000).
29. V. J. Hilser, Biochemistry. An ensemble view of allostery. *Science* **327**, 653-654 (2010).
30. A. Hospital, J. R. Goni, M. Orozco, J. L. Gelpi, Molecular dynamics simulations: advances and applications. *Adv Appl Bioinform Chem* **8**, 37-47 (2015).
31. D. Kern, E. R. Zuiderweg, The role of dynamics in allosteric regulation. *Curr Opin Struct Biol* **13**, 748-757 (2003).
32. C. Meynier, F. Guerlesquin, P. Roche, Computational studies of human galectin-1: role of conserved tryptophan residue in stacking interaction with carbohydrate ligands. *J Biomol Struct Dyn* **27**, 49-58 (2009).
33. M. G. Ford, T. Weimar, T. Kohli, R. J. Woods, Molecular dynamics simulations of galectin-1-oligosaccharide complexes reveal the molecular basis for ligand diversity. *Proteins* **53**, 229-240 (2003).
34. A. E. Garcia, Large-amplitude nonlinear motions in proteins. *Phys Rev Lett* **68**, 2696-2699 (1992).

35. A. Amadei, A. B. Linssen, H. J. Berendsen, Essential dynamics of proteins. *Proteins* **17**, 412-425 (1993).
36. G. Vettoretti *et al.*, Molecular Dynamics Simulations Reveal the Mechanisms of Allosteric Activation of Hsp90 by Designed Ligands. *Sci Rep* **6**, 23830 (2016).
37. S. R. Stowell *et al.*, Ligand reduces galectin-1 sensitivity to oxidative inactivation by enhancing dimer formation. *The Journal of biological chemistry* **284**, 4989-4999 (2009).
38. H. Geng *et al.*, Self-enforcing feedback activation between BCL6 and pre-B cell receptor signaling defines a distinct subtype of acute lymphoblastic leukemia. *Cancer cell* **27**, 409-425 (2015).
39. R. Pelanda, R. M. Torres, Central B-cell tolerance: where selection begins. *Cold Spring Harb Perspect Biol* **4**, a007146 (2012).
40. K. G. Roberts *et al.*, Targetable kinase-activating lesions in Ph-like acute lymphoblastic leukemia. *The New England journal of medicine* **371**, 1005-1015 (2014).
41. C. H. Pui *et al.*, Childhood Acute Lymphoblastic Leukemia: Progress Through Collaboration. *Journal of clinical oncology : official journal of the American Society of Clinical Oncology* **33**, 2938-2948 (2015).
42. T. Perova *et al.*, Therapeutic potential of spleen tyrosine kinase inhibition for treating high-risk precursor B cell acute lymphoblastic leukemia. *Science translational medicine* **6**, 236ra262 (2014).
43. M. L. Dustin, D. Depoil, New insights into the T cell synapse from single molecule techniques. *Nature reviews. Immunology* **11**, 672-684 (2011).
44. J. G. Monroe, ITAM-mediated tonic signalling through pre-BCR and BCR complexes. *Nature reviews. Immunology* **6**, 283-294 (2006).
45. Z. Chen *et al.*, Signalling thresholds and negative B-cell selection in acute lymphoblastic leukaemia. *Nature* **521**, 357-361 (2015).
46. M. Serrano, A. W. Lin, M. E. McCurrach, D. Beach, S. W. Lowe, Oncogenic ras provokes premature cell senescence associated with accumulation of p53 and p16INK4a. *Cell* **88**, 593-602 (1997).
47. C. Michaloglou *et al.*, BRAFE600-associated senescence-like cell cycle arrest of human naevi. *Nature* **436**, 720-724 (2005).

48. S. Courtois-Cox *et al.*, A negative feedback signaling network underlies oncogene-induced senescence. *Cancer cell* **10**, 459-472 (2006).
49. S. Shojaee *et al.*, Erk Negative Feedback Control Enables Pre-B Cell Transformation and Represents a Therapeutic Target in Acute Lymphoblastic Leukemia. *Cancer cell* **28**, 114-128 (2015).
50. J. Chen *et al.*, in *Probe Reports from the NIH Molecular Libraries Program*. (Bethesda (MD), 2010).
51. R. Brooks *et al.*, SHIP1 inhibition increases immunoregulatory capacity and triggers apoptosis of hematopoietic cancer cells. *Journal of immunology* **184**, 3582-3589 (2010).
52. S. Raponi *et al.*, Flow cytometric study of potential target antigens (CD19, CD20, CD22, CD33) for antibody-based immunotherapy in acute lymphoblastic leukemia: analysis of 552 cases. *Leuk Lymphoma* **52**, 1098-1107 (2011).
53. A. Vedi, D. S. Ziegler, Antibody therapy for pediatric leukemia. *Frontiers in oncology* **4**, 82 (2014).
54. E. Jabbour, S. O'Brien, F. Ravandi, H. Kantarjian, Monoclonal antibodies in acute lymphoblastic leukemia. *Blood* **125**, 4010-4016 (2015).
55. K. Matlawska-Wasowska *et al.*, Macrophage and NK-mediated killing of precursor-B acute lymphoblastic leukemia cells targeted with a-fucosylated anti-CD19 humanized antibodies. *Leukemia* **27**, 1263-1274 (2013).
56. P. Chevallier *et al.*, Hyper-CVAD + epratuzumab as salvage regimen for younger patients with relapsed/refractory CD22+ precursor B-cell ALL. *Haematologica*, (2017).
57. J. Carnahan *et al.*, Epratuzumab, a humanized monoclonal antibody targeting CD22: characterization of in vitro properties. *Clin Cancer Res* **9**, 3982S-3990S (2003).
58. R. H. Scheuermann, E. Racila, CD19 antigen in leukemia and lymphoma diagnosis and immunotherapy. *Leuk Lymphoma* **18**, 385-397 (1995).
59. P. P. Piccaluga *et al.*, Surface antigens analysis reveals significant expression of candidate targets for immunotherapy in adult acute lymphoid leukemia. *Leuk Lymphoma* **52**, 325-327 (2011).

60. Y. Hu *et al.*, Investigation of the mechanism of action of alemtuzumab in a human CD52 transgenic mouse model. *Immunology* **128**, 260-270 (2009).
61. D. A. Thomas *et al.*, Chemoimmunotherapy with a modified hyper-CVAD and rituximab regimen improves outcome in de novo Philadelphia chromosome-negative precursor B-lineage acute lymphoblastic leukemia. *Journal of clinical oncology : official journal of the American Society of Clinical Oncology* **28**, 3880-3889 (2010).
62. D. Hoelzer, N. Gokbuget, Chemoimmunotherapy in acute lymphoblastic leukemia. *Blood Rev* **26**, 25-32 (2012).
63. D. Nagorsen, P. Kufer, P. A. Baeuerle, R. Bargou, Blinatumomab: a historical perspective. *Pharmacol Ther* **136**, 334-342 (2012).
64. M. N. Dworzak *et al.*, CD20 up-regulation in pediatric B-cell precursor acute lymphoblastic leukemia during induction treatment: setting the stage for anti-CD20 directed immunotherapy. *Blood* **112**, 3982-3988 (2008).
65. M. S. Topp *et al.*, Phase II trial of the anti-CD19 bispecific T cell-engager blinatumomab shows hematologic and molecular remissions in patients with relapsed or refractory B-precursor acute lymphoblastic leukemia. *Journal of clinical oncology : official journal of the American Society of Clinical Oncology* **32**, 4134-4140 (2014).
66. M. S. Topp *et al.*, Safety and activity of blinatumomab for adult patients with relapsed or refractory B-precursor acute lymphoblastic leukaemia: a multicentre, single-arm, phase 2 study. *Lancet Oncol* **16**, 57-66 (2015).
67. R. J. Kreitman, I. Pastan, Antibody fusion proteins: anti-CD22 recombinant immunotoxin moxetumomab pasudotox. *Clin Cancer Res* **17**, 6398-6405 (2011).
68. A. S. Wayne *et al.*, Anti-CD22 immunotoxin RFB4(dsFv)-PE38 (BL22) for CD22-positive hematologic malignancies of childhood: preclinical studies and phase I clinical trial. *Clin Cancer Res* **16**, 1894-1903 (2010).
69. H. J. Jackson, S. Rafiq, R. J. Brentjens, Driving CAR T-cells forward. *Nat Rev Clin Oncol* **13**, 370-383 (2016).
70. S. A. Grupp *et al.*, Chimeric antigen receptor-modified T cells for acute lymphoid leukemia. *The New England journal of medicine* **368**, 1509-1518 (2013).

71. J. H. Park, M. B. Geyer, R. J. Brentjens, CD19-targeted CAR T-cell therapeutics for hematologic malignancies: interpreting clinical outcomes to date. *Blood* **127**, 3312-3320 (2016).

72. U. N. L. o. Sceince, *ClinicalTrials.gov [online]* **https://clinicaltrials.gov/ct2/show/NCT01044069**, (2016).

73. R. J. Brentjens *et al.*, CD19-targeted T cells rapidly induce molecular remissions in adults with chemotherapy-refractory acute lymphoblastic leukemia. *Sci Transl Med* **5**, 177ra138 (2013).

74. J. Park, Riviere, I, Wang, X, Vernal, Y, Purdon, T, Halton, E, Curran, JK, Sauter, CS, Sadelain, M, and Brentjens, RJ, Efficacy and safety of CD19-targeted 19-28z CAR modified T cells in adult patients with relapsed or refractory B-ALL. *33* **15**, (2015).

75. L. Nitschke, CD22 and Siglec-G: B-cell inhibitory receptors with distinct functions. *Immunological reviews* **230**, 128-143 (2009).

76. G. Dotti, S. Gottschalk, B. Savoldo, M. K. Brenner, Design and development of therapies using chimeric antigen receptor-expressing T cells. *Immunological reviews* **257**, 107-126 (2014).

77. D. L. Porter, B. L. Levine, M. Kalos, A. Bagg, C. H. June, Chimeric antigen receptor-modified T cells in chronic lymphoid leukemia. *The New England journal of medicine* **365**, 725-733 (2011).

78. M. Kalos *et al.*, T cells with chimeric antigen receptors have potent antitumor effects and can establish memory in patients with advanced leukemia. *Sci Transl Med* **3**, 95ra73 (2011).

79. R. A. Morgan *et al.*, Case report of a serious adverse event following the administration of T cells transduced with a chimeric antigen receptor recognizing ERBB2. *Molecular therapy : the journal of the American Society of Gene Therapy* **18**, 843-851 (2010).

80. B. J. Cameron *et al.*, Identification of a Titin-derived HLA-A1-presented peptide as a cross-reactive target for engineered MAGE A3-directed T cells. *Science translational medicine* **5**, 197ra103 (2013).

81. S. L. Maude, D. Barrett, D. T. Teachey, S. A. Grupp, Managing cytokine release syndrome associated with novel T cell-engaging therapies. *Cancer J* **20**, 119-122 (2014).

82. W. Qasim *et al.*, Molecular remission of infant B-ALL after infusion of universal TALEN gene-edited CAR T cells. *Science translational medicine* **9**, (2017).
83. J. A. Fraietta *et al.*, Ibrutinib enhances chimeric antigen receptor T-cell engraftment and efficacy in leukemia. *Blood* **127**, 1117-1127 (2016).
84. S. L. Maude *et al.*, Chimeric antigen receptor T cells for sustained remissions in leukemia. *The New England journal of medicine* **371**, 1507-1517 (2014).
85. D. W. Lee *et al.*, T cells expressing CD19 chimeric antigen receptors for acute lymphoblastic leukaemia in children and young adults: a phase 1 dose-escalation trial. *Lancet* **385**, 517-528 (2015).
86. E. Sotillo *et al.*, Convergence of Acquired Mutations and Alternative Splicing of CD19 Enables Resistance to CART-19 Immunotherapy. *Cancer Discov* **5**, 1282-1295 (2015).
87. M. Hegde *et al.*, Combinational Targeting Offsets Antigen Escape and Enhances Effector Functions of Adoptively Transferred T Cells in Glioblastoma. *Molecular therapy : the journal of the American Society of Gene Therapy* **21**, 2087-2101 (2013).
88. M. Ruella *et al.*, Dual CD19 and CD123 targeting prevents antigen-loss relapses after CD19-directed immunotherapies. *J Clin Invest* **126**, 3814-3826 (2016).
89. X. Zhang *et al.*, Anti-CD20 Antibody with Multimerized Fc Domains: A Novel Strategy To Deplete B Cells and Augment Treatment of Autoimmune Disease. *Journal of immunology* **196**, 1165-1176 (2016).
90. M. Ruella, M. V. Maus, Catch me if you can: Leukemia Escape after CD19-Directed T Cell Immunotherapies. *Comput Struct Biotechnol J* **14**, 357-362 (2016).
91. F. B. Guloglu, E. Bajor, B. P. Smith, C. A. Roman, The unique region of surrogate light chain component lambda5 is a heavy chain-specific regulator of precursor B cell receptor signaling. *Journal of immunology* **175**, 358-366 (2005).
92. B. P. O'Connor *et al.*, BCMA is essential for the survival of long-lived bone marrow plasma cells. *The Journal of experimental medicine* **199**, 91-98 (2004).

93. D. T. Avery *et al.*, BAFF selectively enhances the survival of plasmablasts generated from human memory B cells. *The Journal of clinical investigation* **112**, 286-297 (2003).
94. V. T. Bicocca *et al.*, Crosstalk between ROR1 and the Pre-B cell receptor promotes survival of t(1;19) acute lymphoblastic leukemia. *Cancer cell* **22**, 656-667 (2012).
95. A. Choudhury *et al.*, Silencing of ROR1 and FMOD with siRNA results in apoptosis of CLL cells. *British journal of haematology* **151**, 327-335 (2010).
96. R. Al-Shawi, S. V. Ashton, C. Underwood, J. P. Simons, Expression of the Ror1 and Ror2 receptor tyrosine kinase genes during mouse development. *Dev Genes Evol* **211**, 161-171 (2001).
97. M. Hudecek *et al.*, The B-cell tumor-associated antigen ROR1 can be targeted with T cells modified to express a ROR1-specific chimeric antigen receptor. *Blood* **116**, 4532-4541 (2010).
98. G. L. Beatty, E. K. Moon, Chimeric antigen receptor T cells are vulnerable to immunosuppressive mechanisms present within the tumor microenvironment. *Oncoimmunology* **3**, e970027 (2014).
99. D. M. Pardoll, The blockade of immune checkpoints in cancer immunotherapy. *Nat Rev Cancer* **12**, 252-264 (2012).
100. A. E. Moran, K. A. Hogquist, T-cell receptor affinity in thymic development. *Immunology* **135**, 261-267 (2012).
101. A. Kunkele *et al.*, Functional Tuning of CARs Reveals Signaling Threshold above Which CD8+ CTL Antitumor Potency Is Attenuated due to Cell Fas-FasL-Dependent AICD. *Cancer Immunol Res* **3**, 368-379 (2015).
102. W. Haso *et al.*, Anti-CD22-chimeric antigen receptors targeting B-cell precursor acute lymphoblastic leukemia. *Blood* **121**, 1165-1174 (2013).
103. M. Hudecek *et al.*, Receptor affinity and extracellular domain modifications affect tumor recognition by ROR1-specific chimeric antigen receptor T cells. *Clin Cancer Res* **19**, 3153-3164 (2013).
104. K. Watanabe *et al.*, Target antigen density governs the efficacy of anti-CD20-CD28-CD3 zeta chimeric antigen receptor-modified effector CD8+ T cells. *J Immunol* **194**, 911-920 (2015).

105. A. Hombach, A. A. Hombach, H. Abken, Adoptive immunotherapy with genetically engineered T cells: modification of the IgG1 Fc 'spacer' domain in the extracellular moiety of chimeric antigen receptors avoids 'off-target' activation and unintended initiation of an innate immune response. *Gene Ther* **17**, 1206-1213 (2010).

106. A. Hombach *et al.*, T cell activation by recombinant FcepsilonRI gamma-chain immune receptors: an extracellular spacer domain impairs antigen-dependent T cell activation but not antigen recognition. *Gene Ther* **7**, 1067-1075 (2000).

107. M. Chmielewski, A. Hombach, C. Heuser, G. P. Adams, H. Abken, T cell activation by antibody-like immunoreceptors: increase in affinity of the single-chain fragment domain above threshold does not increase T cell activation against antigen-positive target cells but decreases selectivity. *Journal of immunology* **173**, 7647-7653 (2004).

108. S. Thomas *et al.*, Human T cells expressing affinity-matured TCR display accelerated responses but fail to recognize low density of MHC-peptide antigen. *Blood* **118**, 319-329 (2011).

109. R. Oren *et al.*, Functional comparison of engineered T cells carrying a native TCR versus TCR-like antibody-based chimeric antigen receptors indicates affinity/avidity thresholds. *Journal of immunology* **193**, 5733-5743 (2014).

110. H. G. Caruso *et al.*, Tuning Sensitivity of CAR to EGFR Density Limits Recognition of Normal Tissue While Maintaining Potent Antitumor Activity. *Cancer Res* **75**, 3505-3518 (2015).

111. X. Liu *et al.*, Affinity-Tuned ErbB2 or EGFR Chimeric Antigen Receptor T Cells Exhibit an Increased Therapeutic Index against Tumors in Mice. *Cancer research* **75**, 3596-3607 (2015).

112. A. Viola, A. Lanzavecchia, T cell activation determined by T cell receptor number and tunable thresholds. *Science (New York, N.Y.)* **273**, 104-106 (1996).

113. A. H. Long *et al.*, 4-1BB costimulation ameliorates T cell exhaustion induced by tonic signaling of chimeric antigen receptors. *Nat Med* **21**, 581-590 (2015).

114. B. G. Till *et al.*, CD20-specific adoptive immunotherapy for lymphoma using a chimeric antigen receptor with both CD28 and 4-1BB domains: pilot clinical trial results. *Blood* **119**, 3940-3950 (2012).
115. P. Chames, M. Van Regenmortel, E. Weiss, D. Baty, Therapeutic antibodies: successes, limitations and hopes for the future. *Br J Pharmacol* **157**, 220-233 (2009).
116. N. Shimba *et al.*, Comparative thermodynamic analyses of the Fv, Fab* and Fab fragments of anti-dansyl mouse monoclonal antibody. *FEBS Lett* **360**, 247-250 (1995).
117. R. E. Bird *et al.*, Single-chain antigen-binding proteins. *Science (New York, N.Y.)* **242**, 423-426 (1988).
118. J. S. Huston *et al.*, Protein engineering of antibody binding sites: recovery of specific activity in an anti-digoxin single-chain Fv analogue produced in Escherichia coli. *Proceedings of the National Academy of Sciences of the United States of America* **85**, 5879-5883 (1988).
119. K. M. Arndt, K. M. Muller, A. Pluckthun, Factors influencing the dimer to monomer transition of an antibody single-chain Fv fragment. *Biochemistry* **37**, 12918-12926 (1998).
120. J. M. Perchiacca, M. Bhattacharya, P. M. Tessier, Mutational analysis of domain antibodies reveals aggregation hotspots within and near the complementarity determining regions. *Proteins* **79**, 2637-2647 (2011).
121. B. D. Weitzner, D. Kuroda, N. Marze, J. Xu, J. J. Gray, Blind prediction performance of RosettaAntibody 3.0: grafting, relaxation, kinematic loop modeling, and full CDR optimization. *Proteins* **82**, 1611-1623 (2014).
122. B. G. Pierce *et al.*, ZDOCK server: interactive docking prediction of protein-protein complexes and symmetric multimers. *Bioinformatics (Oxford, England)* **30**, 1771-1773 (2014).
123. S. Chaudhury *et al.*, Benchmarking and analysis of protein docking performance in Rosetta v3.2. *PloS one* **6**, e22477 (2011).
124. J. K. Marzinek *et al.*, Free energy predictions of ligand binding to an alpha-helix using steered molecular dynamics and umbrella sampling simulations. *J Chem Inf Model* **54**, 2093-2104 (2014).
125. M. Kiyoshi *et al.*, Affinity improvement of a therapeutic antibody by structure-based computational design: generation of electrostatic

interactions in the transition state stabilizes the antibody-antigen complex. *PloS one* **9**, e87099 (2014).

126. A. D. Fesnak, C. H. June, B. L. Levine, Engineered T cells: the promise and challenges of cancer immunotherapy. *Nat Rev Cancer* **16**, 566-581 (2016).
127. D. R. Fooksman *et al.*, Functional anatomy of T cell activation and synapse formation. *Annual review of immunology* **28**, 79-105 (2010).
128. D. Sommermeyer *et al.*, Chimeric antigen receptor-modified T cells derived from defined CD8+ and CD4+ subsets confer superior antitumor reactivity in vivo. *Leukemia* **30**, 492-500 (2016).
129. C. J. Turtle *et al.*, CD19 CAR-T cells of defined CD4+:CD8+ composition in adult B cell ALL patients. *The Journal of clinical investigation* **126**, 2123-2138 (2016).
130. C. Duy *et al.*, BCL6 enables Ph+ acute lymphoblastic leukaemia cells to survive BCR-ABL1 kinase inhibition. *Nature* **473**, 384-388 (2011).